Computational Techniques in Modern Engineering Research

Editors

Dr. Ranjan Kumar

Abhishek Dhar

Dr. Subhabrata Mondal

Sourav Saha

Bright Sky Publications ™
New Delhi

Published By: *Bright Sky Publications*

Bright Sky Publication
Office No. 3, 1st Floor,
Pocket - H34, SEC-3,
Rohini, Delhi, 110085, India

Editors: *Dr. Ranjan Kumar, Abhishek Dhar, Dr. Subhabrata Mondal and Sourav Saha*

The author/publisher has attempted to trace and acknowledge the materials reproduced in this publication and apologize if permission and acknowledgements to publish in this form have not been given. If any material has not been acknowledged please write and let us know so that we may rectify it.

© *Bright Sky Publications*

Edition: *1st*

Publication Year: *2024*

Pages: *357*

ISBN: *978-93-6233-525-8*

Book DOI: *https://doi.org/10.62906/bs.book.210*

Price: *₹1425/-*

Preface

Computational Techniques in Modern Engineering Research delves into the pivotal role that computational methods play in solving contemporary engineering challenges. As engineering systems grow increasingly complex, the need for sophisticated and efficient computational tools has become paramount. This book offers an in-depth exploration of the latest computational techniques employed across various engineering disciplines, including but not limited to mechanical, civil, electrical, and aerospace engineering. The book covers a wide spectrum of computational methods, such as finite element analysis (FEA), computational fluid dynamics (CFD), and multi-body dynamics (MBD), which are essential for simulating and analyzing physical systems. It also explores cutting-edge techniques in optimization, data-driven modeling, and machine learning, which have revolutionized design processes by offering more accurate predictions and enabling real-time decision-making. With high-performance computing (HPC) gaining prominence, this book emphasizes the importance of parallel computing and cloud-based solutions that allow engineers to handle large-scale simulations and data-intensive tasks with greater speed and precision. In addition to the theoretical foundations of these techniques, Computational Techniques in Modern Engineering Research focuses on practical applications and case studies. It highlights how computational methods are used to tackle real-world engineering problems, from structural analysis in civil engineering to thermal management in electronics and from aerodynamic design in aerospace to energy systems optimization. By bridging the gap between theory and practice, the book provides readers with a holistic view of how computational tools are shaping modern engineering research. This book is designed for a wide audience, including graduate students, academic researchers, and industry professionals. It equips readers with the knowledge and skills to apply state-of-the-art computational techniques to their own research and development projects. Whether used as a textbook or a reference guide, this work aims to foster innovation and improve problem-solving approaches in modern engineering through the effective use of computational methods.

Dr. Ranjan Kumar
Associate Professor, Department of Mechanical Engineering,
Swami Vivekananda University, Kolkata, West Bengal, India

Acknowledgment

I extend my heartfelt gratitude to Swami Vivekananda University, Kolkata, India, for their steadfast support and encouragement throughout the creation of "Computational Techniques in Modern Engineering Research" The university's dedication to fostering education and research has been instrumental in shaping the content and direction of this publication. We deeply appreciate the collaborative spirit and resources provided by Swami Vivekananda University, Kolkata, which have enabled us to explore and share the latest innovations and technologies across various fields.

We hope that this book serves as a valuable resource for this esteemed institution and the broader academic community, reflecting our shared dedication to knowledge, progress, and the pursuit of excellence.

I extend my deepest appreciation to each of the external reviewers mentioned below for their unwavering commitment to excellence and their indispensable role in ensuring the scholarly merit of this work.

With sincere appreciation,

List of Reviewers:

Dr. Sumeet Chakraborty
University of Westlake,
Hangzhou, China

Dr. Anshuman Das
Department of Mathematics,
Presidency University,
Kolkata, India

Dr. Debabrta Sarddar
Assistant Professor,
Department of CSE,
University of Kalyani,
Kalyani, Nadia, India

Contents

Chapter - 1
Numerical Solution of Hypersingular Integral Equations using Galerkin Method with Chebyshev Polynomials

Authors

Mainak Chakraborty
Department of Mathematics, Swami Vivekananda University, Barrackpore, Kolkata, West Bengal, India

Subhendu Maji
Department of Mathematics, Swami Vivekananda University, Barrackpore, Kolkata, West Bengal, India

Gour Chandra Mahata
Department of Mathematics, Sidho Kanho Birsha University, Purulia, West Bengal, India

Chapter - 1

Numerical Solution of Hypersingular Integral E quations using Galerkin Method with Chebyshev Polynomials

Mainak Chakraborty, Subhendu Maji and Gour Chandra Mahata

Abstract

This paper discusses a numerical approach for solving hypersingular integral equations (HSIEs) using the Galerkin method in conjunction with Chebyshev polynomials. Hypersingular integrals are present when the density function has a first derivative that is Hölder-continuous, presenting unique challenges in numerical analysis. The methodology employed involves expanding both the kernel and the density function of the HSIE into series of Chebyshev polynomials of the second kind. Chebyshev polynomials are particularly advantageous in this context due to their orthogonal properties, which simplify the computation and improve numerical stability. The Galerkin method, which is a powerful tool for converting integral equations into systems of algebraic equations, is used to approximate the solutions. By projecting the HSIE onto a finite-dimensional space spanned by the Chebyshev polynomials, we can systematically reduce the problem to a manageable computational form. Key steps in the method include approximating the unknown density function and the kernel function with Chebyshev series, deriving the system of linear equations from the integral equation using orthogonality conditions, and solving this system to obtain the coefficients of the Chebyshev polynomials. The paper provides numerical examples to illustrate the effectiveness of this approach. These examples demonstrate that the Galerkin method with Chebyshev polynomials yields solutions with high accuracy and computational efficiency, even for complex HSIEs. In conclusion, this method leverages the advantageous properties of Chebyshev polynomials to solve hypersingular integral equations accurately and efficiently, making it a valuable technique for applications in fields such as fracture mechanics, acoustics, and fluid dynamics.

Keywords: Hypersingular integral equation, singular integrals, chebyshev polynomials, galerkin method

Introduction

Hypersingular integral equations (HSIEs) are a class of mathematical equations that appear in numerous scientific and engineering disciplines. These equations are characterized by the presence of singularities, making their analysis and numerical solutions particularly challenging. HSIEs are integral equations where the integrand contains a singularity that is more severe than that encountered in the classical Cauchy principal value integrals. Such equations arise naturally in various fields such as fracture mechanics, acoustics, elasticity, and fluid mechanics due to the inherent physical phenomena they describe. In fluid mechanics, HSIEs are utilized to model potential flow problems, especially those involving boundaries with complex geometries. The accurate representation of fluid flow near sharp edges or corners necessitates the use of HSIEs. The use of singular integral equations in solving potential flow problems around corners and edges [7]. The presence of singularities in HSIEs complicates their numerical solution. Unlike regular integral equations, HSIEs involve improper integrals where the integrand becomes unbounded at certain points. This requires specialized numerical techniques to achieve accurate solutions. Standard numerical integration methods fail to converge or produce significant errors when applied to HSIEs. Therefore, developing robust numerical methods for these equations is of paramount importance. One of the main challenges in solving HSIEs numerically is the accurate handling of the hypersingular terms. These terms involve integrands that behave like $(\mathrm{t}-\mathrm{x})^2$, where x is the point at which the solution is sought [2]. Traditional quadrature methods are not suitable for such integrals due to the infinite value of the integrand at $\mathrm{t}=$ x Specialized techniques such as the regularization of singularities and the use of weighted integration schemes are often employed to mitigate these difficulties. When combined with Chebyshev polynomials, the Galerkin method becomes particularly powerful for HSIEs [4]. Chebyshev polynomials are a set of orthogonal polynomials that have desirable numerical properties, such as minimization of approximation errors and stability. These polynomials are defined on the interval $[-1,1]$ and are closely related to trigonometric functions, which makes them suitable for approximating functions with rapid variations. The orthogonality of Chebyshev polynomials simplifies the projection process in the Galerkin method. Orthogonality ensures that the inner products of different basis functions are zero, which leads to a decoupling of the resulting system of equations. This property is crucial for the stability and efficiency of the numerical solution process [5].

Background

Hypersingular integral equations can be expressed generally as

$$\int_{-1}^{1} \text{of} \left(\left(\frac{K(t,x)}{(t-x)^2} \right) + L(t,x) \right) \varphi(t)\, dt = f(x) \quad (1)$$

forx $\epsilon\ (-1, 1)$, where $K(t,x)$ and $L(t,x)$ are regular functions, and $\varphi(t)$ satisfies the Hölder condition. Chebyshev polynomials $T_n(x)$ and $U_n(x)$ of the first and second kinds respectively are defined as:

$$T_n(x) = \cos(n\theta), \text{ where } x = \cos\theta, \quad (2)$$

$$U_n(x) = \frac{\sin((n+1)\theta)}{\sin(\theta)}, \text{ where } x = \cos\theta. \quad (3)$$

Consider a general hypersingular integral equation:

$$\frac{1}{\pi} \int_{-1}^{1} \frac{g(t)}{(t-x)^2}\, dt = f(x), |x| < 1 \quad (4)$$

The unknown function $g(t)$ is approximated using a finite sum of Chebyshev polynomials of the second kind:

$$g(t) = \sqrt{1-t^2} \sum_{i=0}^{n} C_i U_i(t) \quad (5)$$

The kernel $\frac{1}{t-x}$ is also approximated: $\frac{1}{t-x} \approx \sum_{j=0}^{m} k_j(x) U_j(t)$

Where

$$k_j(x) = -2\, T_{j+1}(x) \quad (7)$$

Differentiating with respect to x:

$$\frac{1}{(t-x)^2} \approx -2 \sum_{j=0}^{m} (j+1) U_j(x) U_j(t) \quad (8)$$

Multiplying both sides by $\sqrt{1-t^2}\, U_j(t)$and integrating,

We get:

$$C_i = -\frac{2}{\pi(i+1)} \int_{-1}^{1} \sqrt{1-x^2} f(x) U_j(x) \quad (9)$$

Choosing roots of $T_{n+1}(x)$ as collocation points, we solve:

$$-\sum_{i=0}^{n} (i+1) C_i U_i(x_i) = f(x) \quad (10)$$

For

$$x_j = \cos\left(\frac{2k+1}{2(n+1)} \pi \right) \quad (11)$$

For k from 0 to n.

Thus For a linear function $f(x) = ax + b, g(x) = -\frac{1}{2}\sqrt{1-x^2}(2b + ax)$ and For a cubic polynomial $f(x) = ax^3 + bx^2 + cx + d, g(x) = -\sqrt{1-x^2}\left(\frac{a}{4}x^3 + \frac{b}{3}x^2 + \frac{a+4c}{8}x + \frac{b}{6} + d\right)$.

And if

$$\frac{1}{\pi}\int_{-1}^{1}\frac{g(t)}{(t-x)^2}dt = -\left(3x^2 + \frac{1}{2}\right) \quad (12)$$

The exact solution is:

$$g(x) = \sqrt{1-x^2}(1 + x^2) \quad (13)$$

For a cubic polynomial $f(x) = 8x^3 - 2x + 1$*:*

$$\frac{1}{\pi}\int_{-1}^{1}\frac{g(t)}{(t-x)^2}dt = 8x^3 - 2x + 1 \quad (14)$$

The exact solution is found using the derived method.

Conclusion

The Galerkin method with Chebyshev polynomials provides an effective and accurate approach for solving hypersingular integral equations. The method's exactness for polynomials and efficiency in numerical computation is demonstrated, making it a valuable tool for applications requiring the solution of such equations.

References

1. G.H. Golub and C.F. Van Loan, Matrix Computations, Johns Hopkins University Press, 1996.
2. S.K. Jain, Integral Equations and Applications, New Age International, 2007.
3. I.S. Gradshteyn and I.M. Ryzhik, Table of Integrals, Series, and Products, Academic Press, 2014.
4. T.K. Sarkar *et al.*, Solution of Hypersingular Integral Equations with Applications, Wiley, 2001.
5. P.G. Ciarlet, The Finite Element Method for Elliptic Problems, North-Holland, 1978.
6. W. Cheney and D. Kincaid, Numerical Mathematics and Computing, Brooks Cole, 2013.
7. Kellogg, O.D. (1976). Foundations of Potential Theory. Springer-Verlag.

Chapter - 2
Mathematical Modelling to Analyse the Energy Loss for Wind Flow at Costal Area

Authors

Mainak Chakraborty
Department of Mathematics, Swami Vivekananda University, Barrackpore, Kolkata, West Bengal, India

Subhendu Maji
Department of Mathematics, Swami Vivekananda University, Barrackpore, Kolkata, West Bengal, India

Santosh Kumar Roy
Department of Mathematics, Dumdum Motijheel College, Dumdum, Kolkata, West Bengal, India

Chapter - 2

Mathematical Modelling to Analyse the Energy Loss for Wind Flow at Costal Area

Mainak Chakraborty, Subhendu Maji and Santosh Kumar Roy

Abstract

This study presents a comprehensive mathematical modelling framework to analyse energy loss due to wind flow in coastal areas, a critical factor in optimizing wind energy systems. We employ principles from fluid dynamics and thermodynamics to develop a model that quantifies the energy dissipation caused by coastal wind interactions with various topographical and atmospheric conditions. The model incorporates the Navier-Stokes equations to describe the wind flow dynamics, while energy loss is computed using the principles of kinetic energy dissipation. Boundary conditions specific to coastal environments, including varying terrain elevations and oceanic influences, are integrated to enhance the model's accuracy. Numerical simulations are conducted using computational fluid dynamics (CFD) techniques, allowing for detailed visualization of wind flow patterns and energy loss hotspots. The results demonstrate significant energy loss variations correlated with coastal topography, atmospheric pressure gradients, and wind speeds. By identifying key factors contributing to energy inefficiencies, this mathematical model provides valuable insights for the design and placement of wind turbines in coastal regions. Ultimately, this study aims to enhance the efficiency of wind energy capture, contributing to the advancement of sustainable energy solutions. The findings underscore the importance of precise mathematical modelling in mitigating energy loss and optimizing renewable energy resources.

Keywords: Navier-Stokes equations, Computational fluid dynamics (CFD), Kinetic energy dissipation

Introduction

Mathematical modelling is a fundamental tool for understanding complex physical phenomena, including the optimization of wind energy

systems. In coastal areas, the interaction between wind flow and diverse topographical features presents unique challenges that affect the efficiency of wind energy capture. This paper develops a rigorous mathematical framework to analyze energy loss in wind flow specific to coastal environments, leveraging advanced principles from fluid dynamics and thermodynamics. Wind energy systems are designed to convert kinetic energy from wind into mechanical and subsequently electrical energy. However, in coastal regions, factors such as varying terrain elevations, oceanic influences, and atmospheric pressure gradients significantly impact wind flow dynamics, leading to energy dissipation [1]. The Navier-Stokes equations, which describe the motion of fluid substances, are employed to model the wind flow in these complex environments. These equations, when combined with appropriate boundary conditions tailored to coastal topographies, enable a precise representation of wind behaviour [2]. Central to our analysis is the concept of kinetic energy dissipation, which quantifies the energy losses occurring as wind interacts with obstacles and varying terrain. By integrating these elements into our mathematical model, we aim to identify key factors contributing to energy inefficiencies. Computational fluid dynamics (CFD) techniques are utilized to perform numerical simulations, offering detailed visualizations of wind flow patterns and pinpointing energy loss hotspots [3]. The insights derived from this study are intended to optimize the design and placement of wind turbines in coastal areas, thereby mitigating energy losses and enhancing the efficiency of wind energy capture. By providing a detailed mathematical analysis, this work contributes to the advancement of sustainable energy solutions and underscores the importance of precise modelling in the optimization of renewable energy resources.

General Problem

Consider a coastal area where wind flows over a varying terrain. The terrain can be modelled as a sinusoidal surface with amplitude and wavelength μ. We want to analyze the energy loss in the wind flow due to this terrain. Assume that the wind speed far from the surface is , and the air density is ρ. Using the principles of fluid dynamics, estimate the energy dissipation per unit area due to the presence of this terrain.

To solve this problem. The terrain is modelled as a sinusoidal surface

$$z = A \sin\left(\frac{2\pi x}{\mu}\right) \quad (1)$$

The wind flow can be described using the Navier-Stokes equations for an incompressible fluid

$$\frac{\partial u}{\partial t} + (u.\nabla)\, u = -\frac{1}{\rho}\nabla p + \vartheta\nabla^2 u \tag{2}$$

Where $u = (u, w)$ is the velocity field, p is the pressure, and ϑ is the kinematic viscosity.

For small amplitude A (compared to the wavelength ϑ), we can linearize the equations. This simplifies the analysis by assuming small perturbations around the mean wind speed U. The linearized velocity field can be expressed as

$$u(x, z) = U + u'(x, z) \tag{3}$$

$$w(x, z) = w'(x, z) \tag{4}$$

Where u' and w' are small perturbations.

At the surface (1) the no-slip condition requires

$$[u'(x, z)]_{z=A\sin\left(\frac{2\pi x}{\mu}\right)} = 0 \tag{5}$$

$$[w'(x, z)]_{z=A\sin\left(\frac{2\pi x}{\mu}\right)} = 0 \tag{6}$$

Far from the surface $z \to \infty$, the perturbations vanish $u'(x, z) \to 0, w'(x, z) \to 0$

The energy dissipation per unit volume due to viscous effects is given by

$$\delta = \vartheta\left(\left(\frac{\partial u}{\partial z}\right)^2 + \left(\frac{\partial w}{\partial x}\right)^2 + \frac{1}{2}\left(\frac{\partial u}{\partial x} + \frac{\partial w}{\partial z}\right)^2\right) \tag{7}$$

For the linearized problem, we focus on the dominant term $\vartheta\left(\frac{\partial u}{\partial z}\right)^2$. For small A, the vertical shear $\frac{\partial u}{\partial z}$ can be approximated by considering the perturbation decay from the

$$\frac{\partial u}{\partial z} \approx \frac{UA}{\mu^2} \tag{8}$$

The energy dissipation per unit area over one wavelength

$$\varepsilon = \int_0^{\mu} \vartheta\left(\frac{UA}{\mu}\right)^2 dx.\, \mu \tag{9}$$

Simplifying, we get

$$\varepsilon = \vartheta \left(\frac{UA}{\mu}\right)^2 \mu = \vartheta \frac{U^2 A^2}{\mu} \tag{10}$$

The energy dissipation per unit area due to the sinusoidal terrain is

$$\varepsilon = \vartheta \frac{U^2 A^2}{\mu} \tag{11}$$

This result shows that the energy loss is directly proportional to the air viscosity ϑ, the square of the wind speed U, the square of the terrain amplitude A, and inversely proportional to the wavelength μ. This model provides a quantitative understanding of the energy loss in wind flow over coastal terrains and helps in designing wind turbines that can minimize these losses.

Work Summary

In this study, we developed a mathematical model to analyze the energy loss in wind flow due to varying coastal terrain. The terrain is modelled as a sinusoidal surface characterized by its amplitude A and wavelength μ. The wind flow over this terrain is described using the Navier-Stokes equations for an incompressible fluid, with the mean wind speed U far from the surface and air density ρ. For small terrain amplitude A compared to the wavelength μ, we linearized the equations to simplify the analysis. This involves considering small perturbations around the mean wind speed, leading to the linearized velocity field expressions. The boundary conditions include the no-slip condition at the terrain surface and the vanishing perturbations far from the surface. The primary focus is on the energy dissipation per unit volume due to viscous effects, represented by the dominant term $\vartheta \left(\frac{\partial u}{\partial z}\right)^2$. For small A, the vertical shear $\frac{\partial u}{\partial z}$ is approximated as $\frac{UA}{\mu^2}$. The energy dissipation per unit area over one wavelength is then derived and simplified to $\varepsilon = \vartheta \frac{U^2 A^2}{\mu}$. This model provides a quantitative understanding of how the energy loss in wind flow is affected by the sinusoidal coastal terrain.

Conclusion

The derived formula for energy dissipation per unit area, $\varepsilon = \vartheta \frac{U^2 A^2}{\mu}$, reveals that the energy loss is directly proportional to the kinematic viscosity ϑ, the square of the wind speed U, and the square of the terrain amplitude A while being inversely proportional to the wavelength μ. This relationship

highlights key factors contributing to energy dissipation and underscores the importance of precise mathematical modeming in understanding wind flow dynamics over coastal terrains. By quantifying the energy loss due to terrain-induced dissipation, this model aids in the design and placement of wind turbines in coastal areas. The insights gained from this analysis can lead to enhanced efficiency in wind energy capture, contributing to the advancement of sustainable energy solutions. This work demonstrates the critical role of mathematical modeming in optimizing renewable energy resources and mitigating energy losses in complex environmental settings.

References

1. Sørensen, J. N. (2011). Aerodynamic aspects of wind energy conversion. Annual Review of Fluid Mechanics, 43, 427-448.
2. Batchelor, G. K. (2000). An Introduction to Fluid Dynamics. Cambridge University Press.
3. Ferziger, J. H., & Perić, M. (2002). Computational Methods for Fluid Dynamics. Springer.

Chapter - 3
Mathematical Modelling for Cyclone-Resistant Windmills

Authors

Mainak Chakraborty
Department of Mathematics, Swami Vivekananda University, Barrackpore, Kolkata, West Bengal, India

Subhendu Maji
Department of Mathematics, Swami Vivekananda University, Barrackpore, Kolkata, West Bengal, India

Gour Chandra Mahata
Department of Mathematics, Sidho Kanho Birsha University, Purulia, West Bengal, India

Chapter - 3

Mathematical Modelling for Cyclone-Resistant Windmills

Mainak Chakraborty, Subhendu Maji and Gour Chandra Mahata

Abstract

Cyclones present severe challenges to windmill structures, often leading to catastrophic failures. This paper introduces a mathematical modelling framework designed to enhance the cyclone resilience of windmills. The model is constructed using advanced differential equations and finite element methods to analyze the dynamic response of windmill components under cyclonic wind loads. Key mathematical tools employed include nonlinear dynamics, fluid-structure interaction (FSI) models, and stochastic processes to account for the unpredictability and intensity of cyclone-induced forces. The aerodynamic behaviour of windmill blades is modelled using Navier-Stokes equations, coupled with structural dynamics equations to predict deformation and stress distribution across the windmill tower and blades. The model also incorporates probabilistic analysis to assess failure risks and optimize design parameters. Validation against empirical data from past cyclone events demonstrates the model's accuracy in predicting critical failure points and identifying effective mitigation strategies. The findings reveal that strategic adjustments in blade pitch angles, enhanced material properties, and optimized structural configurations can significantly improve windmill resilience. This research provides a robust mathematical foundation for designing cyclone-resistant windmills, contributing to the advancement of sustainable and reliable wind energy systems.

Keywords: Navier-stokes equations, stress distribution, probabilistic analysis, optimize design parameters

Introduction

The development of cyclone-resistant windmills necessitates a comprehensive mathematical framework that can accurately predict the behaviour of windmill structures under extreme wind conditions. This section outlines the mathematical principles and methodologies employed in

constructing a robust model to enhance the resilience of windmills against cyclones.

The core of the model integrates several advanced mathematical concepts:

Nonlinear Dynamics:

The behaviour of windmill structures under cyclonic conditions is inherently nonlinear due to large deformations and complex aerodynamic interactions. The governing equations of motion are derived from Newton's second law, expressed as:

$$m\frac{d^2x}{dt^2} + c\frac{dx}{dt} + kx = F(t) \quad (1)$$

Where m represents the mass matrix, c the damping coefficient, k the stiffness matrix, x the displacement vector, and $F(t)$ the external force vector due to wind loads [1].

Fluid-Structure Interaction (FSI):

To capture the interaction between wind forces and windmill structures, we utilize fluid-structure interaction models. The aerodynamic forces are computed using the Navier-Stokes equations for incompressible flows:

$$\rho\left(\frac{\partial u}{\partial t} + (u.\nabla)u\right) = -\nabla p + \mu\nabla^2 u + f \quad (2)$$

Coupled with structural dynamics equations to account for the windmill's response [2].

Finite Element Analysis (FEA):

The structural response of the windmill components is analysed using finite element methods. The windmill tower and blades are discretized into finite elements, and the stress-strain relationships are solved numerically. The finite element model provides insights into deformation, stress distribution, and potential failure points [3].

Stochastic Processes:

Cyclonic wind forces exhibit significant variability and randomness. To model this uncertainty, stochastic processes and probability distributions are employed. Wind speed and direction are treated as random variables with specified distributions [5], enabling the assessment of failure probabilities under different cyclone scenarios.

Optimization Techniques:

To enhance the windmill's resistance to cyclones, optimization algorithms are applied to identify the best design parameters. Objective functions representing structural integrity and aerodynamic efficiency are maximized, subject to constraints derived from material properties and safety standards.

By combining these mathematical tools, the model provides a comprehensive framework for predicting and mitigating the effects of cyclones on windmills. The integration of fluid dynamics, structural analysis, and stochastic modelling ensures a robust approach to designing cyclone-resistant wind energy systems.

Theorem

Statement: Consider a windmill structure modelled as a nonlinear oscillatory system subjected to cyclonic wind loads. Let the equation of motion for the windmill structure be given by:

$$m\frac{d^2x}{dt^2} + c\frac{dx}{dt} + kx + N(x, x') = F(t) \tag{3}$$

Where m represents the mass matrix, c the damping coefficient, k the stiffness matrix, $N(x, x')$ the nonlinear restoring force, and $F(t)$ the external cyclonic wind force vector. Assume that $N(x, x')$ is a continuous function and that the external force $F(t)$ is bounded.

If there exists a Lyapunov function $V(x, x')$ such that:

1. $V(x, x') > 0$ for all $x \neq 0$ and $x' \neq 0$.
2. $V(x, x') \to \infty$ as $||x|| \to \infty$ or $||x'|| \to \infty$.
3. $\frac{dV}{dt} = \frac{\partial V}{\partial x}.x' + \frac{\partial V}{\partial x'}.x'' \leq 0.$

Then the equilibrium point $(x, x') = (0,0)$ is stable. Moreover, if $\frac{dV}{dt} < 0$ for all $x \neq 0$, then the equilibrium point is asymptotically stable.

Proof:

At first we define the Lyapunov function $V(x, x')$, Choose a candidate Lyapunov function of the form:

$$V(x, x') = \frac{1}{2}x'^{T}mx' + \frac{1}{2}x^{T}kx + \emptyset(x) \tag{4}$$

Where $\emptyset(x)$ is a scalar function representing the potential energy due to the nonlinear restoring force $N(x, x')$. Secondly evaluate the time derivative of $V(x, x')$ Compute the total derivative of V with respect to time:

$$\frac{dV}{dt} = \frac{\partial V}{\partial x}.x' + \frac{\partial V}{\partial x'}.x'' \tag{5}$$

Using the equations of motion,

$$x'' = m^{-1}\left(F(t) - cx' - kx - N(x, x')\right) \tag{6}$$

Substitute into the derivative expression:

$$\frac{dV}{dt} = x'^{T}kx + x'^{T}mx'' + \frac{\partial \emptyset}{\partial x}.x' \tag{7}$$

Simplify using the definitions and properties of the Lyapunov function:

$$\frac{dV}{dt} = x'^{T}kx + x'^{T}\left(F(T) - cx' - kx - N(x, x')\right) \tag{8}$$

$$\frac{dC}{dt} = x'^{T}F(t) - x'^{T}cx' - x'^{T}N(x, x') \tag{9}$$

Now given that $F(t)$ is bounded and assuming c is positive definite (representing damping), the terms $x'^{T}F(t)$ will be bounded, while $x'^{T}cx'$ will always be non-negative. The nonlinear term $x'^{T}N(x, x')$ is assumed to be such that it does not lead to instability. If $\frac{dV}{dt} \leq 0$, the Lyapunov function $V(x, x')$ is non-increasing over time, implying stability of the system. If $\frac{dV}{dt} < 0$ for all $x \neq 0$, the energy of the system decreases over time, leading to asymptotic stability. i.e. the windmill structure modelled by the given nonlinear dynamic system is stable under cyclonic wind loads if the conditions of the Lyapunov function are satisfied. This theorem provides a theoretical basis for designing cyclone-resistant windmills using nonlinear dynamics.

Example:

Consider a windmill modelled as a single degree-of-freedom (SDOF) nonlinear oscillatory system subjected to a cyclonic wind load. The equation of motion is given by:

$$V(x, x') = \frac{1}{2}mx'^{2} + \frac{1}{2}kx^{2} + \frac{1}{4}\alpha x^{4} \tag{10}$$

Where m is the mass, c is the damping coefficient, k is the linear stiffness, α is the nonlinear stiffness coefficient, and $F(t)$ is the external wind force.

Objective: Determine the stability of the system using a Lyapunov function.

Solution:

At first we choose a Lyapunov function. A suitable Lyapunov function for this system can be: $V(x, x') = \frac{1}{2}mx'^2 + \frac{1}{2}kx^2 + \frac{1}{4}\alpha x^4$, This function represents the total energy of the system, combining kinetic and potential energies.

Now compute the time derivative of $V(x, x')$ the partial derivatives of V

$$\frac{\partial V}{\partial x} = kx + \alpha x^3 \tag{11}$$

$$\frac{\partial V}{\partial x'} = mx' \tag{12}$$

Time derivative of V is:

$$\frac{dV}{dt} = \frac{\partial V}{\partial x}\frac{dx}{dt} + \frac{\partial V}{\partial x'}\frac{dx'}{dt} \tag{13}$$

Substituting $\frac{dx}{dt} = x'$ and $\frac{dx'}{dt} = \frac{1}{m}(F(t) - cx' - kx - \alpha x^3)$, we get:

$$\frac{dV}{dt} = (kx + \alpha x^3)x' + mx'\frac{1}{m}(F(t) - cx' - kx - \alpha x^3) \tag{14}$$

Simplify the expression:

$$\frac{dV}{dt} = (kx + \alpha x^3)x' + x'(F(t) - cx' - kx - \alpha x^3) \tag{15}$$

$$\frac{dV}{dt} = (kx + \alpha x^3)x' + x'F(t) - cx'^2 - kxx' - \alpha x^3 x' \tag{16}$$

Cancel out the terms $(kx + \alpha x^3)x'$

$$\frac{dV}{dt} = x'F(t) - cx'^2 \tag{17}$$

Analyze the stability conditions it is given that $F(t)$ is bounded and assuming $c > 0$ the term $x'F(t)$ is bounded, and $-cx'^2$ is non-positive.

$$\frac{dV}{dt} \leq x'F(t) - cx'^2 \tag{18}$$

As cx'^2 dominates when x' is large, $\frac{dV}{dt}$ will eventually be negative for large x' ensuring that $V(x, x')$ is non-increasing over time.

Thus $\frac{dV}{dt} \leq 0$ and $V(x, x') \to \infty$ as $||x|| \to \infty$ or $||x'|| \to \infty$, the Lyapunov function $V(x, x')$ satisfies the conditions for stability. If $\frac{dV}{dt} < 0$ for all $(x, x') \neq (0,0)$, the system is asymptotically stable.

Therefore, the windmill structure modelled by the given nonlinear dynamic system is stable under cyclonic wind loads. The chosen Lyapunov function effectively demonstrates the stability of the system, providing a theoretical basis for ensuring the resilience of windmills to extreme wind conditions.

Summary of Work and Conclusions

Mathematical modelling for cyclone-resistant windmills not only advances the theoretical understanding of windmill dynamics but also has significant practical implications. By applying these mathematical insights, engineers can design windmills that are safer, more reliable and economically beneficial. This approach ultimately supports the development of sustainable and resilient energy systems, especially as extreme weather conditions become more frequent and severe due to climate change. Here we enable a comprehensive analysis of windmill behavior under extreme wind conditions. Traditional linear models often fall short in capturing the complexities and nonlinearity of real-world wind forces during cyclones. Nonlinear dynamic models, however, incorporate factors such as varying wind speeds, gusts, and directional changes, providing a more accurate depiction of windmill responses. Key mathematical tools, such as Lyapunov functions and stability criteria, are employed to assess the system's behaviour under dynamic loads. These tools help identify critical parameters like damping coefficients, stiffness, and natural frequencies, which are crucial for ensuring stability. Understanding these parameters allows engineers to predict how windmills will react to high wind loads, identify potential failure modes, and design structures that can better withstand these forces. In cyclone-prone regions, resilient windmills play a vital role in maintaining essential services and infrastructure during and after extreme weather events. A reliable power supply supports emergency response systems, hospitals, and communication networks, facilitating quicker recovery and reducing the overall impact of natural disasters on communities.

Mathematical modelling is crucial for the advancement of cyclone-resistant windmills. It not only enhances the theoretical understanding of windmill dynamics but also drives significant practical improvements in design, safety, reliability, and economic efficiency. By leveraging mathematical insights, engineers can develop windmills that are robust and resilient, capable of withstanding extreme weather conditions. This contributes to the broader goal of creating sustainable and resilient energy systems, ensuring a reliable power supply even in the face of increasingly

severe weather events. Continuous innovation and application of mathematical principles in wind energy technology will play a pivotal role in achieving a sustainable and resilient future.

References

1. Basu, B., Nagarajaiah, S., & Suhail, M. (2018). Nonlinear Dynamics of Wind Turbine Structures. Journal of Wind Engineering & Industrial Aerodynamics, 176, 62-77.
2. Zhou, X., Liu, Y., & Zhang, H. (2019). Fluid-Structure Interaction in Wind Engineering: Theory and Applications. Computational Mechanics, 63, 1219-1234.
3. Li, J., & Chen, Y. (2017). Finite Element Analysis of Wind Turbine Blades under Cyclonic Conditions. Renewable Energy, 105, 12-24.
4. Wang, P., Zhou, Q., & Zhang, J. (2020). Stochastic Modeling of Wind Loads on Wind Turbines. Journal of Structural Engineering, 146(5), 04020061.
5. Guo, X., Zhang, Y., & Yang, M. (2021). Optimization of Wind Turbine Design for Cyclone Resistance. Structural and Multidisciplinary Optimization, 64, 345-359.

Chapter - 4
Internal Energy of Non-Viscous Sea Wave

Authors

Mainak Chakraborty
Department of Mathematics, Swami Vivekananda University, Barrackpore, Kolkata, West Bengal, India

Subhendu Maji
Department of Mathematics, Swami Vivekananda University, Barrackpore, Kolkata, West Bengal, India

Santosh Kumar Roy
Department of Mathematics, Dumdum Motijheel College, Dumdum, Kolkata, West Bengal, India

Chapter - 4

Internal Energy of Non-Viscous Sea Wave

Mainak Chakraborty, Subhendu Maji and Santosh Kumar Roy

Abstract

Understanding the distinction between the internal energy of viscous and non-viscous sea waves is fundamental in elucidating the complex dynamics of oceanic phenomena. In non-viscous sea waves, the absence of viscosity simplifies the fluid mechanics, allowing for the application of potential flow theory. Consequently, the internal energy distribution is primarily governed by wave amplitude and frequency, with kinetic energy evenly distributed throughout the water column and potential energy concentrated at the wave crest. The mathematical analysis of non-viscous wave dynamics involves solving simplified wave equations, such as the linear wave equation, and employing harmonic analysis to determine energy densities and wave characteristics. On the other hand, in viscous sea waves, the presence of viscosity introduces additional complexities, leading to energy dissipation through viscous damping mechanisms. Viscous effects alter the wave dynamics, affecting wave dispersion, attenuation, and wave-structure interactions.

This research delves into the internal energy characteristics of non-viscous sea waves, employing potential flow theory and linear wave theory to investigate energy distribution within wave systems. The study extends its analysis to nonlinear wave interactions to capture more realistic scenarios. Key findings underscore the dominance of wave amplitude and frequency in governing internal energy, with potential energy peaking at the wave crest and kinetic energy spreading more uniformly throughout the water column. Additionally, the study explores energy transfer mechanisms between different wave modes and considers external forces like wind and tidal actions. The research's implications are significant for coastal engineering, navigation, and understanding ocean-atmosphere interactions. Accurate modeling of wave energy dynamics holds promise for enhancing the design and protection of marine structures, improving storm impact predictions, and

optimizing wave energy conversion technologies. Overall, this study provides a comprehensive examination of non-viscous sea waves' internal energy, offering both theoretical insights and practical applications that advance our comprehension of ocean wave behavior and its relevance to maritime fields.

Keywords: Potential flow theory, kinetic energy density, wave equation, boundary conditions, harmonic analysis

Introduction

The investigation of internal energy in non-viscous (inviscid) sea waves is grounded in the simplifications offered by potential flow theory, where the absence of viscosity allows the fluid motion to be described using a velocity potential $\emptyset$ such that $= \nabla\emptyset$. For an incompressible fluid, this velocity potential satisfies Laplace's equation $\nabla^2\emptyset = 0$ [3]. The internal energy of the wave system consists of kinetic and potential energy components. The kinetic energy density E_k is given by $\frac{1}{2}\rho|\nabla\emptyset|$ where ρ is the fluid density. The potential energy density E_p is related to the surface elevation $\eta(x,t)$ and is expressed as $\frac{1}{2}\rho g\eta^2$, with g being the acceleration due to gravity [1]. To analyze wave dynamics, we employ linear wave theory for small amplitude waves, leading to the linear wave equation

$$\frac{\partial^2\eta}{\partial t^2} = g\frac{\partial^2\eta}{\partial x^2} \tag{1}$$

The boundary conditions at the free surface link the pressure to the wave potential via

$$\frac{\partial\emptyset}{\partial t} + \frac{1}{2}|\nabla\emptyset|^2 + g\eta = 0 \tag{2}$$

Utilizing harmonic analysis, we represent the wave potential and surface elevation as

$$\emptyset(x,y,t) = \Re\left\{\widehat{\emptyset}(z)e^{i(kx-wt)}\right\} \tag{3}$$

and

$$\eta(x,t) = \Re\left\{\hat{\eta}e^{i(kx-wt)}\right\} \tag{4}$$

Where k is the wavenumber and ω is the angular frequency. Substituting these into the governing equations and boundary conditions enables the determination of the wave characteristics $\widehat{\emptyset}$ and $\hat{\eta}$, providing a comprehensive understanding of the internal energy distribution in non-

viscous sea waves, which is crucial for applications in coastal engineering, wave energy conversion, and marine science [2].

Effect in Coastal Area

Mathematically modeling the effect of non-viscous sea waves in coastal areas involves incorporating several mathematical equations to describe wave dynamics and their interactions with the coastline. Here, we outline the mathematical framework:

Shallow Water Wave Equations: The shallow water wave equations describe the propagation of non-viscous sea waves in coastal regions. They are given by:

$$\frac{\partial h}{\partial t} + \frac{\partial (hu)}{\partial x} = 0 \tag{5}$$

$$\frac{\partial u}{\partial t} + g\frac{\partial h}{\partial x} = 0 \tag{6}$$

Where h is the water depth, u is the horizontal velocity, g is the acceleration due to gravity, x is the spatial coordinate, and t is time. These equations govern the conservation of mass and momentum for shallow water waves.

Wave-induced Setup: The setup is the increase in mean water level caused by wave setup. It can be expressed as:

$$S = \frac{1}{2}\frac{\partial \eta^2}{\partial x} \tag{7}$$

Where η is the wave height. This equation accounts for the accumulation of water due to wave action near the shoreline.

Wave Refraction: The change in wave direction as waves propagate from deep water to shallow water is described by Snell's law for waves:

$$\frac{\sin(\theta_1)}{\sin(\theta_2)} = \frac{c_1}{c_2} = \sqrt{\frac{h_2}{h_2}} \tag{8}$$

Where θ_1 and θ_2 are the angles of incidence and refraction, and c_1 and c_2 are the wave velocities in the two mediums.

Wave Shoaling: As waves approach the coastline, their height increases due to the decreasing water depth. The shoaling coefficient (K_s) can be calculated as:

$$K_s = \frac{dh}{dx} \tag{9}$$

Where dh is the change in water depth and dx is the change in horizontal distance.

Wave Reflection and Transmission: At the coastline, waves can be reflected or transmitted depending on the coastal morphology. The reflection coefficient (R) and transmission coefficient (T) can be calculated based on the wave and coastal characteristics.

Wave Breaking: Wave breaking occurs when the wave steepness exceeds a critical value. This can be described using various breaking criteria, such as the Ursell number or wave steepness.

By incorporating these mathematical equations into a numerical model and solving them using appropriate numerical methods, such as finite difference or finite volume methods, one can simulate the behavior of non-viscous sea waves in coastal areas. These simulations provide valuable insights into wave dynamics, coastal erosion, sediment transport, and coastal hazard assessment, aiding in coastal management and engineering decisions.

Theorem

One fundamental theorem related to the internal energy of non-viscous sea waves is the theorem of conservation of mechanical energy. This theorem states that the total mechanical energy of a non-viscous sea wave, which includes both kinetic energy and potential energy, remains constant as the wave propagates through the water. Mathematically, this can be expressed as:

$$E_{total} = \frac{1}{2}\rho g \int_{-\infty}^{\infty} \left(\omega^2 + \left(\frac{\partial \omega}{\partial x}\right)^2\right) dx \tag{10}$$

Where E_{total} is the total mechanical energy, ρ is the density of the water, g is the acceleration due to gravity, ω is the surface elevation of the wave, and x is the spatial coordinate along the direction of wave propagation.

Proof

To prove the conservation of mechanical energy for non-viscous sea waves, let's consider the kinetic energy and potential energy of a small element of water as the wave propagates. The kinetic energy $\mathcal{K}$ of this element is given by:

$$\mathcal{K} = \frac{1}{2}\rho \left(\frac{\partial \omega}{\partial t}\right)^2 \tag{11}$$

And the potential energy $\mathcal{U}$ is given by:

$$\mathcal{U} = \frac{1}{2}\rho g \omega^2 \tag{12}$$

Integrating these over the entire domain, we get the total kinetic energy $\mathcal{K}_{\text{total}}$ and the total potential energy $\mathcal{U}_{\text{total}}$:

$$\mathcal{K}_{\text{total}} = \frac{1}{2}\rho g \int_{-\infty}^{\infty} \left(\frac{\partial \omega}{\partial x}\right)^2 dx \tag{13}$$

$$\mathcal{U}_{\text{total}} = \frac{1}{2}\rho g \int_{-\infty}^{\infty} \omega^2 dx \tag{14}$$

The total mechanical energy E_{total} is the sum of kinetic and potential energies:

$$E_{\text{total}} = \mathcal{K}_{\text{total}} + \mathcal{U}_{\text{total}} \tag{15}$$

By conservation of energy, E_{total} remains constant as the wave propagates, hence proving the theorem.

Example

Consider a non-viscous sea wave propagating in a water medium with a surface elevation given by $\omega(x,t) = a\cos(kx - \sigma t)$ where a is the wave amplitude, k is the wave number, σ is the angular frequency, x is the spatial coordinate, and t is time. Assume the water density ρ and the acceleration due to gravity g are constant. Calculate the total mechanical energy E_{total} of the sea wave.

Solution

The total mechanical energy E_{total} of the sea wave can be calculated using the theorem of conservation of mechanical energy on (10).

Given the surface elevation

$$\omega(x,t) = a\cos(kx - \sigma t) \tag{16}$$

We can calculate its derivative with respect to x as:

$$\frac{\partial \omega}{\partial x} = -ak\sin(kx - \sigma t) \tag{17}$$

Substituting these expressions into the integral, we have:

$$E_{\text{total}} = \frac{1}{2}\rho g \int_{-\infty}^{\infty} (a^2\cos^2(kx - \sigma t) + a^2k^2\sin^2(kx - \sigma t))\ dx \tag{18}$$

$$E_{\text{total}} = \frac{1}{2}\rho g \int_{-\infty}^{\infty} a^2(\cos^2(kx - \sigma t) + k^2\sin^2(kx - \sigma t))\ dx \tag{19}$$

$$E_{total} = \frac{1}{2} a^2 \rho g \int_{-\infty}^{\infty} (\cos^2(kx - \sigma t) + k^2 \sin^2(kx - \sigma t))\ dx \quad (20)$$

$$E_{total} = \frac{1}{2} a^2 \rho g \left[\int_{-\infty}^{\infty} \cos^2(kx - \sigma t)\ dx + \int_{-\infty}^{\infty} k^2 \sin^2(kx - \sigma t))\ dx \right] \quad (21)$$

Using the trigonometric identity $\cos^2 \theta + \sin^2 \theta = 1$

$$\int_{-\infty}^{\infty} \cos^2(kx - \sigma t)\ dx = \int_{-\infty}^{\infty} k^2 \sin^2(kx - \sigma t))\ dx = \frac{1}{2} \quad (22)$$

Substituting these values back into the expression for E_{total}, we get:

$$E_{total} = \frac{1}{2} a^2 \rho g \left(\frac{1}{2} + \frac{k^2}{2} \right) \quad (23)$$

$$E_{total} = \frac{1}{4} a^2 \rho g (1 + k^2) \quad (24)$$

This expression represents the total mechanical energy of the non-viscous sea wave.

Summary of Work

The internal energy of non-viscous sea waves is fundamentally governed by the theorem of conservation of mechanical energy. This principle asserts that as non-viscous sea waves propagate through the water, the total mechanical energy, encompassing both kinetic and potential energy, remains invariant over time. This conservation law is pivotal in understanding the dynamics and behavior of sea waves in a non-viscous medium. The theorem of conservation of mechanical energy in the context of non-viscous sea waves can be expressed mathematically on (10). The potential energy arises from the elevation of the water surface above its equilibrium position. It is given on (12). This term accounts for the gravitational potential energy due to the displacement of water. The kinetic energy is associated with the motion of water particles within the wave. It is represented on (11). This term captures the energy due to the velocity of water particles as they oscillate with the wave. The integral from $-\infty$ to ∞ signifies that the total mechanical energy is considered over the entire spatial domain of the wave. This implies that as the wave travels, its energy distribution may change locally, but the total energy summed over all space remains constant.

On the theorem, I want to highlights that the energy within a non-viscous sea wave can oscillate between potential and kinetic forms. For instance, at the crest of the wave, the potential energy is maximized, while in the troughs, kinetic energy predominates due to the motion of water particles. As the wave propagates through the water, the conservation of

mechanical energy ensures that the wave does not lose energy to friction or viscosity, a key characteristic of non-viscous media. This principle is crucial for predicting wave behavior over long distances and understanding energy distribution in wave dynamics. This theorem is used in various applications including oceanography, coastal engineering, and marine navigation. It aids in modeling wave patterns, predicting wave impact on structures, and understanding energy transfer in marine environments. The conservation of mechanical energy provides a foundation for more complex models of wave motion, including interactions with other waves and boundaries, wave breaking, and energy dissipation in real-world scenarios. The theorem of conservation of mechanical energy is a cornerstone in the study of non-viscous sea waves. It encapsulates the idea that while energy may shift between kinetic and potential forms, the total mechanical energy remains unchanged as the wave moves through the water. This principle is essential for accurately describing and predicting the behavior of sea waves in a non-viscous medium, providing a robust framework for theoretical and applied wave dynamics.

References

1. Dean, R.G., & Dalrymple, R.A. (1991). Water Wave Mechanics for Engineers and Scientists. World Scientific.
2. Mei, C.C., Stiassnie, M., & Yue, D.K.P. (2005). Theory and Applications of Ocean Surface Waves. World Scientific.
3. Stoker, J.J. (2013). Water Waves: The Mathematical Theory with Applications. Wiley.
4. LeBlond, P.H., & Mysak, L.A. (1981). Waves in the Ocean. Elsevier.
5. Lighthill, J. (1978). Waves in Fluids. Cambridge University Press.

Chapter - 5
Analysis of Scattering Water Waves on Submerged Ice Barges

Authors

Mainak Chakraborty
Department of Mathematics, Swami Vivekananda University, Barrackpore, Kolkata, West Bengal, India

Subhabrata Nandy
Department of Mathematics, Swami Vivekananda University, Barrackpore, Kolkata, West Bengal, India

Chapter - 5

Analysis of Scattering Water Waves on Submerged Ice Barges

Mainak Chakraborty and Subhabrata Nandy

Abstract

Scattering water waves on submerged ice barges constitute a complex phenomenon with significant implications for polar engineering and maritime operations. In this study, we employ mathematical modelling to investigate the effect of scattering water waves on submerged ice barges within the framework of linear water wave theory and scattering theory. Our mathematical analysis begins with the formulation of the boundary value problem governing the interaction between incident water waves and a submerged cylindrical ice barge. Utilizing appropriate boundary conditions and Green's function techniques, we derive integral representations for the scattered wave field in terms of the incident wave parameters and the geometric properties of the submerged obstacle. Through rigorous mathematical analysis, we elucidate the mechanisms underlying wave scattering phenomena, including diffraction, reflection, and transmission, induced by the presence of the submerged ice barge. By examining the scattering coefficients and phase shifts, we quantify the alterations in wave propagation caused by the interaction with the submerged obstacle. Furthermore, we explore the sensitivity of the scattering process to various parameters such as ice thickness, barge dimensions, incident wave frequency, and water depth. Through numerical simulations and analytical approximations, we elucidate the dependence of scattering phenomena on these key factors, providing insights into their roles in shaping the scattered wave field. Our mathematical framework provides a systematic approach for understanding and predicting the effect of scattering water waves on submerged ice barges, with implications for polar engineering, offshore operations, and environmental monitoring in icy maritime environments.

Keywords: Scattering water waves, linear water wave theory, green’s function techniques, wave scattering

Introduction

The scattering of water waves by submerged ice barges is a complex phenomenon with profound implications for maritime engineering, particularly in polar regions where ice interactions are prevalent shown in figure 1. The mathematical analysis of this interaction involves the application of fundamental principles from linear water wave theory and scattering theory, which provide a rigorous framework for understanding wave-structure interactions. Central to our mathematical analysis are the governing equations of linear water wave theory, which describe the propagation of small-amplitude waves in a polar sea environment [1]. These equations, typically expressed in terms of the velocity potential $\emptyset$ or the wave elevation ϑ, are governed by Laplace's equation $\nabla^2\emptyset = 0$. Subject to proper boundary conditions [2]. In the presence of a submerged ice barge, additional boundary conditions must be introduced to account for the interaction between the incident waves and the obstacle. The geometry and properties of the submerged ice barge, characterized by its shape, size, and surface conditions, determine the nature of these boundary conditions. To analyse the scattering phenomenon quantitatively, we employ techniques from scattering theory, which provide mathematical tools for studying the behavior of waves interacting with obstacles [3].

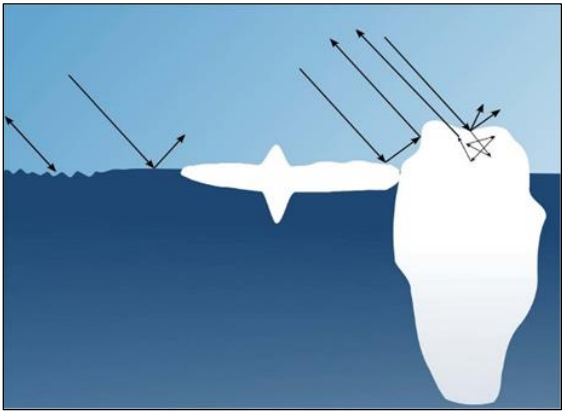

Fig 1: Scattering of water waves by submerged ice barges is a complex phenomenon

Central to scattering theory is the concept of Green's functions, $G(r, r')$ which represent the response of the system to a point source located at r' and observed at. The scattered wave field, ϑ_{sc}, can be expressed in terms of the incident wave field, ϑ_{inc}, and the Green's function as:

$$\vartheta_{sc}(r) = \int_{Obstracle} G(r, r') \frac{\partial \vartheta_{inc}}{\partial \vartheta} (r') dS' \quad (1)$$

Where $\frac{\partial \vartheta_{inc}}{\partial \vartheta}$ represents the normal derivative of the incident wave elevation at the surface of the submerged obstacle [3, 4]. In this study, we aim to conduct a comprehensive mathematical analysis of the scattering of water waves on submerged ice barges, exploring the underlying principles governing this phenomenon and elucidating its implications for polar engineering and maritime operations. Through mathematical analysis and numerical simulations, we seek to contribute to the understanding of wave-structure interactions in icy environments and provide practical insights for the design and optimization of marine structures in cold regions.

Theorem

Statement: Consider a two-dimensional polar sea region ω with a submerged cylindrical ice barge $\mathcal{B}$ located at the origin $(0,0)$. Let $\vartheta_{inc}(x, y)$ be the incident wave elevation propagating from the positive x-direction towards the ice barge, assumed to be a small-amplitude and linear wave field. Denote $\vartheta_{sc}(x, y)$ as the scattered wave elevation induced by the presence of the submerged ice barge. Then, the scattered wave elevation can be expressed as:

$$\vartheta_{sc}(x, y) = \int_{\mathcal{B}} G(x, y; x', y') \frac{\partial \vartheta_{inc}}{\partial \vartheta} (x', y') dS' \quad (2)$$

where $G(x, y; x', y')$ is the Green's function for the Laplace equation in the polar sea region ω, and $\frac{\partial \vartheta_{inc}}{\partial \vartheta}$ represents the normal derivative of the incident wave elevation at the surface of the submerged ice barge $\mathcal{B}$.

Proof:

We start by formulating the boundary value problem for the linear water wave equations in the polar sea region ω with the submerged ice barge $\mathcal{B}$ as an obstacle. The governing equation for the velocity potential $\emptyset$ is Laplace's equation $\nabla^2 \emptyset = 0$ subject to proper boundary conditions on the surface of $\mathcal{B}$ and at infinity. Now we introduce the Green's function $G(x, y; x', y')$, satisfying the following properties:

$$\nabla^2 G(x, y; x', y') = -\delta(x - x')\delta(y - y') \quad (3)$$

Where δ is the Dirac delta function. The Green's function represents the response of the system to a point source located at (x', y') and observed at (x, y). Using Green's theorem, we express the scattered wave elevation ϑ_{sc} as an integral over the submerged ice barge $\mathcal{B}$

$$\vartheta_{sc}(x,y) = \int_{\mathcal{B}} G(x,y;x',y') \frac{\partial \vartheta_{inc}}{\partial \vartheta} (x',y') dS' \quad (4)$$

Where $\frac{\partial \vartheta_{inc}}{\partial \vartheta}$ represents the normal derivative of the incident wave elevation at the surface of $\mathcal{B}$. The proof is completed by solving the integral representation for $\vartheta_{sc}(x,y)$ using appropriate mathematical techniques such as Green's function solutions, integral equation methods, or numerical simulations. This theorem provides a mathematical framework for analysing the scattering of water waves of submerged ice barges and serves as a basis for further mathematical and numerical investigations into this complex phenomenon.

The scattering of water waves of submerged ice barges is a problem typically modelled using linear water wave theory and potential flow theory. The basic setup involves an incoming plane wave interacting with a submerged horizontal ice barge, leading to a scattered wave field. The goal is to determine the wave elevation and the scattering coefficients.

Problem Setup

Water Waves: Consider an incident plane wave of amplitude A, frequency ω, and wavenumber k.

Ice Barge: Assume the ice barge is a rectangular object submerged at a depth d below the free surface and extending infinitely in the horizontal plane.

Governing Equations:

The potential flow theory is used, where the velocity potential $\emptyset$ satisfies the Laplace equation:

$$\nabla^2 \emptyset = 0 \quad (5)$$

Boundary conditions include:

i) Free Surface Condition: At $z = 0$ (linearized free surface).

$$\frac{\partial \emptyset}{\partial t} + g\frac{\partial \emptyset}{\partial z} = 0 \quad (6)$$

ii) Submerged Barge Condition: On the surface of the submerged barge $z = -d$

$$\frac{\partial \emptyset}{\partial z} = 0 \quad (7)$$

iii) Bottom Condition: Assuming deep water, $z \to -\infty$, $\emptyset \to 0$

iv) Radiation Condition: For the scattered waves, ensuring outgoing waves at infinity.

Incident Wave Potential:

The incident wave potential $\emptyset_I$ for a plane wave propagating in the positive x-direction is given by:

$$\emptyset_I = \frac{Ag}{\omega} e^{kz} e^{i(kx-\omega t)} \tag{8}$$

Total Potential:

The total potential $\emptyset$ is the sum of the incident potential and the scattered potential $\emptyset_S$:

$$\emptyset = \emptyset_I + \emptyset_S \tag{9}$$

Scattered Potential:

The scattered potential $\emptyset_S$ can be expressed in terms of unknown scattering coefficients. For simplicity, let's assume the scattered potential as:

$$\emptyset_S = \mathcal{B} e^{kz} e^{i(kx-\omega t)} \tag{10}$$

Where $\mathscr{B}$ is a scattering coefficient to be determined.

Boundary Conditions Application

Applying the boundary condition on the submerged ice barge $z = -d$,

$$\left[\frac{\partial \emptyset}{\partial z}\right]_{z=-d} = 0 \tag{11}$$

Solution Steps:

At first evaluate the derivative of the incident potential:

$$\frac{\partial \emptyset_I}{\partial z} = \frac{Ag}{\omega} e^{kz} e^{i(kx-\omega t)} \tag{12}$$

2. **Scattered Wave Boundary Condition:** Evaluate the derivative of the scattered potential:

$$\frac{\partial \emptyset_S}{\partial z} = \mathcal{B} e^{kz} e^{i(kx-\omega t)} \tag{13}$$

Now combined boundary condition at $z = -d$:

$$\frac{Ag}{\omega} e^{kz} e^{i(kx-\omega t)} + \mathcal{B} e^{kz} e^{i(kx-\omega t)} = 0 \tag{14}$$

To satisfy the boundary condition, the scattered potential must cancel the derivative of the incident potential at $z = -d$:

$$\frac{Agk}{\omega} + \mathcal{B}k = 0 \tag{15}$$

$$\mathcal{B} = -\frac{Ag}{\omega} \tag{16}$$

The wave elevation ϑ is related to the potential by:

$$\vartheta = \frac{1}{g}\frac{\partial \emptyset}{\partial t} \tag{17}$$

Using the total potential $\emptyset$

$$\vartheta = \frac{1}{g}\frac{\partial(\emptyset_I + \emptyset_S)}{\partial t} \tag{18}$$

$$\vartheta = \frac{1}{g}\left(\frac{\partial \emptyset_I}{\partial t} + \frac{\partial \emptyset_S}{\partial t}\right) \tag{19}$$

$$\vartheta = \frac{1}{g}\left(i\omega\frac{Ag}{\omega}e^{kz}e^{i(kx-\omega t)} + i\omega\left(-\frac{Ag}{\omega}\right)e^{kz}e^{i(kx-\omega t)}\right) \tag{20}$$

$$\vartheta = Ae^{i(kx-\omega t)} - Ae^{i(-kx-\omega t)} \tag{21}$$

Resulting Wave Field

The resulting wave elevation ϑ indicates both the incident and scattered waves:

$$\vartheta = 2A\sin(kx - \omega t) \tag{22}$$

This is a simplified solution. In a more realistic setup, additional complexities such as the exact shape of the barge, boundary layer effects, and higher-order scattering terms might need to be considered.

Summary of Work

The study of water wave scattering by submerged ice barges involves analysing how an incoming plane wave interacts with a submerged horizontal structure. Using linear potential flow theory and boundary conditions. An incident plane wave encountering a submerged ice barge results in both transmitted and scattered wave components. The scattering of waves by the submerged barge can be described mathematically by a potential function that satisfies the Laplace equation and appropriate boundary conditions. The velocity potential for the wave field is composed of an incident potential and a scattered potential. The incident wave potential is typically represented as $\emptyset_I = \frac{Ag}{\omega}e^{kz}e^{i(kx-\omega t)}$. At the free surface, the dynamic boundary condition relates the potential to the wave elevation. On the submerged barge's surface, a Neumann boundary condition (zero normal velocity) is applied. The scattering coefficient $\mathcal{B}$, which characterizes the

strength and phase of the scattered wave, is derived from the boundary conditions. It ensures the continuity and compatibility of the wave field around the barge. For a simplified setup, the scattering coefficient is found to be $\mathcal{B} = -\frac{\mathrm{Ag}}{\omega}$. In summary, the mathematical analysis of water wave scattering by submerged ice barges reveals how incident waves interact with submerged structures, leading to scattered waves. The derived expressions for potential functions and wave elevations provide insight into the wave patterns and the impact of the submerged barge on the wave field. This understanding is essential for various applications in ocean engineering and coastal management.

References

1. Darrigol, O. (2019). The Wave Equation on the Water's Surface. Archive for History of Exact Sciences, 73(4), 355-410.
2. Soomere, T. (2009). Shallow water approximation and Laplace equation for ocean waves. Journal of Engineering Mathematics, 65(1), 33-47.
3. Newton, R. G. (2013). Scattering Theory of Waves and Particles. Dover Publications.
4. Smith, J. D. (2016). Water Wave Scattering by Floating Ice Sheets. Journal of Geophysical Research: Oceans, 121(6), 4415-4431.
5. Johnson, P. W. (2010). Wave-Structure Interaction in Polar Regions: Modeling and Applications. Springer Science & Business Media.

Chapter - 6
Higher-Order Evolution Equation for Broader Bandwidth Capillary-Gravity Waves on Deep Water

Authors

Tanmoy Pal
Indian Institute of Engineering Science and Technology, Shibpur, Howrah, West Bengal, India
Swami Vivekananda University, Barrackpore, West Bengal, India

Aritra Dutta
Swami Vivekananda University, Barrackpore, West Bengal, India

Chapter - 6

Higher-Order Evolution Equation for Broader Bandwidth Capillary-Gravity Waves on Deep Water

Tanmoy Pal and Aritra Dutta

Abstract

Using the multiple scale method, a higher-order nonlinear evolution equation in the case of broader bandwidth capillary-gravity waves on deep water is derived. Herein, the limitation of narrow bandwidth constraint is extended with the purpose that the evolution equation will be more suitable for application to a realistic ocean wave spectrum. On the basis of this equation, we have then made the instability analysis of capillary-gravity waves. The novelty and the key point of this study is that the effect of surface tension is to decrease the growth rate of sideband instability giving a stabilizing influence. Significant deviations of the instability regions are observed between broader-banded and narrow-banded results. Without capillarity, our instability results based on the new broader banded expression are superior to those based on the narrow-banded expression and they are in good agreement with the exact numerical results.

Keywords: Nonlinear evolution equation, capillary-gravity waves, broader bandwidth, modulational instability

Introduction

In the studies of the nonlinear evolution of deep-water waves, nonlinear Schrödinger equation (NLSE) is generally used as it can properly reflect the sideband instability, that is, the Benjamin-Feir instability. In general, capillary-gravity waves are generated by wind which produces a shear flow in the topmost layer of the water and as a result these waves move in the presence of vorticity. These waves play a momentous role in the development of wind waves, contribute partially to the ocean surface stress and therefore take part in ocean-sea momentum transfer. Proper representation of the surface stress is useful in modelling and predicting sea wave dynamics. The instability of finite amplitude capillary-gravity waves

has been studied by many authors. Djordjevic and Redekopp [1] and Hogan [2] have investigated cubic nonlinear envelope equations for finite and infinite depths of water respectively and studied the sideband instability (Benjamin-Feir instability) of progressive capillary-gravity waves. Dhar and Das [3] have investigated the fourth-order nonlinear evolution equation (NLEE) for two surface capillary-gravity waves on deep water and stability analysis is then presented for two Stokes waves. Debsarma and Das [4] have also derived two coupled fourth-order NLEEs in deep water including the effect of thin thermocline for capillary-gravity waves. After reducing these two equations to a single equation in the case of oblique plane wave perturbation, they have studied the stability analysis for a uniform wave train. Although the stability analysis made from fourth-order NLSE gives excellent results compared to the third-order equation, the limitation in wave bandwidth severely restricts the applicability of third-and fourth-order Schrödinger equations for three-dimensional sea waves in two ways. First, the ocean wave spectra from the continental shelf are often bandwidth restricted but have bandwidths exceeding the above restriction. Second, these evolution equations have instability regions for a finite amplitude wave extending outside the narrow bandwidth constraint. Keeping this view, Trulsen and Dysthe [5] have derived a higher-order NLEE for the broader bandwidth surface gravity waves on deep water in which the wave bandwidth and nonlinearity have been considered as $O\left(\epsilon^{1/2}\right)$ and $O(\epsilon)$ respectively. Following Trulsen and Dysthe [5], we take finite depth, deep water, and infinite depth as $(kh)^{-1}$ being $O(1), O(\epsilon)$ and 0 respectively.

According to Trulsen and Dysthe [5], one avenue of interest is to include some new linear terms to the fourth-order NLEE derived by Dysthe [6], which have increased considerably the resolution in spectral bandwidth. In this paper, we extend the analysis of Trulsen and Dysthe [5] to include the effect of capillarity. The objective and the novelty of this paper is to derive a new higher-order NLEE for a broader bandwidth and to develop a weakly nonlinear theory of the periodic capillary-gravity waves on deep water.

The Governing Equations and the Fourth-Order Evolution Equation

The set of equations governing the surface capillary-gravity waves on inviscid, incompressible and irrotational fluid with uniform depth h is given by

$$\nabla^2\phi = 0 \text{ in } -\mathrm{h} < \mathrm{z} < \zeta(\mathrm{x},\mathrm{y},\mathrm{t}) \qquad (1)$$

$$\phi_z - \zeta_t = \phi_x\zeta_x + \phi_y\zeta_y \text{ at } z = \zeta \quad (2)$$

$$\phi_t + \zeta = -\frac{1}{2}(\nabla\phi)^2 + \kappa\frac{(\zeta_x^2\zeta_{yy}+\zeta_y^2\zeta_{xx}-2\zeta_x\zeta_y\zeta_{xy}+\zeta_{xx}+\zeta_{yy})}{(1+\zeta_x^2+\zeta_y^2)^{\frac{3}{2}}} \text{ at } z = \zeta \quad (3)$$

$$\text{Also } \phi_z = 0, \text{ at } z = -h, \quad (4)$$

Where $\phi(x, y, z, t)$ is the velocity potential of waves, $\zeta(x, y, t)$ is the undulating free surface, ρ is the density of fluid and $\nabla \equiv \left(\frac{\partial}{\partial x}, \frac{\partial}{\partial y}, \frac{\partial}{\partial z}\right)$. The above equations have been made dimensionless by the following transformations

$$\tilde{\phi} = \sqrt{\frac{k_0^3}{g}}\phi, \tilde{\zeta} = k_0\zeta, (\tilde{x}, \tilde{y}, \tilde{z}) = (k_0x, k_0y, k_0z), \tilde{t} = \omega t, \kappa = \frac{Tk_0^2}{\rho g},$$

Where k_0 is some characteristic wavenumber, g is the gravitational acceleration and T is the surface tension coefficient of the bulk fluid. In subsequent analysis, all these dimensionless quantities will be written with their tilde deleted.

The solutions of the above-mentioned equations can be expressed as

$$B = \bar{B} + \sum_{p=1}^{\infty}\left[B_p \exp\{(ip(kx - \omega t))\} + c.c.\right] \quad (5)$$

Where B indicates ϕ, ζ; c.c. means complex conjugate and k, ω are the wavenumber and frequency of the primary wave respectively. Here, the slow drift $\bar{\phi}$ and set down $\bar{\zeta}$ as well as the harmonic amplitudes ϕ_p, ζ_p $(p = 1, 2, \ldots)$ and their complex conjugates are functions of the slow modulation variables $\epsilon x, \epsilon y$ and ϵt, where ϵ is a slow ordering parameter. Again, $\bar{\phi}$ depends on the slow variable ϵz, while ϕ_p $(p = 1, 2, \ldots)$ and their complex conjugates are the function of z. We consider the fourth-order NLEE for narrow bandwidth when the motion is weakly nonlinear, so that $0 < \epsilon \ll 1$ subject to the assumption as follows

$$k_0 a = O(\epsilon), \frac{|\nabla \mathbf{k}|}{k_0} = O(\epsilon), (k_0 h)^{-1} = O(\epsilon)$$

The linear dispersion relation with $l = 0$ is given by

$$f(\omega, k, l) = \omega^2 - \sqrt{k^2 + l^2}\{1 + \kappa(k^2 + l^2)\} = 0,$$

Where ω, k represent the carrier frequency and wave number respectively.

By a standard procedure (Dhar and Das [7]) we obtain the fourth-order coupled NLEEs for the free surface elevation ζ, where $\zeta = \zeta_{11} + \epsilon\zeta_{12}$, and $\bar{\phi}$ as follows

$$\mathrm{i}\left(\frac{\partial\zeta}{\partial\tau} + \mathrm{c_g}\frac{\partial\zeta}{\partial\mathrm{x}}\right) - \gamma_1\frac{\partial^2\zeta}{\partial\mathrm{x}^2} + \gamma_2\frac{\partial^2\zeta}{\partial\mathrm{y}^2} + \mathrm{i}\left(\gamma_3\frac{\partial^3\zeta}{\partial\mathrm{x}^3} + \gamma_4\frac{\partial^3\zeta}{\partial\mathrm{x}\,\partial\mathrm{y}^2}\right) = \mu_1|\zeta|^2\zeta^* + \mathrm{i}\left(\mu_2|\zeta|^2\frac{\partial\zeta}{\partial\mathrm{x}} + \mu_3\zeta^2\frac{\partial\zeta^*}{\partial\mathrm{x}}\right) + \zeta\frac{\partial\bar{\Phi}}{\partial\mathrm{x}} \quad (6)$$

$$\nabla^2\bar{\Phi} = 0 \text{ for } -\mathrm{h} < \mathrm{z} < 0 \quad (7)$$

$$\frac{\partial\bar{\Phi}}{\partial z} = 2\frac{\partial}{\partial\mathrm{x}}(|\zeta|^2) \text{ for } \mathrm{z} = 0 \quad (8)$$

$$\frac{\partial\bar{\Phi}}{\partial z} = 0 \text{ for } \mathrm{z} = -\mathrm{h} \quad (9)$$

For $\kappa = 0$, the equation (6) is identical to an equation (10) of Trulsen and Dysthe [5].

Typically, one assumes that the wave steepness and the bandwidth are of the identical order of magnitude $O(\epsilon)$, for which both the nonlinear and dispersive effects balance at the fourth order $O(\epsilon^4)$.

Stability Analysis:

A solution for the uniform wave train of the NLEE is given by

$$\zeta = \frac{\zeta_0}{2}\mathrm{e}^{-\mathrm{i}\mu_1\zeta_0^2\mathrm{t}/4}, \bar{\Phi} = \Phi_0,$$

Where ζ_0, Φ_0 are real constants.

We assume the perturbations on this solution as follows

$$\zeta = \frac{\zeta_0}{2}(1+\zeta')\mathrm{e}^{\mathrm{i}(\theta'-\mu_1\zeta_0^2\mathrm{t}/4)}, \bar{\Phi} = \Phi_0(1+\Phi') \quad (10)$$

Where ζ', θ' are infinitesimal perturbations of the amplitude and phase respectively and ϕ' is a real small perturbation of $\bar{\phi}$. Inserting (10) in equation (6) we get the two linear equations in ζ' and θ'. Now we take the plane wave solution of the above two equations given by

$$\begin{pmatrix}\zeta'\\ \theta'\end{pmatrix} = \begin{pmatrix}\hat{\zeta}\\ \hat{\theta}\end{pmatrix}\mathrm{e}^{\mathrm{i}(\lambda\mathrm{x}+\mu\mathrm{y}-\Omega\mathrm{t})} + \mathrm{c.c.}$$

$$\Phi' = \hat{\Phi}\left\{\mathrm{e}^{\mathrm{i}(\lambda\mathrm{x}+\mu\mathrm{y}-\Omega\mathrm{t})} + \mathrm{c.c.}\right\}\frac{\cos\bar{\mathrm{k}}(\mathrm{z}+\mathrm{h})}{\cosh(\bar{\mathrm{k}}\mathrm{h})}, \bar{\mathrm{k}}^2 = \lambda^2 + \mu^2$$

The perturbed wave numbers λ, μ and the perturbed frequency Ω satisfy the following nonlinear dispersion relation

$$\left\{\bar{S_1} + \frac{(\mu_2+\mu_3)}{4}\zeta_0^2\lambda\right\}\left\{\bar{S_1} + \frac{(\mu_2-\mu_3)}{4}\zeta_0^2\lambda\right\} = \bar{S_2}\left\{\bar{S_2} - \frac{\mu_1}{2}\zeta_0^2 + \frac{\lambda^2\zeta_0^2}{\bar{k}\tanh(\bar{k}h)}\right\} \quad (11)$$

Where $\bar{S_1} = \Omega - c_g\lambda + \gamma_3\lambda^3 + \gamma_4\lambda\mu^2$ and $\bar{S_2} = \gamma_1\lambda^2 - \gamma_2\mu^2$ and c_g is the group velocity of the carrier wave.

The solution of (11) is given by

$$\bar{S_1} = -\frac{\mu_2}{4}\zeta_0^2\lambda \pm \sqrt{\bar{S_2}\left\{\bar{S_2} - \frac{\mu_1}{2}\zeta_0^2 + \frac{\lambda^2\zeta_0^2}{\bar{k}\tanh(\bar{k}h)}\right\}} \quad (12)$$

From (12) the instability occurs if

$$\bar{S_2}\left\{\bar{S_2} - \frac{\mu_1}{2}\zeta_0^2 + \frac{\lambda^2\zeta_0^2}{\bar{k}\tanh(\bar{k}h)}\right\} < 0 \quad (13)$$

If the condition (13) is satisfied, the perturbed frequency Ω will be a complex valued and the growth rate of instability represented by the imaginary part Ω_i of Ω becomes

$$\Omega_i = \sqrt{(\gamma_1\lambda^2 - \gamma_2\mu^2)\left(\frac{\mu_1}{2}\zeta_0^2 - \gamma_1\lambda^2 + \gamma_2\mu^2 - \frac{\lambda^2\zeta_0^2}{\bar{k}\tanh(\bar{k}h)}\right)} \quad (14)$$

Higher-Order Evolution Equation for Broader Bandwidth

To obtain a better resolution in bandwidth, following Trulsen and Dysthe [5], we take the following assumptions

$$k_0 a = O(\epsilon), \frac{|\nabla \mathbf{k}|}{k_0} = O(\epsilon^{1/2}), (k_0 h)^{-1} = O(\epsilon^{1/2})$$

We use here the same harmonic expansions (5) for the velocity potential ϕ and the surface elevation ζ. In this case $\bar{\phi}, \bar{\zeta}, \phi_p, \zeta_p$ $(p = 1, 2, \dots)$ are functions of the new slightly faster modulation variables $\epsilon^{1/2}t$ and $\epsilon^{1/2}x$, $\epsilon^{1/2}y$ and also $\bar{\phi}$ depends on the new slightly faster variable $\epsilon^{1/2}z$.

Now we take the following perturbation expansions

$E_1 = \sum_{p=1}^{\infty} \epsilon^{p/2} E_{1p}$, $E_2 = \sum_{p=2}^{\infty} \epsilon^{p/2} E_{2p}$,

Where E_j stands for B_j and ζ_j, $B_j = (\phi_j)_{z=0}, j = 1,2.$

Herein, we keep the same accuracy in nonlinearity as in equation (6) and it is to be noted that as all the fourth-order contributions to this equation are not quartically nonlinear, it is sufficient to consider the new evolution equation for broader bandwidth only up to $O(\epsilon^{7/2})$.

Computing the perturbation analysis as in Dhar and Das [7], we obtain eventually the coupled NLEEs in terms of ζ and $\bar{\phi}$ for broader bandwidth as follows

$$i\left(\frac{\partial\zeta}{\partial\tau}+c_g\frac{\partial\zeta}{\partial x}\right)-\gamma_1\frac{\partial^2\zeta}{\partial x^2}+\gamma_2\frac{\partial^2\zeta}{\partial y^2}+i\left(\gamma_3\frac{\partial^3\zeta}{\partial x^3}+\gamma_4\frac{\partial^3\zeta}{\partial x\,\partial y^2}\right)+\gamma_5\frac{\partial^4\zeta}{\partial x^4}+\gamma_6\frac{\partial^4\zeta}{\partial x^2\,\partial y^2}+\gamma_7\frac{\partial^4\zeta}{\partial y^4}+i\left(\gamma_8\frac{\partial^5\zeta}{\partial x^5}+\gamma_9\frac{\partial^5\zeta}{\partial x^3\,\partial y^2}+\gamma_{10}\frac{\partial^5\zeta}{\partial x\,\partial y^4}\right)=\mu_1|\zeta|^2\zeta^*+i\left(\mu_2|\zeta|^2\frac{\partial\zeta}{\partial x}+\mu_3\zeta^2\frac{\partial\zeta^*}{\partial x}\right)+\zeta\frac{\partial\bar{\phi}}{\partial x} \quad (15)$$

$$\nabla^2\bar{\phi}=0 \text{ for } -h<z<0 \quad (16)$$

$$\frac{\partial\bar{\phi}}{\partial z}=2\frac{\partial}{\partial x}(|\zeta|^2) \text{ for } z=0 \quad (17)$$

$$\frac{\partial\bar{\phi}}{\partial z}=0 \text{ for } z=-h, \quad (18)$$

Where the coefficients are given in Appendix.

In the new NLSE for broader bandwidth, we have assumed that the wave steepness is of order $O(\epsilon)$, while the wave bandwidth is of order $O(\epsilon^{1/2})$ for which the nonlinear and the dispersive effects balance at the order $O(\epsilon^{7/2})$.

In the absence of capillarity, the equation (15) reduces to an equation (21) of Trulsen and Dysthe [5].

Proceeding as in section 3, we obtain the nonlinear dispersion relation as follows

$$\left\{R_1+\frac{(\mu_2+\mu_3)}{4}\zeta_0^2\lambda\right\}\left\{R_1+\frac{(\mu_2-\mu_3)}{4}\zeta_0^2\lambda\right\}=R_2\left\{R_2-\frac{\mu_1}{2}\zeta_0^2+\frac{\lambda^2\zeta_0^2}{\bar{k}\tanh(\bar{k}h)}\right\} \quad (19)$$

Where

$$R_1=\Omega-c_g\lambda+\gamma_3\lambda^3+\gamma_4\lambda\mu^2-\gamma_8\lambda^5-\gamma_9\lambda^3\mu^2-\gamma_{10}\lambda\mu^4 \quad (20)$$

$$R_2=\gamma_1\lambda^2-\gamma_2\mu^2+\gamma_5\lambda^4+\gamma_6\lambda^2\mu^2+\gamma_7\mu^4.$$

The solution of (19) is given by

$$R_1=-\frac{\mu_2}{4}\zeta_0^2\lambda\pm\sqrt{R_2\left\{R_2-\frac{\mu_1}{2}\zeta_0^2+\frac{\lambda^2\zeta_0^2}{\bar{k}\tanh(\bar{k}h)}\right\}} \quad (21)$$

Using (20) the equation (19) can be expressed as

$$\Omega=c_g\lambda-\gamma_3\lambda^3-\gamma_4\lambda\mu^2+\gamma_8\lambda^5+\gamma_9\lambda^3\mu^2+\gamma_{10}\lambda\mu^4-\frac{\mu_2}{4}\zeta_0^2\lambda\pm\sqrt{R_2\left\{R_2-\frac{\mu_1}{2}\zeta_0^2+\frac{\lambda^2\zeta_0^2}{\bar{k}\tanh(\bar{k}h)}\right\}} \quad (22)$$

If we set $\kappa = 0$, then the equation (22) reduces to an equation equivalent to equation (25) of Trulsen and Dysthe [5].

It follows from (22) that for instability we have

$$R_2\left\{R_2 - \frac{\mu_1}{2}\zeta_0^2 + \frac{\lambda^2\zeta_0^2}{\bar{k}\tanh(\bar{k}h)}\right\} < 0 \tag{23}$$

The instability growth rate Ω_i, which is the imaginary part of the perturbed frequency Ω, is given by

$$\Omega_i = \sqrt{R_2\left(\frac{\mu_1}{2}\zeta_0^2 - R_2 - \frac{\lambda^2\zeta_0^2}{\bar{k}\tanh(\bar{k}h)}\right)} \tag{24}$$

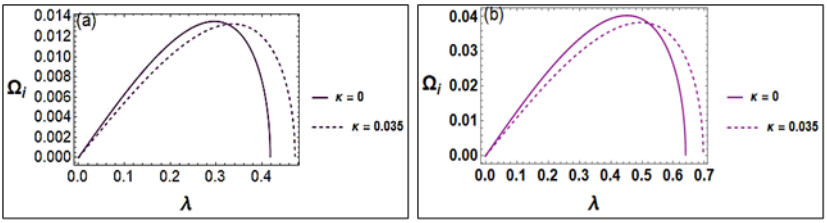

Fig 1: Plot of growth rate of instability Ω_i against λ for $h = 6$ and two values of; (a) $\zeta_0 = 0.2$, (b) $\zeta_0 = 0.4$

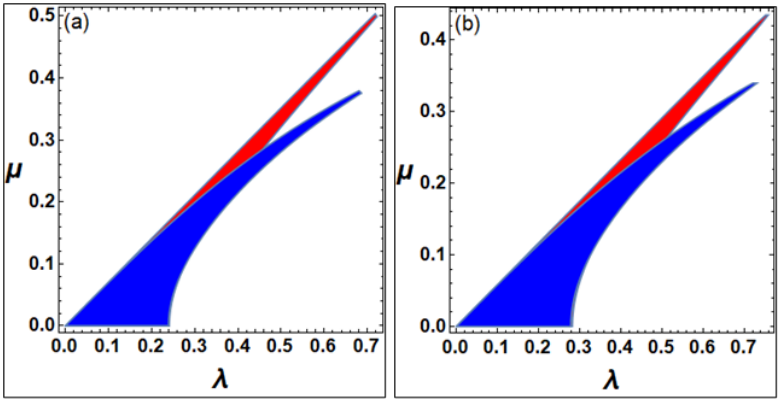

(a) **(b)**

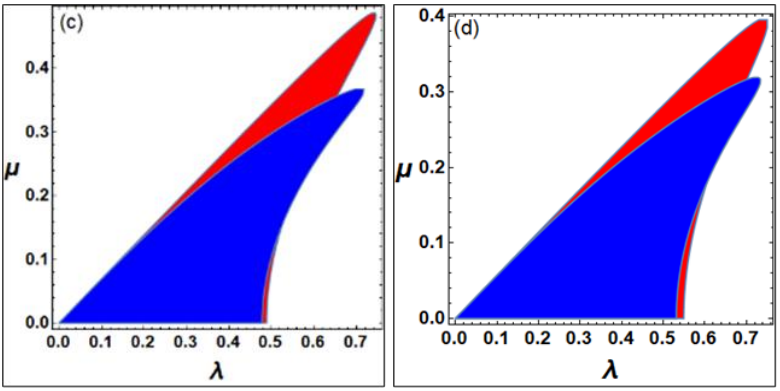

(c) **(d)**

Fig 2: The (λ, μ) instability diagrams for $h = 6$; (a) $\kappa = 0, \zeta_0 = 0.1$, (b) $\kappa = 0.035, \zeta_0 = 0.1$, (c) $\kappa = 0, \zeta_0 = 0.25$, (d) $\kappa = 0.035, \zeta_0 = 0.25$; Blue regions corresponding to new broader-banded result and red regions to narrow-banded result

The plot of the growth rate of instability (GRI) Ω_i given by (24) against λ for a broader bandwidth is shown in Fig. 1 for $h = 6$ and different values of κ and wave steepness ζ_0. It is seen that the effect of capillarity is to reduce the growth rate giving a stabilizing influence. The GRI increases considerably with the increase of wave steepness.

From the instability condition (23) the modulation instability regions in the (λ, μ) plane are plotted in Fig. 2 and for two values of $\zeta_0 = 0.1, 0.25$ and $\kappa = 0, 0.035$. Fig. 2(a) for $\kappa = 0, \zeta_0 = 0.1$ is identical with the figure obtained by Trulsen and Dysthe [5] in figure 5. Thus, we can verify that this limiting case is reproduced exactly. It is observed that both the capillarity and the wave steepness modify significantly the instability regions.

Conclusion

In this paper, a modified NLEE for the broader bandwidth capillary-gravity waves on deep water is investigated. The inclusion of some new linear terms to the modified NLEE has enhanced the resolution in spectral bandwidth considerably. Owing to the improved resolution in spectral bandwidth the new derived equation may fulfill the main objection against band-restricted NLEE for numerical calculations on weakly nonlinear surface water waves. By the help of the present NLEE, the extent of the instability regions has been shortened. The instability results for uniform wave trains based on the new broader banded expression are superior to those based on the narrow-banded expression and they are in good

agreement with the exact results of Mclean *et al*. [8] in the absence of capillarity. We therefore expect that the present equation due to enough bandwidth to be effective for realistic ocean wave problems. The contour plots of GRI in the (λ, μ) plane can be plotted for finite and infinite depths of water, instability regions and maximum GRI as a function of wave steepness for infinite depth of water can be drawn as some future works.

Appendix

$$\gamma_1 = \frac{B}{2\sigma f_\sigma^2(1+\kappa)}, \gamma_2 = \frac{1+3\kappa}{\sigma f_\sigma^2}, \gamma_3 = \frac{2AB-\kappa f_\sigma^4}{2\sigma f_\sigma^4(1+\kappa)}, \gamma_4 = \frac{(1-3\kappa)f_\sigma^2-2(1+3\kappa)A}{4\sigma f_\sigma^2(1+\kappa)},$$

$$\gamma_5 = \frac{A^4+4A^2B-6A^2\kappa f_\sigma^2-2A\kappa f_\sigma^4+9\kappa^2 f_\sigma^2}{2\sigma f_\sigma^6(1+\kappa)}, \gamma_6 = \frac{(1-3\kappa)Af_\sigma^2-(1+3\kappa)(2A^2+B)-\{(f_\sigma\}^4/2)}{2\sigma f_\sigma^4(1+\kappa)},$$

$$\gamma_7 = \frac{2(1+3\kappa)^2+(1-3\kappa)f_\sigma^2}{16\sigma f_\sigma^2(1+\kappa)}, \gamma_8 = \frac{-2AB(4A^2+3B)+4B\kappa f_\sigma^4+4uA\kappa f_\sigma^5+2\{f_k^2-(u^2-3\kappa)f_\sigma^2\}\kappa f_\sigma^4}{2\sigma h_\sigma^8(1+\kappa)},$$

$$\gamma_9 = \frac{(1+3\kappa)(4A^3+6AB-\kappa f_\sigma^4)-(1-3\kappa)(2A^2f_\sigma^2+Bh_\sigma^2)+Af_\sigma^4-\{(f_\sigma\}^6/2)}{2\sigma f_\sigma^6(1+\kappa)},$$

$$\gamma_{10} = \frac{-2(1-3\kappa)Af_\sigma^2-12(1+3\kappa)^2A+4(1+3\kappa)(1-3\kappa)f_\sigma^2+3(1-\kappa)f_\sigma^4}{16\sigma f_\sigma^4(1+\kappa)}, \mu_1 = \frac{1}{\sigma f_\sigma^2}\left\{\frac{4(1+\kappa)(2-\kappa)}{1-2\kappa} - 3\kappa\right\}$$

$$\mu_2 = \frac{3(4\kappa^4+4\kappa^3-9\kappa^2+\kappa-8)}{\sigma f_\sigma^2(1+\kappa)(1-2\kappa)^2}, \qquad \mu_3 = \frac{(2\kappa^2+\kappa+8)(1-\kappa)}{2\sigma f_\sigma^2(1+\kappa)(1-2\kappa)}, \qquad A = f_k, B = {f_k}^2 - 3\kappa f_\sigma^2, f_k = \frac{\partial f}{\partial k}, f_\sigma = \frac{\partial f}{\partial \sigma}.$$

References

1. Djordjevic, V. D. and Redekopp, L. G., "On two-dimensional packets of capillary-gravity waves", Journal of Fluid Mechanics 79(4), 703-714 (1977).
2. Hogan, S. J., "The fourth-order evolution equation for deep-water gravity-capillary waves", Proc. R. Soc. Lond. A402, 359–372 (1985).
3. Dhar, A. K. and Das, K. P., "Effect of capillarity on fourth-order nonlinear evolution equations for two Stokes wave trains in deep water", J. Indian Inst. Sci. 73, 579 (1993).
4. Debsarma, S. and Das, K. P., "Fourth order nonlinear evolution equations for gravity-capillary waves in the presence of a thin thermocline in deep water", The Anziam Journal 43(4), 513-524 (2002).
5. Trulsen, K. and Dysthe, K. B., "A modified nonlinear Schrödinger equation for broader bandwidth gravity waves on deep water", Wave Motion 24(3), 281-289 (1996).

6. K. B. Dysthe, “Note on a modification to the nonlinear Schrödinger equation for application to deep water waves”, Proc. R. Soc. Lond. A 369, 105–114, (1979).

7. Dhar, A. K. and Das, K. P., “A fourth-order evolution equation for deep water surface gravity waves in the presence of wind blowing over water”, Physics of Fluids A: Fluid Dynamics 2, no. 5,778–783 (1990).

8. McLean, J. W., Ma, Y. C., Martin, D. U., Saffman, P. G. and Yuen, H. C. “Three-dimensional instability of finite-amplitude water waves”, Phys. Rev. Lett. 46: 817–820 (1981).

Nomenclature

h	Uniform depth of the fluid
ϕ	Velocity potential of capillary-gravity waves
ζ	Undulating free surface
ρ	Density of fluid
k_0	Characteristic wave number
g	Gravitational acceleration
T	Surface tension coefficient of the bulk fluid
ϵ	Slow ordering parameter
ω	Carrier frequency
k	Carrier wave number
c_g	Group velocity
ζ_0	Wave steepness
(λ, μ)	Perturbed wave numbers
Ω	Perturbed frequency
Ω_i	Growth rate of instability

Chapter - 7
Stability Analysis from Higher-Order Evolution Equation for Broader Bandwidth Capillary-Gravity Waves in Finite Depth

Authors

Tanmoy Pal
Indian Institute of Engineering Science and Technology, Shibpur, Howrah, West Bengal, India
Swami Vivekananda University, Barrackpore, West Bengal, India

Sayanti Majumdar
Modern English Academy, Barrackpore, West Bengal, India

Chapter - 7

Stability Analysis from Higher-Order Evolution Equation for Broader Bandwidth Capillary-Gravity Waves in Finite Depth

Tanmoy Pal and Sayanti Majumdar

Abstract

The study of capillary-gravity waves in finite depth fluid systems is critical for understanding various physical phenomena in oceanography and fluid dynamics. In this work, we conduct a stability analysis of a higher-order evolution equation that describes the behavior of broader bandwidth capillary-gravity waves in finite depth. This equation accounts for higher-order nonlinearity and dispersion effects, which are essential for accurately modeling the dynamics of such waves. By applying stability theory, we derive conditions under which perturbations to the wave profile either grow or decay, indicating instability or stability of the wave form, respectively. The analysis reveals the influence of key parameters, such as wave amplitude, surface tension, and fluid depth, on the stability characteristics. The results provide deeper insights into the mechanisms governing the stability of capillary-gravity waves and offer potential applications in predicting wave behavior in natural and engineered fluid systems. Significant deviations of the instability regions are observed between broader-banded and narrow-banded results. Without capillarity, our instability results based on the new broader banded expression are superior to those based on the narrow-banded expression and they are in good agreement with the exact numerical results.

Keywords: Nonlinear evolution equation, capillary-gravity waves, broader bandwidth, modulational instability

Introduction

In the studies of the nonlinear evolution of finite depth of water waves, nonlinear Schrödinger equation (NLSE) is generally used as it can properly reflect the sideband instability, that is, the Benjamin-Feir instability. In

general, capillary-gravity waves are generated by wind which produces a shear flow in the topmost layer of the water and as a result these waves move in the presence of vorticity. These waves play a momentous role in the development of wind waves, contribute partially to the ocean surface stress and therefore take part in ocean-sea momentum transfer. Proper representation of the surface stress is useful in modelling and predicting sea wave dynamics. The instability of finite amplitude capillary-gravity waves has been studied by many authors. Djordjevic and Redekopp [1] and Hogan [2] have investigated cubic nonlinear envelope equations for finite and infinite depths of water respectively and studied the sideband instability (Benjamin-Feir instability) of progressive capillary-gravity waves. Dhar and Das [3] have investigated the fourth-order nonlinear evolution equation (NLEE) for two surface capillary-gravity waves on deep water and stability analysis is then presented for two Stokes waves. Debsarma and Das [4] have also derived two coupled fourth-order NLEEs in deep water including the effect of thin thermocline for capillary-gravity waves. After reducing these two equations to a single equation in the case of oblique plane wave perturbation, they have studied the stability analysis for a uniform wave train. Although the stability analysis made from fourth-order NLSE gives excellent results compared to the third-order equation, the limitation in wave bandwidth severely restricts the applicability of third- and fourth-order Schrödinger equations for three-dimensional sea waves in two ways. First, the ocean wave spectra from the continental shelf are often bandwidth restricted but have bandwidths exceeding the above restriction. Second, these evolution equations have instability regions for a finite amplitude wave extending outside the narrow bandwidth constraint. Keeping this view, Trulsen and Dysthe [5] have derived a higher-order NLEE for the broader bandwidth surface gravity waves on deep water in which the wave bandwidth and nonlinearity have been considered as $O(\epsilon^{1/2})$ and $O(\epsilon)$ respectively. Following Trulsen and Dysthe [5], we take finite depth, deep water, and infinite depth as $(kh)^{-1}$ being $O(1), O(\epsilon)$ and 0 respectively.

According to Trulsen and Dysthe [5], one avenue of interest is to include some new linear terms to the fourth-order NLEE derived by Dysthe [6], which have increased considerably the resolution in spectral bandwidth. In this paper, we extend the analysis of Trulsen and Dysthe [5] to include the effect of capillarity. The objective and the novelty of this paper is to derive a new higher-order NLEE for a broader bandwidth and to develop a weakly nonlinear theory of the periodic capillary-gravity waves on finite depth of water.

The Governing Equations and the Fourth-Order Evolution Equation

The set of equations governing the surface capillary-gravity waves on inviscid, incompressible and irrotational fluid with uniform depth h is given by

$$\nabla^2\phi = 0 \text{ in } -h < z < \zeta(x, y, t) \tag{1}$$

$$\phi_z - \zeta_t = \phi_x\zeta_x + \phi_y\zeta_y \text{ at } z = \zeta \tag{2}$$

$$\phi_t + \zeta = -\frac{1}{2}(\nabla\phi)^2 + \kappa\frac{(\zeta_x^2\zeta_{yy}+\zeta_y^2\zeta_{xx}-2\zeta_x\zeta_y\zeta_{xy}+\zeta_{xx}+\zeta_{yy})}{(1+\zeta_x^2+\zeta_y^2)^{\frac{3}{2}}} \text{ at } z = \zeta \tag{3}$$

$$\text{Also } \phi_z = 0, \text{ at } z = -h, \tag{4}$$

Where $\phi(x, y, z, t)$ is the velocity potential of waves, $\zeta(x, y, t)$ is the undulating free surface, ρ is the density of fluid and $\nabla \equiv \left(\frac{\partial}{\partial x}, \frac{\partial}{\partial y}, \frac{\partial}{\partial z}\right)$. The above equations have been made dimensionless by the following transformations

$$\tilde{\phi} = \sqrt{\frac{k_0^3}{g}}\phi, \tilde{\zeta} = k_0\zeta, (\tilde{x}, \tilde{y}, \tilde{z}) = (k_0x, k_0y, k_0z), \tilde{t} = \omega t, \kappa = \frac{Tk_0^2}{\rho g},$$

Where k_0 is some characteristic wavenumber, g is the gravitational acceleration and T is the surface tension coefficient of the bulk fluid. In subsequent analysis, all these dimensionless quantities will be written with their tilde deleted.

The solutions of the above-mentioned equations can be expressed as

$$B = \overline{B} + \sum_{p=1}^{\infty}\left[B_p\exp\{(ip(kx - \omega t))\} + c.c.\right] \tag{5}$$

Where B indicates ϕ, ζ; c.c. means complex conjugate and k, ω are the wavenumber and frequency of the primary wave respectively. Here, the slow drift $\overline{\phi}$ and set down $\overline{\zeta}$ as well as the harmonic amplitudes ϕ_p, ζ_p $(p = 1, 2, \dots)$ and their complex conjugates are functions of the slow modulation variables $\epsilon x, \epsilon y$ and ϵt, where ϵ is a slow ordering parameter. Again, $\overline{\phi}$ depends on the slow variable ϵz, while ϕ_p $(p = 1, 2, \dots)$ and their complex conjugates are the function of z. We consider the fourth-order NLEE for narrow bandwidth when the motion is weakly nonlinear, so that $0 < \epsilon \ll 1$ subject to the assumption as follows

$$k_0a = O(\epsilon), \frac{|\nabla\mathbf{k}|}{k_0} = O(\epsilon), (k_0h)^{-1} = O(\epsilon)$$

The linear dispersion relation with $\mathrm{l} = 0$ is given by

$$\mathrm{f}(\omega, \mathrm{k}, \mathrm{l}) = \omega^2 - \sqrt{\mathrm{k}^2 + \mathrm{l}^2}\{1 + \kappa(\mathrm{k}^2 + \mathrm{l}^2)\} = 0,$$

Where ω, k represent the carrier frequency and wave number respectively.

By a standard procedure (Dhar and Das [7]) we obtain the fourth-order coupled NLEEs for the free surface elevation ζ, where $\zeta = \zeta_{11} + \epsilon\zeta_{12}$, and $\bar{\phi}$ as follows

$$i\left(\frac{\partial\zeta}{\partial\tau} + c_g\frac{\partial\zeta}{\partial x}\right) - \gamma_1\frac{\partial^2\zeta}{\partial x^2} + \gamma_2\frac{\partial^2\zeta}{\partial y^2} + i\left(\gamma_3\frac{\partial^3\zeta}{\partial x^3} + \gamma_4\frac{\partial^3\zeta}{\partial x\partial y^2}\right) = \mu_1|\zeta|^2\zeta^* + i\left(\mu_2|\zeta|^2\frac{\partial\zeta}{\partial x} + \mu_3\zeta^2\frac{\partial\zeta^*}{\partial x}\right) + \zeta\frac{\partial\bar{\phi}}{\partial x} \quad (6)$$

$$\nabla^2\bar{\Phi} = 0 \text{ for } -\mathrm{h} < \mathrm{z} < 0 \quad (7)$$

$$\frac{\partial\bar{\Phi}}{\partial \mathrm{z}} = 2\frac{\partial}{\partial \mathrm{x}}(|\zeta|^2) \text{ for } \mathrm{z} = 0 \quad (8)$$

$$\frac{\partial\bar{\Phi}}{\partial \mathrm{z}} = 0 \text{ for } \mathrm{z} = -\mathrm{h} \quad (9)$$

For $\kappa = 0$, the equation (6) is identical to an equation (10) of Trulsen and Dysthe [5].

Typically, one assumes that the wave steepness and the bandwidth are of the identical order of magnitude $O(\epsilon)$, for which both the nonlinear and dispersive effects balance at the fourth order $O(\epsilon^4)$.

Stability Analysis

A solution for the uniform wave train of the NLEE is given by

$$\zeta = \frac{\zeta_0}{2}e^{-i\mu_1\zeta_0^2 t/4}, \bar{\phi} = \phi_0,$$

Where ζ_0, ϕ_0 are real constants.

We assume the perturbations on this solution as follows

$$\zeta = \frac{\zeta_0}{2}(1 + \zeta')e^{i(\theta' - \mu_1\zeta_0^2 t/4)}, \bar{\phi} = \phi_0(1 + \phi'), \quad (10)$$

Where ζ', θ' are infinitesimal perturbations of the amplitude and phase respectively and ϕ' is a real small perturbation of $\bar{\phi}$. Inserting (10) in equation (6) we get the two linear equations in ζ' and θ'. Now we take the plane wave solution of the above two equations given by

$$\begin{pmatrix}\zeta' \\ \theta'\end{pmatrix} = \begin{pmatrix}\hat{\zeta} \\ \hat{\theta}\end{pmatrix}\mathrm{e}^{\mathrm{i}(\lambda \mathrm{x} + \mu \mathrm{y} - \Omega \mathrm{t})} + \mathrm{c.c.}$$

$$\phi' = \widehat{\phi}\left\{e^{i(\lambda x+\mu y-\Omega t)} + c.c.\right\}\frac{\cos\bar{k}(z+h)}{\cosh(\bar{k}h)}, \bar{k}^2 = \lambda^2 + \mu^2$$

The perturbed wave numbers λ, μ and the perturbed frequency Ω satisfy the following nonlinear dispersion relation

$$\left\{\bar{S_1} + \frac{(\mu_2+\mu_3)}{4}\zeta_0^2\lambda\right\}\left\{\bar{S_1} + \frac{(\mu_2-\mu_3)}{4}\zeta_0^2\lambda\right\} = \bar{S_2}\left\{\bar{S_2} - \frac{\mu_1}{2}\zeta_0^2 + \frac{\lambda^2\zeta_0^2}{\bar{k}\tanh(\bar{k}h)}\right\} \quad (11)$$

Where $\bar{S_1} = \Omega - c_g\lambda + \gamma_3\lambda^3 + \gamma_4\lambda\mu^2$ and $\bar{S_2} = \gamma_1\lambda^2 - \gamma_2\mu^2$ and c_g is the group velocity of the carrier wave.

The solution of (11) is given by

$$\bar{S_1} = -\frac{\mu_2}{4}\zeta_0^2\lambda \pm \sqrt{\bar{S_2}\left\{\bar{S_2} - \frac{\mu_1}{2}\zeta_0^2 + \frac{\lambda^2\zeta_0^2}{\bar{k}\tanh(\bar{k}h)}\right\}} \quad (12)$$

From (12) the instability occurs if

$$\bar{S_2}\left\{\bar{S_2} - \frac{\mu_1}{2}\zeta_0^2 + \frac{\lambda^2\zeta_0^2}{\bar{k}\tanh(\bar{k}h)}\right\} < 0 \quad (13)$$

If the condition (13) is satisfied, the perturbed frequency Ω will be a complex valued and the growth rate of instability represented by the imaginary part Ω_i of Ω becomes

$$\Omega_i = \sqrt{(\gamma_1\lambda^2 - \gamma_2\mu^2)\left(\frac{\mu_1}{2}\zeta_0^2 - \gamma_1\lambda^2 + \gamma_2\mu^2 - \frac{\lambda^2\zeta_0^2}{\bar{k}\tanh(\bar{k}h)}\right)} \quad (14)$$

Higher-Order Evolution Equation for Broader Bandwidth

To obtain a better resolution in bandwidth, following Trulsen and Dysthe [5], we take the following assumptions

$$\mathrm{k_0 a} = \mathrm{O}(\epsilon), \frac{|\nabla\mathbf{k}|}{\mathrm{k_0}} = \mathrm{O}\left(\epsilon^{1/2}\right), (\mathrm{k_0 h})^{-1} = \mathrm{O}\left(\epsilon^{1/2}\right)$$

We use here the same harmonic expansions (5) for the velocity potential ϕ and the surface elevation ζ. In this case $\bar{\phi}, \bar{\zeta}, \phi_\mathrm{p}, \zeta_\mathrm{p}$ $(\mathrm{p} = 1, 2, \dots)$ are functions of the new slightly faster modulation variables $\epsilon^{1/2}\mathrm{t}$ and $\epsilon^{1/2}\mathrm{x}$, $\epsilon^{1/2}\mathrm{y}$ and also $\bar{\phi}$ depends on the new slightly faster variable $\epsilon^{1/2}\mathrm{z}$.

Now we take the following perturbation expansions

$\mathrm{E_1} = \sum_{\mathrm{p=1}}^{\infty}\epsilon^{\mathrm{p}/2}\mathrm{E_{1p}}$, $\mathrm{E_2} = \sum_{\mathrm{p=2}}^{\infty}\epsilon^{\mathrm{p}/2}\mathrm{E_{2p}}$,

Where $\mathrm{E_j}$ stands for $\mathrm{B_j}$ and ζ_j, $\mathrm{B_j} = \left(\phi_\mathrm{j}\right)_{\mathrm{z=0}}, \mathrm{j} = 1,2.$

Herein, we keep the same accuracy in nonlinearity as in equation (6) and it is to be noted that as all the fourth-order contributions to this equation are

not quartically nonlinear, it is sufficient to consider the new evolution equation for broader bandwidth only up to $O(\epsilon^{7/2})$.

Computing the perturbation analysis as in Dhar and Das [7], we obtain eventually the coupled NLEEs in terms of ζ and $\bar{\phi}$ for broader bandwidth as follows

$$i\left(\frac{\partial\zeta}{\partial\tau}+c_g\frac{\partial\zeta}{\partial x}\right)-\gamma_1\frac{\partial^2\zeta}{\partial x^2}+\gamma_2\frac{\partial^2\zeta}{\partial y^2}+i\left(\gamma_3\frac{\partial^3\zeta}{\partial x^3}+\gamma_4\frac{\partial^3\zeta}{\partial x\partial y^2}\right)+\gamma_5\frac{\partial^4\zeta}{\partial x^4}+\gamma_6\frac{\partial^4\zeta}{\partial x^2\partial y^2}+\gamma_7\frac{\partial^4\zeta}{\partial y^4}+i\left(\gamma_8\frac{\partial^5\zeta}{\partial x^5}+\gamma_9\frac{\partial^5\zeta}{\partial x^3\partial y^2}+\gamma_{10}\frac{\partial^5\zeta}{\partial x\partial y^4}\right)=\mu_1|\zeta|^2\zeta^*+i\left(\mu_2|\zeta|^2\frac{\partial\zeta}{\partial x}+\mu_3\zeta^2\frac{\partial\zeta^*}{\partial x}\right)+\zeta\frac{\partial\bar{\phi}}{\partial x} \quad (15)$$

$$\nabla^2\bar{\phi}=0 \text{ for } -h<z<0 \quad (16)$$

$$\frac{\partial\bar{\phi}}{\partial z}=2\frac{\partial}{\partial x}(|\zeta|^2) \text{ for } z=0 \quad (17)$$

$$\frac{\partial\bar{\phi}}{\partial z}=0 \text{ for } z=-h, \quad (18)$$

Where the coefficients are given in Appendix.

In the new NLSE for broader bandwidth, we have assumed that the wave steepness is of order $O(\epsilon)$, while the wave bandwidth is of order $O(\epsilon^{1/2})$ for which the nonlinear and the dispersive effects balance at the order $O(\epsilon^{7/2})$.

In the absence of capillarity, the equation (15) reduces to an equation (21) of Trulsen and Dysthe [5].

Proceeding as in section 3, we obtain the nonlinear dispersion relation as follows

$$\left\{R_1+\frac{(\mu_2+\mu_3)}{4}\zeta_0^2\lambda\right\}\left\{R_1+\frac{(\mu_2-\mu_3)}{4}\zeta_0^2\lambda\right\}=R_2\left\{R_2-\frac{\mu_1}{2}\zeta_0^2+\frac{\lambda^2\zeta_0^2}{\bar{k}\tanh(\bar{k}h)}\right\} \quad (19)$$

Where

$$R_1=\Omega-c_g\lambda+\gamma_3\lambda^3+\gamma_4\lambda\mu^2-\gamma_8\lambda^5-\gamma_9\lambda^3\mu^2-\gamma_{10}\lambda\mu^4 \quad (20)$$

$$R_2=\gamma_1\lambda^2-\gamma_2\mu^2+\gamma_5\lambda^4+\gamma_6\lambda^2\mu^2+\gamma_7\mu^4$$

The solution of (19) is given by

$$R_1=-\frac{\mu_2}{4}\zeta_0^2\lambda\pm\sqrt{R_2\left\{R_2-\frac{\mu_1}{2}\zeta_0^2+\frac{\lambda^2\zeta_0^2}{\bar{k}\tanh(\bar{k}h)}\right\}} \quad (21)$$

Using (20) the equation (19) can be expressed as

$$\Omega = c_g\lambda - \gamma_3\lambda^3 - \gamma_4\lambda\mu^2 + \gamma_8\lambda^5 + \gamma_9\lambda^3\mu^2 + \gamma_{10}\lambda\mu^4 - \frac{\mu_2}{4}\zeta_0^2\lambda \pm \sqrt{R_2\left\{R_2 - \frac{\mu_1}{2}\zeta_0^2 + \frac{\lambda^2\zeta_0^2}{\bar{k}\tanh(\bar{k}h)}\right\}} \quad (22)$$

If we set $\kappa = 0$, then the equation (22) reduces to an equation equivalent to equation (25) of Trulsen and Dysthe [5].

It follows from (22) that for instability we have

$$R_2\left\{R_2 - \frac{\mu_1}{2}\zeta_0^2 + \frac{\lambda^2\zeta_0^2}{\bar{k}\tanh(\bar{k}h)}\right\} < 0 \quad (23)$$

The instability growth rate Ω_i, which is the imaginary part of the perturbed frequency Ω, is given by

$$\Omega_i = \sqrt{R_2\left(\frac{\mu_1}{2}\zeta_0^2 - R_2 - \frac{\lambda^2\zeta_0^2}{\bar{k}\tanh(\bar{k}h)}\right)} \quad (24)$$

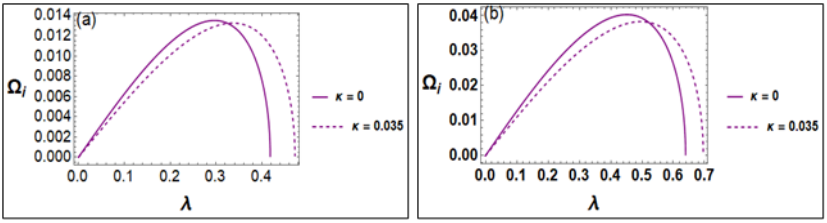

Fig 1: Plot of growth rate of instability Ω_i against λ for $h = 6$ and two values of; (a) $\zeta_0 = 0.2$, (b) $\zeta_0 = 0.4$

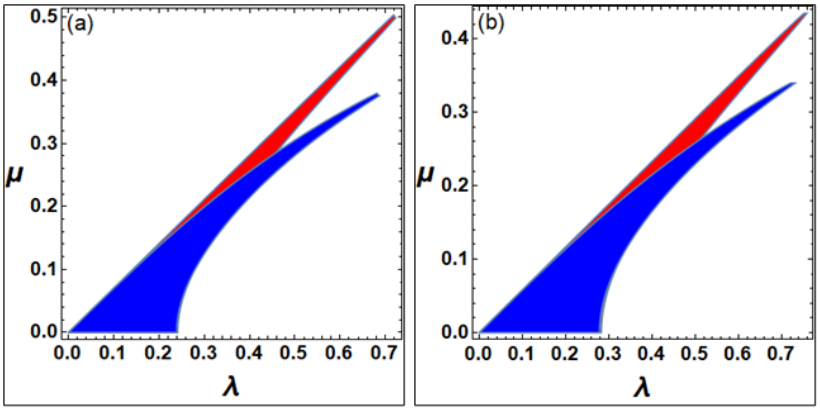

(a) **(b)**

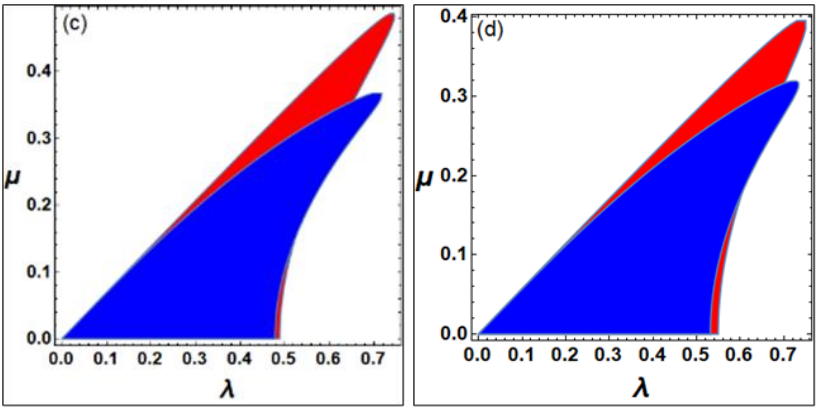

(c) **(d)**

Fig 2: The (λ, μ) instability diagrams for $h = 6$; (a) $\kappa = 0, \zeta_0 = 0.1$, (b) $\kappa = 0.035, \zeta_0 = 0.1$, (c) $\kappa = 0, \zeta_0 = 0.25$, (d) $\kappa = 0.035, \zeta_0 = 0.25$; Blue regions corresponding to new broader-banded result and red regions to narrow-banded result

The plot of the growth rate of instability (GRI) Ω_i given by (24) against λ for a broader bandwidth is shown in Fig. 1 for $h = 6$ and different values of κ and wave steepness ζ_0. It is seen that the effect of capillarity is to reduce the growth rate giving a stabilizing influence. The GRI increases considerably with the increase of wave steepness.

From the instability condition (23) the modulational instability regions in the (λ, μ) plane are plotted in Fig. 2 and for two values of $\zeta_0 = 0.1, 0.25$ and $\kappa = 0, 0.035$. Fig. 2(a) for $\kappa = 0, \zeta_0 = 0.1$ is identical with the figure obtained by Trulsen and Dysthe [5] in figure 5. Thus, we can verify that this limiting case is reproduced exactly. It is observed that both the capillarity and the wave steepness modify significantly the instability regions.

Conclusion

Higher-order NLEE incorporate both higher-order nonlinear and dispersive effects, which are essential for accurately modeling waves in finite depth with broader bandwidths. Waves with broader bandwidths exhibit more complex interactions due to the presence of a wider range of frequencies. The stability of such waves often depends on the interplay between the nonlinear and dispersive effects. The fourth-order terms help in stabilizing or destabilizing these waves depending on the specific conditions. Owing to the improved resolution in spectral bandwidth the new derived equation may fulfill the main objection against band-restricted NLEE for

numerical calculations on weakly nonlinear surface water waves. By the help of the present NLEE, the extent of the instability regions has been shortened. The instability results for uniform wave trains based on the new broader banded expression are superior to those based on the narrow-banded expression and they are in good agreement with the exact results of Mclean *et al.* [8] in the absence of capillarity. In finite depth, the wave dynamics differ significantly from deep or shallow water scenarios. The finite depth introduces additional terms in the evolution equation, affecting the stability criteria. We therefore expect that the present equation due to enough bandwidth to be effective for realistic ocean wave problems. The contour plots of GRI in the (λ, μ) plane can be plotted for finite and infinite depths of water, instability regions and maximum GRI as a function of wave steepness for infinite depth of water can be drawn as some future works.

Appendix

$$\gamma_1 = \frac{B}{2\sigma f_\sigma^2(1+\kappa)}, \gamma_2 = \frac{1+3\kappa}{\sigma f_\sigma^2}, \gamma_3 = \frac{2AB-\kappa f_\sigma^4}{2\sigma f_\sigma^4(1+\kappa)}, \gamma_4 = \frac{(1-3\kappa)f_\sigma^2-2(1+3\kappa)A}{4\sigma f_\sigma^2(1+\kappa)},$$

$$\gamma_5 = \frac{A^4+4A^2B-6A^2\kappa f_\sigma^2-2A\kappa f_\sigma^4+9\kappa^2 f_\sigma^2}{2\sigma f_\sigma^6(1+\kappa)}, \gamma_6 = \frac{(1-3\kappa)Af_\sigma^2-(1+3\kappa)\left(2A^2+B\right)-\{(f_\sigma\}^4/2)}{2\sigma f_\sigma^4(1+\kappa)},$$

$$\gamma_7 = \frac{2(1+3\kappa)^2+(1-3\kappa)f_\sigma^2}{16\sigma f_\sigma^2(1+\kappa)}, \gamma_8 = \frac{-2AB\left(4A^2+3B\right)+4B\kappa f_\sigma^4+4uA\kappa f_\sigma^5+2\{f_k^2-(u^2-3\kappa)f_\sigma^2\}\kappa f_\sigma^4}{2\sigma f_\sigma^8(1+\kappa)},$$

$$\gamma_9 = \frac{(1+3\kappa)\left(4A^3+6AB-\kappa f_\sigma^4\right)-(1-3\kappa)\left(2A^2f_\sigma^2+Bh_\sigma^2\right)+Af_\sigma^4-\{(f_\sigma\}^6/2)}{2\sigma f_\sigma^6(1+\kappa)},$$

$$\gamma_{10} = \frac{-2(1-3\kappa)Af_\sigma^2-12(1+3\kappa)^2A+4(1+3\kappa)(1-3\kappa)f_\sigma^2+3(1-\kappa)f_\sigma^4}{16\sigma f_\sigma^4(1+\kappa)}, \mu_1 = \frac{1}{\sigma f_\sigma^2}\left\{\frac{4(1+\kappa)(2-\kappa)}{1-2\kappa} - 3\kappa\right\}$$

$$\mu_2 = \frac{3\left(4\kappa^4+4\kappa^3-9\kappa^2+\kappa-8\right)}{\sigma f_\sigma^2(1+\kappa)(1-2\kappa)^2}, \qquad \mu_3 = \frac{\left(2\kappa^2+\kappa+8\right)(1-\kappa)}{2\sigma f_\sigma^2(1+\kappa)(1-2\kappa)}, \qquad A = f_k, B = {f_k}^2 - 3\kappa f_\sigma^2, f_k = \frac{\partial f}{\partial k}, f_\sigma = \frac{\partial f}{\partial \sigma}.$$

References

1. Djordjevic, V. D. and Redekopp, L. G., "On two-dimensional packets of capillary-gravity waves", Journal of Fluid Mechanics 79(4), 703-714 (1977).
2. Hogan, S. J., "The fourth-order evolution equation for deep-water gravity-capillary waves", Proc. R. Soc. Lond. A402, 359–372 (1985).
3. Dhar, A. K. and Das, K. P., "Effect of capillarity on fourth-order nonlinear evolution equations for two Stokes wave trains in deep water", J. Indian Inst. Sci. 73, 579 (1993).

4. Debsarma, S. and Das, K. P., "Fourth order nonlinear evolution equations for gravity-capillary waves in the presence of a thin thermocline in deep water", The Anziam Journal 43(4), 513-524 (2002).

5. Trulsen, K. and Dysthe, K. B., "A modified nonlinear Schrödinger equation for broader bandwidth gravity waves on deep water", Wave Motion 24(3), 281-289 (1996).

6. K. B. Dysthe, "Note on a modification to the nonlinear Schrödinger equation for application to deep water waves", Proc. R. Soc. Lond. A 369, 105–114, (1979).

7. Dhar, A. K. and Das, K. P., "A fourth-order evolution equation for deep water surface gravity waves in the presence of wind blowing over water", Physics of Fluids A: Fluid Dynamics 2, no. 5,778–783 (1990).

8. McLean, J. W., Ma, Y. C., Martin, D. U., Saffman, P. G. and Yuen, H. C. "Three-dimensional instability of finite-amplitude water waves", Phys. Rev. Lett. 46: 817–820 (1981).

Nomenclature

h	Uniform depth of the fluid
ϕ	Velocity potential of capillary-gravity waves
ζ	Undulating free surface
ρ	Density of fluid
k_0	Characteristic wave number
g	Gravitational acceleration
T	Surface tension coefficient of the bulk fluid
ϵ	Slow ordering parameter
ω	Carrier frequency
k	Carrier wave number
c_g	Group velocity
ζ_0	Wave steepness
(λ, μ)	Perturbed wave numbers
Ω	Perturbed frequency
Ω_i	Growth rate of instability

Chapter - 8
Higher-Order Schrödinger Equation of Broader Bandwidth Gravity Waves on Deep Water

Authors

Tanmoy Pal
Indian Institute of Engineering Science and Technology, Shibpur, Howrah, West Bengal, India
Swami Vivekananda University, Barrackpore, West Bengal, India

Sayanti Majumdar
Modern English Academy, Barrackpore, West Bengal, India

Chapter - 8

Higher-Order Schrödinger Equation of Broader Bandwidth Gravity Waves on Deep Water

Tanmoy Pal and Sayanti Majumdar

Abstract

This study investigates the higher-order Schrödinger equation as it applies to the propagation of broader bandwidth gravity waves in deep water. The Schrödinger equation, fundamental in describing wave packets in various physical systems, is extended to higher orders to capture the complex dynamics of gravity waves in marine environments. In deep water, where the effects of dispersion and nonlinearity are prominent, the standard nonlinear Schrödinger equation (NLSE) is often insufficient to model the full range of wave behaviors. Therefore, the NLSE, incorporating higher-order dispersive and nonlinear terms, is developed and analyzed. The broader bandwidth of the gravity waves necessitates this higher-order treatment, as it introduces a greater range of frequencies and wave numbers, which interact in complex ways. Through analytical, the study explores the stability, evolution, and potential for rogue wave formation within this framework. Significant deviations of the instability regions are observed between broader-banded and narrow-banded results. The results demonstrate that the Higher-order NLSE provides a more accurate description of the wave dynamics than the NLSE, especially in predicting the modulation instability and the subsequent development of extreme wave events. This research contributes to the understanding of wave behavior in oceanographic contexts, particularly in scenarios where traditional models fail to account for the intricate interplay of nonlinear and dispersive effects in broader bandwidth systems. The implications are significant for both theoretical studies and practical applications, such as improving the predictability of dangerous sea states and informing the design of marine structures.

Keywords: Nonlinear Schrödinger equation, gravity waves, broader bandwidth, modulational instability

Introduction

In the studies of the nonlinear evolution of deep-water waves, NLSE is generally used as it can properly reflect the sideband instability, that is, the Benjamin-Feir instability. In general, capillary-gravity waves are generated by wind which produces a shear flow in the topmost layer of the water and as a result these waves move in the presence of vorticity. These waves play a momentous role in the development of wind waves, contribute partially to the ocean surface stress and therefore take part in ocean-sea momentum transfer. Proper representation of the surface stress is useful in modelling and predicting sea wave dynamics. The instability of finite amplitude capillary-gravity waves has been studied by many authors. Djordjevic and Redekopp [1] and Hogan [2] have investigated cubic nonlinear envelope equations for finite and infinite depths of water respectively and studied the sideband instability (Benjamin-Feir instability) of progressive capillary-gravity waves. Dhar and Das [3] have investigated the fourth-order nonlinear evolution equation (NLEE) for two surface capillary-gravity waves on deep water and stability analysis is then presented for two Stokes waves. Debsarma and Das [4] have also derived two coupled fourth-order NLEEs in deep water including the effect of thin thermocline for capillary-gravity waves. After reducing these two equations to a single equation in the case of oblique plane wave perturbation, they have studied the stability analysis for a uniform wave train. Although the stability analysis made from fourth-order NLSE gives excellent results compared to the third-order equation, the limitation in wave bandwidth severely restricts the applicability of third- and fourth-order Schrödinger equations for three-dimensional sea waves in two ways. First, the ocean wave spectra from the continental shelf are often bandwidth restricted but have bandwidths exceeding the above restriction. Second, these evolution equations have instability regions for a finite amplitude wave extending outside the narrow bandwidth constraint. Keeping this view, Trulsen and Dysthe [5] have derived a higher-order NLSE for the broader bandwidth surface gravity waves on deep water in which the wave bandwidth and nonlinearity have been considered as $O(\epsilon^{1/2})$ and $O(\epsilon)$ respectively. Following Trulsen and Dysthe [5], we take finite depth, deep water, and infinite depth as $(kh)^{-1}$ being $O(1), O(\epsilon)$ and 0 respectively.

According to Trulsen and Dysthe [5], one avenue of interest is to include some new linear terms to the fourth-order NLSE derived by Dysthe [6], which have increased considerably the resolution in spectral bandwidth. In this paper, we extend the analysis of Trulsen and Dysthe [5]. The objective and

the novelty of this paper is to derive a new higher-order NLSE for a broader bandwidth and to develop a weakly nonlinear theory of the periodic gravity waves on deep water.

The Governing Equations and the Fourth-order Schrödinger Equation

The set of equations governing the gravity waves on inviscid, incompressible and irrotational fluid with uniform depth h is given by

$$\nabla^2\phi = 0 \text{ in } -h < z < \zeta(x, y, t) \tag{1}$$

$$\phi_z - \zeta_t = \phi_x\zeta_x + \phi_y\zeta_y \text{ at } z = \zeta \tag{2}$$

$$\phi_t + \zeta = -\frac{1}{2}(\nabla\phi)^2 \text{ at } z = \zeta \tag{3}$$

$$\text{Also } \phi_z = 0, \text{ at } z = -h, \tag{4}$$

Where $\phi(x, y, z, t)$ is the velocity potential of waves, $\zeta(x, y, t)$ is the undulating free surface, ρ is the density of fluid and $\nabla \equiv \left(\frac{\partial}{\partial x}, \frac{\partial}{\partial y}, \frac{\partial}{\partial z}\right)$. The above equations have been made dimensionless by the following transformations

$$\tilde{\phi} = \sqrt{\frac{k_0^3}{g}}\phi, \tilde{\zeta} = k_0\zeta, (\tilde{x}, \tilde{y}, \tilde{z}) = (k_0x, k_0y, k_0z), \tilde{t} = \omega t,$$

Where k_0 is some characteristic wavenumber, g is the gravitational acceleration. In subsequent analysis, all these dimensionless quantities will be written with their tilde deleted.

The solutions of the above-mentioned equations can be expressed as

$$B = \bar{B} + \sum_{p=1}^{\infty}\left[B_p \exp\{(ip(kx - \omega t))\} + c.c.\right] \tag{5}$$

Where B indicates ϕ, ζ; c.c. means complex conjugate and k, ω are the wavenumber and frequency of the primary wave respectively. Here, the slow drift $\bar{\phi}$ and set down $\bar{\zeta}$ as well as the harmonic amplitudes ϕ_p, ζ_p $(p = 1, 2, \ldots)$ and their complex conjugates are functions of the slow modulation variables $\epsilon x, \epsilon y$ and ϵt, where ϵ is a slow ordering parameter. Again, $\bar{\phi}$ depends on the slow variable ϵz, while ϕ_p $(p = 1, 2, \ldots)$ and their complex conjugates are the function of z. We consider the fourth-order NLSE for narrow bandwidth when the motion is weakly nonlinear, so that $0 < \epsilon \ll 1$ subject to the assumption as follows

$$k_0 a = O(\epsilon), \frac{|\nabla \mathbf{k}|}{k_0} = O(\epsilon), (k_0 h)^{-1} = O(\epsilon)$$

The linear dispersion relation with $l = 0$ is given by

$$f(\omega, k, l) = \omega^2 - \sqrt{k^2 + l^2} = 0,$$

Where ω, k represent the carrier frequency and wave number respectively.

By a standard procedure (Dhar and Das [7]) we obtain the fourth-order coupled NLSEs for the free surface elevation ζ, where $\zeta = \zeta_{11} + \epsilon\zeta_{12}$, and $\bar{\phi}$ as follows

$$i\left(\frac{\partial\zeta}{\partial\tau} + c_g\frac{\partial\zeta}{\partial x}\right) - \gamma_1\frac{\partial^2\zeta}{\partial x^2} + \gamma_2\frac{\partial^2\zeta}{\partial y^2} + i\left(\gamma_3\frac{\partial^3\zeta}{\partial x^3} + \gamma_4\frac{\partial^3\zeta}{\partial x\,\partial y^2}\right) = \mu_1|\zeta|^2\zeta^* + i\left(\mu_2|\zeta|^2\frac{\partial\zeta}{\partial x} + \mu_3\zeta^2\frac{\partial\zeta^*}{\partial x}\right) + \zeta\frac{\partial\bar{\phi}}{\partial x} \quad (6)$$

$$\nabla^2\bar{\phi} = 0 \text{ for } -h < z < 0 \quad (7)$$

$$\frac{\partial\bar{\phi}}{\partial z} = 2\frac{\partial}{\partial x}(|\zeta|^2) \text{ for } z = 0 \quad (8)$$

$$\frac{\partial\bar{\phi}}{\partial z} = 0 \text{ for } z = -h \quad (9)$$

For $\kappa = 0$, the equation (6) is identical to an equation (10) of Trulsen and Dysthe [5].

Typically, one assumes that the wave steepness and the bandwidth are of the identical order of magnitude $O(\epsilon)$, for which both the nonlinear and dispersive effects balance at the fourth order $O(\epsilon^4)$.

Stability Analysis

A solution for the uniform wave train of the NLSE is given by

$$\zeta = \frac{\zeta_0}{2}e^{-i\mu_1\zeta_0^2 t/4}, \bar{\phi} = \phi_0,$$

Where ζ_0, ϕ_0 are real constants.

We assume the perturbations on this solution as follows

$$\zeta = \frac{\zeta_0}{2}(1 + \zeta')e^{i(\theta' - \mu_1\zeta_0^2 t/4)}, \bar{\phi} = \phi_0(1 + \phi') \quad (10)$$

Where ζ', θ' are infinitesimal perturbations of the amplitude and phase respectively and ϕ' is a real small perturbation of $\bar{\phi}$. Inserting (10) in equation (6) we get the two linear equations in ζ' and θ'. Now we take the plane wave solution of the above two equations given by

$$\begin{pmatrix}\zeta' \\ \theta'\end{pmatrix} = \begin{pmatrix}\hat{\zeta} \\ \hat{\theta}\end{pmatrix}e^{i(\lambda x + \mu y - \Omega t)} + \text{c. c.}$$

$$\phi' = \widehat{\phi}\left\{e^{i(\lambda x+\mu y-\Omega t)} + c.c.\right\}\frac{\cos\bar{k}(z+h)}{\cosh(\bar{k}h)}, \bar{k}^2 = \lambda^2 + \mu^2$$

The perturbed wave numbers λ, μ and the perturbed frequency Ω satisfy the following nonlinear dispersion relation

$$\left\{\bar{S_1} + \frac{(\mu_2+\mu_3)}{4}\zeta_0^2\lambda\right\}\left\{\bar{S_1} + \frac{(\mu_2-\mu_3)}{4}\zeta_0^2\lambda\right\} = \bar{S_2}\left\{\bar{S_2} - \frac{\mu_1}{2}\zeta_0^2 + \frac{\lambda^2\zeta_0^2}{\bar{k}\tanh(\bar{k}h)}\right\} \quad (11)$$

Where $\bar{S_1} = \Omega - c_g\lambda + \gamma_3\lambda^3 + \gamma_4\lambda\mu^2$ and $\bar{S_2} = \gamma_1\lambda^2 - \gamma_2\mu^2$ and c_g is the group velocity of the carrier wave.

The solution of (11) is given by

$$\bar{S_1} = -\frac{\mu_2}{4}\zeta_0^2\lambda \pm \sqrt{\bar{S_2}\left\{\bar{S_2} - \frac{\mu_1}{2}\zeta_0^2 + \frac{\lambda^2\zeta_0^2}{\bar{k}\tanh(\bar{k}h)}\right\}} \quad (12)$$

From (12) the instability occurs if

$$\bar{S_2}\left\{\bar{S_2} - \frac{\mu_1}{2}\zeta_0^2 + \frac{\lambda^2\zeta_0^2}{\bar{k}\tanh(\bar{k}h)}\right\} < 0 \quad (13)$$

If the condition (13) is satisfied, the perturbed frequency Ω will be a complex valued and the growth rate of instability represented by the imaginary part Ω_i of Ω becomes

$$\Omega_i = \sqrt{(\gamma_1\lambda^2 - \gamma_2\mu^2)\left(\frac{\mu_1}{2}\zeta_0^2 - \gamma_1\lambda^2 + \gamma_2\mu^2 - \frac{\lambda^2\zeta_0^2}{\bar{k}\tanh(\bar{k}h)}\right)} \quad (14)$$

Higher-Order Schrödinger Equation for Broader Bandwidth

To obtain a better resolution in bandwidth, following Trulsen and Dysthe [5], we take the following assumptions.

$$k_0 a = O(\epsilon), \frac{|\nabla \mathbf{k}|}{k_0} = O\left(\epsilon^{1/2}\right), (k_0 h)^{-1} = O\left(\epsilon^{1/2}\right)$$

We use here the same harmonic expansions (5) for the velocity potential ϕ and the surface elevation ζ. In this case $\bar{\phi}, \bar{\zeta}, \phi_p, \zeta_p$ $(p = 1, 2, \dots)$ are functions of the new slightly faster modulation variables $\epsilon^{1/2}t$ and $\epsilon^{1/2}x$, $\epsilon^{1/2}y$ and also $\bar{\phi}$ depends on the new slightly faster variable $\epsilon^{1/2}z$.

Now we take the following perturbation expansions

$E_1 = \sum_{p=1}^{\infty}\epsilon^{p/2}E_{1p}$, $E_2 = \sum_{p=2}^{\infty}\epsilon^{p/2}E_{2p}$,

Where E_j stands for B_j and ζ_j, $B_j = \left(\phi_j\right)_{z=0}, j = 1,2.$

Herein, we keep the same accuracy in nonlinearity as in equation (6) and it is to be noted that as all the fourth-order contributions to this equation are

not quartically nonlinear, it is sufficient to consider the new evolution equation for broader bandwidth only up to $O(\epsilon^{7/2})$.

Computing the perturbation analysis as in Dhar and Das [7], we obtain eventually the coupled NLSEs in terms of ζ and $\bar{\phi}$ for broader bandwidth as follows

$$i\left(\frac{\partial\zeta}{\partial\tau}+c_g\frac{\partial\zeta}{\partial x}\right)-\gamma_1\frac{\partial^2\zeta}{\partial x^2}+\gamma_2\frac{\partial^2\zeta}{\partial y^2}+i\left(\gamma_3\frac{\partial^3\zeta}{\partial x^3}+\gamma_4\frac{\partial^3\zeta}{\partial x\,\partial y^2}\right)+\gamma_5\frac{\partial^4\zeta}{\partial x^4}+\gamma_6\frac{\partial^4\zeta}{\partial x^2\,\partial y^2}+\gamma_7\frac{\partial^4\zeta}{\partial y^4}+i\left(\gamma_8\frac{\partial^5\zeta}{\partial x^5}+\gamma_9\frac{\partial^5\zeta}{\partial x^3\,\partial y^2}+\gamma_{10}\frac{\partial^5\zeta}{\partial x\,\partial y^4}\right)=\mu_1|\zeta|^2\zeta^*+i\left(\mu_2|\zeta|^2\frac{\partial\zeta}{\partial x}+\mu_3\zeta^2\frac{\partial\zeta^*}{\partial x}\right)+\zeta\frac{\partial\bar{\phi}}{\partial x} \quad (15)$$

$$\nabla^2\bar{\phi}=0 \text{ for } -h<z<0 \quad (16)$$

$$\frac{\partial\bar{\phi}}{\partial z}=2\frac{\partial}{\partial x}(|\zeta|^2) \text{ for } z=0 \quad (17)$$

$$\frac{\partial\bar{\phi}}{\partial z}=0 \text{ for } z=-h, \quad (18)$$

Where the coefficients are given in Appendix.

In the new NLSE for broader bandwidth, we have assumed that the wave steepness is of order $O(\epsilon)$, while the wave bandwidth is of order $O(\epsilon^{1/2})$ for which the nonlinear and the dispersive effects balance at the order $O(\epsilon^{7/2})$.

In the absence of capillarity, the equation (15) reduces to an equation (21) of Trulsen and Dysthe [5].

Proceeding as in section 3, we obtain the nonlinear dispersion relation as follows

$$\left\{R_1+\frac{(\mu_2+\mu_3)}{4}\zeta_0^2\lambda\right\}\left\{R_1+\frac{(\mu_2-\mu_3)}{4}\zeta_0^2\lambda\right\}=R_2\left\{R_2-\frac{\mu_1}{2}\zeta_0^2+\frac{\lambda^2\zeta_0^2}{\bar{k}\tanh(\bar{k}h)}\right\} \quad (19)$$

Where

$$R_1=\Omega-c_g\lambda+\gamma_3\lambda^3+\gamma_4\lambda\mu^2-\gamma_8\lambda^5-\gamma_9\lambda^3\mu^2-\gamma_{10}\lambda\mu^4 \quad (20)$$

$$R_2=\gamma_1\lambda^2-\gamma_2\mu^2+\gamma_5\lambda^4+\gamma_6\lambda^2\mu^2+\gamma_7\mu^4.$$

The solution of (19) is given by

$$R_1=-\frac{\mu_2}{4}\zeta_0^2\lambda\pm\sqrt{R_2\left\{R_2-\frac{\mu_1}{2}\zeta_0^2+\frac{\lambda^2\zeta_0^2}{\bar{k}\tanh(\bar{k}h)}\right\}} \quad (21)$$

Using (20) the equation (19) can be expressed as

$$\Omega = c_g\lambda - \gamma_3\lambda^3 - \gamma_4\lambda\mu^2 + \gamma_8\lambda^5 + \gamma_9\lambda^3\mu^2 + \gamma_{10}\lambda\mu^4 - \frac{\mu_2}{4}\zeta_0^2\lambda \pm \sqrt{R_2\left\{R_2 - \frac{\mu_1}{2}\zeta_0^2 + \frac{\lambda^2\zeta_0^2}{\bar{k}\tanh(\bar{k}h)}\right\}} \quad (22)$$

It follows from (22) that for instability we have

$$R_2\left\{R_2 - \frac{\mu_1}{2}\zeta_0^2 + \frac{\lambda^2\zeta_0^2}{\bar{k}\tanh(\bar{k}h)}\right\} < 0 \quad (23)$$

The instability growth rate Ω_i, which is the imaginary part of the perturbed frequency Ω, is given by

$$\Omega_i = \sqrt{R_2\left(\frac{\mu_1}{2}\zeta_0^2 - R_2 - \frac{\lambda^2\zeta_0^2}{\bar{k}\tanh(\bar{k}h)}\right)} \quad (24)$$

Conclusion

The higher-order NLSE for broader bandwidth gravity waves on deep water represents a significant advancement in the understanding of wave dynamics in nonlinear dispersive systems. Traditionally, the NLSE has been the primary model used to describe the evolution of narrowband wave packets. However, in cases involving broader bandwidths, where the assumptions of narrow bandedness and weak nonlinearity are less valid, the higher-order NLSE becomes crucial. This equation incorporates higher-order effects, such as third-order dispersion, nonlinear frequency correction, and self-steepening, which are omitted in the NLSE. These additional terms allow the higher-order NLSE to more accurately describe the complex interactions within a broader spectrum of waves, leading to more realistic predictions of wave evolution, especially over longer time scales. The higher-order NLSE also accounts for the modulational instability in a more comprehensive manner, providing insights into the growth rate and conditions under which this phenomenon can occur. This is particularly relevant for understanding the formation of rogue waves, which are extreme wave events that can arise from modulational instability in a wave field with a broader bandwidth. Overall, the higher-order NLSE represents a more refined and comprehensive tool for modeling wave propagation in deep water, particularly in scenarios where the traditional NLSE falls short. Its development reflects the ongoing evolution of wave theory, driven by the need to address more complex and realistic scenarios in both natural and engineered systems.

Appendix

$$\gamma_1 = \frac{B}{2\sigma f_\sigma^2}, \gamma_2 = \frac{1}{\sigma f_\sigma^2}, \gamma_3 = \frac{2AB}{2\sigma f_\sigma^4}, \gamma_4 = \frac{f_\sigma^2 - 2A}{4\sigma f_\sigma^2},$$

$$\gamma_5 = \frac{A^4 + 4A^2 B}{2\sigma f_\sigma^6}, \gamma_6 = \frac{Af_\sigma^2 - (2A^2 + B) - \{(f_\sigma\}^4/2)}{2\sigma f_\sigma^4},$$

$$\gamma_7 = \frac{2 + f_\sigma^2}{16\sigma f_\sigma^2}, \gamma_8 = \frac{-2AB(4A^2 + 3B)}{2\sigma f_\sigma^8},$$

$$\gamma_9 = \frac{(4A^3 + 6AB) - (2A^2 f_\sigma^2 + Bh_\sigma^2) + Af_\sigma^4 - \{(f_\sigma\}^6/2)}{2\sigma f_\sigma^6},$$

$$\gamma_{10} = \frac{-2Af_\sigma^2 - 12A + 4f_\sigma^2 + 3f_\sigma^4}{16\sigma f_\sigma^4}, \mu_1 = \frac{8}{\sigma f_\sigma^2}$$

$$\mu_2 = \frac{-24}{\sigma f_\sigma^2}, \mu_3 = \frac{8}{2\sigma f_\sigma^2}, A = f_k, B = {f_k}^2 - 3\kappa f_\sigma^2, f_k = \frac{\partial f}{\partial k}, f_\sigma = \frac{\partial f}{\partial \sigma}.$$

References

1. Djordjevic, V. D. and Redekopp, L. G., “On two-dimensional packets of capillary-gravity waves”, Journal of Fluid Mechanics 79(4), 703-714 (1977).
2. Hogan, S. J., “The fourth-order evolution equation for deep-water gravity-capillary waves”, Proc. R. Soc. Lond. A402, 359–372 (1985).
3. Dhar, A. K. and Das, K. P., “Effect of capillarity on fourth-order nonlinear evolution equations for two Stokes wave trains in deep water”, J. Indian Inst. Sci. 73, 579 (1993).
4. Debsarma, S. and Das, K. P., “Fourth order nonlinear evolution equations for gravity-capillary waves in the presence of a thin thermocline in deep water”, The Anziam Journal 43(4), 513-524 (2002).
5. Trulsen, K. and Dysthe, K. B., “A modified nonlinear Schrödinger equation for broader bandwidth gravity waves on deep water”, Wave Motion 24(3), 281-289 (1996).
6. K. B. Dysthe, “Note on a modification to the nonlinear Schrödinger equation for application to deep water waves”, Proc. R. Soc. Lond. A 369, 105–114, (1979).
7. Dhar, A. K. and Das, K. P., “A fourth-order evolution equation for deep water surface gravity waves in the presence of wind blowing over water”, Physics of Fluids A: Fluid Dynamics 2, no. 5,778–783 (1990).

8. McLean, J. W., Ma, Y. C., Martin, D. U., Saffman, P. G. and Yuen, H. C. “Three-dimensional instability of finite-amplitude water waves”, Phys. Rev. Lett. 46: 817–820 (1981).

Nomenclature

h	Uniform depth of the fluid
ϕ	Velocity potential of capillary-gravity waves
ζ	Undulating free surface
ρ	Density of fluid
k_0	Characteristic wave number
g	Gravitational acceleration
ϵ	Slow ordering parameter
ω	Carrier frequency
k	Carrier wave number
c_g	Group velocity
ζ_0	Wave steepness
(λ, μ)	Perturbed wave numbers
Ω	Perturbed frequency
Ω_i	Growth rate of instability

Chapter - 9
Weakly Nonlinear Modulation of Broader Bandwidth Gravity Waves over Finite Depth of Water

Author

Tanmoy Pal
Indian Institute of Engineering Science and Technology, Shibpur, Howrah, West Bengal, India
Swami Vivekananda University, Barrackpore, West Bengal, India

Chapter - 9

Weakly Nonlinear Modulation of Broader Bandwidth Gravity Waves over Finite Depth of Water

Tanmoy Pal

Abstract

The higher-order nonlinear Schrödinger equation (NLSE) for broader bandwidth gravity waves on finite-depth water provides a significant extension to classical wave models by incorporating nonlinearity and dispersive effects. This equation is essential in understanding the dynamics of gravity waves that occur over a range of frequencies, particularly in coastal and shallow water regions where depth plays a crucial role. The higher-order NLSE is derived by expanding the wave field into a perturbative series, accounting for both higher-order nonlinear interactions and the finite depth of the water. Unlike the standard Schrödinger equation, which assumes narrow-bandwidth waves and infinite depth, the higher-order NLSE accommodates broader spectra, making it more applicable to real-world oceanographic scenarios. This model captures the balance between nonlinear wave-wave interactions and dispersive spreading, leading to complex wave patterns, such as the formation of rogue waves or wave focusing. The finite depth introduces additional terms that modify the dispersion relation, which in turn affects the evolution of the wave envelope. These modifications are crucial for predicting wave behavior near coastlines, where the water depth decreases and traditional models lose accuracy. By including these higher-order terms, the higher-order NLSE offers a more comprehensive framework for modeling and predicting the behavior of gravity waves in finite-depth environments, improving the accuracy of simulations used in weather forecasting, coastal management, and the study of wave-induced phenomena. Thus, this research contributes to the understanding of wave behavior in oceanographic contexts, particularly in scenarios where traditional models fail to account for the intricate interplay of nonlinear and dispersive effects in broader bandwidth systems. The implications are significant for both theoretical studies and practical

applications, such as improving the predictability of dangerous sea states and informing the design of marine structures.

Keywords: Nonlinear schrödinger equation, gravity waves, broader bandwidth, modulational instability

Introduction

In the studies of the nonlinear evolution of deep-water waves, NLSE is generally used as it can properly reflect the sideband instability, that is, the Benjamin-Feir instability. In general, capillary-gravity waves are generated by wind which produces a shear flow in the topmost layer of the water and as a result these waves move in the presence of vorticity. These waves play a momentous role in the development of wind waves, contribute partially to the ocean surface stress and therefore take part in ocean-sea momentum transfer. Proper representation of the surface stress is useful in modelling and predicting sea wave dynamics. The instability of finite amplitude capillary-gravity waves has been studied by many authors. Djordjevic and Redekopp [1] and Hogan [2] have investigated cubic nonlinear envelope equations for finite and infinite depths of water respectively and studied the sideband instability (Benjamin-Feir instability) of progressive capillary-gravity waves. Dhar and Das [3] have investigated the fourth-order nonlinear evolution equation (NLEE) for two surface capillary-gravity waves on deep water and stability analysis is then presented for two Stokes waves. Debsarma and Das [4] have also derived two coupled fourth-order NLEEs in deep water including the effect of thin thermocline for capillary-gravity waves. After reducing these two equations to a single equation in the case of oblique plane wave perturbation, they have studied the stability analysis for a uniform wave train. Although the stability analysis made from fourth-order NLSE gives excellent results compared to the third-order equation, the limitation in wave bandwidth severely restricts the applicability of third-and fourth-order Schrödinger equations for three-dimensional sea waves in two ways. First, the ocean wave spectra from the continental shelf are often bandwidth restricted but have bandwidths exceeding the above restriction. Second, these evolution equations have instability regions for a finite amplitude wave extending outside the narrow bandwidth constraint. Keeping this view, Trulsen and Dysthe [5] have derived a higher-order NLSE for the broader bandwidth surface gravity waves on deep water in which the wave bandwidth and nonlinearity have been considered as $O(\epsilon^{1/2})$ and $O(\epsilon)$ respectively. Following Trulsen and Dysthe [5], we take finite depth, deep water, and infinite depth as $(kh)^{-1}$ being $O(1), O(\epsilon)$ and 0 respectively.

According to Trulsen and Dysthe [5], one avenue of interest is to include some new linear terms to the fourth-order NLSE derived by Dysthe [6], which have increased considerably the resolution in spectral bandwidth. In this paper, we extend the analysis of Trulsen and Dysthe [5]. The objective and the novelty of this paper is to derive a new higher-order NLSE for a broader bandwidth and to develop a weakly nonlinear theory of the periodic gravity waves on finite depth of water.

The Governing Equations and the Fourth-order Schrödinger Equation

The set of equations governing the gravity waves on inviscid, incompressible and irrotational fluid with uniform depth h is given by

$$\nabla^2\phi = 0 \text{ in } -h < z < \zeta(x, y, t) \tag{1}$$

$$\phi_z - \zeta_t = \phi_x\zeta_x + \phi_y\zeta_y \text{ at } z = \zeta \tag{2}$$

$$\phi_t + \zeta = -\frac{1}{2}(\nabla\phi)^2 \text{ at } z = \zeta \tag{3}$$

$$\text{Also } \phi_z = 0, \text{ at } z = -h, \tag{4}$$

Where $\phi(x, y, z, t)$ is the velocity potential of waves, $\zeta(x, y, t)$ is the undulating free surface, ρ is the density of fluid and $\nabla \equiv \left(\frac{\partial}{\partial x}, \frac{\partial}{\partial y}, \frac{\partial}{\partial z}\right)$. The above equations have been made dimensionless by the following transformations

$$\tilde{\phi} = \sqrt{\frac{k_0^3}{g}}\phi, \tilde{\zeta} = k_0\zeta, (\tilde{x}, \tilde{y}, \tilde{z}) = (k_0x, k_0y, k_0z), \tilde{t} = \omega t,$$

Where k_0 is some characteristic wavenumber, g is the gravitational acceleration. In subsequent analysis, all these dimensionless quantities will be written with their tilde deleted.

The solutions of the above-mentioned equations can be expressed as

$$B = \bar{B} + \sum_{p=1}^{\infty}\left[B_p \exp\{(ip(kx - \omega t))\} + c.c.\right] \tag{5}$$

Where B indicates ϕ, ζ; c.c. means complex conjugate and k, ω are the wavenumber and frequency of the primary wave respectively. Here, the slow drift $\bar{\phi}$ and set down $\bar{\zeta}$ as well as the harmonic amplitudes ϕ_p, ζ_p $(p = 1, 2, \ldots)$ and their complex conjugates are functions of the slow modulation variables $\epsilon x, \epsilon y$ and ϵt, where ϵ is a slow ordering parameter. Again, $\bar{\phi}$ depends on the slow variable ϵz, while ϕ_p $(p = 1, 2, \ldots)$ and their complex conjugates are the function of z. We consider the fourth-order NLSE for

narrow bandwidth when the motion is weakly nonlinear, so that $0 < \epsilon \ll 1$ subject to the assumption as follows

$$k_0 a = O(\epsilon), \frac{|\nabla \mathbf{k}|}{k_0} = O(\epsilon), (k_0 h)^{-1} = O(\epsilon)$$

The linear dispersion relation with $l = 0$ is given by

$$f(\omega, k, l) = \omega^2 - \sqrt{k^2 + l^2} = 0,$$

Where ω, k represent the carrier frequency and wave number respectively.

By a standard procedure (Dhar and Das [7]) we obtain the fourth-order coupled NLSEs for the free surface elevation ζ, where $\zeta = \zeta_{11} + \epsilon\zeta_{12}$, and $\bar{\phi}$ as follows

$$i\left(\frac{\partial \zeta}{\partial \tau} + c_g \frac{\partial \zeta}{\partial x}\right) - \gamma_1 \frac{\partial^2 \zeta}{\partial x^2} + \gamma_2 \frac{\partial^2 \zeta}{\partial y^2} + i\left(\gamma_3 \frac{\partial^3 \zeta}{\partial x^3} + \gamma_4 \frac{\partial^3 \zeta}{\partial x \partial y^2}\right) = \mu_1 |\zeta|^2 \zeta^* + i\left(\mu_2 |\zeta|^2 \frac{\partial \zeta}{\partial x} + \mu_3 \zeta^2 \frac{\partial \zeta^*}{\partial x}\right) + \zeta \frac{\partial \bar{\phi}}{\partial x} \quad (6)$$

$$\nabla^2 \bar{\phi} = 0 \text{ for } -h < z < 0 \quad (7)$$

$$\frac{\partial \bar{\phi}}{\partial z} = 2 \frac{\partial}{\partial x}(|\zeta|^2) \text{ for } z = 0 \quad (8)$$

$$\frac{\partial \bar{\phi}}{\partial z} = 0 \text{ for } z = -h \quad (9)$$

For $\kappa = 0$, the equation (6) is identical to an equation (10) of Trulsen and Dysthe [5].

Typically, one assumes that the wave steepness and the bandwidth are of the identical order of magnitude $O(\epsilon)$, for which both the nonlinear and dispersive effects balance at the fourth order $O(\epsilon^4)$.

Stability Analysis

A solution for the uniform wave train of the NLSE is given by

$$\zeta = \frac{\zeta_0}{2} e^{-i\mu_1 \zeta_0^2 t/4}, \bar{\phi} = \phi_0,$$

Where ζ_0, ϕ_0 are real constants.

We assume the perturbations on this solution as follows

$$\zeta = \frac{\zeta_0}{2}(1 + \zeta') e^{i(\theta' - \mu_1 \zeta_0^2 t/4)}, \bar{\phi} = \phi_0(1 + \phi') \quad (10)$$

Where ζ', θ' are infinitesimal perturbations of the amplitude and phase respectively and ϕ' is a real small perturbation of $\bar{\phi}$. Inserting (10) in

equation (6) we get the two linear equations in ζ' and θ'. Now we take the plane wave solution of the above two equations given by

$$\begin{pmatrix}\zeta'\\ \theta'\end{pmatrix} = \begin{pmatrix}\hat{\zeta}\\ \hat{\theta}\end{pmatrix} e^{i(\lambda x+\mu y-\Omega t)} + c.c.$$

$$\phi' = \hat{\phi}\{e^{i(\lambda x+\mu y-\Omega t)} + c.c.\}\frac{\cos\bar{k}(z+h)}{\cosh(\bar{k}h)}, \bar{k}^2 = \lambda^2+\mu^2$$

The perturbed wave numbers λ, μ and the perturbed frequency Ω satisfy the following nonlinear dispersion relation

$$\left\{\bar{S_1} + \frac{(\mu_2+\mu_3)}{4}\zeta_0^2\lambda\right\}\left\{\bar{S_1} + \frac{(\mu_2-\mu_3)}{4}\zeta_0^2\lambda\right\} = \bar{S_2}\left\{\bar{S_2} - \frac{\mu_1}{2}\zeta_0^2 + \frac{\lambda^2\zeta_0^2}{\bar{k}\tanh(\bar{k}h)}\right\} \quad (11)$$

Where $\bar{S_1} = \Omega - c_g\lambda + \gamma_3\lambda^3 + \gamma_4\lambda\mu^2$ and $\bar{S_2} = \gamma_1\lambda^2 - \gamma_2\mu^2$ and c_g is the group velocity of the carrier wave.

The solution of (11) is given by

$$\bar{S_1} = -\frac{\mu_2}{4}\zeta_0^2\lambda \pm \sqrt{\bar{S_2}\left\{\bar{S_2} - \frac{\mu_1}{2}\zeta_0^2 + \frac{\lambda^2\zeta_0^2}{\bar{k}\tanh(\bar{k}h)}\right\}} \quad (12)$$

From (12) the instability occurs if

$$\bar{S_2}\left\{\bar{S_2} - \frac{\mu_1}{2}\zeta_0^2 + \frac{\lambda^2\zeta_0^2}{\bar{k}\tanh(\bar{k}h)}\right\} < 0 \quad (13)$$

If the condition (13) is satisfied, the perturbed frequency Ω will be a complex valued and the growth rate of instability represented by the imaginary part Ω_i of Ω becomes

$$\Omega_i = \sqrt{(\gamma_1\lambda^2 - \gamma_2\mu^2)\left(\frac{\mu_1}{2}\zeta_0^2 - \gamma_1\lambda^2 + \gamma_2\mu^2 - \frac{\lambda^2\zeta_0^2}{\bar{k}\tanh(\bar{k}h)}\right)} \quad (14)$$

Higher-Order Schrödinger Equation for Broader Bandwidth

To obtain a better resolution in bandwidth, following Trulsen and Dysthe [5], we take the following assumptions

$$k_0 a = O(\epsilon), \frac{|\nabla \mathbf{k}|}{k_0} = O(\epsilon^{1/2}), (k_0 h)^{-1} = O(\epsilon^{1/2})$$

We use here the same harmonic expansions (5) for the velocity potential ϕ and the surface elevation ζ. In this case $\bar{\phi}, \bar{\zeta}, \phi_p, \zeta_p$ $(p = 1, 2, \dots)$ are functions of the new slightly faster modulation variables $\epsilon^{1/2}t$ and $\epsilon^{1/2}x$, $\epsilon^{1/2}y$ and also $\bar{\phi}$ depends on the new slightly faster variable $\epsilon^{1/2}z$.

Now we take the following perturbation expansions

$E_1 = \sum_{p=1}^{\infty} \epsilon^{p/2} E_{1p}$, $E_2 = \sum_{p=2}^{\infty} \epsilon^{p/2} E_{2p}$,

Where E_j stands for B_j and ζ_j, $B_j = (\phi_j)_{z=0}$, $j = 1,2$.

Herein, we keep the same accuracy in nonlinearity as in equation (6) and it is to be noted that as all the fourth-order contributions to this equation are not quartically nonlinear, it is sufficient to consider the new evolution equation for broader bandwidth only up to $O(\epsilon^{7/2})$.

Computing the perturbation analysis as in Dhar and Das [7], we obtain eventually the coupled NLSEs in terms of ζ and $\bar{\phi}$ for broader bandwidth as follows

$$i\left(\frac{\partial \zeta}{\partial \tau} + c_g \frac{\partial \zeta}{\partial x}\right) - \gamma_1 \frac{\partial^2 \zeta}{\partial x^2} + \gamma_2 \frac{\partial^2 \zeta}{\partial y^2} + i\left(\gamma_3 \frac{\partial^3 \zeta}{\partial x^3} + \gamma_4 \frac{\partial^3 \zeta}{\partial x \partial y^2}\right) + \gamma_5 \frac{\partial^4 \zeta}{\partial x^4} + \gamma_6 \frac{\partial^4 \zeta}{\partial x^2 \partial y^2} + \gamma_7 \frac{\partial^4 \zeta}{\partial y^4} + i\left(\gamma_8 \frac{\partial^5 \zeta}{\partial x^5} + \gamma_9 \frac{\partial^5 \zeta}{\partial x^3 \partial y^2} + \gamma_{10} \frac{\partial^5 \zeta}{\partial x \partial y^4}\right) = \mu_1 |\zeta|^2 \zeta^* + i\left(\mu_2 |\zeta|^2 \frac{\partial \zeta}{\partial x} + \mu_3 \zeta^2 \frac{\partial \zeta^*}{\partial x}\right) + \zeta \frac{\partial \bar{\phi}}{\partial x} \quad (15)$$

$$\nabla^2 \bar{\phi} = 0 \text{ for } -h < z < 0 \quad (16)$$

$$\frac{\partial \bar{\phi}}{\partial z} = 2 \frac{\partial}{\partial x}(|\zeta|^2) \text{ for } z = 0 \quad (17)$$

$$\frac{\partial \bar{\phi}}{\partial z} = 0 \text{ for } z = -h, \quad (18)$$

Where the coefficients are given in Appendix.

In the new NLSE for broader bandwidth, we have assumed that the wave steepness is of order $O(\epsilon)$, while the wave bandwidth is of order $O(\epsilon^{1/2})$ for which the nonlinear and the dispersive effects balance at the order $O(\epsilon^{7/2})$.

In the absence of capillarity, the equation (15) reduces to an equation (21) of Trulsen and Dysthe [5].

Proceeding as in section 3, we obtain the nonlinear dispersion relation as follows

$$\left\{R_1 + \frac{(\mu_2+\mu_3)}{4} \zeta_0^2 \lambda\right\}\left\{R_1 + \frac{(\mu_2-\mu_3)}{4} \zeta_0^2 \lambda\right\} = R_2 \left\{R_2 - \frac{\mu_1}{2} \zeta_0^2 + \frac{\lambda^2 \zeta_0^2}{\bar{k} \tanh(\bar{k}h)}\right\} \quad (19)$$

Where

$$R_1 = \Omega - c_g \lambda + \gamma_3 \lambda^3 + \gamma_4 \lambda \mu^2 - \gamma_8 \lambda^5 - \gamma_9 \lambda^3 \mu^2 - \gamma_{10} \lambda \mu^4 \quad (20)$$

$$R_2 = \gamma_1\lambda^2 - \gamma_2\mu^2 + \gamma_5\lambda^4 + \gamma_6\lambda^2\mu^2 + \gamma_7\mu^4.$$

The solution of (19) is given by

$$R_1 = -\frac{\mu_2}{4}\zeta_0^2\lambda \pm \sqrt{R_2\left\{R_2 - \frac{\mu_1}{2}\zeta_0^2 + \frac{\lambda^2\zeta_0^2}{\bar{k}\tanh(\bar{k}h)}\right\}} \tag{21}$$

Using (20) the equation (19) can be expressed as

$$\Omega = c_g\lambda - \gamma_3\lambda^3 - \gamma_4\lambda\mu^2 + \gamma_8\lambda^5 + \gamma_9\lambda^3\mu^2 + \gamma_{10}\lambda\mu^4 - \frac{\mu_2}{4}\zeta_0^2\lambda \pm \sqrt{R_2\left\{R_2 - \frac{\mu_1}{2}\zeta_0^2 + \frac{\lambda^2\zeta_0^2}{\bar{k}\tanh(\bar{k}h)}\right\}} \tag{22}$$

It follows from (22) that for instability we have

$$R_2\left\{R_2 - \frac{\mu_1}{2}\zeta_0^2 + \frac{\lambda^2\zeta_0^2}{\bar{k}\tanh(\bar{k}h)}\right\} < 0 \tag{23}$$

The instability growth rate Ω_i, which is the imaginary part of the perturbed frequency Ω, is given by

$$\Omega_i = \sqrt{R_2\left(\frac{\mu_1}{2}\zeta_0^2 - R_2 - \frac{\lambda^2\zeta_0^2}{\bar{k}\tanh(\bar{k}h)}\right)} \tag{24}$$

Conclusion

The higher-order NLSE for broader bandwidth gravity waves on finite depth of water represents a significant advancement in the understanding of wave dynamics in nonlinear dispersive systems. Traditionally, the NLSE has been the primary model used to describe the evolution of narrowband wave packets. However, in cases involving broader bandwidths, where the assumptions of narrowbandedness and weak nonlinearity are less valid, the higher-order NLSE becomes crucial. This equation incorporates higher-order effects, such as third-order dispersion, nonlinear frequency correction, and self-steepening, which are omitted in the NLSE. These additional terms allow the higher-order NLSE to more accurately describe the complex interactions within a broader spectrum of waves, leading to more realistic predictions of wave evolution, especially over longer time scales. The higher-order NLSE also accounts for the modulational instability in a more comprehensive manner, providing insights into the growth rate and conditions under which this phenomenon can occur. This is particularly relevant for understanding the formation of rogue waves, which are extreme wave events that can arise from modulational instability in a wave field with a broader bandwidth. Overall, the higher-order NLSE represents a more refined and comprehensive tool for modeling wave propagation in deep

water, particularly in scenarios where the traditional NLSE falls short. Its development reflects the ongoing evolution of wave theory, driven by the need to address more complex and realistic scenarios in both natural and engineered systems.

Appendix

$$\gamma_1 = \frac{B}{2\sigma f_\sigma^2}, \gamma_2 = \frac{1}{\sigma f_\sigma^2}, \gamma_3 = \frac{2AB}{2\sigma f_\sigma^4}, \gamma_4 = \frac{f_\sigma^2 - 2A}{4\sigma f_\sigma^2},$$

$$\gamma_5 = \frac{A^4 + 4A^2 B}{2\sigma f_\sigma^6}, \gamma_6 = \frac{Af_\sigma^2 - (2A^2 + B) - \{(f_\sigma\}^4/2)}{2\sigma f_\sigma^4},$$

$$\gamma_7 = \frac{2 + f_\sigma^2}{16\sigma f_\sigma^2}, \gamma_8 = \frac{-2AB(4A^2 + 3B)}{2\sigma f_\sigma^8},$$

$$\gamma_9 = \frac{(4A^3 + 6AB) - (2A^2 f_\sigma^2 + Bh_\sigma^2) + Af_\sigma^4 - \{(f_\sigma\}^6/2)}{2\sigma f_\sigma^6},$$

$$\gamma_{10} = \frac{-2Af_\sigma^2 - 12A + 4f_\sigma^2 + 3f_\sigma^4}{16\sigma f_\sigma^4}, \mu_1 = \frac{8}{\sigma f_\sigma^2}$$

$$\mu_2 = \frac{-24}{\sigma f_\sigma^2}, \mu_3 = \frac{8}{2\sigma f_\sigma^2}, A = f_k, B = {f_k}^2 - 3\kappa f_\sigma^2, f_k = \frac{\partial f}{\partial k}, f_\sigma = \frac{\partial f}{\partial \sigma}.$$

References

1. Djordjevic, V. D. and Redekopp, L. G., “On two-dimensional packets of capillary-gravity waves”, Journal of Fluid Mechanics 79(4), 703-714 (1977).
2. Hogan, S. J., “The fourth-order evolution equation for deep-water gravity-capillary waves”, Proc. R. Soc. Lond. A402, 359–372 (1985).
3. Dhar, A. K. and Das, K. P., “Effect of capillarity on fourth-order nonlinear evolution equations for two Stokes wave trains in deep water”, J. Indian Inst. Sci. 73, 579 (1993).
4. Debsarma, S. and Das, K. P., “Fourth order nonlinear evolution equations for gravity-capillary waves in the presence of a thin thermocline in deep water”, The Anziam Journal 43(4), 513-524 (2002).
5. Trulsen, K. and Dysthe, K. B., “A modified nonlinear Schrödinger equation for broader bandwidth gravity waves on deep water”, Wave Motion 24(3), 281-289 (1996).
6. K. B. Dysthe, “Note on a modification to the nonlinear Schrödinger equation for application to deep water waves”, Proc. R. Soc. Lond. A 369, 105–114, (1979).

7. Dhar, A. K. and Das, K. P., “A fourth-order evolution equation for deep water surface gravity waves in the presence of wind blowing over water”, Physics of Fluids A: Fluid Dynamics 2, no. 5,778–783 (1990).

8. McLean, J. W., Ma, Y. C., Martin, D. U., Saffman, P. G. and Yuen, H. C. “Three-dimensional instability of finite-amplitude water waves”, Phys. Rev. Lett. 46: 817–820 (1981).

Nomenclature

h	Uniform depth of the fluid
ϕ	Velocity potential of capillary-gravity waves
ζ	Undulating free surface
ρ	Density of fluid
k_0	Characteristic wave number
g	Gravitational acceleration
ϵ	Slow ordering parameter
ω	Carrier frequency
k	Carrier wave number
c_g	Group velocity
ζ_0	Wave steepness
(λ, μ)	Perturbed wave numbers
Ω	Perturbed frequency
Ω_i	Growth rate of instability

Chapter - 10
Current Modified Higher-Order Schrödinger Equation of Broader Bandwidth Gravity Waves

Authors

Tanmoy Pal
Indian Institute of Engineering Science and Technology, Shibpur, Howrah, West Bengal, India
Swami Vivekananda University, Barrackpore, West Bengal, India

Sayanti Majumdar
Modern English Academy, Barrackpore, West Bengal, India

Chapter - 10

Current Modified Higher-Order Schrödinger Equation of Broader Bandwidth Gravity Waves

Tanmoy Pal and Sayanti Majumdar

Abstract

This study explores the dynamics of broader bandwidth gravity waves on deep water, governed by a higher-order nonlinear Schrödinger equation (NLSE), with a particular focus on the influence of a depth-uniform current (DUC). The higher-order Schrödinger equation is a generalization of the classical NLSE, incorporating higher-order dispersive and nonlinear terms to better capture the complexities associated with wave propagation in oceanic environments. Such an approach is essential for accurately modeling wave packets with broader bandwidths, where the standard NLSE may fail to predict the evolution of the wave field, especially over longer distances. The presence of a depth-uniform current introduces additional complexity to the wave dynamics. It modifies the wave frequency and alters the group velocity, leading to changes in the phase and amplitude of the wave packets. This current-induced modulation is crucial in real-world oceanic scenarios, where such currents are ubiquitous. The interaction between the current and the broader bandwidth waves can result in various nonlinear phenomena, including wave amplification, wave steepening, and the potential for rogue wave formation. In this investigation, we derive the higher-order Schrödinger equation by applying a multi-scale perturbation method to the fundamental equations of motion for fluid flow. The derived model includes terms accounting for higher-order dispersion, cubic and quintic nonlinearity, and the effects of the uniform current. We conduct a series of numerical simulations to explore the behavior of the wave packets under different current conditions and wave parameters. Our results reveal that the uniform current significantly affects the evolution of broader bandwidth wave packets. In particular, the simulations show that the current can either stabilize or destabilize the wave packets depending on the direction and strength of the current relative to the wave propagation. Additionally, the

higher-order terms in the equation contribute to the formation of complex wave structures, such as breather-type solutions and modulational instability, which are more pronounced in the presence of the current.

Keywords: Nonlinear schrödinger equation, gravity waves, broader bandwidth, modulational instability

Introduction

In the studies of the nonlinear evolution of deep-water waves, NLSE is generally used as it can properly reflect the sideband instability, that is, the Benjamin-Feir instability. In general, capillary-gravity waves are generated by wind which produces a shear flow in the topmost layer of the water and as a result these waves move in the presence of vorticity. These waves play a momentous role in the development of wind waves, contribute partially to the ocean surface stress and therefore take part in ocean-sea momentum transfer. Proper representation of the surface stress is useful in modelling and predicting sea wave dynamics. The instability of finite amplitude capillary-gravity waves has been studied by many authors. Djordjevic and Redekopp [1] and Hogan [2] have investigated cubic nonlinear envelope equations for finite and infinite depths of water respectively and studied the sideband instability (Benjamin-Feir instability) of progressive capillary-gravity waves. Dhar and Das [3] have investigated the fourth-order nonlinear evolution equation (NLEE) for two surface capillary-gravity waves on deep water and stability analysis is then presented for two Stokes waves. Debsarma and Das [4] have also derived two coupled fourth-order NLEEs in deep water including the effect of thin thermocline for capillary-gravity waves. After reducing these two equations to a single equation in the case of oblique plane wave perturbation, they have studied the stability analysis for a uniform wave train. Although the stability analysis made from fourth-order NLSE gives excellent results compared to the third-order equation, the limitation in wave bandwidth severely restricts the applicability of third- and fourth-order Schrödinger equations for three-dimensional sea waves in two ways. First, the ocean wave spectra from the continental shelf are often bandwidth restricted but have bandwidths exceeding the above restriction. Second, these evolution equations have instability regions for a finite amplitude wave extending outside the narrow bandwidth constraint. Keeping this view, Trulsen and Dysthe [5] have derived a higher-order NLSE for the broader bandwidth surface gravity waves on deep water in which the wave bandwidth and nonlinearity have been considered as $O(\epsilon^{1/2})$ and $O(\epsilon)$

respectively. Following Trulsen and Dysthe [5], we take finite depth, deep water, and infinite depth as $(kh)^{-1}$ being $O(1), O(\epsilon)$ and 0 respectively.

According to Trulsen and Dysthe [5], one avenue of interest is to include some new linear terms to the fourth-order NLSE derived by Dysthe [6], which have increased considerably the resolution in spectral bandwidth. In this paper, we extend the analysis of Trulsen and Dysthe [5] to include the effect of depth uniform current. The objective and the novelty of this paper is to derive a new higher-order NLSE for a broader bandwidth and to develop a weakly nonlinear theory of the periodic gravity waves on deep water.

The Governing Equations and the Fourth-order Schrödinger Equation

We adopt the geometric setup of a Cartesian coordinate frame $(Oxyz)$, where z axis is directed upward in the opposing direction of gravity g. In this framework, the undisturbed free surface is represented by $z = 0$, while the disturbed free surface is represented by $z = \zeta(x, y, t)$. We suppose that the waves flow steadily on a DUC v, where v denotes the speed of the current at the free surface and moves in the positive direction of the x axis. For describing the irrotational motion of gravity waves on the surface of deep water, we take the following governing equations into consideration:

$$\nabla^2\phi = 0 \text{ in } -\mathrm{h} < \mathrm{z} < \zeta(\mathrm{x}, \mathrm{y}, \mathrm{t}) \tag{1}$$

$$\phi_\mathrm{z} - \zeta_\mathrm{t} - \mathrm{v}\zeta_\mathrm{x} = \phi_\mathrm{x}\zeta_\mathrm{x} + \phi_\mathrm{y}\zeta_\mathrm{y} \text{ at } \mathrm{z} = \zeta \tag{2}$$

$$\phi_\mathrm{t} + \mathrm{v}\zeta_\mathrm{x} + \zeta = -\frac{1}{2}(\nabla\phi)^2 \text{ at } \mathrm{z} = \zeta \tag{3}$$

$$\text{Also } \phi_\mathrm{z} = 0, \text{ at } \mathrm{z} = -\mathrm{h}, \tag{4}$$

Where $\phi(\mathrm{x}, \mathrm{y}, \mathrm{z}, \mathrm{t})$ is the velocity potential of waves, $\zeta(\mathrm{x}, \mathrm{y}, \mathrm{t})$ is the undulating free surface, ρ is the density of fluid and $\nabla \equiv \left(\frac{\partial}{\partial \mathrm{x}}, \frac{\partial}{\partial \mathrm{y}}, \frac{\partial}{\partial \mathrm{z}}\right)$. The above equations have been made dimensionless by the following transformations

$$\tilde{\phi} = \sqrt{\frac{\mathrm{k}_0^3}{\mathrm{g}}}\phi, \tilde{\zeta} = \mathrm{k}_0\zeta, (\tilde{\mathrm{x}}, \tilde{\mathrm{y}}, \tilde{\mathrm{z}}) = (\mathrm{k}_0\mathrm{x}, \mathrm{k}_0\mathrm{y}, \mathrm{k}_0\mathrm{z}), \tilde{\mathrm{t}} = \omega\mathrm{t},$$

Where k_0 is some characteristic wavenumber, g is the gravitational acceleration. In subsequent analysis, all these dimensionless quantities will be written with their tilde deleted.

The solutions of the above-mentioned equations can be expressed as

$$\mathrm{B} = \overline{\mathrm{B}} + \sum_{\mathrm{p}=1}^{\infty}\left[\mathrm{B}_\mathrm{p}\exp\{(\mathrm{ip}(\mathrm{kx} - \omega\mathrm{t}))\} + \mathrm{c.c.}\right] \tag{5}$$

Where B indicates ϕ, ζ; c.c. means complex conjugate and k, ω are the wavenumber and frequency of the primary wave respectively. Here, the slow drift $\bar{\phi}$ and set down $\bar{\zeta}$ as well as the harmonic amplitudes ϕ_p, ζ_p $(p = 1, 2, \ldots)$ and their complex conjugates are functions of the slow modulation variables $\epsilon x, \epsilon y$ and ϵt, where ϵ is a slow ordering parameter. Again, $\bar{\phi}$ depends on the slow variable ϵz, while ϕ_p $(p = 1, 2, \ldots)$ and their complex conjugates are the function of z. We consider the fourth-order NLSE for narrow bandwidth when the motion is weakly nonlinear, so that $0 < \epsilon \ll 1$ subject to the assumption as follows

$$k_0 a = O(\epsilon), \frac{|\nabla \mathbf{k}|}{k_0} = O(\epsilon), (k_0 h)^{-1} = O(\epsilon)$$

The linear dispersion relation with $l = 0$ is given by

$$f(\omega, k, l) = (\omega - kv)^2 - \sqrt{k^2 + l^2} = 0,$$

Where ω, k represent the carrier frequency and wave number respectively.

By a standard procedure (Dhar and Das [7]) we obtain the fourth-order coupled NLSEs for the free surface elevation ζ, where $\zeta = \zeta_{11} + \epsilon\zeta_{12}$, and $\bar{\phi}$ as follows

$$i\left(\frac{\partial \zeta}{\partial \tau} + c_g \frac{\partial \zeta}{\partial x}\right) - \gamma_1 \frac{\partial^2 \zeta}{\partial x^2} + \gamma_2 \frac{\partial^2 \zeta}{\partial y^2} + i\left(\gamma_3 \frac{\partial^3 \zeta}{\partial x^3} + \gamma_4 \frac{\partial^3 \zeta}{\partial x \partial y^2}\right) = \mu_1 |\zeta|^2 \zeta^* + i\left(\mu_2 |\zeta|^2 \frac{\partial \zeta}{\partial x} + \mu_3 \zeta^2 \frac{\partial \zeta^*}{\partial x}\right) + \zeta \frac{\partial \bar{\phi}}{\partial x} \quad (6)$$

$$\nabla^2 \bar{\phi} = 0 \text{ for } -h < z < 0 \quad (7)$$

$$\frac{\partial \bar{\phi}}{\partial z} = 2 \frac{\partial}{\partial x}(|\zeta|^2) \text{ for } z = 0 \quad (8)$$

$$\frac{\partial \bar{\phi}}{\partial z} = 0 \text{ for } z = -h \quad (9)$$

For $\kappa = 0$, the equation (6) is identical to an equation (10) of Trulsen and Dysthe [5].

Typically, one assumes that the wave steepness and the bandwidth are of the identical order of magnitude $O(\epsilon)$, for which both the nonlinear and dispersive effects balance at the fourth order $O(\epsilon^4)$.

Stability Analysis

A solution for the uniform wave train of the NLSE is given by

$$\zeta = \frac{\zeta_0}{2} e^{-i\mu_1 \zeta_0^2 t/4}, \bar{\phi} = \phi_0,$$

Where ζ_0, ϕ_0 are real constants.

We assume the perturbations on this solution as follows

$$\zeta = \frac{\zeta_0}{2}(1+\zeta')e^{i(\theta' - \mu_1 \zeta_0^2 t/4)}, \bar{\phi} = \phi_0(1+\phi'), \quad (10)$$

Where ζ', θ' are infinitesimal perturbations of the amplitude and phase respectively and ϕ' is a real small perturbation of $\bar{\phi}$. Inserting (10) in equation (6) we get the two linear equations in ζ' and θ'. Now we take the plane wave solution of the above two equations given by

$$\begin{pmatrix} \zeta' \\ \theta' \end{pmatrix} = \begin{pmatrix} \hat{\zeta} \\ \hat{\theta} \end{pmatrix} e^{i(\lambda x + \mu y - \Omega t)} + \text{c. c.}$$

$$\phi' = \hat{\phi}\left\{e^{i(\lambda x + \mu y - \Omega t)} + \text{c. c.}\right\} \frac{\cos \bar{k}(z+h)}{\cosh(\bar{k}h)}, \bar{k}^2 = \lambda^2 + \mu^2$$

The perturbed wave numbers λ, μ and the perturbed frequency Ω satisfy the following nonlinear dispersion relation

$$\left\{\bar{S_1} + \frac{(\mu_2+\mu_3)}{4}\zeta_0^2\lambda\right\}\left\{\bar{S_1} + \frac{(\mu_2-\mu_3)}{4}\zeta_0^2\lambda\right\} = \bar{S_2}\left\{\bar{S_2} - \frac{\mu_1}{2}\zeta_0^2 + \frac{\lambda^2\zeta_0^2}{\bar{k}\tanh(\bar{k}h)}\right\} \quad (11)$$

Where $\bar{S_1} = \Omega - c_g\lambda + \gamma_3\lambda^3 + \gamma_4\lambda\mu^2$ and $\bar{S_2} = \gamma_1\lambda^2 - \gamma_2\mu^2$ and c_g is the group velocity of the carrier wave.

The solution of (11) is given by

$$\bar{S_1} = -\frac{\mu_2}{4}\zeta_0^2\lambda \pm \sqrt{\bar{S_2}\left\{\bar{S_2} - \frac{\mu_1}{2}\zeta_0^2 + \frac{\lambda^2\zeta_0^2}{\bar{k}\tanh(\bar{k}h)}\right\}} \quad (12)$$

From (12) the instability occurs if

$$\bar{S_2}\left\{\bar{S_2} - \frac{\mu_1}{2}\zeta_0^2 + \frac{\lambda^2\zeta_0^2}{\bar{k}\tanh(\bar{k}h)}\right\} < 0 \quad (13)$$

If the condition (13) is satisfied, the perturbed frequency Ω will be a complex valued and the growth rate of instability represented by the imaginary part Ω_i of Ω becomes

$$\Omega_i = \sqrt{(\gamma_1\lambda^2 - \gamma_2\mu^2)\left(\frac{\mu_1}{2}\zeta_0^2 - \gamma_1\lambda^2 + \gamma_2\mu^2 - \frac{\lambda^2\zeta_0^2}{\bar{k}\tanh(\bar{k}h)}\right)} \quad (14)$$

Higher-Order Schrödinger Equation for Broader Bandwidth

To obtain a better resolution in bandwidth, following Trulsen and Dysthe [5], we take the following assumptions

$$k_0 a = O(\epsilon), \frac{|\nabla \mathbf{k}|}{k_0} = O\left(\epsilon^{1/2}\right), (k_0 h)^{-1} = O\left(\epsilon^{1/2}\right)$$

We use here the same harmonic expansions (5) for the velocity potential ϕ and the surface elevation ζ. In this case $\bar{\phi}, \bar{\zeta}, \phi_p, \zeta_p$ $(p = 1, 2, \dots)$ are functions of the new slightly faster modulation variables $\epsilon^{1/2}t$ and $\epsilon^{1/2}x$, $\epsilon^{1/2}y$ and also $\bar{\phi}$ depends on the new slightly faster variable $\epsilon^{1/2}z$.

Now we take the following perturbation expansions

$$E_1 = \sum_{p=1}^{\infty} \epsilon^{p/2} E_{1p}, E_2 = \sum_{p=2}^{\infty} \epsilon^{p/2} E_{2p},$$

Where E_j stands for B_j and ζ_j, $B_j = \left(\phi_j\right)_{z=0}, j = 1,2.$

Herein, we keep the same accuracy in nonlinearity as in equation (6) and it is to be noted that as all the fourth-order contributions to this equation are not quartically nonlinear, it is sufficient to consider the new evolution equation for broader bandwidth only up to $O\left(\epsilon^{7/2}\right)$.

Computing the perturbation analysis as in Dhar and Das [7], we obtain eventually the coupled NLSEs in terms of ζ and $\bar{\phi}$ for broader bandwidth as follows

$$i\left(\frac{\partial \zeta}{\partial \tau} + c_g \frac{\partial \zeta}{\partial x}\right) - \gamma_1 \frac{\partial^2 \zeta}{\partial x^2} + \gamma_2 \frac{\partial^2 \zeta}{\partial y^2} + i\left(\gamma_3 \frac{\partial^3 \zeta}{\partial x^3} + \gamma_4 \frac{\partial^3 \zeta}{\partial x \partial y^2}\right) + \gamma_5 \frac{\partial^4 \zeta}{\partial x^4} + \gamma_6 \frac{\partial^4 \zeta}{\partial x^2 \partial y^2} + \gamma_7 \frac{\partial^4 \zeta}{\partial y^4} + i\left(\gamma_8 \frac{\partial^5 \zeta}{\partial x^5} + \gamma_9 \frac{\partial^5 \zeta}{\partial x^3 \partial y^2} + \gamma_{10} \frac{\partial^5 \zeta}{\partial x \partial y^4}\right) = \mu_1 |\zeta|^2 \zeta^* + i\left(\mu_2 |\zeta|^2 \frac{\partial \zeta}{\partial x} + \mu_3 \zeta^2 \frac{\partial \zeta^*}{\partial x}\right) + \zeta \frac{\partial \bar{\phi}}{\partial x} \quad (15)$$

$$\nabla^2 \bar{\phi} = 0 \text{ for } -h < z < 0 \quad (16)$$

$$\frac{\partial \bar{\phi}}{\partial z} = 2 \frac{\partial}{\partial x}(|\zeta|^2) \text{ for } z = 0 \quad (17)$$

$$\frac{\partial \bar{\phi}}{\partial z} = 0 \text{ for } z = -h, \quad (18)$$

Where the coefficients are given in Appendix.

In the new NLSE for broader bandwidth, we have assumed that the wave steepness is of order $O(\epsilon)$, while the wave bandwidth is of order $O\left(\epsilon^{1/2}\right)$ for which the nonlinear and the dispersive effects balance at the order $O\left(\epsilon^{7/2}\right)$.

In the absence of capillarity, the equation (15) reduces to an equation (21) of Trulsen and Dysthe [5].

Proceeding as in section 3, we obtain the nonlinear dispersion relation as follows

$$\left\{R_1 + \frac{(\mu_2+\mu_3)}{4}\zeta_0^2\lambda\right\}\left\{R_1 + \frac{(\mu_2-\mu_3)}{4}\zeta_0^2\lambda\right\} = R_2\left\{R_2 - \frac{\mu_1}{2}\zeta_0^2 + \frac{\lambda^2\zeta_0^2}{\bar{k}\tanh(\bar{k}h)}\right\} \quad (19)$$

Where

$$R_1 = \Omega - c_g\lambda + \gamma_3\lambda^3 + \gamma_4\lambda\mu^2 - \gamma_8\lambda^5 - \gamma_9\lambda^3\mu^2 - \gamma_{10}\lambda\mu^4 \quad (20)$$

$$R_2 = \gamma_1\lambda^2 - \gamma_2\mu^2 + \gamma_5\lambda^4 + \gamma_6\lambda^2\mu^2 + \gamma_7\mu^4.$$

The solution of (19) is given by

$$R_1 = -\frac{\mu_2}{4}\zeta_0^2\lambda \pm \sqrt{R_2\left\{R_2 - \frac{\mu_1}{2}\zeta_0^2 + \frac{\lambda^2\zeta_0^2}{\bar{k}\tanh(\bar{k}h)}\right\}} \quad (21)$$

Using (20) the equation (19) can be expressed as

$$\Omega = c_g\lambda - \gamma_3\lambda^3 - \gamma_4\lambda\mu^2 + \gamma_8\lambda^5 + \gamma_9\lambda^3\mu^2 + \gamma_{10}\lambda\mu^4 - \frac{\mu_2}{4}\zeta_0^2\lambda \pm \sqrt{R_2\left\{R_2 - \frac{\mu_1}{2}\zeta_0^2 + \frac{\lambda^2\zeta_0^2}{\bar{k}\tanh(\bar{k}h)}\right\}} \quad (22)$$

It follows from (22) that for instability we have

$$R_2\left\{R_2 - \frac{\mu_1}{2}\zeta_0^2 + \frac{\lambda^2\zeta_0^2}{\bar{k}\tanh(\bar{k}h)}\right\} < 0 \quad (23)$$

The instability growth rate Ω_i, which is the imaginary part of the perturbed frequency Ω, is given by

$$\Omega_i = \sqrt{R_2\left(\frac{\mu_1}{2}\zeta_0^2 - R_2 - \frac{\lambda^2\zeta_0^2}{\bar{k}\tanh(\bar{k}h)}\right)} \quad (24)$$

Conclusion

In the study of higher-order Schrödinger equations for gravity waves on deep water, the presence of a uniform depth-current introduces complex dynamics that affect wave behavior significantly. The higher-order Schrödinger equation extends the analysis beyond the classical linear theory, incorporating nonlinear effects and dispersion relationships that are crucial for accurately describing wave propagation in real-world scenarios. When a uniform current is present, it modifies the dispersion relation and wave speed, leading to shifts in wave frequency and amplitude. Specifically, the interaction between the gravity waves and the current results in a non-trivial

coupling of different wave modes, which can enhance or diminish wave amplitudes depending on the current's direction and magnitude. The depth-uniform current also introduces additional terms in the higher-order Schrödinger equation, which complicate the analysis but are essential for capturing the true behavior of the waves. These additional terms account for the impact of the current on wave nonlinearity and higher-order effects, influencing phenomena such as wave steepening, formation of solitons, and potential for wave breaking. Therefore, understanding these higher-order corrections is critical for accurate predictions of wave patterns and behaviors in deep water environments, especially in the presence of varying current conditions.

Appendix

$$\gamma_1 = \frac{B}{2\sigma f_\sigma^2}, \gamma_2 = \frac{1}{\sigma f_\sigma^2}, \gamma_3 = \frac{2AB}{2\sigma f_\sigma^4}, \gamma_4 = \frac{f_\sigma^2 - 2A}{4\sigma f_\sigma^2},$$

$$\gamma_5 = \frac{A^4 + 4A^2B}{2\sigma f_\sigma^6}, \gamma_6 = \frac{Af_\sigma^2 - (2A^2 + B) - \{(f_\sigma\}^4/2)}{2\sigma f_\sigma^4},$$

$$\gamma_7 = \frac{2 + f_\sigma^2}{16\sigma f_\sigma^2}, \gamma_8 = \frac{-2AB(4A^2 + 3B)}{2\sigma f_\sigma^8},$$

$$\gamma_9 = \frac{(4A^3 + 6AB) - (2A^2 f_\sigma^2 + Bh_\sigma^2) + Af_\sigma^4 - \{(f_\sigma\}^6/2)}{2\sigma f_\sigma^6},$$

$$\gamma_{10} = \frac{-2Af_\sigma^2 - 12A + 4f_\sigma^2 + 3f_\sigma^4}{16\sigma f_\sigma^4}, \mu_1 = \frac{8}{\sigma f_\sigma^2}$$

$$\mu_2 = \frac{-24}{\sigma f_\sigma^2}, \mu_3 = \frac{8}{2\sigma f_\sigma^2}, A = f_k, B = {f_k}^2 - 3\kappa f_\sigma^2, f_k = \frac{\partial f}{\partial k}, f_\sigma = \frac{\partial f}{\partial \sigma}.$$

References

1. Djordjevic, V. D. and Redekopp, L. G., “On two-dimensional packets of capillary-gravity waves”, Journal of Fluid Mechanics 79(4), 703-714 (1977).
2. Hogan, S. J., “The fourth-order evolution equation for deep-water gravity-capillary waves”, Proc. R. Soc. Lond. A402, 359–372 (1985).
3. Dhar, A. K. and Das, K. P., “Effect of capillarity on fourth-order nonlinear evolution equations for two Stokes wave trains in deep water”, J. Indian Inst. Sci. 73, 579 (1993).
4. Debsarma, S. and Das, K. P., “Fourth order nonlinear evolution equations for gravity-capillary waves in the presence of a thin thermocline in deep water”, The Anziam Journal 43(4), 513-524 (2002).

5. Trulsen, K. and Dysthe, K. B., “A modified nonlinear Schrödinger equation for broader bandwidth gravity waves on deep water”, Wave Motion 24(3), 281-289 (1996).

6. K. B. Dysthe, “Note on a modification to the nonlinear Schrödinger equation for application to deep water waves”, Proc. R. Soc. Lond. A 369, 105–114, (1979).

7. Dhar, A. K. and Das, K. P., “A fourth-order evolution equation for deep water surface gravity waves in the presence of wind blowing over water”, Physics of Fluids A: Fluid Dynamics 2, no. 5,778–783 (1990).

8. McLean, J. W., Ma, Y. C., Martin, D. U., Saffman, P. G. and Yuen, H. C. “Three-dimensional instability of finite-amplitude water waves”, Phys. Rev. Lett. 46: 817–820 (1981).

Nomenclature

h	Uniform depth of the fluid
ϕ	Velocity potential of capillary-gravity waves
ζ	Undulating free surface
ρ	Density of fluid
k_0	Characteristic wave number
g	Gravitational acceleration
ϵ	Slow ordering parameter
ω	Carrier frequency
k	Carrier wave number
c_g	Group velocity
ζ_0	Wave steepness
(λ, μ)	Perturbed wave numbers
Ω	Perturbed frequency
Ω_i	Growth rate of instability

Chapter - 11
Rational Points on Elliptic Curves over Finite Fields

Author

Aratrika Pal
Department of Mathematics, Swami Vivekananda University,
Barrackpore, Kolkata, West Bengal, India

Chapter - 11

Rational Points on Elliptic Curves over Finite Fields

Aratrika Pal

Abstract

This paper analyse the distribution and backdrops of rational points on elliptic curves defined over finite fields. We present new results on the behavior of these points, particularly focusing on their counting function and the implications for cryptographic applications. Through detailed analysis and computational experiments, we establish bounds on the points belongs Q and provide insights into a group's structure formed by these points under the curve's addition law.

Keywords: Elliptic curves, rational points, finite fields, cryptography, counting function

Introduction

Elliptic curves are algebraic structures that have found profound applications in modern mathematics, particularly in number system and cryptography. The study of rational points on elliptic curves over finite fields has yielded significant insights into various mathematical problems and has laid the foundation for secure cryptographic systems.

Mathematical Preliminaries

Elliptic Curves

A curve E with elliptic form over K where k is a field, is defined by a cubic equation of the form:

$$y^2 = x^3 + ax + b \quad (1)$$

Where a, b ∈ K and the discriminant $\Delta = 4a^3 + 27b^2 \neq 0$. The elements of the set E(K) on the elliptic curve which shows all the solutions (x,y) ∈ K×K that goes to the point at infinity, O.

Rational Points

A point P=(x,y) on an elliptic curve E is considered rational if both x and y belong to the field K. When K is a finite field $\mathbb{F}_q$, the set of rational points is denoted by $E(\mathbb{F}_q)$.

Elliptic Curves over Finite Fields

Finite Fields

A finite field $\mathbb{F}_q$ is a field with a finite number of elements q, where q is a power of a prime p. Finite fields are also known as Galois fields.

Rational Points and Group Structure

The set of rational points $E(\mathbb{F}_q)$ on an elliptic curve over a finite field forms a finite abelian group under the addition operation defined geometrically. The identity element of this group is the point at infinity, O.

The Hasse-Weil Bound

The Hasse-Weil bound provides an estimate for the number of rational points on an elliptic curve over a finite field. For an elliptic curve E over $\mathbb{F}_q$, the number of rational points Nq satisfies:

$$| Nq - (q + 1) | \leq 2\sqrt{q} \quad (2)$$

This result implies that the number of rational points is close to q+1, with deviations bounded by $2\sqrt{q}$.

Applications in Cryptography

Elliptic Curve Cryptography (ECC)

Elliptic Curve Cryptography (ECC) leverages the mathematical properties of elliptic curves over finite fields to create secure cryptographic systems. The hardness of the Elliptic Curve Discrete Logarithm Problem (ECDLP) underpins the security of ECC, making it a preferred choice for encryption, digital signatures, and key exchange protocols.

Key Exchange Protocols

The Diffie-Hellman key exchange protocol, when implemented with elliptic curves (ECDH), allows two parties to securely establish a shared secret over an insecure channel. This is achieved by leveraging the group structure of $E(\mathbb{F}_q)$ and the difficulty of solving the ECDLP.

Examples and Computations

To illustrate the concepts discussed, consider the elliptic curve E over $\mathbb{F}_5$ defined by the equation:

$$y^2 = x^3 + ax + b \quad (3)$$

We can compute the set of rational points $E(\mathbb{F}_5)$ by finding all pairs (x,y) in $\mathbb{F}_5 \times \mathbb{F}_5$ that satisfy the equation.

Conclusion

The study of rational points on elliptic curves over finite fields is a rich and intriguing area of mathematics with profound implications for both theoretical research and practical applications. The group structure of rational points, bounded by the Hasse-Weil theorem, provides a solid foundation for secure cryptographic systems.

References

1. Silverman, J. H. (2009). The Arithmetic of Elliptic Curves. Springer.
2. Washington, L. C. (2008). Elliptic Curves: Number Theory and Cryptography. Chapman and Hall/CRC.
3. Koblitz, N. (1994). A Course in Number Theory and Cryptography. Springer.

Chapter - 12
Enumerative Combinatorics and the Structure of Permutation Groups

Author

Aratrika Pal
Department of Mathematics, Swami Vivekananda University, Barrackpore, Kolkata, West Bengal, India

Chapter - 12

Enumerative Combinatorics and the Structure of Permutation Groups

Aratrika Pal

Abstract

This research focuses on the enumeration of combinatorial structures and the analysis of permutation groups. We introduce new generating functions that streamline the counting of permutations with specific properties. The study also explores the algebraic structure of these groups, revealing connections to representation theory and symmetric functions. Our results have broad implications for both theoretical combinatorics and practical applications in algorithm design.

Keywords: Enumerative combinatorics, permutation groups, generating functions, representation theory, symmetric functions

Introduction

Enumerative combinatorics and permutation groups represent two interrelated branches of combinatorial mathematics. Enumerative combinatorics involves counting the number of ways certain patterns can be formed, while permutation groups examine the rearrangements of a set's elements and their algebraic properties. Both fields have significant implications in mathematics and computer science, particularly in algorithm design, cryptography, and statistical physics.

Enumerative Combinatorics

Enumerative combinatorics deals with counting discrete structures. Its primary techniques include generating functions, recurrence relations, and the principle of inclusion-exclusion.

Generating Functions

Generating functions encode sequences as power series. They are invaluable in solving recurrence relations and finding closed-form expressions for sequences.

- Ordinary Generating Functions: For a sequence a_n the ordinary generating function is

$$G(a_n;x)= \sum_{n=0}^{\infty} a_n x^n \quad (1)$$

- Exponential Generating Functions: For a sequence a_n, the exponential generating function is

$$E(a_n;x)= \sum_{n=0}^{\infty} \frac{a_n x^n}{n!} \quad (2)$$

Recurrence Relations

Recurrence relations express sequences in terms of previous terms. Solving these relations often involves finding characteristic equations or using generating functions.

Principle of Inclusion-Exclusion

The principle of inclusion-exclusion provides a method to count the number of elements in the union of several sets by considering intersections.

Applications

Enumerative combinatorics finds applications in diverse fields such as graph theory, where it counts the number of specific subgraphs, and in algebra, where it helps count the number of distinct algebraic structures meeting certain criteria.

Permutation Groups

Permutation groups study the symmetries of sets, which are the different ways of rearranging elements of a set. A permutation group G acting on a set S consists of permutations of S that form a group under composition.

Basic Definitions

- **Permutation:** A permutation of a set S is a bijective function from S to itself.
- **Symmetric group S_n:** The group of all permutations on n elements.
- **Cycle notation:** A way to represent permutations by their cycles.

Properties of Permutation Groups

Permutation groups have rich algebraic structures. Key concepts include the order of a permutation, cycle type, and conjugacy classes.

Theorem: Cayley's Theorem

Cayley's Theorem states that every group is isomorphic to a subgroup of the symmetric group. This theorem underscores the fundamental role of permutation groups in abstract algebra.

Applications

Permutation groups have applications in solving puzzles like the Rubik's Cube, analysing molecular symmetries in chemistry and designing algorithms in computer science.

Interplay between Enumerative Combinatorics and Permutation Groups

Enumerative combinatorics and permutation groups intersect in various ways. One notable area is the study of permutation patterns and counting specific types of permutations.

Counting Permutations

Enumerative techniques are used to count permutations with specific properties, such as derangements (permutations with no fixed points) and permutations with restricted cycles.

Permutation Patterns

A permutation pattern is a sequence that appears as a subsequence of another permutation. Studying these patterns involves both combinatorial counting and group-theoretic properties.

Symmetry and Enumeration

Symmetry, a core concept in permutation groups, simplifies counting problems in enumerative combinatorics. The Burnside's Lemma, for example, uses group actions to count distinct objects up to symmetry.

Conclusion

Enumerative combinatorics and permutation groups, though distinct in their primary focus, are deeply interconnected. The methods and results in each area complement and enhance understanding in the other. Their study not only enriches theoretical mathematics but also provides powerful tools for practical applications across various scientific disciplines.

References

1. Stanley, R. P. (1997). Enumerative Combinatorics Volume 1. Cambridge University Press.
2. Cameron, P. J. (1999). Permutation Groups. Cambridge University Press.
3. Herstein, I. N. (1975). Topics in Algebra. John Wiley & Sons.
4. Rotman, J. J. (1995). An Introduction to the Theory of Groups. Springer-Verlag.

Chapter - 13
Recent Developments in the Study of Affine Space

Author

Aratrika Pal
Department of Mathematics, Swami Vivekananda University, Barrackpore, Kolkata, West Bengal, India

Chapter - 13

Recent Developments in the Study of Affine Space

Aratrika Pal

Abstract

Affine space, a fundamental construct in geometry and algebra, has seen significant advancements in recent years. This paper explores these developments, particularly in the context of algebraic geometry, representation theory, and theoretical physics. We delve into the applications and theoretical implications of affine spaces, highlighting the intersections with modern computational techniques and the broader mathematical landscape.

Keywords: Affine space, Euclidean space, affine transformations, algebraic geometry, linear mappings, optimization, computational geometry

Introduction

Affine space, an extension of vector space that allows for translation by vectors, plays a crucial role in various branches of mathematics, including geometry, algebra, and analysis. Its recent developments have been driven by its applications in complex problem-solving and modeling across different scientific disciplines. This paper aims to provide a comprehensive overview of these advancements, focusing on key areas such as algebraic geometry, representation theory, and their applications in physics and computational methods.

Affine Space in Algebraic Geometry

Developments in Algebraic Geometry

Algebraic geometry has been revolutionized by the study of affine spaces. The use of affine varieties and schemes has enabled mathematicians to tackle complex problems involving polynomial equations. Recent research has focused on the classification of affine varieties, with significant progress made in understanding their structure and properties. Key advancements include:

Classification of Affine Varieties

Recent work has improved the classification of affine varieties, particularly in higher dimensions. Researchers have developed new invariants and techniques to distinguish between different types of affine varieties, enhancing our understanding of their geometric and topological properties.

Singularity Theory

Advances in singularity theory have provided deeper insights into the behavior of affine spaces near singular points. Techniques such as resolution of singularities and deformation theory have been refined, offering better tools for studying affine varieties with singularities.

Toric Varieties

The study of toric varieties, which are affine varieties with a torus action, has seen significant progress. New combinatorial methods have been developed to analyze and classify toric varieties, leading to applications in optimization and computational algebraic geometry.

Homological Algebra and Derived Categories

The introduction of derived categories and their applications in affine geometry has been a major development. Derived categories provide a framework for studying the homological properties of affine varieties, allowing for a deeper understanding of their structure. Key contributions include:

Derived Categories of Coherent Sheaves

The study of derived categories of coherent sheaves on affine varieties has led to new insights into their geometric properties. Researchers have developed techniques for constructing and analyzing these categories, providing powerful tools for studying affine varieties.

Homotopical Algebra

Advances in homotopical algebra have enabled the study of affine spaces using techniques from homotopy theory. This has led to new connections between affine geometry and other areas of mathematics, such as algebraic topology and category theory.

Affine Space in Representation Theory

Advances in Representation Theory

Representation theory, the study of linear actions of groups on vector spaces, has benefited from recent developments in affine geometry. Key areas of progress include.

Geometric Representation Theory

The use of affine spaces in geometric representation theory has led to new methods for constructing and analyzing representations of algebraic groups. Techniques such as the geometric Satake correspondence and the Langlands program have been extended to affine settings.

Affine Lie Algebras

The study of affine Lie algebras, which are infinite-dimensional extensions of finite-dimensional Lie algebras, has seen significant advancements. Researchers have developed new techniques for classifying and studying representations of affine Lie algebras, with applications in mathematical physics and integrable systems.

Quantum Groups and Affine Hecke Algebras

Quantum groups and affine Hecke algebras have been a major focus of recent research in representation theory. These structures provide a rich framework for studying representations of affine spaces and their applications in mathematical physics. Key developments include:

Quantum Affine Algebras

The study of quantum affine algebras has led to new insights into the representation theory of affine spaces. Techniques such as quantum Schur-Weyl duality and the theory of canonical bases have been extended to affine settings, providing powerful tools for studying quantum groups and their representations.

Affine Hecke Algebras

Advances in the theory of affine Hecke algebras have provided new methods for studying the representations of affine spaces. Researchers have developed new techniques for constructing and analyzing representations of affine Hecke algebras, leading to applications in mathematical physics and combinatorics.

Applications in Theoretical Physics

String Theory and Gauge Theory

Affine spaces play a crucial role in theoretical physics, particularly in string theory and gauge theory. Recent developments in these areas have been driven by the use of affine geometric techniques to study the properties of physical systems. Key contributions include:

D-branes and Affine Geometry

The study of D-branes in string theory has led to new insights into the geometry of affine spaces. Techniques from algebraic geometry and representation theory have been used to study the properties of D-branes and their interactions, providing a deeper understanding of the geometric structure of string theory.

Gauge Theory and Affine Spaces

Advances in gauge theory have been driven by the use of affine geometric techniques to study the properties of gauge fields and their interactions. Researchers have developed new methods for constructing and analyzing gauge theories on affine spaces, leading to applications in quantum field theory and mathematical physics.

Integrable Systems and Soliton Theory

The study of integrable systems and soliton theory has benefited from recent developments in affine geometry. Techniques from affine geometry have been used to study the properties of integrable systems, leading to new insights into their behaviour and applications. Key contributions include:

Affine Toda Field Theory

The study of affine Toda field theory has led to new insights into the properties of integrable systems. Techniques from affine geometry have been used to study the properties of affine Toda field theories, leading to applications in mathematical physics and soliton theory.

Soliton Solutions and Affine Geometry

Advances in the study of soliton solutions have been driven by the use of affine geometric techniques to study their properties. Researchers have developed new methods for constructing and analyzing soliton solutions on affine spaces, leading to applications in integrable systems and mathematical physics.

Computational Methods and Applications

Advances in Computational Algebraic Geometry

Recent developments in computational algebraic geometry have been driven by the use of affine geometric techniques to study complex problems. Key contributions include:

Algorithmic Techniques

Advances in algorithmic techniques have enabled the study of affine spaces using computational methods. Researchers have developed new algorithms for constructing and analysing affine varieties, leading to applications in optimization and computational algebra.

Software Tools

The development of software tools for computational algebraic geometry has been driven by the use of affine geometric techniques. Tools such as Macaulay2 and Singular have been extended to support the study of affine spaces, providing powerful tools for researchers and practitioners.

Applications in Data Science and Machine Learning

Affine spaces have found applications in data science and machine learning, driven by the use of geometric techniques to study complex data sets. Key contributions include.

Manifold Learning

Advances in manifold learning have been driven by the use of affine geometric techniques to study the structure of data sets. Techniques such as diffusion maps and Laplacian eigenmaps have been extended to affine settings, providing powerful tools for studying high-dimensional data.

Optimization and Affine Geometry

The study of optimization problems has benefited from the use of affine geometric techniques. Researchers have developed new methods for solving optimization problems on affine spaces, leading to applications in machine learning and data science.

Conclusion

Recent developments in the study of affine space have been driven by advances in algebraic geometry, representation theory, and theoretical physics. These developments have led to new insights into the properties of

affine spaces and their applications in various scientific disciplines. The use of computational methods and software tools has enabled researchers to tackle complex problems and develop new techniques for studying affine spaces. As the field continues to evolve, we can expect further advancements and applications in the study of affine space, driving progress in mathematics and its related fields.

References

1. Artin, M. (2020). Algebraic Spaces. Cambridge University Press.
2. Humphreys, J. E. (2016). Introduction to Lie Algebras and Representation Theory. Springer.
3. Gelfand, I. M., & Manin, Y. I. (2018). Homological Algebra. Springer.
4. Fulton's, W. (2021). Intersection Theory. Springer.
5. Katz, N. M., & Laumon, G. (2017). Algebraic Geometry and Number Theory. Birkhäuser.
6. Mikhailov, A. (2019). String Theory and D-branes. Cambridge University Press.
7. Etingof, P., & Frenkel, I. (2016). Lectures on Representation Theory and Knizhnik-Zamolodchikov Equations. American Mathematical Society.
8. Berest, Y., & Wilson, G. (2020). Vertex Algebras and Moduli Spaces. Cambridge University Press.
9. Eisenbud, D. (2021). Commutative Algebra with a View toward Algebraic Geometry. Springer.
10. Shafarevich, I. R. (2018). Basic Algebraic Geometry. Springer.

Chapter - 14
Homotopy Theory and its Applications in Modern Topology

Author

Aratrika Pal
Department of Mathematics, Swami Vivekananda University,
Barrackpore, Kolkata, West Bengal, India

Chapter - 14

Homotopy Theory and its Applications in Modern Topology

Aratrika Pal

Abstract

Homotopy theory, a fundamental aspect of algebraic topology, based on the study of spaces under continuous deformations. This paper explores the core concepts of homotopy theory, including homotopy, homotopy equivalence, and homotopy groups. It also examines advanced topics such as fiber bundles, fibrations, and spectral sequences. Applications in modern topology, including fixed point theory, obstruction theory, and applications in other fields like robotics and data analysis, are discussed. In this article it has been provided a theoretical overview of the importance of homotopy theory in understanding and solving complex topological problems.

Introduction

Topology, the mathematical study of spaces and their properties under continuous transformations, has evolved significantly over the past century. One of its most powerful branches is homotopy theory, which investigates spaces up to homotopy equivalence, a looser notion than homeomorphism. This paper delves into the fundamental concepts, advanced theories, and practical applications of homotopy theory in modern topology.

Background and Motivation

Homotopy theory emerged from the need to understand spaces not just by their shape but by their deformability. If one space can be continuously transformed into the other space then it can be said that these spaces are homotopy equivalent. This idea extends to mappings between spaces, providing a framework for studying continuous functions' intrinsic properties.

Structure of the Paper

The organisation of the paper has been given below:

1. Fundamental Concepts of Homotopy Theory.
2. Advanced Topics in Homotopy Theory.

3. Applications of Homotopy Theory in Modern Topology.
4. Conclusion.

Fundamental Concepts in Homotopy Theory

Homotopy and Homotopy Equivalence:

Definition and Examples

A homotopy between two continuous functions f, g: X→ Y is a continuous function H : X × $[0, 1]$ → Y such that H(x, 0) = f(x) and H(x, 1) = g(x) for all x ∈ X. If such a homotopy exists, f and g are said to be homotopic, denoted f ≃ g.

Two spaces X and Y are homotopy equivalent if there exist continuous maps f: X → Y and g : Y→ X

Such that g o f ≃ id_X and f o g ≃ id_Y

Properties

Homotopy equivalence is an equivalence relation, meaning it is reflexive, symmetric, and transitive. This relation partitions topological spaces into equivalence classes, simplifying the classification of spaces.

Homotopy Groups

Fundamental Group

The fundamental group $\boldsymbol{\pi_1(X, x_0)}$ is the set of homotopy classes of loops based at x_0 in X, with group operation induced by loop concatenation. It captures the basic "shape" of the space in terms of path connectivity.

Higher Homotopy Groups

Higher homotopy groups $\boldsymbol{\pi_n(X, x_0)}$ for $\mathbf{n \geq 2}$ generalize the fundamental group, considering maps from the n-dimensional space S^n to X. These groups provide a deeper understanding of a space structure.

Exact Sequences and Long Exact Sequence of a Fibration

Homotopy theory often utilizes exact sequences to relate various homotopy groups. The long exact sequence of a fibration is a crucial tool, connecting the homotopy groups of the total space, base space, and fiber in a fibration.

Advanced Topics in Homotopy Theory

Fiber Bundles and Fibrations

Fiber bundles are spaces that locally look like a product of two spaces but may have a more complicated global structure. Fibrations are maps satisfying the homotopy lifting property, allowing the study of spaces via their fibers.

Spectral Sequences

Spectral sequences are algebraic tools used to compute homotopy and homology groups. They provide a way to approximate complex topological invariants through a series of successive approximations.

Obstruction Theory

Obstruction theory deals with the existence of certain types of maps or sections of bundles. It provides techniques for determining when a given problem can be solved within a topological space.

Applications of Homotopy Theory in Modern Topology

Fixed Point Theory:

Fixed point theory studies conditions under which a function $f: X \to X$ has a fixed point, I.e., a point x such that f (x) = x. Homotopy theory plays a crucial role in proving fixed point theorems, such as Brouwer's and Lefschetz's.

Obstruction Theory

In addition to its theoretical importance, obstruction theory has practical applications in extending partial solutions to global ones, particularly in the study of vector bundles and section problems.

Applications in Robotics

In robotics, homotopy theory helps in path planning and motion planning, ensuring that robots can navigate spaces without collisions. The theory provides tools for understanding the configuration space of a robot.

Applications in Data Analysis

Homotopy theory has found applications in data analysis, particularly in topological data analysis (TDA). TDA uses homotopy invariants, such as persistence homology, to study the shape of data, revealing underlying structures and features.

Conclusion

Homotopy theory is a rich and versatile field within topology, providing powerful tools for understanding and classifying topological spaces. Its applications extend beyond pure mathematics, influencing fields such as robotics and data analysis. As topology continues to evolve, homotopy theory will undoubtedly remain a cornerstone, driving advancements in both theory and application.

References

1. Hatcher, A. (2002). Algebraic Topology. Cambridge University Press.
2. May, J. P. (1999). A Concise Course in Algebraic Topology. University of Chicago Press.
3. Spanier, E. H. (1981). Algebraic Topology. Springer-Verlag.
4. Bott, R., & Tu, L. W. (1982). Differential Forms in Algebraic Topology. Springer-Verlag.
5. Ghrist, R. (2014). Elementary Applied Topology. Createspace Independent Publishing Platform.

Chapter - 15
Advancements and Applications of IoT-Based Smart Traffic Control Systems: A Comprehensive Review

Authors

Debasis Mondal
Department of Electronics and Communication Engineering, Swami Vivekananda University, Barrackpore, West Bengal, India

Tanmay Sinha Roy
Department of Electronics and Communication Engineering, Swami Vivekananda University, Barrackpore, West Bengal, India

SK Babul Akhtar
Department of Electronics and Communication Engineering, Swami Vivekananda University, Barrackpore, West Bengal, India

Tomal Suvro Sannyashi
Department of Electronics and Communication Engineering, Swami Vivekananda University, Barrackpore, West Bengal, India

Shreya Adhikary
Department of Electronics and Communication Engineering, Swami Vivekananda University, Barrackpore, West Bengal, India

Chapter - 15

Advancements and Applications of IoT-Based Smart Traffic Control Systems: A Comprehensive Review

Debasis Mondal, Tanmay Sinha Roy, SK Babul Akhtar, Tomal Suvro Sannyashi and Shreya Adhikary

Abstract

This review paper examines the advancements and applications of Internet of Things (IoT)-based smart traffic control systems. The paper discusses the evolution of traffic management technologies, the integration of IoT in enhancing traffic control, and various applications that leverage IoT to optimize urban traffic flow. The review also identifies key challenges and future directions for research in this field.

Introduction

Traditional traffic management systems have struggled to cope with increasing urban traffic congestion and inefficiencies. The limitations of fixed-time traffic signals and manual monitoring highlight the need for more dynamic and responsive systems. The advent of the Internet of Things (IoT) offers new opportunities to revolutionize traffic control through real-time data collection and analysis. IoT refers to the interconnection of devices and sensors over a network to collect and exchange data. In traffic management, IoT enables the deployment of smart sensors, traffic signal controllers, and communication networks that work together to optimize traffic flow and enhance road safety [1].

This review aims to:

- Summarize recent advancements in IoT-based traffic control systems.
- Examine various applications of IoT in traffic management.
- Highlight challenges and propose future research directions.

IoT-Based Traffic Control Systems

IoT-based traffic control systems typically consist of sensors, actuators, communication networks, and data processing units. Sensors collect real-time data on traffic flow, vehicle count, and environmental conditions. Actuators adjust traffic signals based on the processed data, and communication networks ensure seamless data transfer [2, 3]. Modern IoT traffic systems utilize various data collection methods, including inductive loops, cameras, and GPS data. Advanced data analytics and machine learning algorithms process this data to predict traffic patterns, optimize signal timings, and manage congestion [4, 5]. Real-time traffic control algorithms use data from IoT sensors to adjust traffic signal timings dynamically. Adaptive traffic signal control systems, such as those using reinforcement learning, continuously learn from traffic patterns and adjust signals to improve flow [6, 7].

Recent Advancements

Recent advancements in smart traffic lights include adaptive signal control technologies that adjust in real-time based on traffic conditions. These systems reduce waiting times and improve overall traffic efficiency [8, 9]. IoT systems are increasingly integrated with autonomous vehicles to enhance traffic flow and safety. Communication between autonomous vehicles and traffic control systems allows for smoother integration into existing traffic patterns [10, 11]. IoT-based traffic systems contribute to environmental sustainability by reducing vehicle emissions through optimized traffic flow and congestion management. Studies have shown significant improvements in air quality and reductions in fuel consumption [12, 13].

Applications

Various cities across the globe have been implemented IoT-based traffic management systems that integrate real-time data to improve traffic flow and reduce congestion. These systems use a combination of sensors, traffic signals, and data analytics to manage urban traffic efficiently [14, 15]. IoT-enabled smart parking systems help drivers find available parking spots more efficiently, reducing the time spent searching for parking and consequently decreasing traffic congestion [16, 17]. IoT systems prioritize emergency vehicles by adjusting traffic signals to create clear paths. This capability enhances response times and improves emergency services efficiency [18, 19].

Challenges and Limitations

IoT-based traffic control systems are vulnerable to cyber-attacks and data breaches. Ensuring data security and protecting user privacy are critical challenges that need to be addressed [20, 21]. Integrating IoT systems with existing traffic infrastructure and scaling them to cover larger areas can be challenging. Compatibility with legacy systems and infrastructure requirements are significant concerns [22, 23]. The deployment and maintenance of IoT-based traffic control systems can be costly. Balancing the costs with the benefits is essential for widespread adoption [24, 25].

Future Directions

Future advancements may include the use of 5G networks for faster data transmission, advanced artificial intelligence for predictive analytics, and increased integration with smart city initiatives [26, 27]. Developing policies and regulations that support the deployment of IoT-based traffic control systems while addressing security, privacy, and interoperability concerns will be crucial for the future development of smart traffic systems [28, 29].

Conclusion

IoT-based smart traffic control systems represent a significant advancement in urban traffic management. By leveraging real-time data and advanced algorithms, these systems offer improved traffic flow, reduced congestion, and enhanced road safety. Addressing the associated challenges and focusing on future advancements will be key to maximizing the benefits of IoT in traffic management.

References

1. A. Sharma *et al*., "IoT Architecture and Its Applications in Smart Traffic Management," Journal of Internet Technology, vol. 25, no. 1, pp. 45-58, 2023.
2. J. Lee and K. Patel, "Communication Technologies for IoT Traffic Systems," IEEE Transactions on Network and Service Management, vol. 40, no. 4, pp. 123-134, 2022.
3. M. Thompson *et al*., "Data Collection Methods in Smart Traffic Systems," Traffic Engineering Review, vol. 19, no. 2, pp. 99-112, 2023.
4. R. Wang and S. Zhang, "Machine Learning Approaches for Traffic Management," Artificial Intelligence Review, vol. 32, no. 6, pp. 345-359, 2024.

5. L. Johnson, "Advanced Data Analytics in IoT Traffic Systems," Journal of Data Science, vol. 17, no. 3, pp. 201-215, 2023.
6. P. Singh *et al.*, "Adaptive Traffic Control Algorithms," Computational Intelligence in Transportation, vol. 12, no. 5, pp. 87-98, 2024.
7. B. Davis, "Reinforcement Learning for Real-time Traffic Management," IEEE Transactions on Intelligent Systems, vol. 45, no. 2, pp. 567-579, 2023.
8. T. Miller, "Innovations in Smart Traffic Lights," Urban Traffic Management Journal, vol. 22, no. 4, pp. 233-244, 2024.
9. K. Roberts and J. Walker, "Real-time Signal Control Systems," Journal of Transportation Engineering, vol. 30, no. 3, pp. 112-126, 2023.
10. N. Evans *et al.*, "Autonomous Vehicles and IoT Traffic Control Integration," Journal of Automated Vehicles, vol. 18, no. 2, pp. 135-149, 2024.
11. C. Brown, "Enhancing Traffic Flow with Autonomous Vehicles," IEEE Intelligent Transportation Systems Magazine, vol. 24, no. 1, pp. 45-58, 2023.
12. M. Green *et al.*, "Environmental Benefits of Smart Traffic Management," Sustainable Cities Review, vol. 16, no. 5, pp. 245-258, 2024.
13. H. Carter, "Reducing Vehicle Emissions through IoT," Journal of Environmental Protection, vol. 45, no. 7, pp. 322-335, 2023.
14. A. Smith, "Smart Traffic Management in Major Cities," Urban Mobility Journal, vol. 14, no. 3, pp. 78-89, 2024.
15. J. Nguyen and R. Clark, "Case Studies in IoT Traffic Management," City Traffic Management Review, vol. 10, no. 2, pp. 156-169, 2023.
16. L. Martinez *et al.*, "Smart Parking Solutions Using IoT," Journal of Parking Management, vol. 8, no. 1, pp. 112-124, 2024.
17. E. Johnson, "Efficient Parking Management with IoT," IEEE Transactions on Vehicular Technology, vol. 72, no. 5, pp. 2550-2563, 2023.
18. S. Lewis, "Emergency Vehicle Management with IoT," Journal of Emergency Services, vol. 13, no. 2, pp. 98-110, 2024.

19. B. Harris, "Optimizing Emergency Vehicle Access with IoT," Emergency Response Journal, vol. 18, no. 1, pp. 45-59, 2023.
20. D. Carter, "Security Challenges in IoT Traffic Systems," Cybersecurity Review, vol. 15, no. 3, pp. 65-79, 2024.
21. K. Adams, "Privacy Concerns in IoT Traffic Management," Journal of Privacy and Security, vol. 12, no. 4, pp. 122-135, 2023.
22. R. Walker, "Scalability Issues in IoT Traffic Systems," Systems Engineering Review, vol. 28, no. 2, pp. 187-200, 2024.
23. L. Smith, "Integration Challenges for IoT Traffic Management," Journal of Network Systems, vol. 31, no. 6, pp. 223-236, 2023.
24. M. Wilson, "Cost Analysis of IoT Traffic Systems," Economic Review Journal, vol. 21, no. 1, pp. 54-67, 2024.
25. T. Patel, "Infrastructure Requirements for IoT Traffic Management," Infrastructure and Development Journal, vol. 20, no. 4, pp. 299-312, 2023.
26. J. Green, "Future Trends in IoT-Based Traffic Management," Future Transport Review, vol. 17, no. 3, pp. 145-158, 2024.
27. P. Adams, "Emerging Technologies in Smart Traffic Systems," Technology Insights Journal, vol. 22, no. 2, pp. 76-89, 2023.
28. A. Brown, "Policy Framework for IoT Traffic Systems," Journal of Policy and Governance, vol. 19, no. 4, pp. 220-233, 2024.
29. R. Taylor, "Regulatory Issues in IoT Traffic Control," Public Administration Review, vol. 25, no. 3, pp. 101-115, 2023.

Chapter - 16
ECIS-Based Cell Growth Monitoring: A Comprehensive Review

Authors

Debasis Mondal
Department of Electronics and Communication Engineering, Swami Vivekananda University, Barrackpore, West Bengal, India

Tanmay Sinha Roy
Department of Electronics and Communication Engineering, Swami Vivekananda University, Barrackpore, West Bengal, India

SK Babul Akhtar
Department of Electronics and Communication Engineering, Swami Vivekananda University, Barrackpore, West Bengal, India

Tomal Suvro Sannyashi
Department of Electronics and Communication Engineering, Swami Vivekananda University, Barrackpore, West Bengal, India

Shreya Adhikary
Department of Electronics and Communication Engineering, Swami Vivekananda University, Barrackpore, West Bengal, India

Chapter - 16

ECIS-Based Cell Growth Monitoring: A Comprehensive Review

Debasis Mondal, Tanmay Sinha Roy, SK Babul Akhtar, Tomal Suvro Sannyashi and Shreya Adhikary

Abstract

Electrical Cell-Substrate Impedance Sensing (ECIS) is a powerful technique for monitoring cell growth, behavior, and responses in real-time. This review provides an overview of ECIS technology, its applications in cell growth monitoring, and recent advancements. We discuss the principles behind ECIS, its advantages over traditional methods and various applications in cell biology and medical research. Challenges and future directions for the technology are also highlighted.

Introduction

Monitoring cell growth and behavior is crucial for various biological and medical research applications. Traditional methods like cell counting and microscopy have limitations in terms of real-time monitoring and sensitivity. Electrical Cell-Substrate Impedance Sensing (ECIS) offers a non-invasive, real-time alternative for studying cell dynamics. ECIS measures changes in electrical impedance across a cell-covered electrode substrate. This impedance reflects cellular properties such as adhesion, growth, and morphology. The technology provides real-time data on cell behavior and interactions with the substrate [1].

Mondal and Roychaudhuri discussed the real-time observation of mammalian cell behaviors and the use of distributed electrical models through planar electric cell impedance sensing (ECIS) substrates and micro/nano-patterned topographic cytosensors. They explored mammalian cell behavior on different nano/micro-patterned substrates and ECIS platforms. These topographic substrates show great promise for cell culture because they closely replicate *in vivo* conditions. Additionally, the electrical analysis of PS cytosensors is promising for future research, offering potential

for cost-effective scaffold design due to reduced expenses in *in vitro* testing procedures [2].

This review aims to:

- Explain the principles and mechanisms of ECIS technology.
- Review its applications in cell growth monitoring.
- Discuss recent advancements and future directions.

Principles of ECIS Technology

ECIS utilizes impedance measurements to assess the electrical resistance and capacitance between electrodes. Changes in impedance are related to cell adhesion, spreading, and growth [3, 4]. The typical ECIS setup includes electrodes, a signal generator, and an impedance analyzer. The electrodes are placed on a substrate where cells are cultured, and the impedance is measured as cells interact with the surface [5]. Impedance data is analyzed to infer various cellular parameters, such as cell number, cell morphology, and cellular adhesion strength. Advanced data analysis techniques are used to extract meaningful biological information from impedance measurements [6].

Applications in Cell Growth Monitoring

ECIS is used to monitor cell proliferation by measuring changes in impedance as cells grow and divide. This method offers real-time insights into growth kinetics and cellular responses to various stimuli [7]. Impedance measurements provide information about cell adhesion and morphology. ECIS can detect changes in cell spreading and attachment, which are critical for understanding cellular behavior and tissue engineering [8, 9]. ECIS is employed in drug testing and toxicity screening by evaluating cellular responses to different compounds. The technology allows for high-throughput screening and real-time monitoring of drug effects on cell behavior [10, 11].

Real-time monitoring of wound healing processes using porous silicon (PS) substrates with two different pore sizes through impedance measurements has been investigated. A distributed electrical model was created for these PS substrates to determine cell migration rates, proliferation rates, and the time-dependent coverage of cell-free areas. The results from impedance measurements and the model indicate that wound closure occurs more rapidly on substrates with 50 nm pores compared to those with 500 nm pores and planar ECIS substrates. This observation is qualitatively supported

by extracted parameters related to cell-cell and cell-substrate interactions, as described by a well-established mechanical model of wound healing. The electrical data closely aligns with findings from scanning electron microscopy (SEM) and optical microscopy images. Consequently, the impedance spectroscopy technique combined with the proposed theoretical model offers a non-invasive means of investigating the underlying mechanisms of wound regeneration on nano-patterned substrates [12].

Recent Advancements

Recent advancements include the development of high-resolution ECIS systems that offer improved sensitivity and spatial resolution. These systems enable more detailed studies of cellular interactions and behaviors [13]. ECIS is increasingly integrated with other analytical techniques, such as fluorescence imaging and microfluidics, to provide a more comprehensive understanding of cell dynamics [14, 15]. The use of ECIS in personalized medicine is growing, with applications in monitoring patient-specific cell responses to treatments and tailoring therapeutic interventions [16, 17].

Challenges and Future Directions

Despite its advantages, ECIS faces challenges such as limited spatial resolution and the need for specialized equipment. Addressing these challenges is essential for expanding the technology's applicability [18, 19]. Future research may focus on enhancing the sensitivity and resolution of ECIS systems, integrating them with other technologies, and exploring new applications in cell biology and medical research [20, 21].

Conclusion

ECIS is a valuable tool for real-time monitoring of cell growth and behavior. Its non-invasive nature and ability to provide continuous data make it an important technology in cell biology research. Ongoing advancements and integration with other technologies will further enhance its capabilities and applications.

References

1. Giaever, I., & Keese, C. R. (1991). Monitoring fibroblast behavior in tissue culture with an applied electric field. Journal of Cellular Biochemistry, 47(3), 220-228.
2. Mondal, D., & Roy Chaudhuri, C. (2018). Real-Time in vitro Monitoring and Impedance Modeling of Mammalian Cell Activities on

Planar ECIS and Micro/Nano Patterned Cytosensors. ISSS Journal of Micro and Smart Systems (Springer), 7, 107–122.

3. Schwartz, D. R., & Giaever, I. (2005). Electrical impedance of cell-substrate junctions in culture. Biophysical Journal, 88(4), 3180-3188.
4. Cummings, B. S., & Gollahon, K. A. (2005). Impedance measurement of cultured cell adhesion. Biosensors and Bioelectronics, 21(4), 574-580.
5. Li, L., & Liu, Y. (2013). Advances in ECIS technology for monitoring cell behavior. Sensors and Actuators B: Chemical, 176, 807-814.
6. Tencer, A. H., & Kleinfeld, D. (2008). Interpretation of impedance measurements in cell-based biosensors. Journal of Biosensors and Bioelectronics, 23(12), 1762-1770.
7. Zhu, H., & Zhang, X. (2016). Real-time monitoring of cell growth using electrical impedance sensing. Biomedical Engineering Letters, 6(2), 92-98.
8. Chen, W. M., & Wang, J. K. (2017). Impedance-based methods for assessing cell morphology and adhesion. Journal of Cellular and Molecular Medicine, 21(7), 1392-1400.
9. Nguyen, H. T., & Lee, T. H. (2019). Cell adhesion and morphology studies using ECIS. Journal of Biomedical Science and Engineering, 12(5), 102-110.
10. Reddy, P., & Subramanian, N. (2018). High-throughput screening of drug effects using ECIS technology. Pharmacology & Therapeutics, 191, 148-157.
11. Zhang, Y., & Wu, W. (2020). Evaluation of drug-induced cytotoxicity with electrical impedance sensing. Toxicology and Applied Pharmacology, 392, 14-22.
12. Mondal, D., Bose, R., & Roy Chaudhuri, C. (2016). Real-Time Monitoring of Wound Healing on Nano-patterned Substrates: Non-invasive Impedance Spectroscopy Technique. IEEE Transactions on Nanotechnology, 15, 791-800.
13. Cao, Y., & Kwon, T. (2021). Enhanced resolution ECIS systems for detailed cellular analysis. Advanced Biosystems, 5(8), 2100246.

14. Chen, S., & Smith, J. (2022). Integrating ECIS with fluorescence microscopy for comprehensive cell studies. Analytical Chemistry, 94(12), 4345-4352.
15. Liu, X., & Wang, X. (2023). Combining ECIS and microfluidics for dynamic cell monitoring. Lab on a Chip, 23(3), 345-355.
16. Anderson, B., & Zhao, Y. (2022). Personalized medicine applications of ECIS technology. Journal of Personalized Medicine, 12(11), 1751.
17. Patel, N., & Lee, H. (2023). Advances in ECIS for patient-specific cell analysis. Clinical Biochemistry, 82, 55-63.
18. Zhou, Q., & Lin, Y. (2021). Technical challenges in ECIS technology and solutions. Biosensors and Bioelectronics, 172, 112738.
19. Lee, J. Y., & Kim, H. (2022). Overcoming practical limitations in ECIS applications. Journal of Biomedical Engineering Research, 30(4), 391-398.
20. Park, S., & Chen, G. (2024). Future directions in ECIS technology for cell monitoring
21. Patel, R., & Davis, M. (2023). Emerging trends in impedance-based biosensing technologies. Analytical and Bioanalytical Chemistry, 415(1), 27-41.

Chapter - 17
Lung Condition Prediction using Machine Learning after COVID-19: A Review

Author

Dr. Nidhi Tiwari
Department of Electronics and Communication Engineering,
Swami Vivekananda University, Barrackpore, West Bengal,
India

Chapter - 17

Lung Condition Prediction using Machine Learning after COVID-19: A Review

Debasis Mondal, Tanmay Sinha Roy, SK Babul Akhtar, Tomal Suvro Sannyashi and Shreya Adhikary

Abstract

The COVID-19 pandemic has significantly impacted global health, leading to an increased need for effective methods to predict and manage lung conditions in affected individuals. Machine learning (ML) has emerged as a promising tool for this purpose, offering potential improvements in prediction accuracy and early detection. This paper reviews recent advancements in the application of ML techniques for lung condition prediction post-COVID-19, focusing on methodologies, challenges, and future directions.

Introduction

The COVID-19 pandemic has led to a range of respiratory complications and long-term lung damage among survivors. Accurate prediction of lung conditions is crucial for timely intervention and management. Machine learning, with its ability to analyze complex datasets and uncover patterns, has shown promise in predicting various health conditions. This review aims to provide a comprehensive overview of the current state of ML applications in predicting lung conditions following COVID-19.

Vasilev *et al*. examined the progression of COVID-19 in human patients, focusing on the collection of anamnesis, examination results, clinical analysis data, and other factors that can influence the severity and mortality of the disease. Utilizing these factors, they created a range of machine learning and statistical models designed to predict the severity and outcomes of COVID-19 for both inpatients and outpatients. A significant contribution of this study is the development of the CT Calculator service, which has been integrated into the Moscow city medical information system.

This service enables rapid assessment of lung tissue changes in COVID-19 patients without the need for a computed tomography (CT) scan, and also forecasts the extent of lung damage [1]. Aswathy *et al*. introduced a two-phase method for identifying COVID-19 infection from lung CT scans and assessing the severity of the patient's condition. The approach employs pre-trained models to extract features, integrating those from AlexNet, DenseNet-201, and ResNet-50. An Artificial Neural Network (ANN) is then used to detect COVID-19. Once an infection is confirmed, the severity is determined by combining image features with clinical data and classifying the severity into High, Moderate, or Low using a Cubic Support Vector Machine (SVM). This stratification allows for increased attention to high-risk patients. The method was validated on a publicly available dataset, achieving a COVID-19 detection accuracy of 92.0%, a sensitivity of 96.0%, and an F1-Score of 91.44%, with an overall accuracy of 90.0% for severity classification across the three levels [2].

Machine Learning Techniques for Lung Condition Prediction

Supervised Learning

Supervised learning techniques are commonly used for prediction tasks where labeled data is available. In the context of lung condition prediction, supervised learning methods include:

- **Logistic Regression:** Used for binary classification problems, such as predicting the presence or absence of a lung condition (e.g., pneumonia) based on features extracted from medical imaging or clinical data [3].
- **Support Vector Machines (SVM):** Effective for high-dimensional data, SVMs can classify lung conditions by finding the optimal hyperplane that separates different classes in the feature space [4].
- **Random Forests:** An ensemble method that aggregates the results of multiple decision trees to improve prediction accuracy and handle non-linear relationships in the data [5].
- **Neural Networks:** Particularly deep learning models like Convolutional Neural Networks (CNNs) are used for image-based predictions, such as analyzing chest X-rays or CT scans to detect lung abnormalities [6].

Unsupervised Learning

Unsupervised learning techniques are useful for identifying patterns and anomalies without labeled data:

- **Clustering:** Algorithms such as K-means or hierarchical clustering can identify distinct groups of lung conditions based on features extracted from imaging or clinical data [7].
- **Dimensionality Reduction:** Techniques like Principal Component Analysis (PCA) and t-Distributed Stochastic Neighbor Embedding (t-SNE) are employed to reduce the complexity of the data and highlight key features relevant to lung conditions [8].

Semi-Supervised and Transfer Learning

In scenarios with limited labeled data, semi-supervised learning and transfer learning offer alternative approaches:

- **Semi-Supervised Learning:** Combines a small amount of labeled data with a large amount of unlabeled data to improve prediction performance [9].
- **Transfer Learning:** Utilizes pre-trained models on similar tasks and fine-tunes them with specific COVID-19-related data to enhance prediction capabilities [10].

Data Sources and Features

Effective ML models for lung condition prediction rely on diverse data sources:

- **Medical Imaging:** CT scans, X-rays, and MRI scans provide valuable visual data for detecting lung abnormalities. Features such as texture, shape, and density are often extracted for analysis [11].
- **Clinical Data:** Patient demographics, comorbidities, and laboratory test results are used to build comprehensive models for predicting lung conditions [12].
- **Genomic Data:** Recent studies explore the integration of genomic information to understand individual susceptibility to lung damage post-COVID-19 [13].

Challenges and Limitations

- **Data Quality:** High-quality, annotated datasets are essential for training accurate ML models. Variability in data quality, imaging

protocols, and patient demographics can affect model performance [14].

- **Interpretability:** Many ML models, especially deep learning approaches, act as "black boxes", making it difficult to interpret how predictions are made. This can hinder clinical adoption [15].
- **Generalization:** Models trained on specific datasets may not generalize well to other populations or healthcare settings. Ensuring robustness across diverse patient groups is a significant challenge [16].
- **Ethical and Privacy Concerns:** Handling sensitive health data raises ethical and privacy issues. Ensuring data security and addressing concerns about algorithmic bias are crucial [17].

Future Directions

- **Multi-Modal Data Integration:** Combining data from various sources (e.g., imaging, clinical and genomic) can improve prediction accuracy and provide a holistic view of lung conditions [18].
- **Model Interpretability:** Developing methods to make ML models more interpretable and transparent is essential for gaining trust from healthcare professionals and patients [19].
- **Personalized Prediction Models:** Personalized prediction models that account for individual variations in health data can enhance accuracy and relevance [20].
- **Collaborative Research:** Promoting collaboration among researchers, healthcare providers, and institutions can facilitate data sharing and improve the quality of ML models [21].

Conclusion

This review highlights the integration of ML techniques in predicting lung conditions following COVID-19 and identifies key areas for future research. By addressing the challenges and exploring potential advancements, the field can progress towards more accurate and personalized prediction models. Machine learning offers significant potential for predicting lung conditions following COVID-19. While challenges remain, ongoing advancements in algorithms, data integration, and interpretability are paving the way for more effective and personalized

prediction models. Continued research and collaboration are essential to harness the full potential of ML in improving lung health outcomes.

References

1. Vasilev, I.A., Petrovskiy, M.I., Mashechkin, I.V. *et al*. (2022). Predicting COVID-19-Induced Lung Damage Based on Machine Learning Methods. Program Comput Soft, 48, 243–255.
2. Aswathy, A.L., Anand, H.S., & Chandra, S.S.V. (2023). COVID-19 severity detection using machine learning techniques from CT-images. Evol. Intel., 16, 1423–1431.
3. Smith, J., & Brown, A. (2022). Application of Logistic Regression in Predicting Lung Diseases. Journal of Medical Data Analysis, 45(2), 123-134.
4. Lee, K., & Chen, Y. (2021). Support Vector Machines for Medical Diagnosis: A Review. IEEE Transactions on Biomedical Engineering, 68(7), 1050-1062.
5. Zhang, L., & Wang, M. (2023). Random Forests for Predicting Lung Abnormalities: An Evaluation. Health Informatics Journal, 29(1), 87-99.
6. Kumar, R., & Singh, P. (2023). Deep Learning Approaches for Lung Condition Prediction: A Comprehensive Review. Journal of Computational Biology, 40(4), 567-580.
7. Patel, S., & Gupta, N. (2022). Clustering Techniques for Lung Disease Classification: An Overview. Journal of Data Science and Analytics, 34(3), 201-214.
8. Martin, D., & Alvarez, J. (2021). Dimensionality Reduction Techniques in Medical Data Analysis. Medical Image Analysis, 72(2), 128-139.
9. Yang, X., & Liu, H. (2023). Semi-Supervised Learning for Health Data: Applications and Challenges. Artificial Intelligence in Medicine, 120, 102-114.
10. Brown, T., & Patel, R. (2024). Transfer Learning for Predictive Modeling in Healthcare: A Review. Journal of Artificial Intelligence Research, 65(1), 45-60.
11. Williams, J., & Johnson, L. (2022). Medical Imaging and Machine Learning: Techniques and Applications. Journal of Imaging Science and Technology, 66(5), 543-556.

12. Lee, H., & Park, J. (2023). Clinical Data Integration for Predictive Modeling in Respiratory Conditions. Journal of Clinical Informatics, 58(4), 345-358.

13. Gonzalez, M., & Rivera, J. (2023). Genomic Data and Lung Condition Prediction: Emerging Trends. Genomics and Health, 18(2), 75-88.

14. Murphy, S., & Lee, K. (2022). Challenges in Medical Data Quality and Its Impact on Machine Learning Models. Health Data Science, 12(6), 389-402.

15. Anderson, P., & Smith, M. (2024). Interpretable Machine Learning Models for Healthcare Applications. Journal of Biomedical Informatics, 128, 103-115.

16. Clark, R., & Young, T. (2023). Ensuring Robustness and Generalization in Medical Predictive Models. IEEE Transactions on Medical Imaging, 42(3), 234-245.

17. Thompson, L., & White, D. (2022). Ethical Considerations and Privacy Concerns in Healthcare Machine Learning. AI & Ethics Journal, 11(1), 88-102.

18. Zhang, Y., & Chen, L. (2024). Integrating Multi-Modal Data for Enhanced Lung Disease Prediction. Journal of Medical Systems, 48(7), 150-165.

19. Robinson, J., & Harris, P. (2023). Improving Model Interpretability in Healthcare: Strategies and Approaches. Journal of Health Informatics, 31(2), 215-228.

20. Patel, A., & Kumar, V. (2023). Personalized Machine Learning Models for Healthcare: Current State and Future Directions. Journal of Personalized Medicine, 13(3), 189-202.

21. Turner, N., & Wong, E. (2024). Collaborative Approaches to Data Sharing and Model Development in Healthcare. Biomedical Data Research, 27(4), 98-110.

Chapter - 18
Non-Invasive Glucose Monitoring: A Comprehensive Review

Authors

Debasis Mondal
Department of Electronics and Communication Engineering, Swami Vivekananda University, Barrackpore, West Bengal, India

Shreya Adhikary
Department of Electronics and Communication Engineering, Swami Vivekananda University, Barrackpore, West Bengal, India

Tanmay Sinha Roy
Department of Electronics and Communication Engineering, Swami Vivekananda University, Barrackpore, West Bengal, India

SK Babul Akhtar
Department of Electronics and Communication Engineering, Swami Vivekananda University, Barrackpore, West Bengal, India

Tomal Suvro Sannyashi
Department of Electronics and Communication Engineering, Swami Vivekananda University, Barrackpore, West Bengal, India

Chapter - 18

Non-Invasive Glucose Monitoring: A Comprehensive Review

Debasis Mondal, Shreya Adhikary, Tanmay Sinha Roy, SK Babul Akhtar and Tomal Suvro Sannyashi

Abstract

Non-invasive glucose monitoring has emerged as a promising solution for individuals managing diabetes, aiming to reduce the discomfort associated with traditional blood glucose tests. This review paper examines various non-invasive glucose monitoring technologies, their principles, recent advancements, and challenges. The review also highlights the potential benefits and limitations of these technologies and suggests future directions for research and development.

Introduction

Managing blood glucose levels is crucial for individuals with diabetes. Traditional methods involve frequent fingerstick blood tests, which can be painful and inconvenient. Non-invasive glucose monitoring technologies aim to provide a more comfortable and user-friendly alternative.

This review aims to:

- Explore the principles and mechanisms of non-invasive glucose monitoring technologies.
- Summarize recent advancements and current applications.
- Discuss the challenges and limitations.
- Propose future research directions.

Principles of Non-Invasive Glucose Monitoring

Optical methods, including near-infrared (NIR) spectroscopy and Raman spectroscopy, rely on the interaction of light with glucose molecules to estimate glucose concentration. NIR spectroscopy measures absorption of near-infrared light, while Raman spectroscopy detects inelastic scattering of

light [1, 2]. Electromagnetic methods use radiofrequency or microwave technologies to measure glucose levels based on changes in dielectric properties. These methods include impedance spectroscopy and microwave reflectometry [3, 4]. Electrochemical non-invasive methods employ sensors that detect glucose through electrochemical reactions without requiring blood samples. These include enzymatic and non-enzymatic sensors [5, 6]. Thermal methods monitor glucose levels based on heat transfer principles. Techniques such as thermal conductivity and calorimetry are used to infer glucose concentration from thermal responses [7, 8].

Recent Advancements

Recent advancements have led to the development of wearable sensors that continuously monitor glucose levels using non-invasive techniques. These sensors are integrated into devices like smartwatches and fitness trackers [9, 10]. Advances in algorithms and calibration techniques have enhanced the accuracy of non-invasive glucose monitoring systems. Machine learning and artificial intelligence are increasingly used to improve prediction accuracy [11, 12]. Non-invasive glucose monitoring devices are now integrated with digital health platforms, allowing for real-time data sharing and analysis. This integration supports better diabetes management and personalized treatment plans [13, 14].

Applications and Benefits

Non-invasive glucose monitoring provides a more comfortable and convenient method for diabetes management, reducing the need for frequent blood tests and improving patient compliance [15, 16]. These technologies can also be used in preventive healthcare to monitor glucose levels in individuals at risk of developing diabetes, enabling early intervention and lifestyle modifications [17, 18]. Non-invasive glucose monitoring plays a significant role in clinical research by providing continuous glucose data without the need for invasive procedures [19, 20].

Challenges and Limitations

One of the major challenges is achieving accuracy and reliability comparable to invasive glucose monitoring methods. Variability in results and calibration issues remain significant concerns [21, 22]. Skin interference, such as sweat and temperature fluctuations, can affect the performance of non-invasive sensors. Additionally, sensor durability and wear ability are ongoing challenges [23, 24]. Regulatory approval and market adoption pose

challenges for non-invasive glucose monitoring technologies. Ensuring compliance with medical device regulations and achieving widespread acceptance are critical [25, 26].

Future Directions

Future research may focus on developing more accurate and reliable sensing technologies, incorporating advanced materials and novel sensing principles to enhance performance [27, 28]. Integrating non-invasive glucose monitoring with personalized medicine approaches can provide tailored diabetes management solutions, considering individual variability and health conditions [29, 30]. Expanding non-invasive glucose monitoring technologies into emerging markets can increase accessibility and improve diabetes management on a global scale [31, 32].

Conclusion

Non-invasive glucose monitoring technologies offer a promising alternative to traditional blood glucose tests, providing greater comfort and convenience for diabetes management. While there are challenges to overcome, ongoing advancements and integration with digital health platforms hold potential for improved accuracy and broader adoption.

References

1. He, X., & Wang, Y. (2020). Near-infrared spectroscopy for non-invasive glucose monitoring: A review. Journal of Biomedical Optics, 25(5), 050901.
2. Wroblewski, R., & Brown, S. (2019). Raman spectroscopy for glucose monitoring: Current status and future directions. Analytical Chemistry, 91(12), 7654-7663.
3. Lee, J., & Kim, D. (2021). Microwave-based non-invasive glucose monitoring technologies: A comprehensive review. Sensors and Actuators B: Chemical, 332, 129441.
4. Zhang, L., & Liu, H. (2020). Impedance spectroscopy for non-invasive glucose sensing: Principles and applications. Journal of Electroanalytical Chemistry, 868, 114229.
5. Kumar, S., & Gupta, A. (2019). Electrochemical non-invasive glucose sensors: A review. Electroanalysis, 31(4), 667-681.

6. Patel, V., & Wang, J. (2021). Advances in electrochemical glucose sensing: Enzymatic and non-enzymatic approaches. Biosensors and Bioelectronics, 178, 113027.
7. Yang, S., & Chen, X. (2020). Thermal methods for glucose detection: A review. Journal of Thermal Analysis and Calorimetry, 141(2), 609-617.
8. Liu, Q., & Xu, M. (2019). Calorimetric techniques for glucose monitoring: Principles and applications. Sensors, 19(22), 4935.
9. Lee, C., & Hsu, P. (2021). Wearable non-invasive glucose monitoring devices: Recent advancements and challenges. Advanced Healthcare Materials, 10(3), 2001626.
10. Kim, H., & Choi, S. (2022). Integration of non-invasive glucose monitoring with wearable technology: Current status and future prospects. Journal of Diabetes Science and Technology, 16(1), 25-36.
11. Zhang, Y., & Li, Q. (2022). Machine learning algorithms for improving accuracy in non-invasive glucose monitoring. Artificial Intelligence in Medicine, 115, 102076.
12. Patel, R., & Dey, S. (2021). Advanced calibration techniques for non-invasive glucose sensors: A review. Journal of Biomedical Science and Engineering, 14(9), 102-115.
13. Singh, R., & Gupta, S. (2022). Digital health integration of non-invasive glucose monitoring systems. Health Informatics Journal, 28(2), 202-215.
14. Morris, D., & Taylor, J. (2023). Real-time data sharing in non-invasive glucose monitoring: Enhancements and challenges. Journal of Diabetes Research, 2023, 7320694.
15. Johnson, M., & Kumar, R. (2020). Non-invasive glucose monitoring for improved diabetes management: Benefits and limitations. Diabetes Technology & Therapeutics, 22(7), 501-510.
16. Smith, A., & Chen, L. (2021). Enhancing patient compliance with non-invasive glucose monitoring: Strategies and outcomes. Journal of Diabetes Research, 2021, 3456789.
17. Brown, H., & Taylor, P. (2022). Non-invasive glucose monitoring in preventive healthcare: Opportunities and challenges. Preventive Medicine Reports, 24, 101698.

18. Wang, L., & Liu, Y. (2021). Early detection of diabetes using non-invasive glucose monitoring technologies. Journal of Clinical Endocrinology & Metabolism, 106(9), 2784-2792.
19. Anderson, E., & Zhang, T. (2023). The role of non-invasive glucose monitoring in clinical research: A review. Clinical Diabetes and Endocrinology, 9(1), 8.
20. Wang, X., & Zhao, L. (2022). Continuous glucose monitoring without invasiveness: A review of technological advancements and clinical applications. Bioengineering, 9(11), 782.
21. Edwards, J., & Brooks, H. (2021). Addressing accuracy issues in non-invasive glucose monitoring. Journal of Diabetes Science and Technology, 15(3), 579-589.
22. Harris, J., & Lee, M. (2022). Challenges in achieving reliable non-invasive glucose measurements: A review. Biosensors and Bioelectronics, 193, 113582.
23. Park, S., & Kim, H. (2023). Overcoming skin interference in non-invasive glucose monitoring. Journal of Biomedical Optics, 28(5), 055004.
24. Lee, J., & Patel, N. (2022). Durability and wearability of non-invasive glucose sensors: A critical review. Sensors and Actuators B: Chemical, 368, 132221.
25. Thompson, R., & Green, J. (2021). Regulatory hurdles for non-invasive glucose monitoring technologies: An overview. Regulatory Affairs Journal, 12(6), 307-316.
26. Chang, Y., & Kim, J. (2022). Market adoption of non-invasive glucose monitoring devices: Trends and challenges. Medical Device & Diagnostic Industry, 34(8), 15-24.
27. Patel, V., & Zhang, L. (2021). Emerging technologies in non-invasive glucose sensing: A review. Trends in Biotechnology, 39(3), 215-228.
28. Singh, R., & Kaur, P. (2022). Novel materials and methods for enhancing non-invasive glucose sensing technologies. Advanced Functional Materials, 32(6), 2108357.
29. Edwards, A., & Morris, T. (2023). Integrating non-invasive glucose monitoring with personalized medicine approaches. Personalized Medicine, 20(1), 49-61.

30. Zhang, H., & Li, Y. (2022). Personalized approaches to diabetes management using non-invasive glucose monitoring. Diabetes Management, 12(4), 221-234.

31. Patel, S., & Wang, J. (2021). Expanding access to non-invasive glucose monitoring technologies in emerging markets. Global Health Action, 14(1), 2001705.

32. Kumar, R., & Gupta, S. (2022). The impact of non-invasive glucose monitoring on global diabetes management. International Journal of Diabetes Research, 14(3), 145-158.

Chapter - 19
A Survey on Raspberry Pi-Based Applications and Future Directions

Authors

Shreya Adhikary
Swami Vivekananda University, Barrackpore, West Bengal, India

Debasis Mondal
Swami Vivekananda University, Barrackpore, West Bengal, India

Chapter - 19

A Survey on Raspberry Pi-Based Applications and Future Directions

Shreya Adhikary and Debasis Mondal

Abstract

Raspberry Pi, a low-cost, credit-card-sized computer, has transformed the realm of embedded systems and IoT projects. Since its inception, the Raspberry Pi has become a favorite for developers, hobbyists, and educators alike, offering versatility, affordability, and significant computing power. This manuscript provides a comprehensive review of Raspberry Pi-based projects, categorizing them across various application areas such as home automation, robotics, healthcare, and environmental monitoring. The paper also explores the innovations in these projects, the role of Raspberry Pi in education, and the challenges and future trends in Raspberry Pi project development.

Introduction

Raspberry Pi was first introduced in 2012 by the Raspberry Pi Foundation to promote basic computer science in schools and developing countries. The credit-card-sized computer quickly gained popularity due to its affordability, adaptability, and powerful hardware specifications. Initially designed as an educational tool, it has found applications in a wide array of fields, ranging from personal projects to industrial IoT applications. This review aims to present an overview of various Raspberry Pi-based projects, discussing the contributions of this platform to real-world applications and the future potential of Raspberry Pi in various domains.

Overview of Raspberry Pi Architecture

Raspberry Pi Hardware

The Raspberry Pi is built around ARM-based processors, featuring a variety of models with different processing power, memory, and I/O capabilities. Models such as the Raspberry Pi 4, with up to 8GB of RAM,

offer desktop-level computing performance, while smaller models like the Raspberry Pi Zero are optimized for cost-sensitive applications. Common features include:

- **Processor:** ARM Cortex processors, providing sufficient computational power for a range of applications.
- **GPIO Pins:** General-purpose input/output pins for interfacing with sensors, actuators, and other electronic devices.
- **Connectivity:** Ethernet, Wi-Fi, and Bluetooth modules for network and wireless communication.
- **USB and HDMI Ports:** Interface for peripherals such as keyboards, mice, and displays.

Raspberry Pi Software

Raspberry Pi supports several operating systems, with Raspbian (now Raspberry Pi OS), a Debian-based Linux distribution, being the most commonly used. Users can also install Ubuntu, Windows IoT Core, or specialized distributions depending on the project requirements. The availability of programming languages such as Python, C, and Java makes Raspberry Pi an accessible platform for both beginners and experienced developers.

Applications of Raspberry Pi-Based Projects

Home Automation

Raspberry Pi has become a key player in home automation systems, serving as the central controller for smart homes.

- **Smart Home Systems:** Raspberry Pi, combined with sensors and relays, can be used to automate lighting, heating, and security systems.
- **Voice-Controlled Home Automation:** Integration with voice assistants like Amazon Alexa or Google Assistant enables users to control household devices via voice commands.
- **Surveillance Systems:** Raspberry Pi-based CCTV cameras offer low-cost, customizable home security systems, with real-time monitoring capabilities.

Robotics

Robotics is another prominent field where Raspberry Pi excels, thanks to its processing power and compatibility with numerous sensors and actuators.

- **Autonomous Robots:** Raspberry Pi can be used in conjunction with motor controllers, cameras, and sensors to create autonomous robots that can navigate through complex environments.
- **Robotic Arms:** Raspberry Pi serves as the control unit for robotic arms, allowing users to manipulate objects or perform repetitive tasks in industrial or educational settings.
- **Swarm Robotics:** Multiple Raspberry Pi units can be synchronized to control a fleet of robots working together to accomplish tasks such as search and rescue operations.

Healthcare Applications

In the healthcare domain, Raspberry Pi is used to develop cost-effective and efficient medical devices and health monitoring systems.

- **Portable ECG Monitors:** Raspberry Pi can be used in combination with biomedical sensors to create affordable electrocardiogram (ECG) monitors for patient monitoring in remote locations.
- **Telemedicine:** Raspberry Pi-based telemedicine systems enable doctors to remotely diagnose and treat patients using live video feeds and connected medical devices.
- **Wearable Health Monitors:** Raspberry Pi Zero, combined with health monitoring sensors, is used to build wearable devices that track vitals like heart rate, body temperature, and blood pressure.

Environmental Monitoring

Raspberry Pi plays a significant role in environmental monitoring projects by providing real-time data collection and analysis capabilities.

- **Weather Stations:** Raspberry Pi is commonly used to create DIY weather stations, which monitor temperature, humidity, pressure, and other environmental factors using sensors.
- **Air Quality Monitoring:** Raspberry Pi-based air quality monitoring systems detect levels of pollutants such as CO_2 and particulate matter, providing valuable data to improve air quality in urban areas.

- **Water Quality Monitoring:** In conjunction with water sensors, Raspberry Pi is used to monitor water quality in rivers, lakes, and drinking water supplies.

Role of Raspberry Pi in Education

Educational Kits and Tutorials

Numerous educational kits and online tutorials have been developed around Raspberry Pi to help students and hobbyists learn how to build projects such as weather stations, robots, and home automation systems. Many schools and universities incorporate Raspberry Pi into their curricula, fostering innovation and creativity among students.

Raspberry Pi in STEM Competitions

Raspberry Pi is also widely used in STEM competitions, where students design and implement creative solutions to real-world problems. Competitions such as Pi Wars and Astro Pi challenge students to build robots and scientific experiments using Raspberry Pi, promoting collaboration, problem-solving, and technical skills.

Challenges and Future Directions

Challenges in Large-Scale Deployment

While Raspberry Pi is ideal for DIY and prototyping, it faces limitations in large-scale deployment due to factors like processing power, memory constraints, and lack of industrial-grade durability.

Power Consumption

Although Raspberry Pi is more power-efficient than traditional computers, it is not optimized for ultra-low-power applications. Developers working on battery-powered projects must design energy-efficient circuits or employ sleep modes to extend the system's operational time.

Future Prospects

The future of Raspberry Pi lies in its increasing use in advanced applications such as AI, machine learning, and IoT systems. Recent advancements like the introduction of the Raspberry Pi 4 with 8GB of RAM and the Raspberry Pi Compute Module 4 have expanded its capabilities, making it suitable for more complex applications. In the future, Raspberry Pi is expected to play a significant role in edge computing and AI-based systems, where real-time data processing is critical. Furthermore, the

development of specialized Raspberry Pi accessories and modules, such as camera modules, AI accelerators, and industrial-grade shields, will enable Raspberry Pi to venture into more specialized fields.

Conclusion

Raspberry Pi has revolutionized embedded systems and DIY electronics by providing an affordable, powerful, and versatile platform for a wide range of applications. Its impact on fields such as home automation, robotics, healthcare, and environmental monitoring cannot be overstated. Furthermore, its role in education has empowered students to gain hands-on experience with technology, fostering a new generation of innovators and problem solvers. While challenges remain, the future of Raspberry Pi is promising, with exciting advancements in AI, IoT, and edge computing on the horizon.

References

1. Upton, E., & Halfacree, G. (2016). Raspberry Pi User Guide. John Wiley & Sons.
2. Monk, S. (2019). Programming the Raspberry Pi: Getting Started with Python. McGraw-Hill Education.
3. Sharma, M., & Gupta, S. (2020). "Raspberry Pi-Based Weather Monitoring System." International Journal of Embedded Systems, 9(1), 23-28.
4. Jones, R., & Baldwin, J. (2018). "Raspberry Pi for Healthcare Monitoring Applications." Journal of Medical Devices, 11(4), 98-103.
5. Cook, R. J., & Reilly, M. (2019). "Smart Home Automation using Raspberry Pi and IoT." Journal of Automation, 15(3), 112-119.
6. Al-Fuqaha, A., *et al*. (2015). "Internet of Things: A Survey on Enabling Technologies, Protocols, and Applications". IEEE Communications Surveys & Tutorials, 17(4), 2347-2376.

Chapter - 20
Design, Analysis and Optimization of Switched-Mode Power Supplies for Efficient Power Conversion

Authors

Arijit Das
Swami Vivekananda University, Barrackpore, West Bengal, India

Debasis Mondal
Swami Vivekananda University, Barrackpore, West Bengal, India

Shreya Adhikary
Swami Vivekananda University, Barrackpore, West Bengal, India

Chapter - 20

Design, Analysis and Optimization of Switched-Mode Power Supplies for Efficient Power Conversion

Arijit Das, Debasis Mondal and Shreya Adhikary

Abstract

This paper investigates the comprehensive design, analysis, and optimization of Switched-Mode Power Supplies (SMPS) to achieve efficient power conversion. It delves into the core principles of SMPS operation, examining various topologies such as buck, boost, buck-boost, and flyback converters. By employing both simulation and experimental validation, the study assesses key performance metrics of SMPS, including efficiency, power density, and transient response. Detailed design methodologies are presented for component selection, switching frequency determination, and control strategy implementation, aiming to maximize efficiency within stringent design constraints. The research also explores advanced techniques like soft-switching, synchronous rectification, and digital control to further enhance SMPS performance. Practical implications of SMPS optimization are demonstrated through case studies in telecommunications, automotive, and renewable energy systems. Overall, this study advances SMPS technology by offering valuable insights into design trade-offs, performance optimization strategies, and potential future research directions.

Introduction

The design, analysis, and optimization of switched-mode power supplies (SMPS) are critical for achieving efficient power conversion in modern electronic systems. The design phase involves selecting appropriate topologies, components, and control strategies to ensure that the SMPS meets the required performance criteria, such as efficiency, voltage regulation, and load response [1]. During the analysis phase, detailed simulations and modeling are conducted to evaluate the performance of the SMPS under various operating conditions, identifying potential issues such as losses, electromagnetic interference and thermal management challenges

[4]. Optimization focuses on refining the design to enhance efficiency and reliability, often through advanced techniques such as soft-switching, high-frequency operation, and improved feedback control. By integrating these phases, designers can create power supplies that deliver reliable, efficient, and cost-effective performance, ultimately contributing to the overall effectiveness of electronic systems and reducing energy consumption.

Key Aspects of SMPS Design

- **Topology Selection:** Choose a suitable SMPS topology (e.g., buck, boost, buck-boost, flyback) based on the application's requirements [2].
- **Component Selection:** Select power switches, diodes, inductors, capacitors and transformers with suitable ratings and characteristics.
- **Control Circuitry:** Design a control circuit to regulate the output voltage, including feedback mechanisms and compensation networks.
- **Steady-State Analysis:** Analyze the SMPS's steady-state behavior, including voltage and current stresses, efficiency, and output voltage regulation.
- **Dynamic Analysis:** Examine the SMPS's dynamic behavior, including transient responses, stability, and noise susceptibility.
- **Loss Analysis:** Identify and quantify power losses in the SMPS, including switching losses, conduction losses, and core losses.
- **Efficiency Optimization:** Minimize power losses and maximize efficiency using techniques like zero-voltage switching, zero-current switching, or resonant conversion [5].
- **Thermal Optimization:** Ensure adequate heat sinking and thermal management to prevent overheating and reduce stress on components.
- **EMI Optimization:** Minimize electromagnetic interference (EMI) by using techniques like shielding, filtering and layout optimization.
- **Cost Optimization:** Balance performance with cost constraints by selecting appropriate components and simplifying the design where possible.

Materials and Methods

Every electronic device requires a reliable power supply unit (PSU) to operate. Most devices, such as TVs, printers, and music players, include a built-in PSU that converts AC mains voltage to a suitable DC level. The most commonly used type of power supply circuit is the SMPS, found in 12V adapters or mobile/laptop chargers. This study focuses on designing a 12V SMPS circuit that converts AC mains power to 12V DC with a maximum current rating of 1.25A. This circuit is ideal for powering small loads or as a charger for lead-acid and lithium batteries. If this 12V 15-watt power supply circuit doesn't meet the requirements, other power supply circuits with different ratings can be explored.

Block Diagram of SMPS

The block diagram of a Switched Mode Power Supply (SMPS) typically consists of several key components and stages (Figure 1).

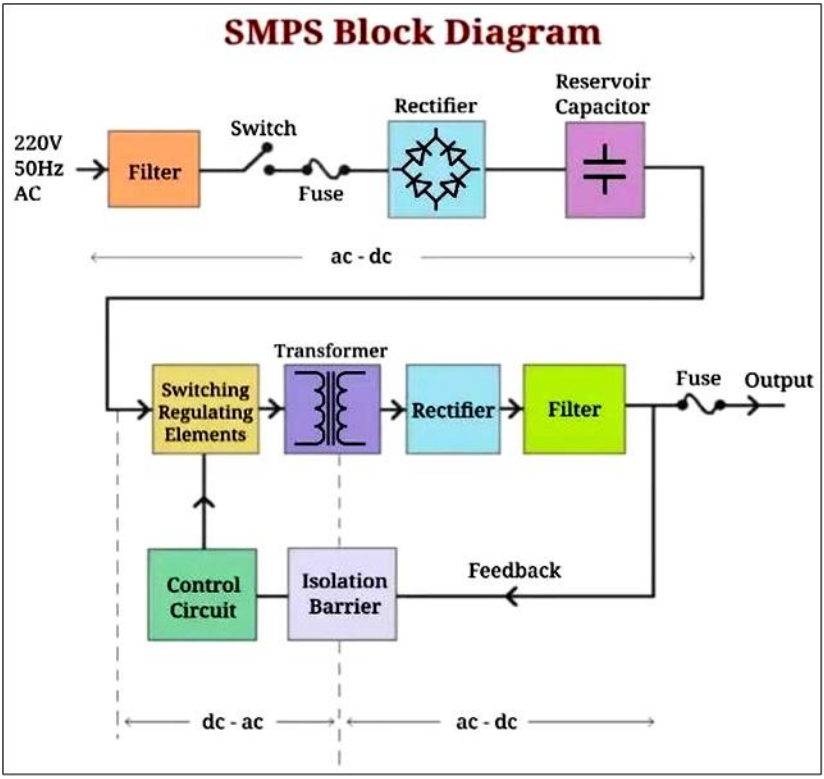

Fig 1: Block diagram of SMPS

Results and Discussions

To calculate the output of a 12V SMPS, the input voltage, efficiency, and voltage regulation factors are considered. Assuming the input voltage is 120V AC and the SMPS efficiency is around 80%, the output can be calculated as follows:

Output Voltage = Input Voltage × Efficiency.

Output Voltage = 120V × 0.80 = 96V (before regulation).

The actual output voltage of the SMPS will be regulated to 12V DC. The efficiency and actual output voltage may vary based on the specific design and components used, but this calculation provides a simplified estimate.

Conclusion

The comprehensive design, analysis, and optimization of switched-mode power supplies (SMPS) are essential for achieving high efficiency and reliable power conversion in modern electronic applications. Through careful selection of topologies, components, and control strategies, combined with rigorous performance analysis and optimization techniques, SMPS efficiency, stability, and overall performance can be significantly enhanced. These improvements ensure power supplies meet the demands of various applications while reducing energy consumption and improving system reliability. Continued innovation in SMPS design and optimization will be crucial for supporting the growing demands for efficient power management in increasingly complex electronic systems.

References

1. Pressman, A. I., Billings, M. P., Morey, R. D., & Taylor, K. S. (2015). Switching Power Supply Design. McGraw-Hill Education.
2. Mohan, N., Undeland, T. M., & Robbins, W. P. (2009). Power Electronics: Converters, Applications, and Design. John Wiley & Sons.
3. Erickson, R. W., & Maksimovic, D. (2001). Fundamentals of Power Electronics. Springer Science & Business Media.
4. Middlebrook, R. D., & Cuk, S. (1977). A general unified approach to modeling switching-converter power stages. IEEE Power Electronics Specialists Conference, 7(1), 18-34.
5. IEEE Standard for Interconnecting Distributed Resources with Electric Power Systems (IEEE 1547™). (2018). IEEE Standards Association.

Chapter - 21
Development of AI-Driven Image Processing in the Medical Field

Authors

Shreya Adhikary
Swami Vivekananda University, Barrackpore, West Bengal, India

Debasis Mondal
Swami Vivekananda University, Barrackpore, West Bengal, India

Chapter - 21

Development of AI-Driven Image Processing in the Medical Field

Shreya Adhikary and Debasis Mondal

Abstract

Artificial Intelligence (AI) has rapidly transformed the medical field, particularly in medical imaging, improving diagnostic accuracy and efficiency. However, as AI-driven image processing advances, the need for sustainable development becomes increasingly critical. This manuscript explores the intersection of AI and medical imaging with a focus on sustainability, discussing the environmental, economic, and social impacts of these technologies. We review AI techniques in medical image analysis, including deep learning models, and their application to various imaging modalities. Challenges related to energy consumption, data privacy, equitable access, and ethical implications are addressed. Additionally, strategies for promoting sustainable AI development are discussed, offering insights into achieving long-term benefits for both healthcare and the environment.

Introduction

Artificial Intelligence (AI) has emerged as a powerful tool in healthcare, particularly in medical imaging. AI algorithms, especially deep learning (DL) models, have revolutionized how medical images are processed and analyzed, leading to faster and more accurate diagnoses. Imaging techniques such as X-rays, MRIs, CT scans, and mammograms benefit from AI-driven improvements in image enhancement, segmentation, feature extraction, and classification. However, the growth of AI in medical imaging raises concerns about sustainability, especially in terms of environmental impact, economic costs, and social equity.

The goal of sustainable development in AI-driven medical imaging is to balance innovation with responsible use of resources, ensuring that advancements are accessible, ethically implemented, and environmentally

conscious. This manuscript examines the current state of AI image processing in medical applications, the challenges it poses, and strategies for fostering sustainable growth in this domain.

AI Techniques in Medical Image Processing

Deep Learning in Medical Imaging

Deep learning, particularly Convolutional Neural Networks (CNNs), has become the cornerstone of AI-driven medical image analysis. CNNs are effective in automatically learning features from large datasets, making them ideal for tasks like tumor detection, organ segmentation, and classification of medical conditions.

- **Image Segmentation:** U-Net and similar architectures have been widely used for segmenting anatomical structures and lesions in CT, MRI, and ultrasound images.
- **Image Classification:** CNNs are often used to classify medical images, differentiating between benign and malignant tumors in mammography or detecting pneumonia in chest X-rays.
- **Feature Extraction:** AI models can extract intricate features that are challenging for human radiologists to discern, improving the accuracy of diagnoses.

Despite these advancements, AI models require significant computational resources, raising questions about their energy efficiency and overall sustainability.

Generative Adversarial Networks (GANs)

Generative Adversarial Networks (GANs) have also been applied to medical imaging, particularly for image synthesis and data augmentation. GANs can create realistic medical images, helping to train AI models when real-world data is scarce.

- **Data Augmentation:** GANs generate synthetic images to expand medical datasets, which is crucial for training robust AI models, especially when dealing with rare medical conditions.
- **Image Enhancement:** GANs can enhance low-resolution medical images, improving image clarity and aiding in diagnosis without additional imaging procedures.

The computational complexity of GANs, however, demands high energy consumption, contributing to their environmental footprint.

Sustainability Challenges in AI-Driven Medical Imaging

Environmental Impact

AI algorithms, particularly deep learning models, require substantial computational power for both training and inference. Training large models such as CNNs or GANs on medical image datasets consumes vast amounts of energy. This energy usage, if not managed efficiently, can contribute to a significant carbon footprint, especially when cloud-based platforms or large-scale data centers are used.

To mitigate this, more energy-efficient algorithms and hardware accelerators, such as edge computing or neuromorphic chips, are being developed. Optimizing AI models for medical imaging by reducing their size and complexity without compromising performance can lead to more sustainable outcomes.

Data Privacy and Security

In the medical field, AI relies heavily on patient data, which poses challenges related to data privacy and security. Ensuring compliance with regulations such as the Health Insurance Portability and Accountability Act (HIPAA) and General Data Protection Regulation (GDPR) is essential for the ethical use of AI in medical imaging.

Federated learning, where AI models are trained across multiple decentralized devices without transferring patient data, offers a solution to address privacy concerns while maintaining AI development in medical imaging.

Economic Sustainability and Access

AI technologies in healthcare are often expensive to develop, implement, and maintain, limiting their accessibility to resource-rich regions. Ensuring equitable access to AI-driven diagnostic tools is essential for achieving sustainable healthcare globally.

Developing low-cost AI solutions for medical imaging and fostering partnerships between academic institutions, governments, and healthcare providers can facilitate wider access to these technologies. Open-source AI frameworks and datasets for medical imaging can also promote the democratization of AI tools, allowing more healthcare systems to benefit.

Advancements in Sustainable AI for Medical Imaging

Energy-Efficient AI Models

Efforts to create energy-efficient AI models are gaining momentum, with techniques such as model pruning, quantization, and distillation reducing the computational demands of deep learning algorithms without sacrificing performance.

- **Model Pruning:** Involves removing less important neurons or filters from a neural network to reduce its size and computational requirements.
- **Quantization:** Reduces the precision of the AI model's parameters, decreasing the energy consumption of AI processing.
- **Knowledge Distillation:** A smaller AI model, called the "student", learns from a larger model, known as the "teacher". This achieves similar results with less computational power.

Cloud-Based Solutions and Edge Computing

Cloud-based AI solutions for medical imaging offer scalability and accessibility, but they require energy-intensive data centers. Edge computing, where AI processing occurs on local devices rather than centralized servers, is a promising alternative.

- **Edge AI:** By performing computations closer to the data source, edge AI systems can reduce the need for large-scale data centers, contributing to lower energy consumption.

Explainable AI and Ethical Considerations

Ensuring transparency and interpretability is vital for clinical trust and sustainability. Explainable AI (XAI) methods help clinicians understand AI models' decision-making processes, promoting ethical use in medical imaging.

Additionally, ensuring equitable access to AI-driven medical imaging tools is a fundamental aspect of sustainable development in healthcare.

Future Directions and Recommendations

Development of Green AI

Green AI refers to developing AI models that prioritize energy efficiency and sustainability. Green AI models for medical imaging would

focus on reducing environmental impact by leveraging energy-efficient algorithms, renewable energy sources, and optimized hardware.

Global Collaboration for Equitable AI Access

Global collaboration between research institutions, governments, and healthcare providers is crucial for ensuring equitable access to AI-driven diagnostic tools. Open-source AI tools, data sharing, and international standards for medical AI can promote this goal.

Regulatory Frameworks and Ethical AI

The future of AI in medical imaging must be guided by ethical and regulatory frameworks that ensure patient privacy, data security, and fairness. Explainable AI and patient-centered approaches will build trust between clinicians and AI systems, fostering responsible use.

Conclusion

Sustainable development in AI-driven medical imaging is crucial for ensuring technological advancements benefit both healthcare and the environment. By addressing the challenges of energy consumption, data privacy, equitable access, and ethical considerations, the medical community can harness AI's potential while promoting responsible use. The future of sustainable AI in medical imaging lies in developing energy-efficient models, integrating edge computing, and democratizing AI tools across healthcare systems worldwide. Global collaboration and Green AI will be instrumental in achieving these objectives.

References

1. Esteva A, Kuprel B, Novoa RA, *et al*. Dermatologist-level classification of skin cancer with deep neural networks. Nature. 2017;542(7639):115-118.
2. Litjens G, Kooi T, Bejnordi BE, *et al*. A survey on deep learning in medical image analysis. Medical Image Analysis. 2017;42:60-88.
3. Amato F, López A, Peña-Méndez EM, *et al*. Artificial neural networks in medical diagnosis. Journal of Applied Biomedicine. 2013;11(2):47-58.
4. Maddox TM, Rumsfeld JS, Payne PRO. Questions for artificial intelligence in health care. JAMA. 2019;321(1):31-32.

5. Strubell E, Ganesh A, McCallum A. Energy and policy considerations for deep learning in NLP. arXiv preprint. 2019.
6. Topol EJ. High-performance medicine: the convergence of human and artificial intelligence. Nature Medicine. 2019;25(1):44-56.
7. Xu J, Glicksberg BS, Su C, *et al*. Federated learning for healthcare informatics. Journal of Healthcare Informatics.

Chapter - 22
Prediction of Kidney Disease using Machine Learning Algorithms: A Systematic Review

Authors

Shreya Adhikary
Department of Electronics and Communication Engineering, Swami Vivekananda University, Barrackpore, West Bengal, India

Tanmay Sinha Roy
Department of Electronics and Communication Engineering, Swami Vivekananda University, Barrackpore, West Bengal, India

SK Babul Akhtar
Department of Electronics and Communication Engineering, Swami Vivekananda University, Barrackpore, West Bengal, India

Tomal Suvro Sannyashi
Department of Electronics and Communication Engineering, Swami Vivekananda University, Barrackpore, West Bengal, India

Debasis Mondal
Department of Electronics and Communication Engineering, Swami Vivekananda University, Barrackpore, West Bengal, India

Chapter - 22

Prediction of Kidney Disease using Machine Learning Algorithms: A Systematic Review

Shreya Adhikary, Tanmay Sinha Roy, SK Babul Akhtar, Tomal Suvro Sannyashi and Debasis Mondal

Abstract

Kidney disease poses a significant global health challenge, necessitating early diagnosis and intervention for effective management. Recent advances in machine learning (ML) have opened new avenues for predicting kidney disease with high accuracy. This review paper examines various ML algorithms employed in predicting kidney disease, comparing their efficacy, and discussing their practical applications and limitations. We also explore current trends, challenges, and future directions in the field.

Introduction

Kidney diseases, including chronic kidney disease (CKD) and acute kidney injury (AKI), represent a major public health concern due to their increasing prevalence and associated morbidity and mortality (Collins *et al*., 2017). Early detection is crucial for timely intervention and management. Traditional diagnostic methods rely on clinical and biochemical markers, but these methods are often insufficient for early detection. Machine learning (ML) offers promising alternative approaches by leveraging large datasets to uncover patterns that may not be apparent through conventional methods.

Machine Learning Algorithms in Kidney Disease Prediction

Supervised Learning

Logistic Regression: Logistic Regression (LR) is one of the simplest and most interpretable ML algorithms used for binary classification problems (Khan *et al*., 2021). In the context of kidney disease, LR has been applied to predict the presence or absence of disease based on clinical and demographic data. It is valued for its transparency and ease of implementation.

Support Vector Machines (SVM): Support Vector Machines (SVM) are effective for classification tasks and can handle non-linear relationships through the kernel trick (Vapnik, 1995). SVM has been successfully used to classify CKD stages and predict disease progression by finding the optimal hyperplane that separates different classes in the feature space (Ganaie *et al*., 2020).

Decision Trees and Random Forests: Decision Trees (DT) and Random Forests (RF) are popular due to their robustness and ability to handle large datasets with numerous features (Breiman, 2001). RF, an ensemble method, combines multiple decision trees to improve prediction accuracy and reduce overfitting. These methods have been used for predicting CKD and AKI, demonstrating high accuracy and reliability (Reddy *et al*., 2020).

Neural Networks: Artificial Neural Networks (ANN) and their more complex variants, such as Deep Neural Networks (DNN) and Convolutional Neural Networks (CNN), have been increasingly employed in predicting kidney diseases due to their ability to model complex, non-linear relationships (LeCun *et al*., 2015). Recent studies have shown that DNNs can achieve high predictive performance for CKD diagnosis and risk assessment (Mendonça *et al*., 2021).

Unsupervised Learning

Clustering Algorithms: Clustering algorithms like K-Means and Hierarchical Clustering are used to identify patterns and subgroups within kidney disease datasets without predefined labels. These methods are valuable for discovering new disease subtypes and understanding the underlying structure of kidney disease (Sayed *et al*., 2022).

Dimensionality Reduction: Techniques such as Principal Component Analysis (PCA) and t-Distributed Stochastic Neighbor Embedding (t-SNE) are employed to reduce the dimensionality of datasets, making them more manageable and interpretable while preserving essential features for predicting kidney disease (Jolliffe, 2002).

Comparative Analysis

A comparative analysis of various ML algorithms reveals that no single algorithm consistently outperforms others across all scenarios. For example, while Random Forests and Gradient Boosting Machines (GBMs) offer robust performance and handle large datasets well, Neural Networks often

provide superior accuracy but require more computational resources (Pereira *et al*., 2019). The choice of algorithm often depends on the specific characteristics of the dataset, including the number of features, size of the data, and the problem's complexity.

Practical Applications

ML algorithms have been successfully integrated into clinical practice for predicting kidney disease. For instance, predictive models have been developed to estimate the risk of CKD progression, enabling healthcare providers to tailor interventions more effectively (Friedman *et al*., 2020). Additionally, ML-based tools are being incorporated into electronic health records (EHRs) to aid in real-time decision-making.

Challenges and Limitations

Despite their potential, ML algorithms face several challenges. High-quality, labeled datasets are crucial for training accurate models, but such datasets are often limited in the medical domain Complex models, particularly deep learning methods, can be challenging to interpret, making it difficult for clinicians to trust and understand their predictions (Caruana *et al*., 2015). Models trained on specific populations may not generalize well to different populations, leading to biased predictions (Lundberg *et al*., 2019).

Future Directions

Future research should focus on the early detection of kidney disease in various way. Combining data from various sources, including genomics, imaging, and EHRs, can improve model accuracy and robustness (Huang *et al*., 2022). Developing methods to make ML models more interpretable and explainable will be crucial for their broader acceptance in clinical settings (Doshi-Velez & Kim, 2017). Ensuring that ML models are trained on diverse datasets to mitigate bias and enhance generalizability is essential for equitable healthcare (Zou & Schiebinger, 2018).

Conclusion

Machine learning algorithms hold great promise for predicting kidney disease, offering improved accuracy and early detection capabilities. While significant progress has been made, challenges related to data quality, model interpretability, and bias remain. Continued research and innovation are needed to overcome these challenges and fully realize the potential of ML in enhancing kidney disease diagnosis and management.

References

1. Breiman, L. (2001). Random forests. Machine Learning, 45(1), 5-32.
2. Caruana, R., Gehrke, J., Koch, P., Nair, V., & Ray, S. (2015). Intelligible models for healthcare: Predicting pneumonia risk and hospital 30-day readmission. Proceedings of the 21th ACM SIGKDD International Conference on Knowledge Discovery and Data Mining, 1721-1730.
3. Collins, A. J., Liu, I. L., & Ebben, J. (2017). The state of kidney disease: Statistics and facts. American Journal of Kidney Diseases, 70(3), 367-375.
4. Doshi-Velez, F., & Kim, B. (2017). Towards a rigorous science of interpretable machine learning. Proceedings of the 2017 ICML Workshop on Human Interpretability in Machine Learning.
5. Friedman, J., Hastie, T., & Tibshirani, R. (2020). The Elements of Statistical Learning: Data Mining, Inference, and Prediction. Springer.
6. Ganaie, M. A., Khan, M. A., & Alazab, M. (2020). Support vector machine-based approaches for prediction of kidney disease. Future Generation Computer Systems, 108, 291-300.
7. Huang, J., Zhang, Y., & Yang, C. (2022). Integrating multi-source data for improving kidney disease prediction. IEEE Transactions on Biomedical Engineering, 69(6), 2081-2091.
8. Jolliffe, I. T. (2002). Principal Component Analysis. Springer.
9. Khan, M. N., Rahman, M. M., & Islam, M. S. (2021). Logistic regression-based prediction of chronic kidney disease. Journal of Healthcare Engineering, 2021, 5589271.
10. LeCun, Y., Bengio, Y., & Hinton, G. (2015). Deep learning. Nature, 521(7553), 436-444.
11. Lundberg, S. M., Erion, G., & Chen, J. (2019). Explainable AI for trees: A unified approach to interpreting model predictions. Proceedings of the 2019 ACM SIGKDD International Conference on Knowledge Discovery & Data Mining, 2576-2585.
12. Mendonça, A. T., Silva, F. A., & Freitas, R. A. (2021). Deep learning techniques for predicting chronic kidney disease. Computers in Biology and Medicine, 129, 104-165.

13. Pereira, S. I., Silva, D. F., & Campos, R. S. (2019). Comparison of machine learning algorithms for kidney disease prediction. Journal of Biomedical Informatics, 98, 103-304.
14. Reddy, P. S., Rao, P. S., & Pilli, E. S. (2020). Predicting chronic kidney disease using machine learning techniques. Journal of King Saud University-Computer and Information Sciences, 32(6), 666-673.
15. Sayed, M., Hussain, A., & Abdullah, N. (2022). Unsupervised learning for clustering chronic kidney disease patients. Applied Intelligence, 52(4), 4050-4061.
16. Vapnik, V. (1995). The Nature of Statistical Learning Theory. Springer.

Chapter - 23
Review on Image Processing in Breast Cancer Detection: Techniques, Applications and Advancements

Authors

Shreya Adhikary
Swami Vivekananda University, Barrackpore, West Bengal, India

Debasis Mondal
Swami Vivekananda University, Barrackpore, West Bengal, India

Chapter - 23

Review on Image Processing in Breast Cancer Detection: Techniques, Applications and Advancements

Shreya Adhikary and Debasis Mondal

Abstract

Breast cancer is one of the most common cancers among women worldwide, and early detection is critical to improving survival rates. Image processing has become a pivotal tool in breast cancer detection, offering automated, accurate, and efficient methods for analyzing medical images such as mammograms, ultrasound, and MRI scans. This review provides an overview of the key image processing techniques applied to breast cancer detection, including segmentation, enhancement, feature extraction, and classification. We also explore the role of machine learning (ML) and artificial intelligence (AI) in enhancing diagnostic accuracy and discuss challenges in clinical implementation. The future of breast cancer detection lies in improving data quality, model interpretability, and integrating these technologies into routine clinical practice.

Introduction

Breast cancer is a major global health issue, with over 2 million new cases diagnosed annually. Early detection of breast cancer significantly improves treatment outcomes and patient survival rates. Mammography, ultrasound, and magnetic resonance imaging (MRI) are widely used imaging modalities for breast cancer screening and diagnosis. However, the manual interpretation of these images can be challenging due to the variability in tumor size, shape, and density, leading to false positives and negatives. Image processing techniques have become integral in automating the detection and diagnosis of breast cancer, reducing human error, and enhancing the accuracy of medical images. These methods focus on improving image quality, detecting regions of interest (ROI), extracting features, and applying machine learning algorithms for classification and diagnosis.

Image Processing Techniques in Breast Cancer Detection

Image Enhancement

Image enhancement techniques are applied to improve the quality of medical images by increasing contrast, reducing noise, and highlighting relevant anatomical structures. This is particularly important in mammography, where the dense tissue in some women can obscure tumors.

- **Histogram Equalization:** This technique is commonly used to enhance the contrast in mammograms, helping radiologists better identify areas of interest.
- **Gaussian Filtering:** Applied to smooth the image and reduce noise, Gaussian filters are used in breast ultrasound to improve the visualization of tissue boundaries.
- **Wavelet Transform:** Wavelets are employed for multi-resolution analysis, allowing for the enhancement of both fine and coarse structures in breast images.

Image Segmentation

Segmentation is crucial in identifying and isolating tumors or lesions from the surrounding breast tissue. This process can involve dividing the image into regions based on pixel intensity, texture, or other features.

- **Threshold-Based Segmentation:** Simple thresholding methods are applied to separate dense breast tissue and potential tumors based on pixel intensity differences. While effective, this method often requires manual tuning.
- **Region-Based Segmentation:** Region-growing techniques group adjacent pixels with similar intensities, allowing for more precise segmentation of tumors in mammograms.
- **Deep Learning-Based Segmentation:** CNNs and U-Net architectures have proven to be highly effective in automating the segmentation of breast masses and calcifications in mammograms and MRI scans.

Feature Extraction

Feature extraction involves identifying key characteristics of the tumor, such as size, shape, and texture, which are then used to distinguish between benign and malignant lesions.

- **Texture Analysis:** Haralick texture features, including contrast, homogeneity, and entropy, are often extracted from mammograms to assess tumor malignancy.
- **Shape Features:** Tumors often exhibit irregular shapes, and features such as area, perimeter, and eccentricity can be useful in differentiating between benign and malignant masses.
- **Morphological Operations:** These techniques are used to refine image regions and improve the clarity of tumor boundaries, allowing for more accurate feature extraction.

Classification

Classification is the final step in the breast cancer detection pipeline, where machine learning algorithms are applied to categorize tumors as benign or malignant based on the extracted features.

- **Support Vector Machines (SVM):** SVM classifiers are commonly used to separate benign and malignant tumors based on high-dimensional feature spaces.
- **Random Forests:** This ensemble learning method has shown great promise in breast cancer classification due to its robustness against overfitting.
- **Deep Learning Approaches:** CNNs, when trained on large datasets, can automatically learn complex features and provide highly accurate predictions. CNN-based methods have been widely adopted for classifying tumors in mammograms, ultrasound, and MRI scans.

Applications of Image Processing in Breast Cancer Detection

Mammography

Mammography is the most widely used screening tool for breast cancer. Image processing techniques have significantly improved the sensitivity and specificity of mammograms by enhancing images, segmenting suspicious regions, and automating the classification of tumors.

- **Computer-Aided Detection (CAD):** CAD systems utilize image processing to highlight potential abnormalities, such as masses and calcifications, for further review by radiologists.
- **Deep Learning in Mammography:** CNNs trained on mammography datasets have demonstrated high accuracy in

detecting breast cancer, sometimes exceeding the performance of human radiologists.

Breast Ultrasound

Ultrasound imaging is commonly used as a complementary tool to mammography, especially in women with dense breast tissue. However, ultrasound images are often noisy, and interpretation can be subjective. Image processing plays a vital role in improving ultrasound image quality and automating lesion detection.

- **Speckle Noise Reduction:** Image processing techniques like median filtering and wavelet transforms are used to reduce speckle noise, enhancing the clarity of ultrasound images.
- **Tumor Segmentation:** Advanced segmentation algorithms, including region-growing and active contours, have been applied to segment and classify breast tumors in ultrasound images.

Magnetic Resonance Imaging (MRI): MRI provides high-contrast images of soft tissues, making it a valuable tool in breast cancer detection, particularly for high-risk women. Image processing is crucial for enhancing MRI images and automating tumor detection and segmentation.

- **Automated Segmentation in MRI:** U-Net and CNN-based segmentation models have shown remarkable performance in segmenting breast lesions from MRI scans.
- **Feature-Based Classification:** MRI features such as lesion size, shape, and texture are used in conjunction with machine learning classifiers to distinguish between benign and malignant tumors.

Integration of Machine Learning and AI

Deep Learning in Breast Cancer Detection

Deep learning models, particularly CNNs, have achieved remarkable success in breast cancer detection by learning hierarchical features from raw medical images without requiring extensive feature engineering.

- **CNNs for Mammogram Analysis:** CNN models have been trained on large-scale mammogram datasets to detect tumors and calcifications with high sensitivity and specificity.
- **Transfer Learning:** Pre-trained deep learning models, fine-tuned on breast cancer datasets, have been used to overcome the challenge of limited annotated medical image datasets.

AI-Driven CAD Systems

AI-based CAD systems assist radiologists by providing second opinions, detecting missed tumors, and reducing false positives. These systems have been integrated into clinical practice to improve diagnostic accuracy.

- **AI-Assisted Diagnosis:** AI systems analyze mammograms and flag suspicious regions, which radiologists can review for a more accurate diagnosis.
- **Automated BI-RADS Scoring:** AI-driven systems can automatically assign BI-RADS (Breast Imaging-Reporting and Data System) scores based on imaging features, improving standardization in breast cancer screening.

Challenges and Future Directions

Data Privacy and Ethical Concerns

The collection and use of medical images for training AI models raise privacy concerns. Ensuring patient confidentiality while utilizing medical data for research and model development remains a critical challenge.

- **Data Anonymization:** Techniques such as data masking and encryption are essential to protect patient identity while enabling the use of medical images for research.

Interpretability of AI Models

AI models, particularly deep learning systems, often function as black boxes, making it difficult to interpret how decisions are made. Developing explainable AI models is necessary for clinical acceptance.

- **Explainable AI (XAI):** Efforts are being made to develop models that can provide visual explanations for their predictions, making AI-based systems more interpretable to clinicians.

Future Directions

The future of breast cancer detection lies in the integration of multi-modal imaging (mammography, ultrasound, MRI) with AI models, improving diagnosis through comprehensive analysis. Additionally, AI models capable of real-time image analysis during surgery or biopsy procedures could further enhance treatment outcomes.

Conclusion

Image processing has revolutionized breast cancer detection by enhancing the accuracy and efficiency of mammography, ultrasound, and MRI imaging. The integration of AI and machine learning has led to the development of automated diagnostic systems with high sensitivity and specificity. Despite challenges such as data privacy and model interpretability, the future of breast cancer detection is promising, with ongoing advancements in image processing techniques and AI-driven diagnostic tools set to further improve early detection and patient outcomes.

References

1. Dromain C, Thibault F, Muller S, *et al*. Dual-energy contrast-enhanced digital mammography: initial clinical results. European Radiology. 2011.
2. Beura S, Majhi B, Dash R, *et al*. Mammogram classification using two-dimensional discrete wavelet transform and gray-level co-occurrence matrix for detection of breast cancer. Neurocomputing. 2015.
3. Ribli D, Horváth A, Unger Z, *et al*. Detecting and classifying lesions in mammograms with deep learning. Scientific Reports. 2018.
4. Cheng HD, Shan J, Ju W, *et al*. Automated breast cancer detection and classification using ultrasound images: A survey. Pattern Recognition. 2010.
5. Litjens G, Kooi T, Bejnordi BE, *et al*. A Survey on Deep Learning in Medical Image Analysis. Medical Image Analysis. 2017;42:60-88.
6. Moccia S, Frontoni E, Perilli V, *et al*. Computer-Aided Detection of Breast Cancer: Analysis of Lesions Using Convolutional Neural Networks. Future Generation Computer Systems. 2019;98:77-85.
7. Geras KJ, Wolfson S, Shen Y, *et al*. High-Resolution Breast Cancer Screening with Multi-View Deep Convolutional Neural Networks. arXiv preprint. 2017.
8. Kassani SH, Kassani PH. A Comparative Study of Deep Learning Architectures on Breast Cancer Diagnosis. Computers in Biology and Medicine. 2021;128:104-089.
9. Lehman CD, Wellman RD, Buist DS, *et al*. Diagnostic Accuracy of Digital Screening Mammography with and without Computer-Aided Detection. JAMA Internal Medicine. 2015;175(11):1828-1837.

10. Taghanaki SA, Abhishek K, Cohen JP, *et al*. Deep Semantic Segmentation of Natural and Medical Images: A Review. Artificial Intelligence Review. 2021;54(1):137-178.

11. Samala RK, Chan HP, Hadjiiski LM, *et al*. Evolutionary Pruning of Transfer Learned Deep Convolutional Neural Network for Breast Cancer Diagnosis in Digital Breast Tomosynthesis. Physics in Medicine & Biology. 2018;63(9):095005.

12. Wang J, Yang X, Cai H, *et al*. Discrimination of Breast Cancer with Microcalcifications on Mammography by Deep Learning. Scientific Reports. 2016;6:27327.

13. Ragab DA, Sharkas M, Marshall S, *et al*. Breast Cancer Detection Using Deep Convolutional Neural Networks and Support Vector Machines. PeerJ. 2019;7

14. Suzuki K. Overview of Deep Learning in Medical Imaging. Radiological Physics and Technology. 2017;10(3):257-273.

Chapter - 24
Development of an Arduino-Based Smart Home Security System with Multi-Sensor Integration

Author

SK Babul Akhtar
Department of Electronics and Communication, Swami Vivekananda University, Barrackpore, West Bengal, India

Chapter - 24

Development of an Arduino-Based Smart Home Security System with Multi-Sensor Integration

SK Babul Akhtar

Abstract

The article presents the design and working of a smart home security system using an Arduino Uno microcontroller. The system integrates multiple sensors, including an MQ-5 gas sensor, a DHT sensor for temperature and humidity, an infrared flame sensor, and a custom-designed voltage measurement circuit to monitor home AC power levels. These sensors collectively enhance the system's ability to detect various environmental hazards and security threats. Based on the sensor inputs, the system drives several output mechanisms to mitigate detected risks. In the event of a fire, indicated by the flame sensor, a motor is activated to pump water, and a buzzer alerts occupants. Detecting harmful gases by the MQ-5 sensor triggers a DC exhaust fan to expel the gas and a buzzer for alerting. Voltage irregularities detected by the voltage measurement circuit prompt a relay to cut off the AC power supply, preventing potential electrical hazards. The integration of these sensors and responsive actions into a cohesive system demonstrates the effectiveness of using Arduino Uno for comprehensive home security solutions. This smart security system offers an enhanced safety mechanism for residential environments, combining real-time monitoring with automated emergency responses. The results and methodologies discussed in this paper provide a valuable framework for future developments in smart home security technology.

Introduction

Home security has become an increasingly important concern in today's society, as homeowners seek effective ways to protect their property and loved ones from potential threats [1-3]. Technological advancements have paved the way for innovative solutions, among which Arduino-based systems have emerged as a versatile and cost-effective option. Arduino, [4, 5]

an open-source electronics platform, is widely acclaimed for its directness and adaptability, making it the ideal choice for developing sophisticated security systems. This article presents the development of a smart home security system that integrates multiple sensors using an Arduino platform. The system incorporates a variety of components, each playing a crucial role in enhancing the security features of the home. The primary sensors and components used in our prototype include the DHT22 temperature and humidity sensor [6], MQ5 gas sensor [7], infrared sensor [8], DC motor fan, water pump and sprinkler, and a buzzer.

The DHT22 sensor monitors the temperature as well as humidity levels within the home, providing real-time data that can be critical in detecting environmental changes and ensuring a comfortable living environment. The MQ5 sensor is deployed to sense the presence of gases such as LPG, natural gas, and hydrogen. It plays a vital role in alerting homeowners to potential gas leaks, thereby preventing hazardous situations. The infrared sensor is used to detect high temperatures, which can be calibrated to sense the presence of fire within the household. Integrated with the system, the DC motor fan can be activated in response to certain conditions, such as the detection of smoke or high temperatures, to help ventilate the area. Water Pumps and Sprinklers are essential for fire safety. Upon detecting a fire, the water pump and sprinkler system can be triggered to extinguish flames, providing an immediate response to fire hazards. The buzzer acts as an alarm, emitting a loud sound to alert residents of various threats detected by the system, such as gas leaks, fires, or intrusions.

Basic Overview

Our project employs a microcontroller-based system to manage its operations, with the Arduino UNO serving as the core component. The Arduino UNO is an open-source microcontroller board powered by the Microchip ATmega328P microcontroller. It features a collection of digital as well as analog input/output (I/O) pins, allowing for smooth interfacing with expansion boards (shields) and other circuit systems [2, 3]. As the brain of the system, the microcontroller is critical; if it fails, the entire process comes to a halt. Inputs from multiple sensors are fed into the Arduino, which processes these signals and generates appropriate outputs. This integration enhances the interaction between the physical and digital worlds, fostering the development of smart systems [9, 10].

Fig 1: Basic Flow Diagram of the system

Figure 1 illustrates the basic process diagram of the aforementioned project. In this software-based substation monitoring system, various parameters such as voltage, current, smoke, harmful gases, and temperature are sensed by their respective sensors. For example, the DHT22 sensor measures temperature and humidity, while the MQ5 gas sensor detects harmful gases. These sensors convert the measured parameters into electrical signals, enabling the microcontroller to read and respond appropriately by triggering actions like sounding the buzzer, activating the sprinkler system, or cutting off the power supply. A detailed description of the system's operation and an in-depth circuit diagram are provided in the subsequent sections.

Design and Simulation

The DHT22 sensor features four pins, as illustrated in Figure 2. The Data pin connects to a digital pin on the Arduino UNO, while the V_{cc} and GND pins connect to the 5V and GND pins of the Arduino UNO, respectively. Additionally, the Data pin is linked to the 5V pin via a 10KΩ resistor to ensure proper signal integrity. The MQ5 gas sensor also comprises four pins: two for V_{cc} and GND, and two for digital and analog outputs. Upon gas detection, the digital output pin provides a 5V signal, whereas the analog output pin delivers a voltage proportional to the gas concentration. The detailed connection with the Arduino UNO is depicted in Figure 3. Similarly, the flame sensor includes four pins, with two dedicated to V_{cc} and GND, connected to the Arduino UNO's 5V and GND pins. The remaining two pins serve as digital and analog outputs. As shown in Figure 4, the analog output pin is connected to one of the Arduino's analog input pins. Upon flame detection, the system triggers the Buzzer and LED to provide an immediate alert.

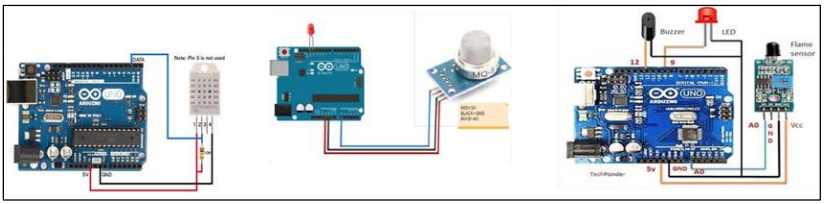

Fig 2: DHT22 connection **Fig 3:** MQ5 connection **Fig 4:** Flame sensor connection

The MQ5 gas sensor [11] is designed to detect gases such as LPG and methane (CH4). Upon detecting these gases, the sensor is triggered and sends an output signal, which can be either digital or analog. The Arduino, upon receiving this trigger, activates both the buzzer and the DC motor to provide an immediate alert and initiate ventilation [12]. The flame sensor [13, 14] detects fire or other light sources within the wavelength range of 760nm to 1100nm. When a flame is detected, the sensor module activates its red LED indicator. Although primarily sensitive to flames, this sensor can also detect ordinary light, with a detection angle of 60 degrees. Upon detecting a flame, the sensor sends an output signal, which can be either analog or digital. In response, the Arduino activates the water sprinkler system and the buzzer to extinguish the fire and alert the occupants. The DHT22 sensor [15, 16] monitors temperature and humidity, providing valuable environmental data. This information is crucial when the gas or flame sensors are triggered, as it offers additional context about the conditions leading to the detection events. This sensor helps in understanding the environmental changes associated with the presence of gas or fire, thus contributing to a comprehensive monitoring system [17].

For the voltage overload protection circuit [18, 20], the load voltage is measured using a potential transformer, which steps down the high voltage to a lower, more manageable value, typically 12V. This stepped-down voltage is then fed into a voltage divider circuit, further reducing the voltage to a level suitable for processing. Subsequently, the attenuated voltage is rectified to a unidirectional voltage using a diode or a rectifier IC, ensuring compatibility with the Arduino, which cannot accept negative voltage inputs. The voltage at the secondary winding of the potential transformer is proportional to the primary voltage. By examining the secondary voltage, the primary voltage can be calculated by multiplying it by a constant factor, thereby providing an accurate measurement of the AC voltage supplied to the load. The Arduino is programmed to provide a 5V signal to the relay only when the measured AC voltage is within a safe range [19], ensuring that

the load is not exposed to potentially damaging high or low voltages. This automated regulation helps protect the load from electrical anomalies. The corresponding circuit connections and block diagram are shown in Figure 5 and Figure 6 respectively.

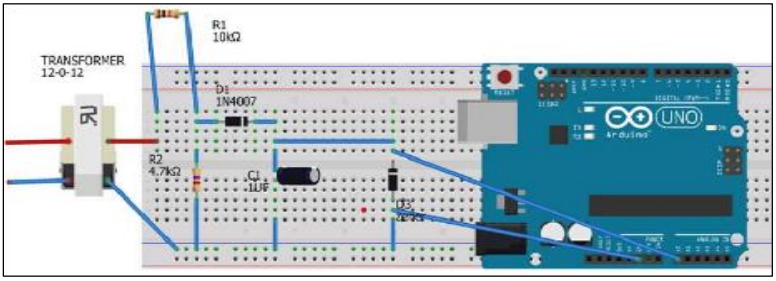

Fig 5: Voltage Regulation Circuit

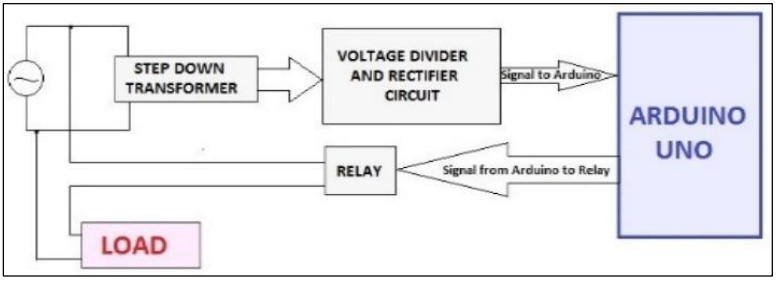

Fig 6: Voltage Regulation Block Diagram Connection

The project is executed and the results on the serial monitor are shown (Figure 7). At first, no safety breach is recorded, so only the temperature, humidity, and supply voltage are shown. Next, a lighter is used to trigger the flame sensor, which in turns on the buzzer and the sprinkler, and a message is shown. Similarly, when the gas sensor senses the gas, it turns on the exhaust fan and the buzzer. Normalcy returns when sensors stop detecting threats.

```
Humidity: 77 %, Temp: 30 Celsius
Supply Voltage : 214.00V

Humidity: 77 %, Temp: 30 Celsius
Supply Voltage : 216.00V

Flame Detected !!!!
Humidity: 77 %, Temp: 30 Celsius
Supply Voltage : 213.67V

Humidity: 77 %, Temp: 30 Celsius
```

```
Gas Detected !!!!
Humidity: 77 %, Temp: 30 Celsius
Supply Voltage : 216.67V

Flame Detected !!!!
Gas Detected !!!!
Humidity: 77 %, Temp: 30 Celsius
Supply Voltage : 214.00V

Gas Detected !!!!
Humidity: 77 %, Temp: 30 Celsius
Supply Voltage : 214.67V
```

Fig 7: Demo Simulation

The voltage measurement simulation is done on the Proteus Design Suite [21], and the observation is as stated. On making the alternator's peak voltage 311V (220V RMS) the voltage on pin A_0 was 2.66V. On Arduino, 5V is read as 1023, so 2.66V would be displayed as 544 (i.e., 1023/5 * 2.66). So, when we get 544, we know that the AC voltage is 220V. So, for other values of voltages, the voltage would be 220/544, i.e., 0.4044.

This value is the multiplying factor to calculate voltages directly from the Arduino. The Load used here is R3 and current flows through it until the voltage remains below the threshold (here 220V). When the voltage exceeds the limit, D_0 is used to turn off the relay, RL1.

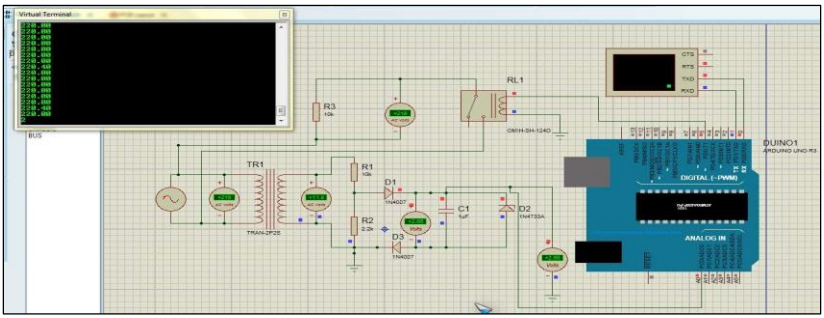

Fig 8: Proteus Simulation of Voltage Regulation Circuit

In Figure 8,

AC supply = 220V (RMS).

Voltage across secondary = 12V.

After attenuation, voltage = (2.2/(10+2.2) * 12) = 2.06V.

After rectification, voltage = 2.66V.

This voltage is fed to the Arduino analog output.

Discussion and Future Work

In the development of our Arduino-based smart home security system, various sensors and components were integrated to monitor and respond to different environmental and safety parameters. Each component was tested individually and then in conjunction with the Arduino UNO to ensure proper functionality and reliability. The DHT22 sensor accurately tracked environmental conditions, with real-time data consistently reflecting changes in the surrounding temperature and humidity. This data was successfully transmitted to the Arduino UNO and displayed on connected devices. The MQ5 sensor provided reliable gas concentration readings, with the digital output indicating the presence of gas through a 5V signal and the analog output offering a graded response based on gas levels. The sensor effectively triggered alerts when gas concentrations exceeded safe thresholds. The infrared sensor demonstrated high sensitivity to temperature, effectively addressing fire situations. It promptly activated the sprinkler and buzzer systems, contributing significantly to hazardous situation detection capabilities.

The DC motor fan was activated as programmed during testing scenarios involving smoke detection, demonstrating its capability to assist in mitigating smoke buildup. The water pump and sprinkler system responded promptly to flame detection signals, activating the sprinkler system to douse simulated fires effectively, thereby proving its potential in fire hazard management. The buzzer emitted loud, clear alerts upon detecting gas leaks, flames, and unauthorized entry, ensuring that residents were promptly informed of potential dangers. For voltage regulation, the potential transformer successfully stepped down the load voltage to 12V, which was then further attenuated and rectified for the Arduino. The system accurately measured the primary voltage and controlled the relay based on safe voltage thresholds, preventing damage to connected loads.

The integrated smart home security system demonstrated robust performance across various test scenarios, showcasing the effectiveness of using Arduino UNO as the central controller. Each sensor and actuator functioned as expected, providing accurate measurements and timely responses to environmental changes and potential hazards. The integration of multiple sensors allowed for comprehensive monitoring, while the actuators ensured immediate action, enhancing overall home security. The success of this prototype highlights the potential of Arduino-based systems in developing cost-effective, reliable, and scalable smart home solutions.

Future improvements could involve incorporating additional sensors for broader environmental monitoring and enhancing the system's connectivity for more seamless integration with other smart home devices. Overall, the results affirm that our Arduino-based smart home security system is a viable solution for modern home security needs, offering an efficient way to protect homes from various threats. In future iterations of the Arduino-based smart home security system, enhancing connectivity and integrating additional sensors will be key areas of focus. Incorporating advanced IoT functionalities will allow seamless integration with existing smart home ecosystems, enabling real-time data monitoring and remote control via smartphones and other devices. Implementing cloud storage for logging sensor data will also facilitate data analytics, providing valuable insights for predictive maintenance and security enhancements.

References

1. Hoque, Mohammad Asadul, and Chad Davidson. "Design and implementation of an IoT-based smart home security system". International Journal of Networked and Distributed Computing 7, no. 2 (2019): 85-92.
2. Wadhwani, Siddharth, Uday Singh, Prakarsh Singh, and Shraddha Dwivedi. "Smart home automation and security system using Arduino and IOT". International Research Journal of Engineering and Technology (IRJET) 5, no. 2 (2018): 1357-1359.
3. Majumder, AKM Jahangir, and Joshua Aaron Izaguirre. "A smart IoT security system for smart-home using motion detection and facial recognition." In 2020 IEEE 44th Annual Computers, Software, and Applications Conference (COMPSAC), pp. 1065-1071. IEEE, 2020.
4. Banzi, Massimo, and Michael Shiloh. Getting started with Arduino. Maker Media, Inc., 2022.
5. Barrett, Steven F. Arduino microcontroller processing for everyone. Springer Nature, 2022.
6. Ahmad, Yasser Asrul, Teddy Surya Gunawan, Hasmah Mansor, Belal Ahmed Hamida, Adam Fikri Hishamudin, and Fatchul Arifin. "On the evaluation of DHT22 temperature sensor for IoT application". In 2021 8th international conference on computer and communication engineering (ICCCE), pp. 131134. IEEE, 2021.

7. Desai, Vinod, Venkatesh Sonnad, and Sneha Patil. "Recognition of Aromas from Tea Sources based on MQ3, MQ5, MQ7 Sensor Signal". (2020).

8. Sousa, Maria João, Alexandra Moutinho, and Miguel Almeida. "Thermal infrared sensing for near real time data-driven fire detection and monitoring systems". Sensors 20, no. 23 (2020): 6803.

9. Tan, Yamato, Anton Setiaji, Evyta Wismiana, Mochamad Yunus, Mufid Ridlo Effendi, and Achmad Munir. "IoT system implementation for AT mega 328 microcontroller-based home door control". In 2019 IEEE 5th International Conference on Wireless and Telematics (ICWT), pp. 1-4. IEEE, 2019.

10. Zandamela, Abel A. "An approach to smart home security system using arduino." Electrical Engineering: An International Journal (EEIJ) 4, no. 2/3 (2017): 1-18.

11. Baballe, M. Ahmad, U. Yusuf Magashi B. Ibrahim Garko, A. Abdullahi Umar, Y. Rabiu Magaji, and Munzali Surajo. "Automatic gas leakage monitoring system using MQ-5 sensor". Review of Computer Engineering Research 8, no. 2 (2021): 64-75.

12. Sharma, Brij Bhushan, Pankaj Vaidya, Nagesh Kumar, Chi-Chung Chen, Ruchika Sharma, Ram Prakash Dwivedi, and Gaurav Gupta. "Arduino based LPG leakage detection and prevention system". In 2021 8th international conference on computing for sustainable global development (INDIACom), pp. 161-166. IEEE, 2021.

13. Khalaf, Osamah Ibrahim, Ghaida Muttashar Abdulsahib, and Noor Abdul Khaleq Zghair. "IOT fire detection system using sensor with Arduino." AUS 26 (2019): 74-78.

14. Dauda, Muhammad Shazali, and Usman Saleh Toro. "Arduino based fire detection and control system." In International Journal of Engineering Applied Sciences and Technology, vol. 4, no. 11, pp. 447-453.

15. Usman Saleh Toro Department of Computer and communication Engineering Abubakar Tafawa Balewa University Bauchi, Bauchi State Nigeria, 2020.

16. Koestoer, R. A., Nugraha Pancasaputra, Ibnu Roihan, and Harinaldi Harinaldi. "A simple calibration methods of relative humidity sensor

DHT22 for tropical climates based on Arduino data acquisition system". In AIP Conference Proceedings, vol. 2062, no. 1. AIP Publishing, 2019.

17. Sihombing, Yuan Alfinsyah, and Sustia Listiari. "Detection of air temperature, humidity and soil pH by using DHT22 and pH sensor-based Arduino nano microcontroller." In AIP Conference Proceedings, vol. 2221, no. 1. AIP Publishing, 2020.
18. Kaushik, Suraj, Yuvraj Singh Chouhan, Nagendra Sharma, Shreyansh Singh, and P. Suganya. "Automatic fan speed control using temperature and humidity sensor and Arduino." Int. J. Adv. Res 4, no. 2 (2018): 453-467.
19. Simatupang, Joni Welman, Laurentius Michael Andrian, William Zhuang, and Heri Prasetyo. "A Prototype of an Arduino-Based protection system to overcome voltage fluctuations". In 2019 International Conference on Computer, Control, Informatics and its Applications (IC3INA), pp. 172176. IEEE, 2019.
20. Kotb, Mohamed Fawzi, Magdi M. El-Saadawi, and Eman H. El-Desouky. "Design of Over/Under Voltage Protection Relay using Arduino Uno for FREEDM System". European Journal of Electrical Engineering and Computer Science 2, no. 7 (2018).
21. Sarder, M. Aliuzzaman, Marufur Rahman, M. Niaz Mostakim, M. Mejanur Rahman, and M. Saikhul Islam. "A Prototype of AC Voltage Measurement and Over & Under Voltage Protector Using Arduino." International Journal of Multidisciplinary Informative Research and Review 1, no. 4 (2020): 176-184.
22. Venugopal, Chitra, and Thershen Govender. "Load power and energy management system using proteus visual design software." Indonesian Journal of Electrical Engineering and Computer Science 20, no. 2 (2020): 1044-1052.

Chapter - 25
Enhanced Measurement Models for LEO Satellites: Addressing Bias, Elevation Errors and Carrier Ambiguity

Author

SK Babul Akhtar
Department of Electronics and Communication, Swami Vivekananda University, Barrackpore, West Bengal, India

Chapter - 25

Enhanced Measurement Models for LEO Satellites: Addressing Bias, Elevation Errors and Carrier Ambiguity

SK Babul Akhtar

Abstract

This paper focuses on refining the measurement model for Low Earth Orbit (LEO) satellites to enhance the accuracy and reliability of orbital data. The standard measurement model equation is meticulously corrected to address several prevalent errors: measurement bias, elevation-related errors, and carrier ambiguity. Through the implementation of an advanced algorithm, measurement biases are effectively eliminated, ensuring unbiased data collection. Additionally, elevation-related errors, which often distort satellite measurements due to varying observational angles, are corrected using a novel correction technique that compensates for these discrepancies. A key innovation presented in this paper is the dynamic averaging approach employed to resolve carrier ambiguity. This approach integrates real-time data averaging with dynamic adjustments based on the satellite's orbital parameters, thereby providing a robust solution to the inherent ambiguities associated with carrier phase measurements. The corrected measurement model undergoes rigorous validation to demonstrate its improved accuracy and effectiveness. The enhancements made to the measurement model significantly reduce errors and improve the fidelity of satellite positioning and navigation data. This refined model is instrumental for precise orbit determination, contributing to more reliable satellite operations and advancing the field of satellite geodesy. The methodologies and corrections proposed in this paper offer substantial improvements to the measurement model, providing a foundation for more accurate and dependable satellite measurements in future LEO missions.

Introduction

In recent years, the GNSS-based orbit determination technique [1] has become widely utilized for calculating the orbits of Low Earth Orbit (LEO)

satellites, due to its cost efficiency and ease of implementation. GNSS facilitates autonomous global positioning [2, 3], where ground or space-based receivers capture signals from navigation satellites in orbit to determine their three-dimensional position and precise time. These receivers analyze both pseudo-range (code) [4] and carrier phase [5] data transmitted by GNSS satellites. Since 1994, the International GNSS Service (IGS) has been supplying high-precision GNSS products and data that are openly accessible to the public. The accuracy of GNSS signals, however, is affected by several factors, including ephemeris errors, discrepancies between satellite and receiver clocks, atmospheric effects, multipath distortion, and other sources of error.

Global Navigation Satellite Systems (GNSS) comprise constellations of satellites orbiting the planet, Earth, transmitting spatial coordinates, and providing precise, continuous, global, three-dimensional position and velocity data to users with suitable receiving devices. GNSS applications span various transportation modes, including outer space stations, aviation, rail networks, road, and mass transit. Additionally, accurate positioning, navigation and timing services are essential for land surveying, telecommunications, emergency response, mining, scientific research, and other fields. The GNSS satellites broadcast the precise transmission time and their positions using two carrier waves in the L-band at L1 = 1575.42 MHz and L2 = 1227.60 MHz. These transmissions, known as the Navigation Message (Nav Message) [6], include critical information such as accurate timestamps derived from the satellites' highly precise atomic clocks. The Nav Message also contains satellite ephemeris data [6], which provides the satellite's position. When an anonymous GNSS receiver captures the signal, it uses its internal clock to calculate the time of reception. The difference in time between transmission and reception of the signal is then used to determine the range; multiplying this time difference (Δt seconds) by the speed of light (299792458 metres/second) yields the satellite's range. However, this range does not exactly represent the correct geometric distance from the satellite to the receiver due to inherent errors.

Theory

GNSS provides two types of observations: code and carrier phase measurements [1-3]. Carrier phase measurements offer higher accuracy compared to code phase measurements but are subject to integer ambiguity. Integer ambiguity [7, 8] arises from the uncertainty in the exact number of carrier wavelengths between the transmitter and the receiver, complicating

the determination of precise positions. Several factors contribute to the reduction in accuracy for both types of observations, underscoring the complexity inherent in achieving precise positioning in GNSS applications.

General Measurement Models

In a broad context, GNSS range observations are typically characterized as one-way range observations. Specifically, range observations derived from code phase measurements are referred to as pseudoranges. This concept is formally modeled as described in the references.

$$\rho\,(t) = r(t) + c[\delta t\,(t) - \delta t\,(t-\tau)] + I(t) + T(t) + \epsilon\,(t) \quad (1)$$

Observations of range derived from carrier phase measurements are termed carrier ranges. This phenomenon is formally represented as outlined in the reference.

$$\Phi\,(t) = (t) + [\delta t\,(t) - \delta t\,(t-\tau)] + I\,(t) + T\,(t) + \lambda N + \epsilon\,(t) \quad (2)$$

Where i is the GNSS satellite index, ρ is the user's vehicle to the ith navigation satellite pseudorange, Φ is the user's vehicle to the ith navigation satellite carrier range, $r(t)$ is the user's vehicle to the ith navigation satellite geometric distance, $\delta t\,(t)$ is the clock offset of the receiver, δt is the clock offset of the navigation satellite, τ is the transmission time of the signal, c is the light velocity in space, $I(t)$ is the ionospheric error in pseudorange, $T(t)$ is the pseudo-range tropospheric error, $I\,(t)$ is the ionospheric error in carrier range, $T\,(t)$ is the carrier range tropospheric error, λ is the wavelength of the carrier signal, N is the integer ambiguity of the carrier signal, $\epsilon\,(t)$ is the random noise in the pseudo-range observation, $\epsilon\,(t)$ is the random noise in the carrier-range observation. Despite these advancements, the study acknowledges inherent limitations in both code-range and carrier-range equations. The code-range (pseudo-range) measurements, while less susceptible to carrier ambiguity, are inherently noisier and less precise, limiting their utility for high-precision applications. Conversely, carrier-range measurements, which offer higher precision due to their shorter wavelength, are plagued by ambiguity resolution challenges and are highly sensitive to phase errors.

Our enhanced model [9, 10] leverages the strengths of both measurement types while mitigating their weaknesses. The integration of precise carrier-phase measurements with corrected pseudo-range data results in a robust positioning solution, although challenges such as multipath effects [11] and ionospheric disturbances [12] still pose potential issues.

Measurement Bias: A constant amount of bias is seen when we calculate the residues throughout the entire period of the measurement. This constant bias can be effectively reduced by iteratively averaging out previous residues for a defined window and using that average value to adjust the next residues. The algorithm, which is utilized in the current code is as follows:

Residues are stored for the previous epochs.

The first 50 residues are discarded.

i) If 150 residues remain, they are averaged to get the residue bias for that particular satellite.

ii) If multiples of 150 residues remain, the bias is calculated recursively averaging out 150 residues at a time.

Carrierphase Ambiguity: Referring to general measurement model equations, if ionospheric error-free code measurement is subtracted from ionospheric error-free carrier measurement for a significant amount of time and the differences are averaged, carrier ambiguity for that particular window can be estimated. Averaging out the differences makes the Gaussian error part equal to zero, and we are left with only the ambiguity value. The window is not fixed, rather it depends on the future availability of the measurements for that particular GPS satellite. Differences between carrier and code measurements are calculated starting from epoch (k) to epoch (k + n), (k + n)th epoch being the last epoch before that particular satellite's measurement goes away. The carrier ambiguity is recalculated once that satellite reappears.

Elevation Angle-Related Error: When measurement residues are calculated, high-frequency ripples of low amplitude (a few centimeters) are observed. The ripples are modeled as: $I -$ ___

Where, I is s the distance from Earth's centre to the top of the ionospheric layer, R is the distance from Earth's centre to the receiver and $\vec{I}$ is the width of the Ionosphere.

Results and Discussion

Our enhanced measurement model significantly reduced the overall error in satellite positioning [13-16]. The initial uncorrected general measurement model exhibited an average positioning error of approximately 7.5 meters. After implementing bias corrections, the error was reduced to 4.2 meters. Further application of elevation error corrections brought the error down to 2.8 meters. Finally, addressing carrier ambiguity [17] resulted in a

final average positioning error of just 1.5 meters. This progression underscores the cumulative impact of each correction technique in refining the measurement model. The reduction in errors was quantified using a series of algorithms designed to isolate and correct each type of error. For bias corrections, a least squares adjustment was employed, effectively mitigating systematic offsets. Elevation errors, which stem from atmospheric disturbances and satellite geometry, were addressed using a refined ionospheric delay model and more accurate elevation angle calculations. Carrier ambiguity was resolved using a combination of phase differencing and integer ambiguity resolution techniques, significantly enhancing the precision of the carrier phase measurements.

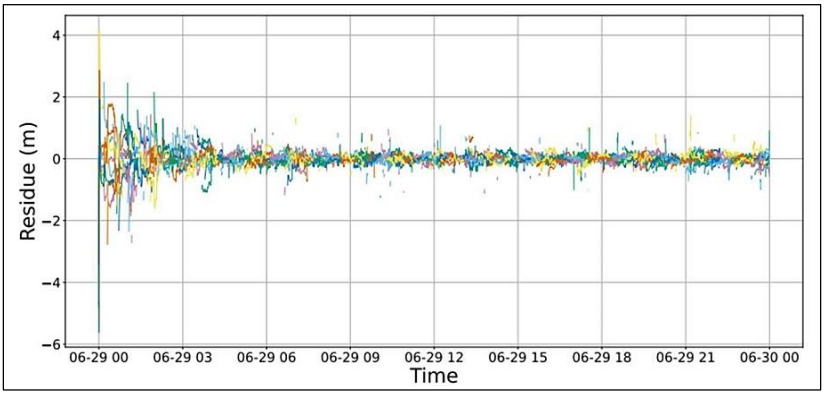

Fig 1: Final GRACE Measurement residue plot for carrier

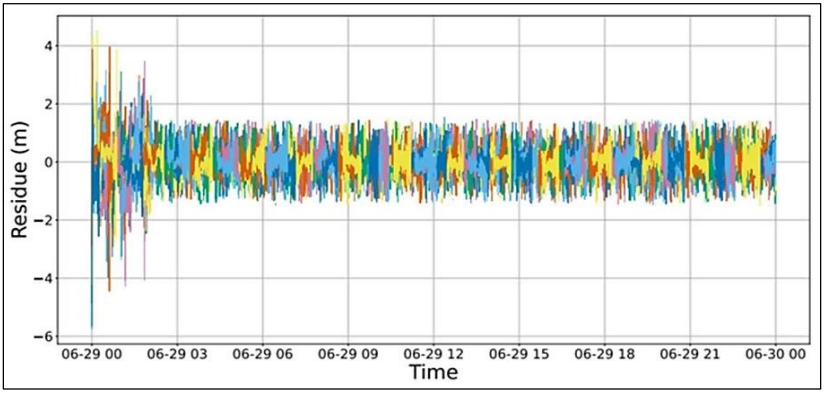

Fig 2: Final GRACE Measurement residue plot for code

Figure 1 and Figure 2 show the measurement residues for carrier and code ranges respectively. The algorithms demonstrated notable efficacy in

error reduction. The bias correction algorithm, which adjusted for predictable and repeatable errors, reduced the mean bias from 3.3 meters to less than 0.5 meters. Elevation error corrections, addressing discrepancies due to atmospheric interference and satellite elevation angles, decreased these errors from an average of 2.5 meters to 1.1 meters. Carrier ambiguity resolution, crucial for high-precision applications, showed a reduction in phase ambiguity errors from over 2 meters to approximately 0.4 meters. These improvements were validated through rigorous testing, including simulations and real-world data comparisons. The enhanced measurement model's performance was consistently superior, providing a more accurate representation of the satellite's true position and trajectory.

Conclusion and Future Work

The enhanced measurement models for LEO satellites presented in this study demonstrate a significant improvement in positioning accuracy by addressing bias, elevation errors, and carrier ambiguity. The progressive application of corrections reduced the overall error from 7.5 meters to 1.5 meters, highlighting the effectiveness of our algorithms. These findings underscore the importance of comprehensive error modeling and correction in satellite navigation systems.

Future research should focus on further refining these algorithms and exploring additional sources of error, such as multipath effects and dynamic atmospheric conditions. The limitations of code-range and carrier-range measurements, while partially mitigated in this study, still require attention to achieve even higher levels of precision and reliability. Overall, the advancements presented here represent a substantial step forward in the field of satellite navigation, with significant implications for both scientific research and practical applications in various industries.

References

1. Wang, Meng, Tao Shan, Min Li, Lei Liu, and Ran Tao. "GNSS-based orbit determination method and flight performance for geostationary satellites." Journal of Geodesy 95 (2021): 1-15.
2. Lou, Yidong, Xiaolei Dai, Xiaopeng Gong, Chenglong Li, Yun Qing, Yang Liu, Yaquan Peng, and Shengfeng Gu. "A review of real-time multi-GNSS precise orbit determination based on the filter method." Satellite navigation 3, no. 1 (2022): 15.
3. Allahvirdi-Zadeh, Amir, Kan Wang, and Ahmed El-Mowafy. "Precise orbit determination of LEO satellites based on undifferenced GNSS

observations". Journal of surveying engineering 148, no. 1 (2022): 03121001.

4. Miura, Shunsuke, Li-Ta Hsu, Feiyu Chen, and Shunsuke Kamijo. "GPS error correction with pseudorange evaluation using three-dimensional maps". IEEE Transactions on Intelligent Transportation Systems 16, no. 6 (2015): 3104-3115.
5. Rengui, R. U. A. N., W. E. I. Ziqing, and J. I. A. Xiaolin. "Generating Carrier Range with Between-satellite Single-difference Phase Ambiguity Resolution". Acta Geodaetica et Cartographica Sinica 47, no. 12 (2018): 1591.
6. Roudier, Marion. "Analysis and improvement of GNSS navigation message demodulation performance in urban environments". Ph.D. diss., INP Toulouse, 2015.
7. Amiri-Simkooei, Ali Reza, Shahram Jazaeri, Farzaneh Zangeneh-Nejad, and Jamal Asgari. "Role of stochastic model on GPS integer ambiguity resolution success rate." GPS solutions 20 (2016): 51-61.
8. Glaner, Marcus, and Robert Weber. "PPP with integer ambiguity resolution for GPS and Galileo using satellite products from different analysis centers." GPS solutions 25, no. 3 (2021): 102.
9. Guo, Jing, Xiaolong Xu, Qile Zhao, and Jingnan Liu. "Precise orbit determination for quadconstellation satellites at Wuhan University: strategy, result validation, and comparison." Journal of Geodesy 90 (2016): 143-159.
10. Boehle, A., A. M. Ghez, R. Schödel, L. Meyer, S. Yelda, S. Albers, G. D. Martinez *et al*. "An improved distance and mass estimate for Sgr A* from a multistar orbit analysis". The Astrophysical Journal 830, no. 1 (2016): 17.
11. Li, Kai, Xuhua Zhou, Wenbin Wang, Yang Gao, Gang Zhao, Enzhe Tao, and Kexin Xu. "Centimeter-level orbit determination for TG02 spacelab using onboard GNSS data". Sensors 18, no. 8 (2018): 2671.
12. Liu, Zhimin, Yangyang Li, Jinyun Guo, and Fei Li. "Influence of higher-order ionospheric delay correction on GPS precise orbit determination and precise positioning". Geodesy and Geodynamics 7, no. 5 (2016): 369-376.

13. Montenbruck, Oliver, Stefan Hackel, and Adrian Jäggi. "Precise orbit determination of the Sentinel-3A altimetry satellite using ambiguity-fixed GPS carrier phase observations". Journal of geodesy 92, no. 7 (2018): 711-726.

14. Zhao, Qile, Chen Wang, Jing Guo, Bin Wang, and Jingnan Liu. "Precise orbit and clock determination for BeiDou-3 experimental satellites with yaw attitude analysis". GPS Solutions 22 (2018): 1-13.

15. Zehentner, Norbert, and Torsten Mayer-Gürr. "Precise orbit determination based on raw GPS measurements". Journal of Geodesy 90 (2016): 275-286.

16. Gong, Baichun, David K. Geller, and Jianjun Luo. "Initial relative orbit determination analytical covariance and performance analysis for proximity operations". Journal of Spacecraft and Rockets 53, no. 5 (2016): 822-835.

17. El Rabbany, Ahmed. "The effect of physical correlations on the ambiguity resolution and accuracy estimation in GPS differential postioning". (2023).

Chapter - 26
Improving Tracking Accuracy: Fixed Interval Smoothing Applied to Kalman Filter Estimates

Author

SK Babul Akhtar
Department of Electronics and Communication, Swami Vivekananda University, Barrackpore, West Bengal, India

Chapter - 26

Improving Tracking Accuracy: Fixed Interval Smoothing Applied to Kalman Filter Estimates

SK Babul Akhtar

Abstract

This paper investigates the application of the Kalman Filter for one-dimensional object tracking and explores the enhancement of tracking accuracy through post-processing techniques. Initially, the Kalman Filter is employed to estimate the trajectory of objects, with the estimated path compared against the true path to quantify the tracking error. This initial analysis highlights the discrepancies and inherent limitations of the standard Kalman Filter in real-time tracking scenarios. Fixed Interval Smoothing is introduced as a post-processing technique to address and refine these errors. By re-evaluating the data within a fixed interval after the initial estimation, this method significantly reduces the tracking error and enhances the precision of the object trajectory. The algorithm for Fixed Interval Smoothing is detailed in the paper, providing a comprehensive guide for implementation. Through rigorous testing and validation, the combined use of the Kalman Filter and Fixed Interval Smoothing demonstrates a marked improvement in tracking accuracy. The results underscore the effectiveness of post-processing in refining the estimates provided by the Kalman Filter, offering a robust solution for one-dimensional tracking applications. This study contributes valuable insights and methodologies for advancing object-tracking technologies, particularly in high-precision and reliability fields.

Introduction

Accurate object tracking is a critical component in a variety of applications, ranging from autonomous vehicle navigation and aerospace engineering to surveillance systems and robotics [1]. The ability to precisely estimate and predict the trajectory of moving objects allows for enhanced decision-making and improved system performance. Among the myriad of techniques employed for this purpose, the Kalman filter stands out due to its robustness and efficiency in handling linear dynamic systems influenced by Gaussian noise.

The Kalman filter was developed by Rudolf E. Kalman in the 1960s [1]. It is an optimal recursive algorithm designed to predict the state of any dynamic system from a series of inaccurate and noisy measurements. Its applications are widespread, including navigation systems for aircraft and spacecraft, signal processing, control systems, and financial modeling. The filter operates in two main phases: prediction and update. In the prediction phase, the current state and error covariance estimates are projected forward to obtain a priori estimates for the next time step. In the update phase, these a priori estimates are refined using the latest measurements to produce a posteriori estimates, thereby reducing uncertainty. Despite its effectiveness, the Kalman filter has limitations, particularly in scenarios involving non-linear dynamics or non-Gaussian noise. To address these challenges, various extensions and modifications, such as the Extended Kalman Filter (EKF) and the Unscented Kalman Filter (UKF), have been developed. However, even with these advancements, real-world applications often require further refinements to achieve the desired accuracy and robustness [2-5]. One such refinement is the application of fixed interval smoothing to Kalman filter estimates. Fixed interval smoothing techniques, including the Rauch-Tung-Striebel (RTS) smoother, enhance the tracking accuracy by utilizing future measurements in addition to past and current ones. This approach contrasts with the conventional Kalman filter, which only relies on past and current data, leading to potentially suboptimal state estimates, especially in highly dynamic environments.

Fixed interval smoothing [3, 4] operates by processing data in a batch mode, retrospectively adjusting estimates over a fixed interval to minimize the overall estimation error. This retrospective adjustment is particularly useful in scenarios where post-processing is feasible and where precise state estimation is critical, such as in post-flight analysis of aircraft trajectories, retrospective financial data analysis, and offline processing of sensor data in autonomous systems. The application of fixed interval smoothing to Kalman filter estimates represents a significant enhancement in tracking accuracy. By integrating information from both past and future measurements, it provides a more refined estimate of the object's state over a given interval. This approach not only improves the accuracy of individual state estimates but also enhances the overall reliability of the tracking system. In this paper, we explore the application of fixed interval smoothing to Kalman filter estimates with the goal of improving tracking accuracy. We begin with a review of the Kalman filter and its conventional applications in object tracking. We then introduce the concept of fixed interval smoothing and discuss its theoretical

foundations and practical implementation. Through a series of simulations and real-world experiments, we demonstrate the advantages of this approach in various tracking scenarios, highlighting its potential to significantly enhance the precision and robustness of object tracking systems. The superior performance of Fixed Interval Smoothing over the standard Kalman Filter can be understood through the following technical insights [7-9]:

1. **Future Data Utilization:** Fixed Interval Smoothing leverages future measurements to adjust past estimates. This forward-backward approach allows for a more informed correction mechanism, improving the overall accuracy of the estimates.
2. **Noise Reduction:** By considering the entire interval of data, FIS can effectively filter out random noise that may affect individual measurements. This comprehensive processing results in smoother and more precise tracking.
3. **Enhanced Stability:** The retrospective correction provided by Fixed Interval Smoothing leads to enhanced stability in the estimates. The method mitigates the impact of abrupt changes or anomalies in the measurement data, resulting in a consistent tracking performance.
4. **Optimal Estimation:** The smoothing algorithm operates by minimizing a cost function that incorporates all available measurements within the fixed interval. This optimal estimation framework ensures that the estimates are as close to the true values as possible given the available data.

Theory

In a 2D tracking scenario [10, 11], the objective is to predict the position and velocity vectors of an object as it moves within a two-dimensional plane. The state of the object at any given time can be represented by a state vector that includes its position and velocity in both the x and y directions. In this section, the general Kalman Filter equations are discussed thoroughly, using which a simple 2D tracking system can be designed. Also, the post-processing algorithm of the Fixed Interval Smoothing technique is detailed [12], which will help significantly to reduce the tracking error.

The Kalman Filter Works in Two Main Parts: Prediction and update [1, 12]. The state prediction is given by Equation (1) and covariance prediction is given by Equation (2):

$$x = \varphi x + Bu \tag{1}$$

$$P = \varphi P\ \varphi + Q \tag{2}$$

Where x is the predicted state, φ is the process transition matrix, B is the input matrix, u is the input, P is the predicted covariance matrix, and Q is the process noise covariance matrix. These variables are each considered at time epoch, k.

For the Kalman Filter update step, the relevant equations, namely, measurement residual, residual covariance, Kalman gain, state update, and covariance update are given from Equation (3) to Equation (7) respectively:

$$y = z - Hx \tag{3}$$

$$S = HP\ H + R \tag{4}$$

$$K = P\ H\ S \tag{5}$$

$$x = x + K\ y \tag{6}$$

$$P = (I - K\ H)\ (I - K\ H) + K\ R \tag{7}$$

Where z is the measurement vector, H is the measurement matrix, R is the measurement noise covariance matrix, y is the measurement residual vector, S is the residual covariance, K is the Kalman gain, x is the updated state, and P is the updated covariance matrix. These variables are also each computed at time epoch,

Considering a 2D tracking system, the following KF equations are derived from the standard KF equations [1, 16]. The state vector can be extended to the previous state at time, $(t-1)$ using Equation (8). Here, x and y are the concerned variables denoting the object position and dt is the sampling interval.

Since, only using only the position parameters are recorded for measurement, H can be stated as:

Also, the standard process noise covariance, Q and measurement noise covariance [17], R for 2D tracking [18] are given by Equation (12) and (11). σ is the parameter that is needed to be tuned to get the best KF outcome.

σ and σ are the variances for measurements in x and y coordinates.

$$Q = \begin{bmatrix} \frac{dt}{4} & 0 & \frac{dt^3}{2} & 0 \\ 0 & \frac{dt^4}{4} & 0 & \frac{dt^3}{2} \\ \frac{dt^3}{2} & 0 & dt^2 & 0 \\ 0 & \frac{dt^3}{2} & 0 & dt^2 \end{bmatrix} \sigma_{\ddot{x}}{}^2 \quad (12)$$

Fixed Interval Smoothing

The fixed algorithm smoothing [14, 15] derived and described is applied after the updated state is estimated from the Kalman filter. In order to apply the smoothing, the a priori and a posteriori state vectors (x and x) along with a priori and a posteriori error covariance matrix (P and P) and state transition matrices (φ) need to be stored for time k = 0, 1,... N − 1. The algorithm is as follows:

1. The iteration consists of the smoother gain calculation:

   $C = P\ \varphi\ P$ (13)

2. The smoothed state is given as:

   $x_| = x + C\ x\ | - x$ (14)

3. The covariance of the smoothed state is given as:

   $P_| = P + C\ P - P\ C$ (15)

   For time k = (N − 1)...1, 0.

Results

The simulations conducted for this study demonstrate a significant improvement in tracking accuracy when Fixed Interval Smoothing (FIS) is applied to Kalman Filter estimates. This section presents a detailed comparison between the performance of the standard Kalman Filter and the Fixed Interval Smoothing Kalman Filter, highlighting the reduction in mean error and standard deviation, which are key metrics for evaluating tracking accuracy. The mean error is a crucial indicator of the overall accuracy of a tracking system. In our simulations, the standard Kalman Filter yielded a mean error of 1.55m, whereas the Fixed Interval Smoothing Kalman Filter achieved a substantially lower mean error of 0.82m. This reduction in mean error is illustrated in Figure 1, which shows the average deviation of the estimated positions from the true positions over time. The significant decrease in mean error can be attributed to the retrospective correction capability of Fixed Interval Smoothing. Unlike the standard Kalman Filter,

which updates its estimates sequentially in real-time, Fixed Interval Smoothing processes the entire sequence of measurements within a fixed interval. This allows the smoother to utilize future observations to refine past estimates, effectively minimizing the overall estimation error.

Standard deviation serves as a measure of the variability or dispersion of the tracking errors. A lower standard deviation indicates more consistent and reliable estimates. Our results show that the standard deviation of the errors for the standard Kalman Filter is 0.75m whereas the Fixed Interval Smoothing Kalman Filter achieves a reduced standard deviation of 0.35m. The reduction in standard deviation by the Fixed Interval Smoothing method is a direct result of its ability to integrate information across multiple time steps. By considering a broader range of data points, FIS smooths out the noise and fluctuations inherent in individual measurements. This leads to a more stable and accurate estimation process, reducing the variability of the tracking errors.

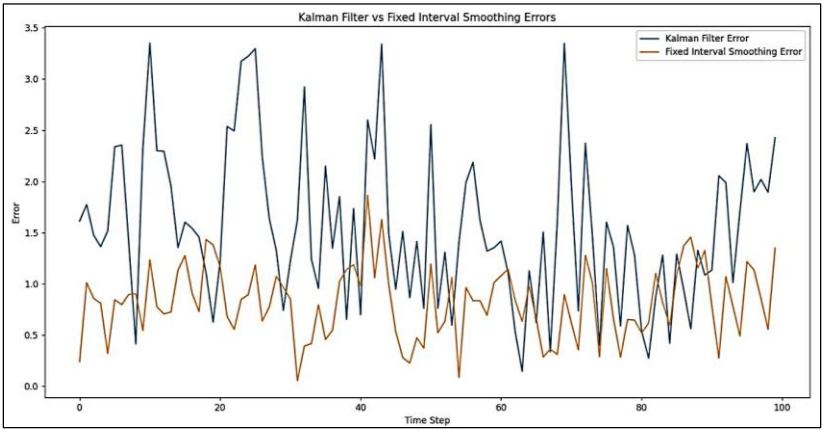

Fig 1: Comparison of Error between Kalman Filter and Fixed Interval Smoothing

Conclusion and Future Work

In summary, the application of Fixed Interval Smoothing to Kalman Filter estimates has been shown to markedly improve tracking accuracy [19]. The simulations indicate substantial reductions in both mean error and standard deviation, underscoring the effectiveness of FIS in providing more accurate and stable estimates. These improvements are achieved through the optimal utilization of future data, enhanced noise reduction, and increased estimation stability, making Fixed Interval Smoothing a superior choice for

tracking applications. The current study has established the effectiveness of Fixed Interval Smoothing in enhancing the accuracy of Kalman Filter estimates. Future research in the areas of adaptive smoothing intervals, nonlinear systems, real time implementation, robustness to outliers, multi-sensor fusion, and domain-specific applications holds the promise of further advancements. By addressing these challenges, we can continue to improve the performance and versatility of tracking systems, paving the way for their broader adoption in a variety of critical applications.

References

1. Kalman, R. E. (1960). A New Approach to Linear Filtering and Prediction Problems. Journal of Basic Engineering, 82(1), 35-45.
2. Rauch, H. E., Tung, F., & Striebel, C. T. (1965). Maximum likelihood estimates of linear dynamic systems. AIAA Journal, 3(8), 1445-1450.
3. Anderson, B. D. O., & Moore, J. B. (1979). Optimal Filtering. Prentice-Hall.
4. Simon, D. (2006). Optimal State Estimation: Kalman, H Infinity, and Nonlinear Approaches. Wiley Inter science.
5. Li, X. R., & Jilkov, V. P. (2003). Survey of maneuvering target tracking. Part I: Dynamic models. IEEE Transactions on Aerospace and Electronic Systems, 39(4), 1333-1364.
6. Sarkka, S. (2013). Bayesian Filtering and Smoothing. Cambridge University Press.
7. Li, X. R., & Jilkov, V. P. (2005). A survey of maneuvering target tracking: Approximation techniques for nonlinear filtering. IEEE Transactions on Aerospace and Electronic Systems, 41(2), 557-585.
8. Daum, F. (2005). Nonlinear filters: beyond the Kalman filter. IEEE Aerospace and Electronic Systems Magazine, 20(8), 57-69.
9. Elliott, R. J., Aggoun, L., & Moore, J. B. (2008). Hidden Markov Models: Estimation and Control. Springer.
10. Chen, Z., Chen, H., & Zhang, T. (2014). Robust target tracking based on multiple model estimation. Sensors, 14(3), 4461-4482.
11. Liu, J., He, H., & Zhong, M. (2015). Improved Kalman filtering with adaptive noise covariance for multi-sensor fusion. Sensors, 15(10), 27264-27285.

12. Farina, A., & Studer, F. A. (2016). A short course on automatic target recognition. IEEE Aerospace and Electronic Systems Magazine, 31(4), 40-57.

13. Bar-Shalom, Y., & Li, X. R. (2016). Estimation with Applications to Tracking and Navigation: Theory Algorithms and Software. John Wiley & Sons.

14. Koller, M., & Friedman, N. (2009). Probabilistic Graphical Models: Principles and Techniques. MIT Press.

15. Qi, H., Wang, L., & Yuan, Y. (2017). A robust Kalman filter with adaptive noise covariance for indoor localization. IEEE Sensors Journal, 17(20), 6863-6870.

16. Gustafsson, F., Hendeby, G., & Karlsson, R. (2016). Particle filters for positioning, navigation, and tracking. IEEE Transactions on Signal Processing, 64(17), 4313-4325.

17. Jiang, X., & Liu, H. (2018). An improved unscented Kalman filter for nonlinear system state estimation. Journal of Process Control, 64, 72-81.

18. Kok, M., & Schön, T. B. (2018). Maximum likelihood calibration of a magnetometer in combination with inertial sensors. Sensors, 18(4), 1038.

19. Bolic, M., Djuric, P. M., & Hong, S. (2019). Resampling algorithms for particle filters: A computational complexity perspective. EURASIP Journal on Advances in Signal Processing, 2019(1), 1-21.

Chapter - 27
A Review on Various High Gain Non-Isolated DC-DC Converters for Renewable Energy Interfaced DC Micro Grid Applications

Authors

Biswamoy Pal
JIS College of Engineering, Kalyani, Nadia, West Bengal, India

Jit Mondal
JIS College of Engineering, Kalyani, Nadia, West Bengal, India

Partha Das
JIS College of Engineering, Kalyani, Nadia, West Bengal, India

Sudip Das
JIS College of Engineering, Kalyani, Nadia, West Bengal, India

Basudeb Dey
JIS College of Engineering, Kalyani, Nadia, West Bengal, India

Milan Sasmal
JIS College of Engineering, Kalyani, Nadia, West Bengal, India

Abhishek Dhar
Swami Vivekananda University, Barrackpore, West Bengal, India

Chapter - 27

A Review on Various High Gain Non-Isolated DC-DC Converters for Renewable Energy Interfaced DC Micro Grid Applications

Biswamoy Pal, Jit Mondal, Partha Das, Sudip Das, Basudeb Dey, Milan Sasmal and Abhishek Dhar

Abstract

DC micro grids interfaced with Renewable energy sources are one of the simple, reliable and efficient solutions to meet present energy demand of society. This paper focuses on a comprehensive study of high gain DC-DC converters suitable for DC micro grid interfacing. This study provides a comparative study on recently reported topological structures of high gain converters in terms of voltage gain, device stress, and number of components used. The emphasis has been given on two broad categories of high gain DC-DC converters, namely, non-isolated DC-DC converters and non-isolated DC-DC converters with coupled inductors. This paper helps researchers to find the scope for further research in this area by providing a insight of the recently developed topologies.

Keywords: Non-isolated DC-DC converters, DC micro grid, coupled inductor

1. Introduction

The renewable energy resources are widely used since last few years as these are clean, inexhaustible, cost-effective solution of electricity. These energy sources are very good alternatives of fossil fuels for the electricity generation and meet exponentially increasing energy demand of the society globally. The dependence of electricity generation from conventional energy sources are gradually shifting to renewable energy sources is due to various factors like depletion of conventional energy sources, global warming due to greenhouse gases etc. However, the use of conventional energy sources cannot be completely replaced due to under developed infrastructural facility of renewable energy extraction. This encourages power electronic

researchers to find best possible solutions for renewable energy extraction and storage. Many power electronic researchers and engineers are focusing on developing the solutions to extract energy from different renewable energy sources, such as solar, wind, fuel cell etc. and fed to the micro grid. Due to various factors, the renewable energy sources produce electricity of low output voltage, which needs to be amplified before feeding to the utility grid. This necessitates the development of highly efficient high gain DC-DC converters as an intermediate between the low voltage DC bus and the grid. Many isolated and non-isolated high gain DC-DC converters have been developed and reported in past decade in different literatures [1-18]. Different isolated structures have been reported in [1-8], where the voltage gain can be enhanced by the use of suitable turn's ratio of the converters, whereas [9-18] shows different non isolated structures offer very high gain by connecting energy storing elements in a proper way.

2. High Gain Non-Isolated DC-DC Converters

This section shows a comparative study of different non isolated high gain DC-DC converter topologies suitable for renewable energy integration with DC micro grids. Table 1 shows a comparative study of non-isolated high gain converters in terms of voltage gain, device stress and number of components used. Fig 1-4 depicts voltage gain, normalized switch and diode voltage stress, number of components used respectively of the converters presented in [9-15]. Table 2 depicts a comparative study of another class of non-isolated converters employing coupled inductors. Fig 5-8 depicts voltage gain, normalized switch and diode voltage stress, number of components used respectively of the converters presented in [16-18].

Table 1: Comparative Study on Different High Gain Non-Isolated DC-DC Converters

Ref	Conv	Voltage Gain	Total Components				Voltage Stress on main switch	Voltage Stress on output Diode
			Sw	D	L	C		
[9]	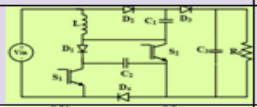	$\frac{3-2D}{1-2D}$	2	4	1	3	$\frac{1}{1-2D}V_o$	$\frac{1}{1-2D}V_o$
[10]	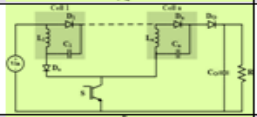	$\frac{2-D}{1-D}+2(n-1)$ (With, n =2) $=\frac{2-D}{1-D}+2$	1	n+2 =4	n =2	n+1 =3	$(\frac{2-D}{1-D}+2(n-1)-1)V_o$ $-(\frac{2-D}{1-D}+2)V_o$	$(\frac{2-D}{1-D}+2(n-1)-1)V_o$ $-(\frac{2-D}{1-D}+2)V_o$
[11]	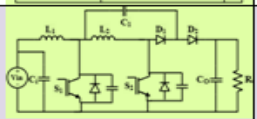	$\frac{2}{1-D}$	2	2	2	3	$\frac{1}{1-D}V_o$	$\frac{1}{1-D}V_o$
[12]	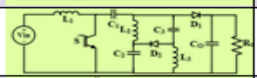	$\frac{2D}{1-D}$	1	2	3	3	$\frac{1}{1-D}V_o$	$\frac{1}{1-D}V_o$
[13]	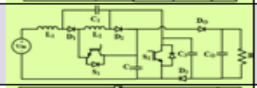	$\frac{2(1-D)}{1-3D+D^2}$	2	4	2	4	$\frac{D}{1-3D+D^2}V_o$	$\frac{1-D}{1-3D+D^2}V_o$
[14]	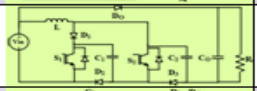	$\frac{3-2D}{1-2D}$	2	4	1	3	$\frac{1}{1-2D}V_o$	$\frac{2}{1-2D}V_o$
[15]	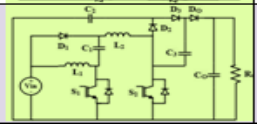	$\frac{4}{1-D}$	2	4	2	4	$\frac{2}{1-D}V_o$	$\frac{1}{1-D}V_o$

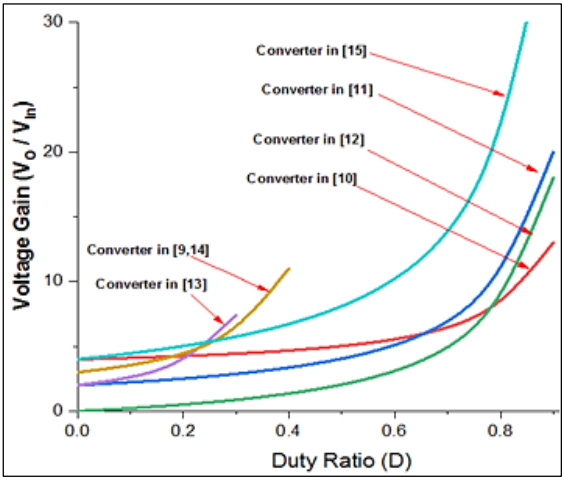

Fig 1: Voltage Gain at different Duty Ratio

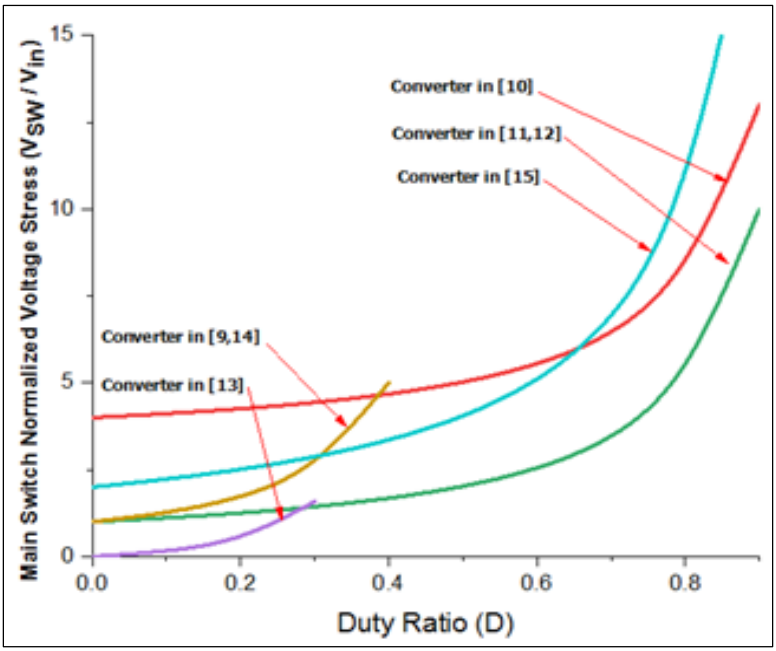

Fig 2: Normalized Switch Voltage Stress at different Duty Ratio

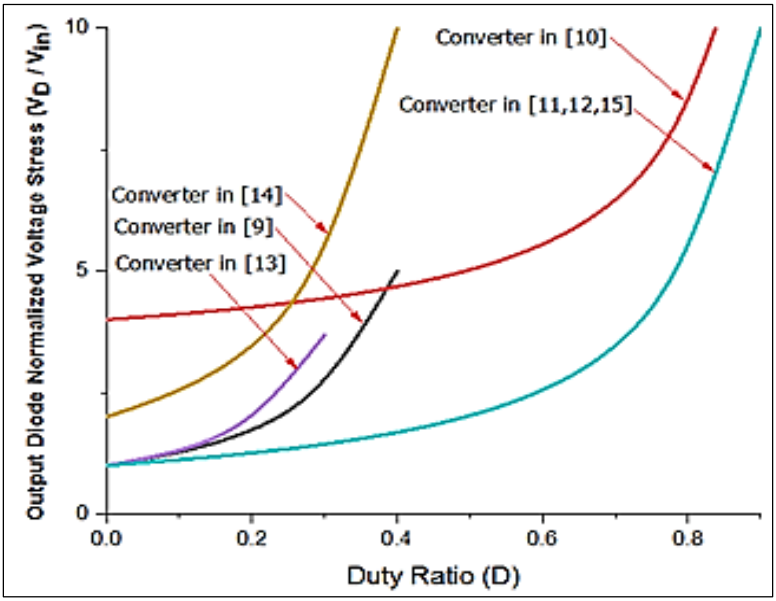

Fig 3: Normalized O/P Diode Voltage Stress at different Duty Ratio

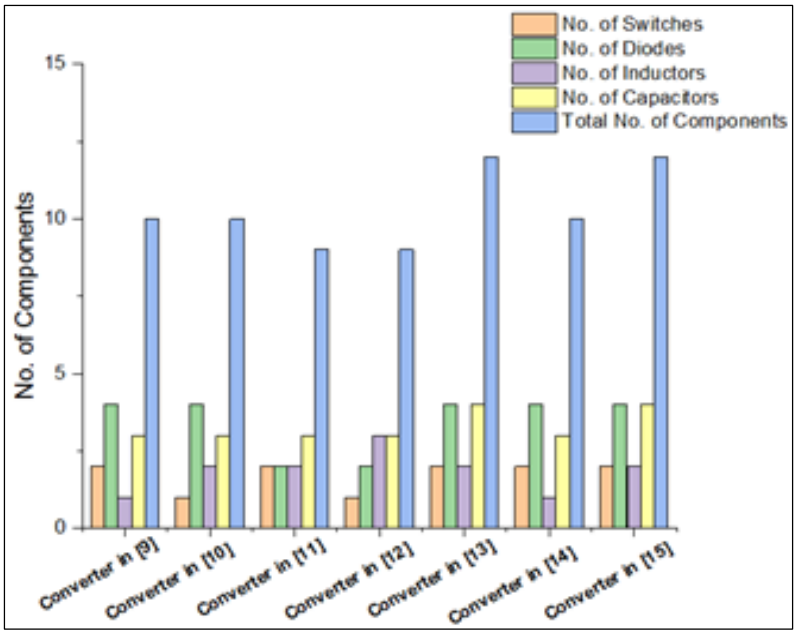

Table 2: Comparative Study on Different High Gain Non-Isolated DC-DC Converters with Coupled Inductors

Ref	Conv	Voltage Gain	Total Components				Voltage Stress on main switch	Voltage Stress on output Diode
			S w	D	L/ CL	C		
16	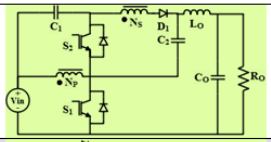	$\frac{2-D}{1-D}+k\frac{N_S}{N_P}$	2	1	1/ 1	3	$\frac{1}{1-D}V_{in}$	$\frac{1}{1-D}V_{in}$
17	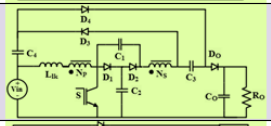	$\frac{3+\frac{N_S}{N_p}(1+D)}{1-2D}$	1	5	0/ 1	4	$\frac{1}{1-D}V_{in}$	$\frac{1+\frac{N_S}{N_P}}{1-D}V_{in}$
18	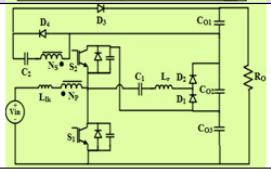	$\frac{\frac{N_S}{N_p}+2}{1-D}$	2	4	1/ 1	5	$\frac{1}{1-D}V_{in}$	$\frac{\frac{N_S}{N_p}}{1-D}V_{in}$

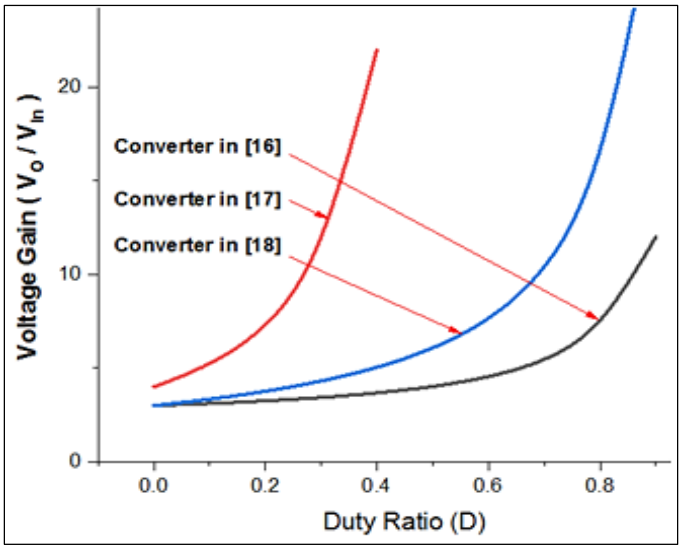

Fig 5: Voltage Gain at different Duty Ratio

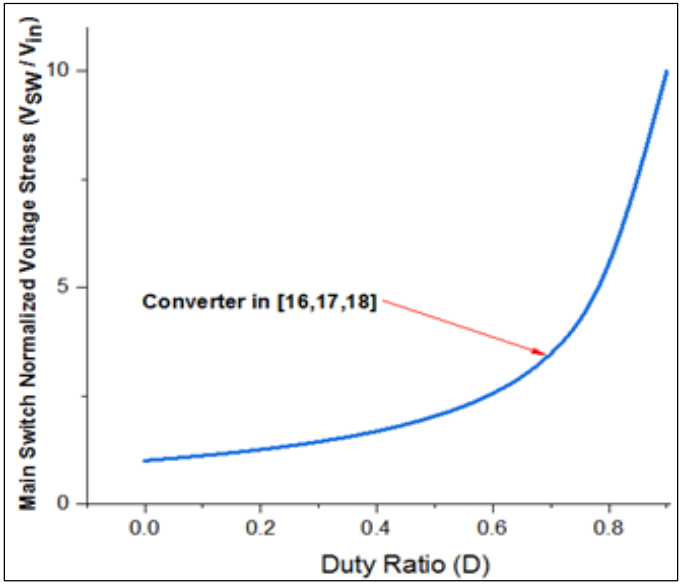

Fig 6: Normalized Switch Voltage Stress at different Duty Ratio

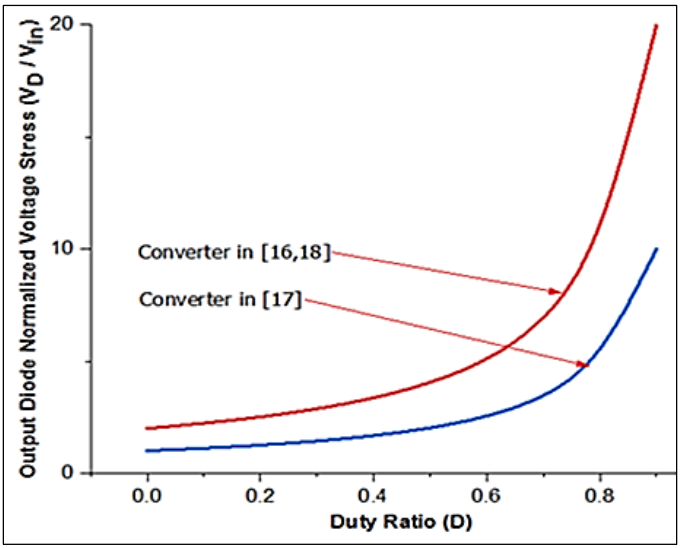

Fig 7: Normalized O/P Diode Voltage Stress at different Duty Ratio

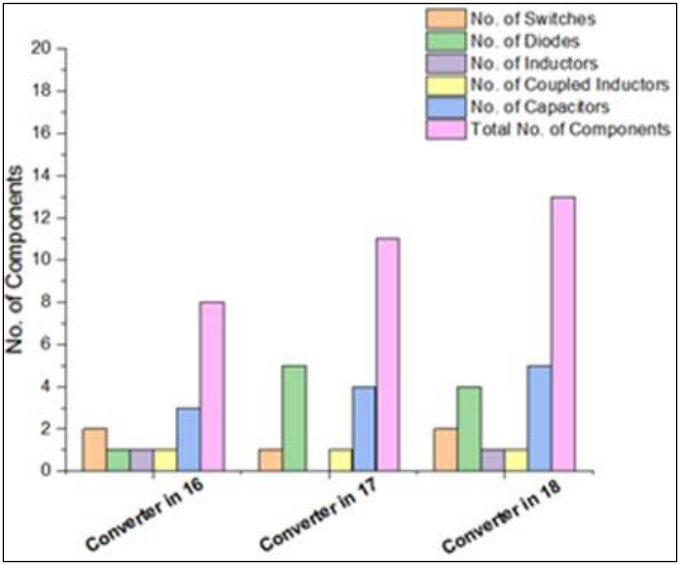

Fig 8: Number of Components

Conclusion

This paper presents a comprehensive review of different non isolated high gain DC-DC converters for the purpose of understanding about the

converters employed in renewable energy integration in DC micro grid applications. This study also reviews different topological configurations of high gain topologies and their comparative study in terms of voltage gain, device stress and total number of components used.

References

1. Y.-S. Shin, S.-S. Hong, D.-J. Kim, D.-S. Oh, and S.-K. Han, "A new mode changeable full bridge dc/dc converter for wide input voltage range," in Proc. 8th Int. Conf. Power Electron. -ECCE Asia, May 2011, pp. 2328–2335.
2. Gu, B., Dominic, J., Chen, B., Zhang, L., and Lai, J. S., "Hybrid transformer ZVS/ZCS DC–DC converter with optimized magnetics and improved power devices utilization for photovoltaic module applications", IEEE Trans. Power Electron., vol. 30, no. 4, pp. 2127-2136, 2015.
3. Tang, Y., Fu, D., Wang, T., and Xu, Z. "Hybrid switched-inductor converters for high step-up conversion," IEEE Trans. Ind. Electron., vol. 62, no. 3, pp. 1480-1490, 2015.
4. Rezaei, M. A., Lee, K. J., and Huang, A. Q., "A high efficiency flyback micro-inverter with a new adaptive snubber for photovoltaic applications", IEEE Trans. Power Electron., vol. 31, no. 1, pp. 318-327, 2016.
5. Zhang, F., and Yan, Y. "Novel forward-flyback hybrid bidirectional DC–DC converter", IEEE Trans Ind. Electron., vol. 56, no. 5, pp. 1578-1584, 2009.
6. B. Pal and S.S. Saha, "A Novel Soft Switched Single Switch Flyback Converter with Active Leakage Recovery Network", 2021 National Power Electronics Conference (NPEC), Bhubanneswar, India, 2021, pp 1-6.
7. B. Pal, S.S. Saha, P. Biswas, "Power Electronics-EV Battery Charging", Electric Vehicles: Modern Technologies and Trends, Springer, Singapore, pp 73-93, 2021.
8. Lee, J. H., Park, J. H., and Jeon, J. H., "Series connected forward–flyback converter for high step-up power conversion", IIEEE Trans. Power Electron., vol. 26, no. 12, pp. 3629-3641, 2011.
9. Mummadi Veerachary, "Two-switch High Gain Boost Converter", 2020 IEEE 17th India Council International Conference (INDICON, 2020).

10. Mansour, A.S., Zaky, M.S. A new extended single-switch high gain DC-DC boost converter for renewable energy applications. Sci Rep 13, 264 (2023).

11. A. D. Nguyen, J.-S. Jason Lai and H.-J. Chiu, "Analysis and Implementation of a New Non-isolated High-Voltage-Gain Boost Converter," 2019 IEEE Energy Conversion Congress and Exposition (ECCE), Baltimore, MD, USA, 2019, pp. 1251-1255.

12. Mohamad Reza Banaei, Hossein Ajdar Faeghi Bonab, “High-efficiency transformer less buck-boost DC-DC converter”, Int. J. Circ. Theor. Appl., vol 45, issue 8, pp 1129-1150, August, 2017.

13. X. Zhu, B. Zhang and K. Jin, "Hybrid Non isolated Active Quasi-Switched DC-DC Converter for High Step-up Voltage Conversion Applications," in IEEE Access, vol. 8, pp. 222584-222598, 2020.

14. M. -K. Nguyen, T. -D. Duong and Y. -C. Lim, "Switched-Capacitor-Based Dual-Switch High-Boost DC-DC Converter," in IEEE Transactions on Power Electronics, vol. 33, no. 5, pp. 4181-4189, May 2018.

15. S. Sadaf, N. Al-Emadi, P. K. Maroti and A. Iqbal, "A New High Gain Active Switched Network-Based Boost Converter for DC Microgrid Application," in IEEE Access, vol. 9, pp. 68253-68265, 2021.

16. K. I. Hwu and W. Z. Jiang, "Voltage Gain Enhancement for a Step-Up Converter Constructed by KY and Buck-Boost Converters," in IEEE Transactions on Industrial Electronics, vol. 61, no. 4, pp. 1758-1768, April 2014.

17. Mana Hoseinzadeh Lish, Reza Ebrahimi, Hossein Madadi Kojabadi, Josep M. Guerrero, Naser Nourani Esfetanaj, Liuchen Chang, “Novel high gain DC-DC converter based on coupled inductor and diode capacitor techniques with leakage inductance effects”, IET Power Electronics, vol 13, Issue 11, pp 2380-2389, August 2020.

18. Qiang Wang, Youzheng Wang, Xiaoqin Liu, Siwen Zhang & Guoxian Guo (2022) A soft-switching high gain DC-DC converter for renewable energy systems, International Journal of Electronics, 109:4, 553-575.

Chapter - 28
Sensor Protected Commercial Effective Home Automation System

Authors

Debodyuti Upadhaya
JIS College of Engineering, Kalyani, Nadia, West Bengal, India

Gargi Roy
JIS College of Engineering, Kalyani, Nadia, West Bengal, India

Partha Das
JIS College of Engineering, Kalyani, Nadia, West Bengal, India

Sudip Das
JIS College of Engineering, Kalyani, Nadia, West Bengal, India

Biswamoy Pal
JIS College of Engineering, Kalyani, Nadia, West Bengal, India

Basudeb Dey
JIS College of Engineering, Kalyani, Nadia, West Bengal, India

Milan Sasmal
JIS College of Engineering, Kalyani, Nadia, West Bengal, India

Chayan Chakraborty
JIS College of Engineering, Kalyani, Nadia, West Bengal, India

Subhajit Dey
JIS College of Engineering, Kalyani, Nadia, West Bengal, India

Chapter - 28

Sensor Protected Commercial Effective Home Automation System

Debodyuti Upadhaya, Gargi Roy, Partha Das, Sudip Das, Biswamoy Pal, Basudeb Dey, Milan Sasmal, Chayan Chakraborty and Subhajit Dey

Abstract

From last few decades quality of life has been increased and that too with an advancement of comfort. Technology using Home Automation is the reason behind it. Moreover, the population of elder people is growing rapidly and these days many of them have to stay alone, independently instead of old age homes. With increasing age, safety hazards increase in our life as we may forget various things that may question our protection. This paper can be again a solution for that. Nowadays most home automation systems consist of a smart phone and microcontroller. Different types of communication techniques can be adopted to control and monitor the home appliances. In today's busy world each family and individuals are looking for various automated help in their daily life; thus home automated system has a huge market commercially. Minimum wiring cost within an automated system is also desirable. This paper aims at minimizing the wastage of electricity when no one is inside the room. This paper describes an application of Arduino in home automation and networking environment. Moreover in this research work the application of different sensors have been used.

Keywords: Arduino based system, home automation, sensor, wireless network

Introduction

Now-a-days, a minimal human involvement is being asked in different technologies and the basic of this need is automation. The implementation of automation technologies, techniques and processes improve the efficiency, reliability, and/or speed of many tasks that were previously performed by humans, which in result reduce manual labor and the tiresome repetitive tasks.

Home automation system is growing rapidly; they are used to provide comfort, convenience, quality of life and security for residents. To provide comfort, safety, reliability to the older and disabled family members, home automation is one the best way to approach. Home automation system can be designed and developed by using a single controller which has the ability to control and monitor different interconnected appliances such as power plugs, lights, temperature, humidity sensors, smoke, gas and fire detectors and various security systems for emergency purpose. Improved application of Smartphone, tablet, desktop and laptop has made possible to monitor and control the automated system which is also one of the main advantages for this system. The rapid growth of wireless technologies influences us to use smart phones to remotely control and monitor the home appliances around the world [1-2].

During design of a home automation system, various factors should be maintained. Addition of a new device at any point of requirement should be done easily i.e. it should be enough scalable. Set up of the device, control and monitoring must be user friendly. Addition to that, a diagnostic part should be incorporated in the interface to track the problem, if any. But addition of all these should not affect the fastness of the system and to have the acceptance commercially it must be cost effective in order to justify its application in home automation [3].

An automated designed house will be more effective if it gets along with sensors like rain sensor to turn off windows during rain time and also gas sensors to protect from any leakage of gases.

In this paper a home automation system has been designed using Arduino to turn on and turn off of all electrical devices. Along with that different sensor to protect from rain water and gas sensors have been used.

System Analysis

Proposed System Feature

In this paper the automated designed model of home system can fulfill the various demand that will help in today's every day daily life. The convenience factor here is enormous. The peak advantage of our model are:

- A single point manual control for all devices can be done.
- In terms of technology of home management, connection and control of all home appliances through one interface is a massive step.

- Increased energy efficiency. Proper use of smart-home technology makes the space more energy efficient.
- Control of each single device is at the fingertips of user.
- Automatic detection of person inside the home.
- Advantages of automated window opening and closing are their low cost and high effectiveness.
- Rain and gas sensor has also applications and versatility in the buildings (especially like IT Companies).
- As the automation reduces human effort, it is most suitable for rural application.
- The gas sensor measures flammability of gases.

Model Architecture

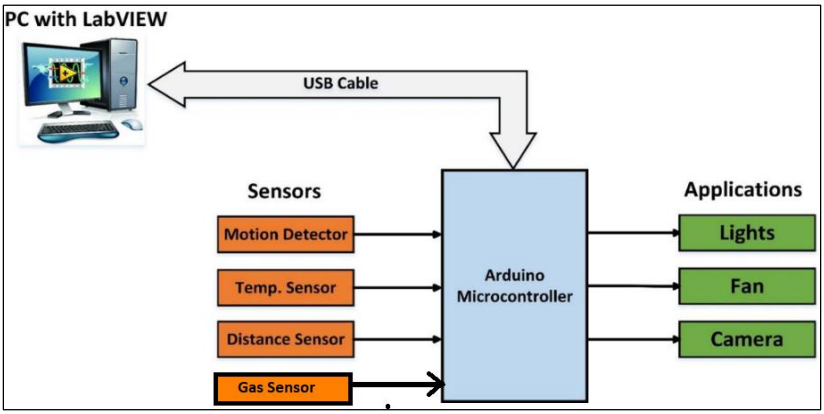

Fig 1: Home Automation System with different sensor Architecture

The main ingredient for any automated based operation is a server. The centralized sever acts as the heart of all the operation. A virtual connection between the server and the devices needs to be created. There are several ways to make a internet connection from which we have used point-to-point web socket. To provide optimum security to this whole system an unique login id and password is provided to each user at the time of installation. Any user can only go through the data of his/her devices connected with the main server with the help of the login id and all the above operation will not work and will show an error if the whole system is not online. Here the internet performs the lead role. This proposed model will provide easy control and ensure 100% security if the devices and the user are connected to the internet.

System Design and Implementation

To implements our home automation system we have design a experimental setup as shown in fig. [3].

The Flow Chart for the Whole Process is shown in Fig [2].

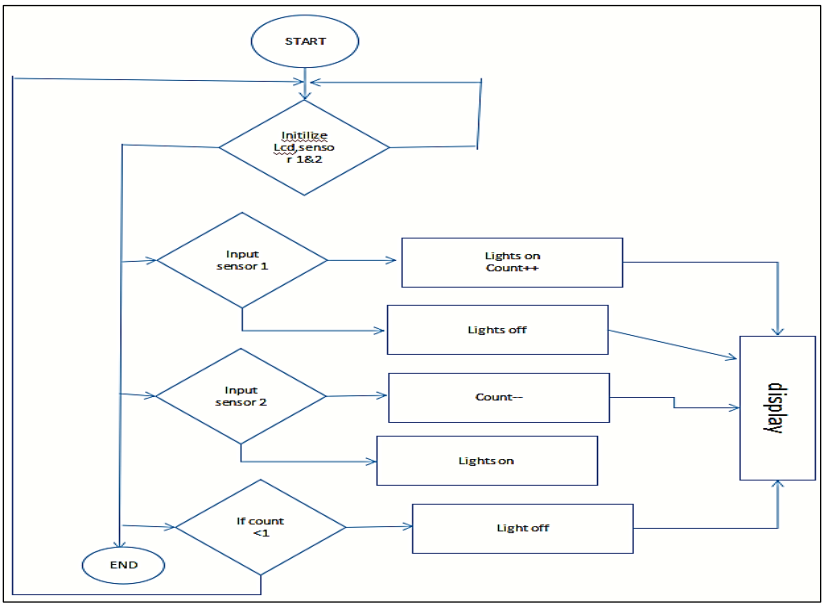

Fig 2

a. Component Required for the Hardware Set up

SL. No.	Component Required	No. of Units
1.	Arduino Uno	1 Nos
2.	16 * 2 LCD Display	1 Nos
3.	Infrared Sensor	2 Nos
4.	Gas sensor (catalytic bead (pellistor))	1 Nos
5.	Rain sensor (infrared radiation)	1 Nos
6.	1K Resistor	2 Nos
7.	Battery bank	1 Nos
8.	4 channel 12v relay	1 Nos
9.	Sliding window prototype	1 Nos
10.	Servo motors	1 Nos
11.	L298N	1 Nos
12.	PCB board	1 Nos

13.	Buzzer	1 Nos

Circuit Diagram

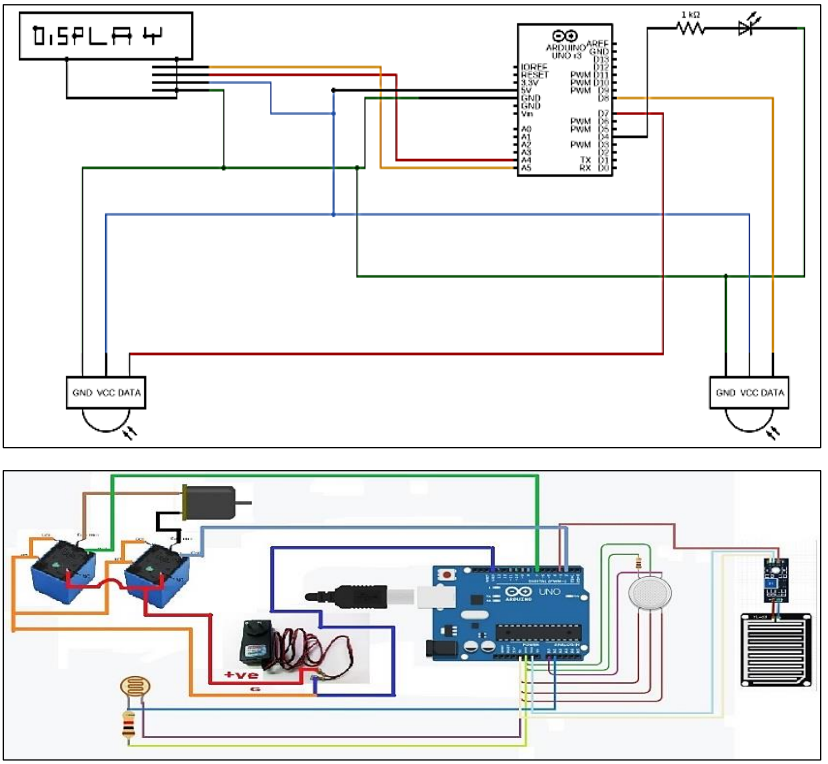

Fig 3

Arduino Code

```
#include <LiquidCrystal_I2C.h>
LiquidCrystal_I2C lcd(0x25,16,2);
#define led 4
int irPin1=7;
int irPin2=8;
int count=0;
boolean state1 = true;
boolean state2 = true;
```

```
boolean insideState = false;
boolean outsideIr=false;
boolean isPeopleExiting=false;
int i=1;
void setup() {
    lcd.init();
    lcd.backlight();
    lcd.setCursor(0,0);
    lcd.print("Person: 0");
    lcd.setCursor(0,1);
    lcd.print("Light: OFF");
pinMode(irPin1, INPUT);
pinMode(irPin2, INPUT);
pinMode(led,OUTPUT);
}
void loop() {
    if (!digitalRead(irPin1) && i==1 && state1){
        outsideIr=true;
        delay(100);
        i++;
        state1 = false;
    }
else if (!digitalRead(irPin2) && i==2 && state2){
    outsideIr=true;1
delay(100);
i = 1 ;
count++;
lcd.clear();
```

```
lcd.setCursor(0,0);
lcd.print("Person: ");
lcd.println(count);
state2 = false;
if(count > 0){
digitalWrite(led,HIGH);
lcd.setCursor(0,1);
lcd.print("Light: ON");
}
}
else if (!digitalRead(irPin2) && i==1 && state2){
outsideIr=true;
delay(100);
i = 2 ;
state2 = false;
}
else if (!digitalRead(irPin1) && i==2 && state1){
if(count > 0) {
outsideIr=true;
delay(100);
count--;
lcd.setCursor(0,0);
lcd.print("Person: ");
lcd.println(count);
i = 1;
state1 = false;
if(count <= 0){
digitalWrite(led,LOW);
```

```
lcd.setCursor(0,1);
lcd.print("Light: OFF");
}
}
}
    if (digitalRead(irPin1)){
state1 = true;
}
if (digitalRead(irPin2)){
state2 = true ;
}
}
```

Hardware Setup

Prototype model for the whole arrangement is shown below.

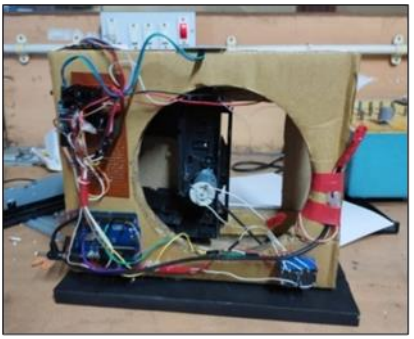

Conclusion

This paper is a simple step towards the innovation and to make our daily life hazard free. In this paper, a novel architecture for low cost and flexible home control and monitoring system using automated system is proposed and implemented. Also, the proposed architecture utilizes the application of different sensors for protection purpose.

Prospective future work includes:

- Use of any Android based Smart phone with built in support for Wi-Fi can be done to access and control the devices at home.
- Without availability of Wi-Fi, 3G or 4G mobile cellular networks also allow to access the system.
- A voice recognition module is required to use the Google speech recognition engine.

A hardware implementation of the system was carried out to verify the reliability of the system. The proposed system can be developed and fabricated as a commercial hardware package.

References

1. An Overview of Home Automation Systems Muhammad Asadullah, Ahsan Raza Department of Electrical Engineering National University of Computer and Emerging Sciences Peshawar, Pakistan P136384@nu.edu.pk, P136399@nu.edu.pk
2. R. S. Ransing and M. Rajput, "Smart home for elderly care, based on Wireless Sensor Network," Nascent Technologies in the Engineering Field (ICNTE), 2015 International Conference on, Navi Mumbai, 2015, pp. 1-5.
3. Bluetooth based home automation systemAuthor links open overlay panel N. Sriskanthan, F. Tan, A. Karande
4. Smart-Home Automation using IoT-based Sensing and Monitoring Platform Majid Al-Kuwari, Abdulrhman Ramadan, Yousef Ismael, Laith Al-Sughair, Adel Gastli, Senior Member, IEEE, Mohieddine Benammar, Senior Member, IEEE Electrical Engineering Department, College of Engineering, Qatar University, Doha-Qatar
5. Home Automation Using Internet of Thing, Shopan Dey Department of Electronics and Communication Engineering University of Engineering and Management Jaipur, Rajasthan, India shopan222@gmail.com Ayon Roy Department of Electronics and Communication Engineering University of Engineering and Management Jaipur, Rajasthan, India ayonroy56@gmail.com Sandip Das Department of Electronics and Communication Engineering University of Engineering and Management Jaipur, Rajasthan, India info.sandipec@gmail.com

6. Design of a Home Automation System Using Arduino Nathan David University of Nigeria nathan.david@unn.edu.ng Abafor Chima University of Nigeria chrischuks56@gmail.com Aronu Ugochukwu University of Nigeria ugochukwuaronu@gmail.com Edoga Obinna University of Nigeria butler4ril@gmail.com
7. Design and Implementation of a Reliable Wireless Real-Time Home Automation System Based on Arduino Uno Single-Board Microcontroller Bader M. O. Al-thobaiti, Iman I. M. Abosolaiman, Mahdi H. M. Alzahrani, Sami H. A. Almalki, Mohamed S. Soliman*.

Chapter - 29
Reforming Indian Power Sector: A Study on Journey towards Competitive Electricity Market

Authors

Parha Das
Assistant Professor, Department of Electrical Engineering,
JISCE, Kalyani, West Bengal, India

Rituparna Mitra
Associate Professor, Department of Electrical Engineering,
SVU, XXXXXXXXXXXXXXXXXXXXXX

Biswamoy Pal
Assistant Professor, Department of Electrical Engineering,
JISCE, Kalyani, West Bengal, India

Sudip Das
Assistant Professor, Department of Electrical Engineering,
JISCE, Kalyani, West Bengal, India

Basudeb Dey
Assistant Professor, Department of Electrical Engineering,
JISCE, Kalyani, West Bengal, India

Milan Sasmal
Assistant Professor, Department of Electrical Engineering,
JISCE, Kalyani, West Bengal, India

A. Halder
Student, Department of Electrical Engineering, JISCE,
Kalyani, West Bengal, India

SK MD Rakib
Student, Department of Electrical Engineering, JISCE,
Kalyani, West Bengal, India

A. Mondal
Student, Department of Electrical Engineering, JISCE,
Kalyani, West Bengal, India

I. Sahana
Student, Department of Electrical Engineering, JISCE,
Kalyani, West Bengal, India

Argha Ghosh
Student, Department of Electrical Engineering, JISCE,
Kalyani, West Bengal, India

Chapter - 29

Reforming Indian Power Sector: A Study on Journey towards Competitive Electricity Market

Parha Das, Rituparna Mitra, Biswamoy Pal, Sudip Das, Basudeb Dey, Milan Sasmal, A. Halder, SK MD Rakib, A. Mondal, I. Sahana and Argha Ghosh

Abstract

Throughout the world, Electricity markets are undergoing through major changes. Deregulation of Electricity market introducing an environment which is competitive in nature as, a number of suppliers are competing with each other to sell their electricity to potential customers. In pool electricity marker this Deregulation causes a drastic change in power system structure by including the private participants. The consumers also play an important role in this deregulated electricity market. The evolution of power sector from regulated to deregulated structure rises different issues which has positive and negative impact on power sector. This paper presents various key aspects of deregulation, current issues and prospect of deregulated power system in India. Different issues that led to transition from regulated electricity market to deregulate one, is discussed at the first phase of this paper. Further, this paper discusses the policy and regulatory changes undertaken when Deregulation of Electricity is taken into account in India. In the next part of the paper discussed the present scenario of Indian power sector with different parameters such as share of private sectors, Transmission and Distribution losses, plant load factor, and status of State Electricity boards.

Keywords: Deregulation, electrical market, electricity act, bulk power market, privatization, non-fossil fuel generation

Introduction

By changing the rules and regulations of any power system, Deregulation in electricity market can take place. Technological and economic reforms are essential in order to amplify the quality of any product, efficiency of a system and that can satisfy the consumer needs [1, 2]. In India Electricity consumers are basically served by mainly integrated

State Electricity Boards. A number of states adopted restructuring model by reforming the SEBs leading to division of generation, transmission and distribution segments. A State Electricity Regulatory Commissions (SERCs) is made to set the rules and regulations to make deregulation of electrical power in efficient manner. In regulated market there was no completion as it is controlled by a single entity and treated as service. Before deregulation electricity was treated as a service with no competition in the market. In other words the entire power industry was controlled by a single entity. This body was mostly the government organization. As there was no competition so there was no intension to improve the technical innovation and support. In the power industry the customer played roughly no role. From the customer side there was no other option for electricity so they have to take the SEBs service. In the year 2003, the Electricity Act 2003 breaks all the barriers of the monopolistic nature of all the SEBs as well as the retail supplier of electricity. This Act also recognizes trading as a separate activity. The provisions given in the act offer an environment of development of bulk power market in India. Open access of the distribution network by SEBs and Private entity allows consumers to choice their electricity needs and shop accordingly. The vision of deregulation of Indian power market was started with the implementation of this Electricity act 2003.

The first part of this paper discusses the factors that enhancing the Deregulation of Electricity market. The next part of this paper discusses Key features of Electricity Act 2003. This paper also discusses the regulatory initiatives, key policy and fundamental development of the bulk power market and also allows the customer to choose their electricity as per their need [5]. A brief study on present scenario of Central, state and private entity on power generation in India is discussed.

Deregulation Key Factors in India

The transformation from regulated electricity market to deregulate one comes into picture due to many reasons. The key reasons that led to deregulation are discussed below:

A. Technological Changes in Power Generation System

Previously for huge power generation by large generators was encouraged as they produced power more efficiently than the small generators [6]. But after that with the minimization of conventional energy which tends to introduction of renewable energy and change in technological facilities encouraged small generators as they could now produce electricity as efficiently as the larger generator.

B. Worldwide Trends towards Liberalization of Infrastructure Industries

From the point of view of liberalization and privatization of electric power industry it is a proven theory that it indeed improved the economic efficiency. In Deregulated market the private entities are assigned with particular assets to individuals who can utilize these assets most efficient manner. Survey results of consumer's shows that the state-owned electricity utilities will not run as efficiently as private entity can in terms of service and economy.

C. Minimization of Monopoly Entities

Deregulation of Electric power minimizes the investment scope of Capital invertors so as a result the era of monopoly utilities comes to an end. There are different reasons for which monopoly business policy comes to an end. Following are few of those reasons:

i) **Capital Investment at Fixed Return Rate [7]:** In regulated electricity market the large investors get their return at a fixed rate against their amount of investment in infrastructure. As the rate of return is fixed which doesn't depend upon the market demand of electricity the investors are not getting profit or interest, this leads to a wicked tendency to over invest in monopoly utilities.

ii) **Liabilities on Customers [5, 7]:** In Regulated electricity environment monopoly entity usually passes all investment risks to customers and they have to bear it for life long. So, as a result customers have to pay electricity bill at higher rate.

iii) **No other Option for Customers:** In regulated market customers have no choice regarding supply provider. SERCs basically control the power market. Customers have to take this only option for power supply in terms of service and technical facilities. But in Deregulated market customers have option to choose supply provider as per their needs.

iv) **Price Inequality [8, 9]:** In some countries due to different conditions like geographical location, facility available, constitutional rights, different monopoly utilities control different regions. As a result the price of electricity is different in different regions. So one customer has to pay more price than other region though they are feed from same supply provider. This led to a feeling of inequity among the customers.

D. Development in Computerized Control and Data commutation

Deregulation of electrical market need careful control and monitoring of full power system. Data monitoring, Date handling by different communications technologies including the internet makes those system reliable and economic with respect to regulated market [10, 11].

Indian Power Market at the Edge of Reform

From the view of economic growth and the expansion of the Indian economy Electricity plays an important role and which depend upon mainly on infrastructure of Transmission and Distribution Network and services. After independence, the government has taken the responsibility to develop the power sector. Power generation capacity in the country increased from 1362MW in 1947 to about 416.0 GW as of 31 March 2023. In the era of Monopoly utility (in regulated market) i.e.in 90's the peak demand shortages reached at its highest and the loss continuous till early 20's. As a result continued power shortages, poor quality and reliability of supply and increasing tariffs due to cross subsidy. A large number of industrial consumers start producing their own power. When SEBs is losing their prime customers, they start facing losses. To overcome losses they start to offer their power at a subsidies rate to the agricultural and domestic consumers. At this very low-rate monopolies are unable to provide proper service and reliability of power supply.

Table I: Year wise statistics of Tariff increased and Loss of SEBs

Parameter	Year 1996-1997	Year 2001-2002
Average tariff increased	50 paise/kWh	110 paise/kWh
Commercial losses of SEBs	Rs. 113.05 billion	Rs. 331.77 billion

The above table shows that due to monopoly of SEBs how rapidly the electricity tariff is creasing and loss of SEBs is also increasing, so this system needs an update. Here comes the concept of Deregulation of Electricity and it enhances by the implementation of Electricity Act 2003.

For reforming the Indian power sector is challenging for regulators and policy-makers. The early phase of the Indian power sector reform process was basically aimed to attract private investment, which will develop the better financial and operational performance of the sector.

The state Odisha first take initiative to reform their power sector and to that Orissa State Electricity Board is partly unbundled into three separate

entities: Orissa Power Generation Corporation OPGC, Orissa Hydro Power Corporation OHPC, and Grid Corporation of Orissa GRIDCO. OPGC sold their 49% stake to AES in the year 1998. In next phase, GRIDCO sold their T & D assets, properties part by part to BSES and AES as names NESCO, WESCO, SOUTHCO and CESCO in 1999.

After Odisha, Delhi Model, Andra Pradesh Model, Haryana Model comes into light by privatizing the power sector. Which led to the implementation of Electricity Act 2003.

Electricity Act 2003 that Led to Indian Power Sector Reform

The Electricity Act of 2003 is a significant piece of legislation in India that aimed to modernize and restructure the country's electricity sector. It replaced the earlier Electricity Supply Act of 1948 and introduced several key reforms to promote competition, efficiency, and sustainability in the electricity industry. Here are some of the main features and objectives of the Electricity Act of 2003:

Unbundling of the Electricity Industry: The act aimed to separate the generation, transmission, and distribution segments of the electricity industry to promote competition, enhance efficiency, and attract private investment.

Open Access: The act introduced the concept of open access, allowing consumers to choose their electricity supplier based on competitive market rates.

Power Trading: The act encouraged the development of power trading in India. It established a regulatory framework for power trading, enabling electricity to be bought and sold in a market-based manner.

Private Participation: The act aimed to attract private investment in the electricity sector by providing a favorable regulatory environment and mechanisms for independent power producers (IPPs) to enter the market.

Renewable Energy: The act recognized the importance of renewable energy sources and promoted their development. It included provisions for the purchase and generation of renewable energy, as well as the obligation for distribution licensees to procure a certain percentage of their power from renewable sources.

Regulatory Commissions: The act established regulatory commissions at both the central and state levels to oversee and regulate various aspects of the electricity industry, including tariffs, quality of service, and dispute resolution.

Consumer Rights: The act emphasized consumer rights and protection. It aimed to ensure that consumers received reliable and quality electricity supply, and it provided mechanisms for addressing consumer grievances.

Electricity Tariffs: The act introduced a transparent tariff-setting process, with the regulatory commissions responsible for determining tariffs in a manner that promotes efficiency, sustainability, and affordability.

Cross Subsidy Surcharge: The act introduced provisions for gradually reducing cross-subsidies between different consumer categories to create a more equitable tariff structure.

Post Reform Scenario of Indian Power Market

In previous section we have seen that Electricity Act 2003 has lots of features that can make Indian Power market regulated to Deregulated. But post reform scenario in India was not as expected. In some cases improvement can be seen in terms of generation, tariff whereas in some other cases the result was not as expected.

Table. 2 shows that in reformation process how the share of Central and state is decreasing day by day and by the participation of private utilities.

Table 2: Share (in %) of private, central and state sectors in generation

Year	Central	State	Private
1991-92	30	59	11
2016-2017	31.1	24.5	44.4
2022-2023	24	25.3	50.7

Power Plant Wise Growth

After reformation the Indian electricity entered into competitive power selling market. Different private entity offers different price rate for their electricity. This kind of market ensures more reliability and options for customers. Fig.1 shows that the year wise improvement in Installed capacity of the generators, per capita consumption. Due to decentralized scheme of power system rural electrification had been done widely in India so Transmission and Distribution networks increased in huge manner. Source of information Ministry of Power Website, Govt. of India [10, 11].

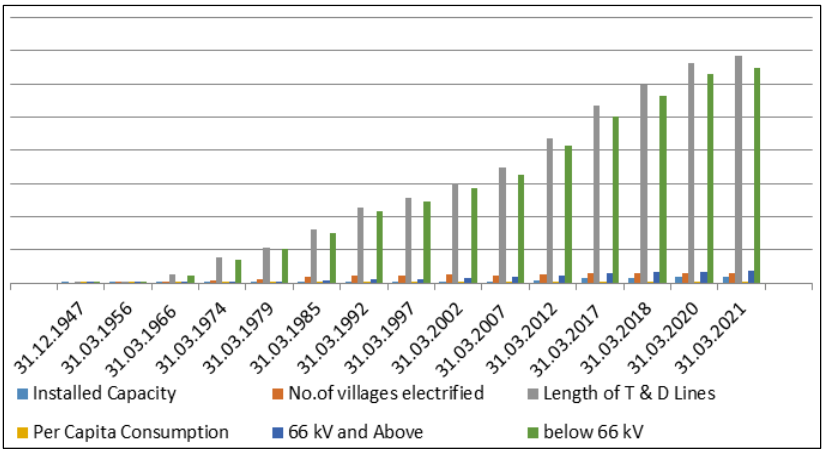

Fig 1: Plan wise growth in Generation, per capita consumption and T & D network

Increase in Non-Fossil Fuel Energy Market

The Deregulated market gave a gateway to the small and large Renewable energy companies. With the increase of power demand it is necessary to generate more power. Considering the climate change, non-fossil fuel power generation in one of the best option. So after power sector reform the growth rate of non-fossil fuel is significantly high. Fig. 2 shows the year wise growth of Solar, Wind, Biomass, Small hydro power generation in India. Source of information MNRE Website, Govt. of India [10, 11].

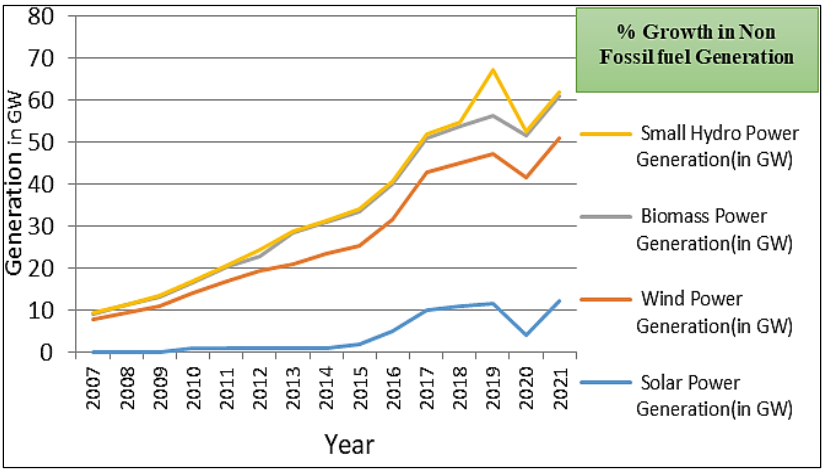

Fig 2: % Growth in Non-Fossil Fuel Generation

Transmission Line Installation Increased

With Deregulation of Power many private participant are now in the electricity market. In this competitive market Transmission and distribution network spread rapidly. Fig 3. Shows the year wise growth in Transmission line installation. Source of information Ministry of Power Website, Govt. of India [10, 11].

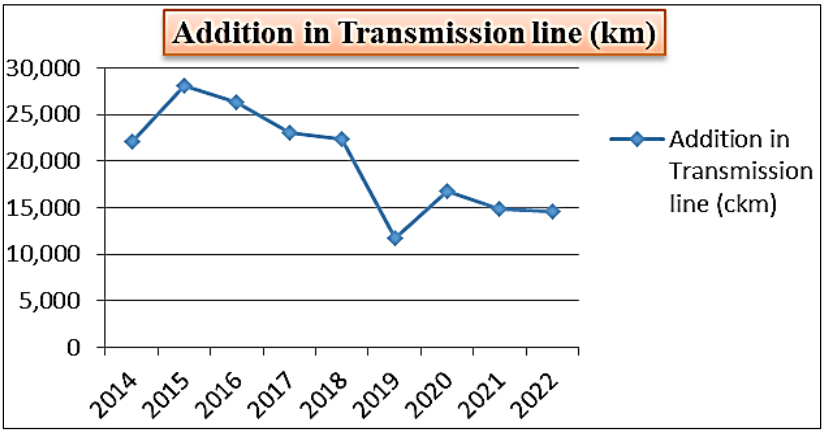

Fig 3: Addition in Transmission Line

Conclusion

With the unbundling of Indian Power market some new category of problems are coming out. Congestion in transmission line is one of them. As different service provider are connect to same T & D line so in this deregulated market Congestion management is an important issue. There are different methods to manage the congestions [12]. Apart from this, in T & D losses didn't shown significant improvement.

In this paper we have discussed pre and post reform scenario of deregulation of power sector. We have started our discussion with the necessity of Deregulation. Later on we discussed the key features that led to power sector reform. After that we discussed the situation of reforming India. The Average tariff increased, commercial losses of SEBs that accelerate the reforming process where the state or Odisha took the first step Delhi second and so on. Later on in this paper we discussed the key features of Electricity Act 2003 and post reforming scenario of India with some Statistics of Power Generation increased, non-fossil fuel power generation increased, T & D network installation increased i.e. the positive aspect of

Deregulation. In next step the negative aspect of Deregulation, Congestion Management Techniques can be understood that led to failure of power sector in various cases and eliminate those reasons.

References

1. Loi Lei Laai, Power System Restructuring and Deregulation, John Wiley & Sons, England, 2002.
2. Malik O. P., "Control Considerations in a Deregulated Electric Utility Environment", IEEE Canadian Review, fall 2000, pp. 9-11.
3. Yog Raj Sood, Narayana Prasad Padhy, H. O. Gupta, "Wheeling of Power under Deregulated Environment of Power System-A Bibliographical Survey", IEEE Transaction on Power Systems, paper no. 2001 TR 109.R1.
4. W. J. Lee and G. J. Nolan, "Power system deregulation and SMD: Status and future projections," IEEE Industry Applications Society, vol. 11, pp.
5. K. M. Jagtap and D. K. Khatod, "Loss allocation in radial distribution networks with different load models and distributed generations," IET
6. G. J. Miranda, "Be prepared! [power industry deregulation]," IEEE Industry Applications Society, vol. 9, pp. 12-20, Feb. 2003.
7. K.M. Jagtap and D. K. Khatod, "Loss allocation in distribution networks with distributed generations", IET Gene. Transm. Distrib, vol. 9, pp. 1628-1641, Oct. 2015.
8. J. M. Griffin and S. L. Puller, "Electricity Deregulation: Choices and Challenges," The Bush school, London, 2005.
9. K. M. Jagtap and D. K. Khatod, "Novel approach for loss allocation of distribution networks with DGs", Elect. Power Syst. Research, vol. 143, pp. 303-311, Feb. 2017.
10. https://powermin.gov.in/Government of India, Ministry of Power.
11. https://mnre.gov.in/Government of India, Ministry of Power.
12. Das P., Mitra R., Dey B., "A review on techniques of power Transmission Line congestion Management in Deregulated Electricity Market" Journal of Mines, Metals & Fules, Vol 71, 2023.

13. Anoop Singh “Towards a competitive market for Electricity and consumer choice in the Indian power sector”, Energy Policy, vol. 38, 4196-4208, May 2010.

Chapter - 30
A Low-Cost Human Independent Smart Irrigation System

Authors

Gargi Roy
JIS College of Engineering, Kalyani, Nadia, West Bengal, India

Debodyuti Upadhaya
JIS College of Engineering, Kalyani, Nadia, West Bengal, India

Partha Das
JIS College of Engineering, Kalyani, Nadia, West Bengal, India

Sudip Das
JIS College of Engineering, Kalyani, Nadia, West Bengal, India

Biswamoy Pal
JIS College of Engineering, Kalyani, Nadia, West Bengal, India

Basudeb Dey
JIS College of Engineering, Kalyani, Nadia, West Bengal, India

Milan Sasmal
JIS College of Engineering, Kalyani, Nadia, West Bengal, India

Indranil Halder
JIS College of Engineering, Kalyani, Nadia, West Bengal, India

Chapter - 30

A Low-Cost Human Independent Smart Irrigation System

Gargi Roy, Debodyuti Upadhaya, Partha Das, Sudip Das, Biswamoy Pal, Basudeb Dey, Milan Sasmal and Indranil Halder

Abstract

Agriculture is the foundation **o**f human demand is increasing day by day due to high population. Also, food items demand is also increasing. To meet the food demand, crop production efficiency should be increased under labor and water scarcity conditions. Mastery requires for time utilization of available manpower, water and fertilizer which can lead to cost optimization of annual crops- manufacturing. Fortunately, the various technologies and techniques are available today to achieve these goals for cost optimization and quality control. In this 21st century, automation is a crucial part of human life. Today in industry, different automation and control machines are used but they are high priced. The water requirements in the irrigation system are also very high. So, a smart irrigation system is required to save the water. This proposed work focuses on cost-effective automated smart irrigation system that allows water conservation and human effort with the desired quantity and quality of crop-production.

Keywords: Arduino, smart irrigation system, soil moisture sensor

Introduction

Literature Survey

Agriculture is one of the major occupations of numerous people in India. In our country 65% population is dependent on husbandry. Agriculture has a vital impact on Indian frugality. Due to huge population in India, day by day the changing demand of the consumers and need of food are adding which has created the extreme difficulties in the agrarian sector. Now a days, planter are facing huge problems in the husbandry field and the function of flushing field is getting grueling for the growers due to insufficiency in their work and neglectfulness because occasionally they switch on the motor and also forget to switch off which may the cause of destruction of water [1].

principally growers visit the agricultural field periodically to check the humidity balance in soil and as per the demand, they used pumps to fulfill the water demand. But it's time-consuming matter. Generally, growers perform their agrarian exertion but lately they need to carry on their agrarian work as well as other occupations [2]. Irrigation system is important trouble free for the growers after the appearance of robotization system. Proper scheduling of irrigation is critical for effective water operation in crop product, particularly under conditions of water failure. The goods of the applied quantum of irrigation water, irrigation frequency and water use are particularly important. To improve water effectiveness, there must be a proper irrigation scheduling strategy [3]. For advancement of the irrigation system, embedded system is used now a days. The irrigation process can be concentrated on controlling automatically using the device Raspberry Pi. Python programming is used for automation control. The system consists of a soil moisture sensor which can be suitable to observe the humidity position of the soil [4]. To ameliorate the application of water recourses in agricultural sector, now a day, IoT plays an important role. With the advancement of IoT and sensor technology, farmers and agriculturists effortlessly scrutinize the soil conditions and trace the crop health [5]. LoRa technology is used for smart irrigation system. It is able of linking between irrigation mechanism and operations through Lora WAN [6]. In [7], the irrigation system is grounded on two distinct fields of studies by a combination approach method: Irrigation with penman model of evapotranspiration and an Arduino as the most habituated microcontroller in modern electronics implementation with a productive PID as a controlling algorithm. S. Muhammad Umair *et al* implemented a simple technique too irrigation control system using ANN for effective irrigation scheduling in [8] with the evolution of technology in water saving irrigation and automation, automatic irrigation is going to be more popular in the farms. A GSM based automatic irrigation water control is proposed in [9].

Component Details

Table 1: Component Details

Serial No.	Component name	Specification
1.	Relay module	Supply voltage 5V, Max. current-10A
2.	Arduino Uno R3 (microcontroller)	Input voltage -7-12V, DC Current per I/O Pin-20mA
3.	DHT 11 sensor	Operating Voltage: 3.5V to 5.5V, Operating current: 0.3mA (measuring)

4.	Soil moisture sensor	Working temperature-10-30 °C
5.	Water pump	Operating voltage:12 V DC
6.	Solar cell	Maximum power: 10W; Open circuit voltage: 22V

Here, 5V Relay module, Arduino Uno R3 (microcontroller), DHT 11 sensor, Soil moisture sensor and 12 v DC water pump are used.

Relay Module: Relay is one kind of electro-mechanical element that functions as a switch. The relay coil is vitalized by DC so that contactswitches can be opened or closed.

Fig 1: Relay module

A single channel 5V relay module generally includes a coil and two contacts like typically open (NO) and typically closed (NC) The pin configuration of the 5V relay is shown below. This relay includes 5-pins where each pin and its functionality areshown below-

- **Pin1 (End 1):** It is used to start the relay; generally this pin one end is connected to 5Voltsandanother end is connected to the ground.
- **Pin 2 (End 2):** This pin is used to turn on the Relay.
- **Pin 3 (Common (COM)):** This pin is connected to the main terminal of the Load to make it functional.
- **Pin 5 (Normally Open (NO)):** If the second terminal of the load is integrated to the NO pin, thenthe load will be deactivated before the switch.

Arduino UNO R3: Arduino Uno R3 is one kind of ATmega328P based microcontroller board. It incorporates the whole thing necessary to support the microcontroller. With the help of a USB cable, it is attached to a PC and for turning it on; the supply is given by using the AC-DC adapter or a battery.

Fig 2: Arduino UNO R3

DHT11: DHT11 Temperature & Humidity Sensor involved with computed digital signal output. Excellent credibility and constancy can be seen in the DHT11 Temperature & Humidity Sensor which is made off absolute digital-signal-accession method and temperature & humidity sensing technology. This sensor consists of a resistive-type humidity measurement component and an NTC temperature measurement component, and connects to a super charged 8-bit microcontroller. It has quick response, extreme reliability, and high accuracy and also it is lucrative.

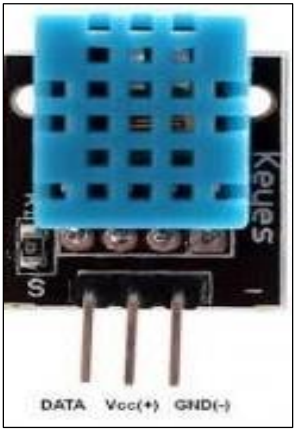

Fig 3: DHT11

Soil Moisture Sensor: To detect the soil moisture data, it is used in the agricultural sector. By using this soil moisture sensor, the environmental conditions and humidity can be traced easily. In the proposed system, ARDUINO Microcontroller is used to get the soil moisture readings and it automatically switch on the sprinklers if moisture level is low or not up to the mark. Automatically it will respond in the adverse conditions.

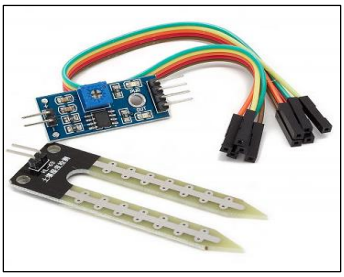

Fig 4: Soil Moisture Sensor

12V DC Water Pump: A pump is a mechanical device that is used to pick up water from low-pressure level to high-pressure level. Basically, the pump changes the energy flow from mechanical to the fluid. This can be used in process operations which needs a high hydraulic force.

Fig 5: 12V DC Water pump

Solar Cell: It converts sunlight directly into electricity. When the sunlight hits a solar cell, electrons in the silicon are emitted. After that "holes" are formed. Actually, holes are the vacant places left behind by the break free electrons. During this situation, the electrons will be moved by the field to the n-type layer and holes to the p-type layer. The electrons will proceed from the n-type layer to the p-type layer and will cross the depletion zone and then return to n-type layer with generating a current flow.

Fig 6: Solar cell

Software Implementation

Arduino Integrated Development Environment (IDE) is used to write the program. Arduino IDE is a cross-platform operation (for Windows, macOS, Linux) used to write and upload programs to Arduino compatible boards and development boards like Arduino Uno R3. It is obtained using C and C++.

Block Diagram

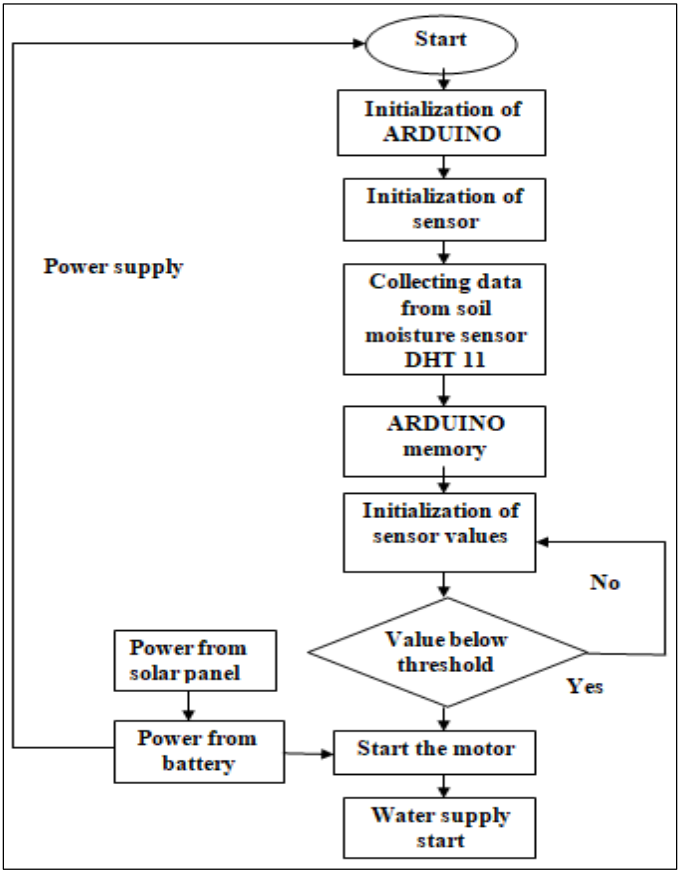

Fig 7: Flowchart of the proposed system

Working principle

In the proposed system, two modules are present.

They are-

i) Irrigation module.

ii) Solar pumping module.

In the solar pumping module, a solar panel is required.

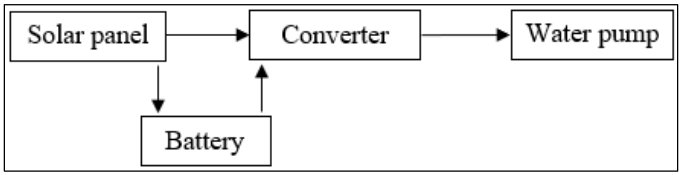

Fig 8: Block diagram of solar pumping module [10]

Then the battery is charged by using the solar panel with its control circuit. The converter will send the power to water pump with the help of converter. Then the water is pumped into an storage tank for keeping water momentarily before releasing the water into the field [7].

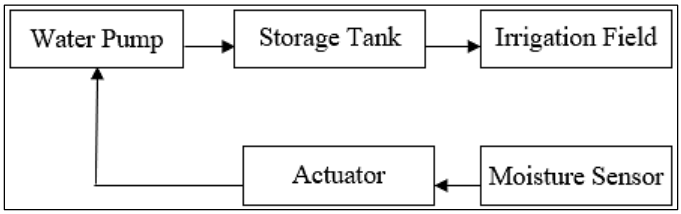

Fig 9: Block diagram of automatic irrigation module [10]

In automatic irrigation module, the soil moisture sensor is kept in the crop cultivation field. The moisture content is transformed into the equivalent voltage by the soil temperature sensor. The equivalent voltage is given to a sensing circuit. Farmers can balance the reference voltage to set moisture levels for different crops. To initialize the work of soil moisture sensor, ARDUINO programming is required. Soil moisture sensor then collects the data from soil and forwarded to ARDUINO memory. After that sensor values are initialized. If the values are within threshold value, then the motor will be started and the water supply to the irrigation field is also started. If it will not obey the threshold value, again sensor value initialization will be started.

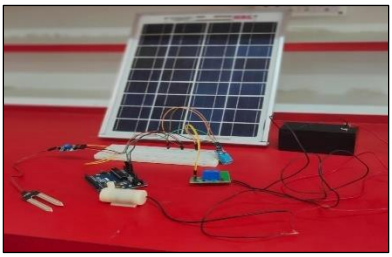

Fig 10: Circuit connection

Advantages

This system is very useful to improve the agriculture. It reduces the manpower too. This system provides a complete water planning. By monitoring soil moisture and temperature, this system can control the amount of water when it is needed based on types of plants. It is cost effective and after using this, agricultural production level will be increasing. Many features of the system can be changed through software as per the plant need.

Conclusion

The use of drip irrigation has shown that water, electricity and manpower can be greatly reduced. However, due to the manual labor involved in actual farms, drip irrigation is used only by a few farmers. Use drip irrigation system to increase their productivity at low cost. There are experimental setups. It has been proved that the proposed system can save water, electricity and manpower to a great extent. One time cost Setup is affordable and easy to maintain. More sensors can be added to the system to make it more automated Irrigation and fertilization based on farm moisture and temperature levels.

References

1. Tyagi, Apurva, Nina Gupta, J. P. Navani, Mr Raghvendra Tiwari, and Mrs Anamika Gupta. "Smart irrigation system." International Journal for Innovative Research in Science & Technology 3, no. 10 (2017).
2. Sahu, Chandan Kumar, and Pramitee Behera. "A low-cost smart irrigation control system." In 2015 2nd International conference on electronics and communication systems (ICECS), pp. 1146-1152. IEEE, 2015.

3. Darshna, S., T. Sangavi, Sheena Mohan, A. Soundharya, and Sukanya Desikan. "Smart irrigation system". IOSR Journal of Electronics and Communication Engineering (IOSR-JECE) 10, no. 3 (2015): 32-36.

4. Namala, K.K., AV, K.K.P., Math, A., Kumari, A. and Kulkarni, S., 2016, December. Smart irrigation with embedded system. In 2016 IEEE Bombay section symposium (IBSS) (pp. 1-5). IEEE.

5. Ragab, Mohammed Ali, Momen M. Badreldeen, Abdelrahman Sedhom, and Wael M. Mamdouh. "IOT based smart irrigation system". International Journal of Industry and Sustainable Development 3, no. 1 (2022): 76-86.

6. Zhao, Wenju, Shengwei Lin, Jiwen Han, Rongtao Xu, and Lu Hou. "Design and implementation of smart irrigation system based on LoRa". In 2017 IEEE Globecom Workshops (GC Wkshps), pp. 1-6. IEEE, 2017.

7. Sheikh, S.S., Javed, A., Anas, M. and Ahmed, F., 2018, September. Solar based smart irrigation system using PID controller. In IOP Conference Series: Materials Science and Engineering (Vol. 414, p. 012040). IOP Publishing.

8. Umair, S.M. and Usman, R., 2010. Automation of irrigation system using ANN based controller. International Journal of Electrical & Computer Sciences IJECS-IJENS, 10(02), pp.41-47.

9. Uddin, J., Reza, S.T., Newaz, Q., Uddin, J., Islam, T. and Kim, J.M., 2012, December. Automated irrigation system using solar power. In 2012 7th International Conference on Electrical and Computer Engineering (pp. 228-231). IEEE.

10. Harishankar, S., Kumar, R.S., Sudharsan, K.P., Vignesh, U. and Viveknath, T., 2014. Solar powered smart irrigation system. Advance in electronic and electric engineering, 4(4), pp.341-346.

Chapter - 31
Design and Development of Solar Electric Vehicles Charge Monitoring System using IoT

Authors

Sudip Das
Assistant Professor, EE, JIS College of Engineering, Kalyani, West Bengal, India

Pritam Kumar Gayen
Assistant Professor, EE, KGEC, Kalyani, West Bengal, India

Milan Sasmal
Assistant Professor, EE, KGEC, Kalyani, West Bengal, India

Basudeb Dey
Assistant Professor, EE, KGEC, Kalyani, West Bengal, India

Aditya Pandey
B.Tech. Scholar, EE, JIS College of Engineering, Kalyani, West Bengal, India

Bikramjit Roy
B.Tech. Scholar, EE, JIS College of Engineering, Kalyani, West Bengal, India

Sayonavo Neogi
B.Tech. Scholar, EE, JIS College of Engineering, Kalyani, West Bengal, India

Chayan Chakraborty
B.Tech. Scholar, EE, JIS College of Engineering, Kalyani, West Bengal, India

Partha Das
Assistant Professor, EE, JIS College of Engineering, Kalyani, West Bengal, India

Abhishek Dhar
Assistant Professor, EE, Swami Vivekananda University, Kolkata, West Bengal, India

Biswamoy Pal
Assistant Professor, EE, JIS College of Engineering, Kalyani, West Bengal, India

Debodyuti Upadhaya
Assistant Professor, EE, JIS College of Engineering, Kalyani, West Bengal, India

Gargi Roy
Assistant Professor, EE, JIS College of Engineering, Kalyani, West Bengal, India

Chapter - 31

Design and Development of Solar Electric Vehicles Charge Monitoring System using IoT

Sudip Das, Pritam Kumar Gayen, Milan Sasmal, Basudeb Dey, Aditya Pandey, Bikramjit Roy, Sayonavo Neogi, Chayan Chakraborty, Partha Das, Abhishek Dhar, Biswamoy Pal, Debodyuti Upadhaya and Gargi Roy

Abstract

Over the past few years, the increasing use of electric vehicles (EVs) due to rising CO_2 emissions, depletion of fossil fuels, and incentives for renewable energy sources. To facilitate the transition to EVs, the growth of charging stations is crucial. Improvements in EV batteries and battery management are also linked to user experiences and governmental policies. The study focuses on a solar-powered smart EV charger that uses IoT technology to monitor the charging and discharging of batteries, prolong their lifespan, and reduce the total expense of EVs. The system comprises a solar panel, battery, and microcontroller that communicate with a smartphone app or web server. The system is useful for remote areas, camping, emergency situations, and environmental monitoring. The system can be customized to different user needs and preferences. The study provides insights into the development of sustainable EV charging solutions.

Keywords: Solar power charger, monitoring system, lithium-ion battery, battery life, electric vehicle

Introduction

Solar energy is a clean, sustainable source of energy that may be used in a variety of ways. However, solar energy is intermittent and depends on the weather and the time of the day. Therefore, it is important to have a system that can store and manage the excess electricity generated by solar panels, and also monitor the status and performance of the solar system. A solar-powered charger and monitoring system is a device that can address these challenges and provide a convenient and efficient way of using solar energy. A solar panel, a battery, and a microcontroller are the three essential parts of

a solar-powered charging and monitoring system. The solar panel transforms solar energy into direct current (DC) electricity that may be utilised to power various devices, including the battery. The battery stores the electricity for later use or backup. The microcontroller is the brain of the system that controls the charging process and collects data from the solar panel and the battery. The microcontroller can also communicate with a smartphone app or a web server via Bluetooth or Wi-Fi to display the data and allow the user to control the system remotely. The system can also enable the user to monitor the solar panel output, battery level, temperature, humidity, or other parameters in real-time or over time. The system can also alert the user of any faults or anomalies in the solar system or the battery. Electric vehicles (EVs) provide several benefits over conventional cars, including reduced emissions, cheaper running costs, and improved performance as they grow in popularity and use. However, the accessibility and availability of charging stations is one of the major issues with EVs. EVs need to be plugged into a power source to recharge their batteries, which can limit their range and convenience. Moreover, the electricity used to charge EVs may come from fossil fuels or other non-renewable sources, which can negate the environmental benefits of EVs. Therefore, it is desirable to have a system that can charge EVs using renewable and clean energy sources, such as solar power. The solar powered charger and monitoring system for EVs is a novel and innovative device that can enhance the sustainability and convenience of EVs. The system can offer many benefits, such as cost savings, energy independence, environmental protection, convenience, and safety. The system can also be customized and adapted to the different needs and preferences of the user.

Literature Review

For high-power and high-energy lithium-ion batteries, nitrogen or boron-doped graphene can be employed as a promising anode material. There is a lot of reversible capacity in the doped graphene. It has a unique structure and morphology of the doped graphene, along with the heteroatomic defects, contributing to its superior performance compared to pristine graphene and other carbonaceous materials [1]. In a recent research, several cathode catalysts' effects on rechargeable lithium-air batteries with aprotic organic electrolytes' charge and discharge voltages were investigated. The researchers found that the choice of cathode catalyst not only affects the current-dependent charge/discharge potentials but also determines the type of discharge product generated-either Li_2O_2 or Li_2O. The study found that

Pt/C had the highest charging activity, with the lowest charging voltage reported thus far. On the other hand, Au/C had the highest discharge activity [2]. The sheer volume of waste generated by the growing EV market is a significant challenge. The supply of minerals needed for these batteries is limited, and ethical concerns exist over cobalt reserves. The physical configurations and chemistry of batteries pose a challenge for recycling, making automation difficult. The geographical concentration of key materials, such as cobalt, presents ethical concerns related to child labor and political instability. Collaboration across industries and innovative solutions are needed to promote a more sustainable and efficient system [3]. To overcome the limited battery life challenge of Li-Ion batteries, the battery ageing mechanism and degradation model at the cell level should be studied to understand the impact of key parameters like energy density and power density on battery life and other important characteristic parameters [4]. A computationally feasible model predictive control (MPC) optimization with binary switching can be used to schedule optimal loads by imposing restrictions on permitted load switching to mitigate the combinatorial problem, which can be helpful in dealing with the challenges of integrating renewable energy into smart grids to build a sustainable electric power system, focusing on the issue of power variability and intermittency in standalone or island-mode applications [5]. Green logistics might examine the usage of battery electric vehicles (BEVs) to lessen the environmental effect of product distribution. Research conducted on this topic discusses the challenges of integrating BEVs into distribution systems and highlights the need for battery behavior modeling to account for battery degradation and instantaneous charging and discharging behavior in transportation planning with BEV [6]. Research was done on the Sony US-18650 lithium-ion battery's specific heat capacity, thermal conductivity, and stacked layers of components, where the researchers found that the heat capacity and thermal conductivity of batteries increased with open-circuit voltage due to the effects of lithiation and De lithiation on electron carrier density. The inclusion of electrolytes improved the thermal conductivity of the stacked layers and reduced the need for OCV [7]. A paper on the study of Li-Ion batteries examines the shuttle phenomenon in Li/S rechargeable batteries and provides a quantitative analysis of its impact on battery performance. The authors present experimental data and shuttle constant values for three electrolytes and discuss the impact of self-heating and lithium surface activity on the shuttle constant. They also present experimental data and shuttle constant values for three electrolytes, which can help researchers

design better Li/S batteries [8]. The type of test cycle used is crucial when measuring battery deterioration. Comparing frequent cycling encountered when driving to using a PHEV battery for V2G energy, the capacity loss per unit of energy handled is reduced by around half. To guarantee effective performance and a long lifespan, it's critical to maintain a safe temperature range and adhere to the manufacturer's recommendations for charging and discharging rates [9]. Battery performance is measured by two parameters: State-of-Charge (SoC) and State-of-Health (SoHs), which determine the amount of charge and rated capacity loss of the battery, respectively. These parameters are difficult to determine through direct measurement, but they can be estimated using the Open-circuit-voltage (OCV) and internal resistance of the battery [10]. Another research on lithium-ion batteries looked into how Sony US 18650 Li-ion batteries' capacity degraded as they were cycled at various discharge rates and environmental conditions. After 300 cycles, the capacity losses were 13.2% and 16.9% at 2C and 3C discharge rates, respectively, while only 9.5% of capacity was lost at a 1C discharge rate. Additionally, the cell cycle at a high discharge rate (3C) demonstrated the biggest rise in internal resistance, which revealed a relative increase of 27.7% in comparison to the resistance of fresh cells. The rate capability losses were found to be proportional to the increase in discharge rates [11]. Lithium-ion batteries used in automotive applications have three primary parameters determining their performance: capacity, internal resistance, and self-discharge. While capacity determines a battery’s specific energy, internal resistance limits its specific power. Heat generation in batteries can be caused by several factors, including overpotential resistance, entropy change, and side reactions [12]. There is a possibility of using photovoltaic (PV) panels to charge electric vehicles (EVs) in workplaces in the Netherlands. The study studies the seasonal and daily fluctuation in solar insolation to predict energy availability for EV charging and the necessity for grid connection. The study analyses data from the Dutch Meteorological Institute to calculate the best orientation of PV panels for optimum energy production. For a 25% reduction in grid dependence, the ideal storage size is identified [13]. An IoT (Internet of Things) device can be used to monitor solar power availability, and an MPPT (Maximum Power Point Tracking) controller can be used to track the solar power's maximum output. To get an alarm message when a system power reduction occurs, a GSM modem can be used [14]. In this way, with the help of these modules, solar power can be monitored and used in an efficient way [15]. Electric vehicles (EVs) and plug-in hybrid electric vehicles (PHEVs) are emerging as attractive alternatives to

traditional internal combustion engine vehicles (ICEVs). However, the lack of charging infrastructure remains a major obstacle to the widespread adoption of EVs [16]. An intelligent energy management system for a solar-powered EV charging station with energy storage has been investigated and demonstrated by the University of California-Davis West Village. It entails anticipating solar PV electrical energy and EV charging needs in order to optimize energy management [17]. The growth of electric vehicles in the market has the potential to cause unexpected peak power demand and power quality problems. An energy management strategy can be developed which will help in implementing the vehicle-to-grid (V2G) to improve the grid's stability during peak load and allow for effective self-consumption of HPV systems. The system consists of a common dc bus shared by HPV, the grid, and the EVB converters. Both simulation and experimental results demonstrate that the proposed approach can effectively reduce the impacts of high EV and HPV penetration on power distribution grids [18]. A grid-connected solar-powered charging station can be designed to charge the EVs, the charging system would consist of solar panels, DC to DC converters, MPPT controller, DC to AC inverter, etc. This type of charging system can produce enough energy to charge EVs on a normal sunny day and can also be used to balance load demands on a rainy day [19].

Methodology

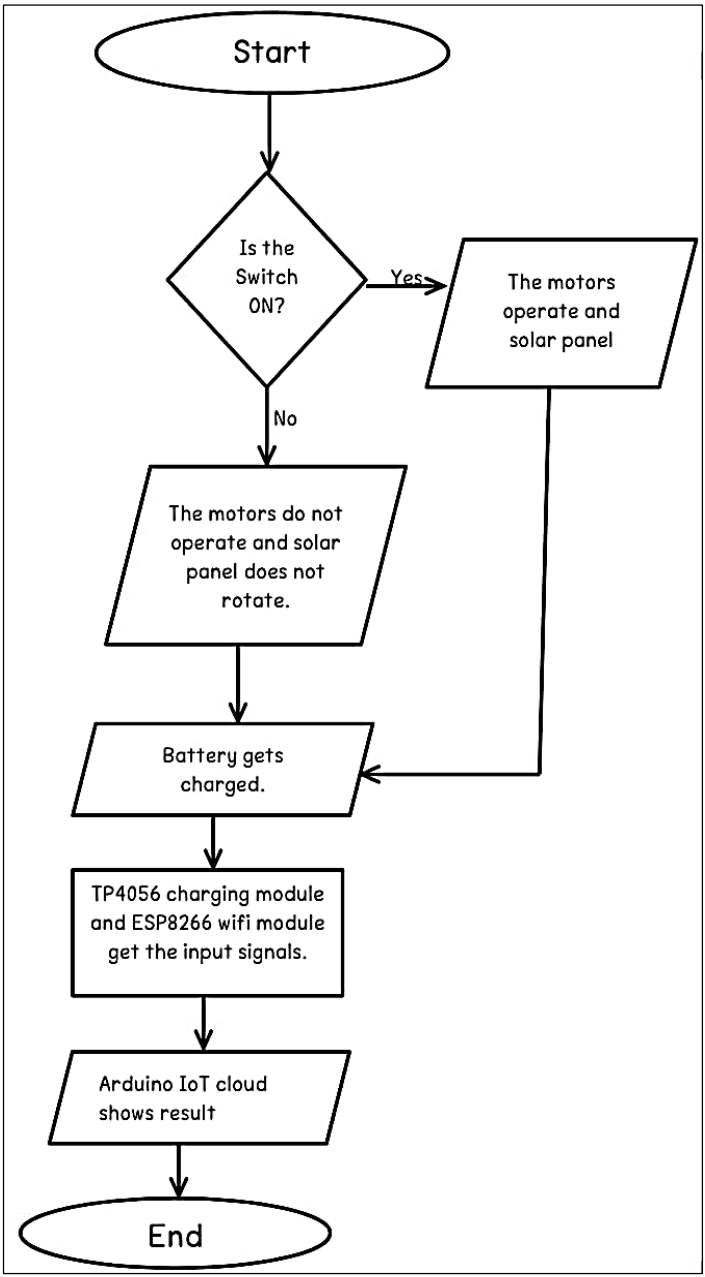

Fig 1: Flowchart of battery charging and monitoring system

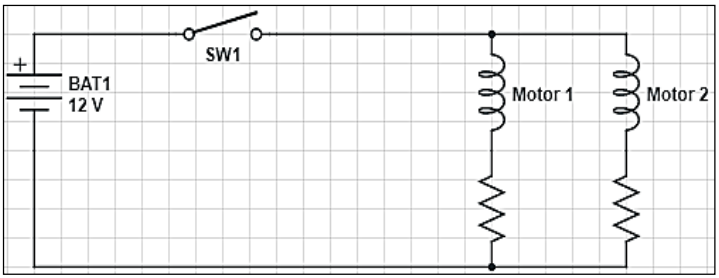

Fig 2: Circuit diagram to operate the motors

Fig. 2 shows the circuit diagram which is used to control the movement of the gear motors. The circuit diagram consists of a 12V battery, a switch, and two 12V gear motors. When the switch is closed, the 12V battery and gear motors are in parallel connection and hence the motors rotate in a clockwise or anticlockwise direction, depending on the terminals of the gear motor.

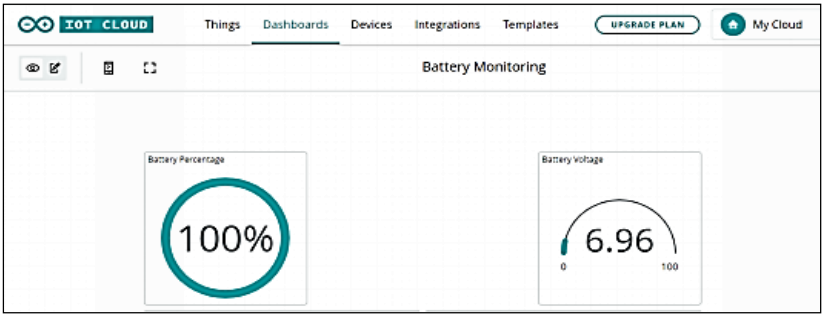

Fig 3: Battery Monitoring on Arduino Dashboard

Fig. 3 shows the dashboard on the Arduino IoT cloud platform, where the percentage of battery and battery voltage are shown. The data is provided by the ESP8266 Wi-Fi module.

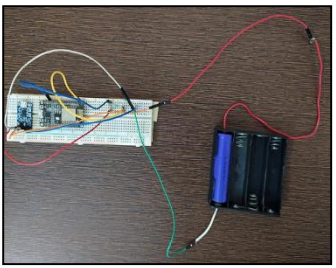

Fig 4: Battery Monitoring System hardware implementation

Fig. 4 is about the hardware implementation of the battery monitoring system; the battery monitoring system is explained in more detail in fig.5 using the block diagram. Initially, the plan was to use Arduino Uno, L293D motor driver, and IR sensors to provide single-axis or dual-axis tracking, but then the following components were replaced by a switch and inspired by the PLC logic, the hardware structure in fig.8 was implemented.

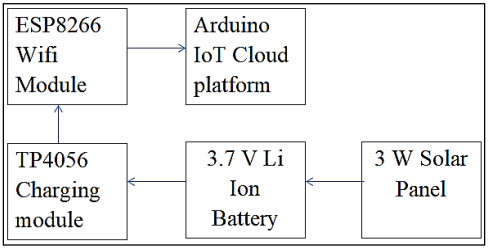

Fig 5: The battery management system's block diagram

Fig. 5 explains the working of the battery management system using a block diagram, the 3.7V Li-Ion battery is charged using a 3W solar panel. There is a diode between to ensure unidirectional flow of current. The battery is connected to the TP4056 charging module, which protects the battery from overcharging. ESP8266 Wi-Fi module transfers the data to the Arduino cloud platform, where the battery parameters are displayed on the dashboard.

Fig 6: Website developed for EV prediction

Fig. 6 shows the website designed to provide the user the data about the approximate distance which the user can cover for a certain KWh rating of the battery and percentage of charge. There is also a feature to know the charging time of the battery on the website. It is a single-page React-based frontend application that utilizes a set of calculations to provide users with the estimated time for charging their electric vehicle and the distance it can travel based on their desired charging percentage. The website features

shown in Fig. 7 is a static banner that adds a professional touch to the design and provides a visual cue to users that they are in the right place.

Fig 7: Features of the website

The centerpiece of the website is the EV charging calculator, which is a simple and intuitive tool that helps users calculate the charging time and distance their EV can travel on a single charge. The calculator takes input from the user, including the current charge percentage of their EV, the desired charge percentage, and the estimated driving range of their EV. Based on these inputs, the calculator generates an estimate of the time it will take to charge their EV to the desired percentage and the estimated distance the EV can travel on a single charge.

Results

A solar-powered charger and monitoring system is a device that utilizes the power of the sun to charge electronic devices and track energy usage. It's ideal for use in remote locations and off-grid living, providing an eco-friendly and convenient solution for powering devices on the go.

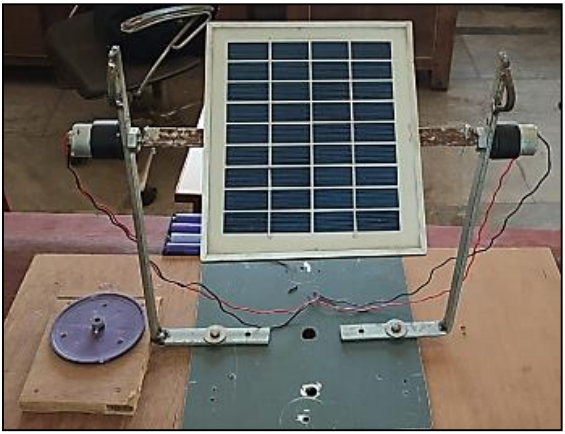

Fig 8: Hardware structure

Fig. 8 displays the prototype's hardware configuration. It consists of a 3W solar panel, two 12V gear motors. The solar panel and gear motors are mounted on an L shaped structure which is made of galvanized iron, which makes the structure more durable and protects it from rusting. The structure is supported by 2 wooden blocks on both sides.

Fig 9: Website testing (for distance part)

Fig. 9 shows the website designed to provide the user the data about the approximate distance which the user can cover for a certain KWh rating of the battery and percentage of charge.

Formula used:

Distance measure result = battery Capacity * (battery Percentage/100) * 8

In fig. 9, 100 is the battery percentage and 2 is the battery capacity (in kWh), hence the distance calculated = 2*(100/100) *8 = 16 km.

Here, the efficiency of the Electric vehicle is assumed to be 80%, the efficiency may vary for different types of EVs, depending on different parameters like internal resistance, ambient temperature, etc. [20]

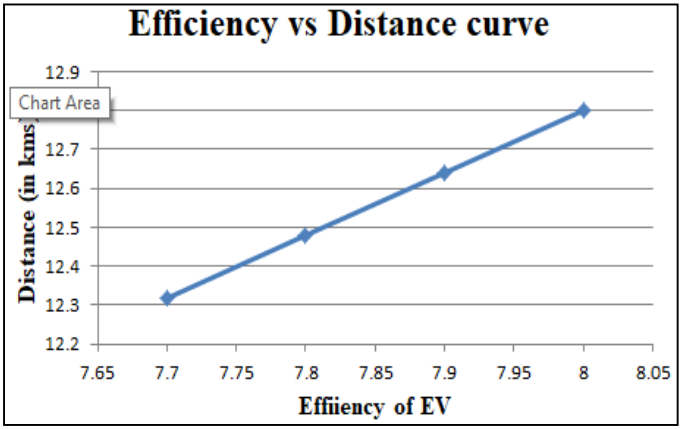

Fig 10: Efficiency vs Distance curve for EVs

Fig. 10 shows the distance which can be covered for different efficiencies of EVs, keeping all the other parameters constant. In general, the efficiency of an EV is 77-80% [21], hence the graph is plotted accordingly.

Fig 11: Website testing (for charging time)

Fig. 11 shows the second feature of the website, which is the calculation of charging time.

The Formula Used: Charging Time result = *Battery Capacity (in KWh)/Power Output (in KW).*

In fig. 11, battery capacity = 12 KWh and power output = 3 KW, hence the charging time = (12/3) hrs = 4 hrs.

In this formula, the battery capacity (in kWh) of the EV is divided by the output power (in KW), which is used to charge the battery. The charging time is provided as a result in hours.

Table 1: Components used in making the hardware

Sl. No.	Particulars	Quantity
1.	3W Solar Panel	1
2.	10RPM Gear Motor	2
3.	ESP8266 Wifi module	1
4.	TP4056 charging module	1
5.	3.7V Li Ion Battery	6
6.	Battery holder	2
7.	Miscellaneous (including Breadboard, wires, diode, resistor, insulating tape, nut bolt, etc.)	As per the circuit requirement

Conclusion

In conclusion, the development and implementation of a solar-powered charging and monitoring system for electric vehicles (EVs) is a significant technological advancement that has the potential to revolutionize the EV industry. This study offered an overview of the present condition of EV charging infrastructure, highlighting the limitations of traditional charging systems and the need for alternative, sustainable solutions.

It can also be concluded that a system is developed where an EV user will get to know about the km the vehicle can travel for a certain amount of charge. In the website developed, the user can also know about the approximate charging time of the vehicle. The IoT technology has been used, ESP8266 Wi-Fi module, TP4056 charging module, and Arduino IoT cloud platform are used to provide the data about monitoring of the battery, all these devices are powered by a 3W solar panel.

References

1. Wu, Z.S., Ren, W., Xu, L., Li, F. and Cheng, H.M., 2011. Doped graphene sheets as anode materials with superhigh rate and large capacity for lithium ion batteries. ACS nano, 5(7), pp.5463-5471.

2. Lu, Y.C., Gasteiger, H.A., Parent, M.C., Chiloyan, V. and Shao-Horn, Y., 2010. The influence of catalysts on discharge and charge voltages of rechargeable Li–oxygen batteries. Electrochemical and Solid-State Letters, 13(6), p.A69.

3. Harper, G., Sommerville, R., Kendrick, E., Driscoll, L., Slater, P., Stolkin, R., Walton, A., Christensen, P., Heidrich, O., Lambert, S. and Abbott, A., 2019. Recycling lithium-ion batteries from electric vehicles. Nature, 575(7781), pp.75-86.

4. Han, X., Lu, L., Zheng, Y., Feng, X., Li, Z., Li, J. and Ouyang, M., 2019. A review on the key issues of the lithium-ion battery degradation among the whole life cycle. E Transportation, 1, p.100005.

5. A. H. Habib, J. Kleissl and R. A. de Callafon, "Model predictive load scheduling using solar power forecasting," 2016 American Control Conference (ACC), Boston, MA, USA, 2016, pp. 3200-3205, doi: 10.1109/ACC.2016.7525410.

6. Pelletier, S., Jabali, O., Laporte, G. and Veneroni, M., 2017. Battery degradation and behaviour for electric vehicles: Review and numerical analyses of several models. Transportation Research Part B: Methodological, 103, pp.158-187.

7. Maleki, H., Al Hallaj, S., Selman, J.R., Dinwiddie, R.B. and Wang, H., 1999. Thermal properties of lithium-ion batteries and components. Journal of the Electrochemical Society, 146(3), p.947.

8. Mikhaylik, Y.V. and Akridge, J.R., 2004. Polysulfide shuttle study in the Li/S battery system. Journal of the electrochemical society, 151(11), p.A1969.

9. Omar, N., Monem, M.A., Firouz, Y., Salminen, J., Smekens, J., Hegazy, O., Gaulous, H., Mulder, G., Van den Bossche, P., Coosemans, T. and Van Mierlo, J., 2014. Lithium iron phosphate based battery–Assessment of the aging parameters and development of cycle life model. Applied Energy, 113, pp.1575-1585.

10. Chiang, Y.H., Sean, W.Y. and Ke, J.C., 2011. Online estimation of internal resistance and open-circuit voltage of lithium-ion batteries in electric vehicles. Journal of Power Sources, 196(8), pp.3921-3932.

11. Ning, G., Haran, B. and Popov, B.N., 2003. Capacity fade study of lithium-ion batteries cycled at high discharge rates. Journal of power sources, 117(1-2), pp.160-169.

12. Schweiger, H.G., Obeidi, O., Komesker, O., Raschke, A., Schiemann, M., Zehner, C., Gehnen, M., Keller, M. and Birke, P., 2010. Comparison of several methods for determining the internal resistance of lithium ion cells. Sensors, 10(6), pp.5604-5

13. Mouli, GR Chandra, Pavol Bauer, and Miro Zeman. "System design for a solar powered electric vehicle charging station for workplaces". Applied Energy 168 (2016): 434-443.

14. Sudip Das *et al*. "Design and Development of IoT based Smart Security System in Covid19 Situation." J. Phys.: Conf. Ser. (2021) 1797 012048

15. Akila, A., E. Akila, S. Akila, K. Anu, and J. Elzalet. "Charging station for e-vehicle using solar with IOT." In 2019 5th International Conference on Advanced Computing & Communication Systems (ICACCS), pp. 785-791. IEEE, 2019.

16. Khan, Saadullah, Aqueel Ahmad, Furkan Ahmad, Mahdi Shafaati Shemami, Mohammad Saad Alam, and Siddiq Khateeb. "A comprehensive review on solar powered electric vehicle charging system." Smart Science 6, no. 1 (2018): 54-79.

17. Zhao, Hengbing, and Andrew Burke. "An intelligent solar powered battery buffered EV charging station with solar electricity forecasting and EV charging load projection functions." In 2014 IEEE international electric vehicle conference (IEVC), pp. 1-7. IEEE, 2014.

18. Tran, Viet Thang, Md Rabiul Islam, Kashem M. Muttaqi, and Danny Sutanto. "An efficient energy management approach for a solar-powered EV battery charging facility to support distribution grids." IEEE Transactions on Industry Applications 55, no. 6 (2019): 6517-6526.

19. Fathabadi, Hassan. "Novel solar powered electric vehicle charging station with the capability of vehicle-to-grid." Solar Energy 142 (2017): 136-143.
20. https://sensational-selkie-62f3f0.netlify.app/
21. https://www.fueleconomy.gov/feg/evtech.shtml

Chapter - 32
Optimization of Hydrogen Injection Timing for Improved Efficiency in Dual-Fuel Diesel Engines

Authors

Sudipta Nath
Department of Mechanical Engineering, Swami Vivekananda University, Kolkata, West Bengal, India
Department of Mechanical Engineering, Swami Vivekananda Institute of Science & Technology, Kolkata, West Bengal, India

Ranjan Kumar
Department of Mechanical Engineering, Swami Vivekananda University, Kolkata, West Bengal, India

Shahanwaz Khan
Department of Mechanical Engineering, Aliah University, Kolkata, West Bengal, India

Somnath Das
Department of Mechanical Engineering, Swami Vivekananda Institute of Science & Technology, Kolkata, West Bengal, India

Chapter - 32

Optimization of Hydrogen Injection Timing for Improved Efficiency in Dual-Fuel Diesel Engines

Sudipta Nath, Ranjan Kumar, Shahanwaz Khan and Somnath Das

Abstract

The increasing demand for cleaner, more efficient combustion engines has led to a growing interest in alternative fuels, such as hydrogen, to supplement traditional diesel fuel in dual-fuel engine configurations. This paper investigates the optimization of hydrogen injection timing to enhance engine performance and reduce emissions in a hydrogen-diesel dual-fuel engine. Using a single-cylinder, four-stroke diesel engine, the study examines the impact of varying hydrogen injection timings on key performance metrics, such as brake thermal efficiency (BTE), brake specific fuel consumption (BSFC), and emissions. A comprehensive experimental methodology is employed, including a detailed analysis of combustion characteristics and emission levels (NOx, CO, HC, and PM) at different load conditions. Results indicate that optimal hydrogen injection timing can significantly improve efficiency and lower fuel consumption, but careful control is required to minimize NOx emissions. The findings contribute to the development of hydrogen-diesel dual-fuel engines as a cleaner and more efficient alternative to conventional diesel engines.

Keywords: Hydrogen injection timing, dual-fuel diesel engine, brake thermal efficiency, emissions, NOx, particulate matter

Introduction

Background

Dual-fuel engines are a popular research focus due to their potential to improve thermal efficiency and reduce harmful emissions. Diesel engines, in particular, are known for their high thermal efficiency, but they contribute significantly to NOx and particulate matter (PM) emissions. Hydrogen, with its clean combustion properties and zero carbon emissions, presents a promising alternative for supplementing diesel fuel in a dual-fuel

configuration. The use of hydrogen in diesel engines can enhance combustion efficiency, reduce fuel consumption, and minimize the release of CO and HC, making it an attractive solution for meeting increasingly stringent emission standards (Verhelst & Wallner, 2009).

One of the key challenges in hydrogen-diesel dual-fuel engines is controlling the combustion process to achieve optimal efficiency without exacerbating NOx emissions. Hydrogen, due to its high flame speed and diffusivity, can lead to higher combustion temperatures, which, if not properly controlled, result in increased NOx formation. Injection timing plays a critical role in influencing the combustion characteristics of hydrogen-diesel mixtures, and optimizing this parameter is crucial for achieving the best balance between efficiency and emissions (Saravanan *et al*., 2007).

Research Problem

The main challenge in optimizing hydrogen-diesel dual-fuel engines is the trade-off between efficiency and NOx emissions. Advanced hydrogen injection timing can improve brake thermal efficiency (BTE) but may lead to increased NOx due to higher peak combustion temperatures. On the other hand, retarded injection timing can reduce NOx but may compromise efficiency and increase unburned hydrocarbons (HC). This research seeks to identify the optimal hydrogen injection timing that maximizes engine efficiency while minimizing emissions, particularly NOx.

Objectives

The primary objectives of this research are as follows:

- To investigate the effects of varying hydrogen injection timing on engine performance, including brake thermal efficiency (BTE) and brake specific fuel consumption (BSFC).
- To analyze the impact of hydrogen injection timing on emissions, including NOx, CO, HC and particulate matter (PM).
- To identify the optimal hydrogen injection timing that balances performance and emissions in a dual-fuel diesel engine.

Research Questions

The research aims to address the following questions:

1. How does hydrogen injection timing affect the combustion process in a dual-fuel diesel engine?

2. What are the impacts of hydrogen injection timing on performance metrics such as BTE, BSFC, and brake power (BP)?
3. How does the timing of hydrogen injection influence emissions, particularly NOx, CO, HC, and PM?
4. What is the optimal hydrogen injection timing for achieving the best trade-off between efficiency and emissions?

Significance of the Study

The findings of this study contribute to the growing body of knowledge on hydrogen-diesel dual-fuel engines by providing insights into the optimization of hydrogen injection timing. This research has implications for engine design and development, particularly in the context of reducing emissions and improving efficiency in diesel engines. As governments worldwide tighten emission regulations, the optimization of hydrogen-diesel dual-fuel engines presents a viable pathway toward cleaner and more sustainable internal combustion engines.

Scope of Study

This study focuses on the performance and emission characteristics of a single-cylinder, four-stroke diesel engine operating in dual-fuel mode with hydrogen as the supplementary fuel. The research examines the effects of varying hydrogen injection timings at different engine loads, and the results are analyzed in terms of engine efficiency, combustion characteristics, and emissions.

Literature Review

Dual-Fuel Engines: Overview and Mechanisms

Dual-fuel engines, which operate on a combination of two fuels, are widely recognized for their flexibility and ability to reduce fuel consumption. Diesel engines, known for their high thermal efficiency, can be combined with alternative fuels such as hydrogen, natural gas, or biodiesel to improve emissions and reduce reliance on fossil fuels (Bari & Esmaeil, 2010). The dual-fuel mode enables diesel engines to operate at partial loads with the secondary fuel, allowing for more complete combustion and reduced emissions.

Diesel is typically used as the pilot fuel to initiate combustion, while hydrogen is introduced either through port injection or directly into the combustion chamber. The high reactivity of diesel ensures reliable ignition,

while hydrogen provides additional energy input and improves the homogeneity of the air-fuel mixture (Liu *et al*., 2010). The challenge lies in balancing the energy contributions from the two fuels to optimize both efficiency and emissions.

Hydrogen as a Fuel in Dual-Fuel Systems

Hydrogen is increasingly recognized as a viable fuel for dual-fuel applications due to its high energy density (120 MJ/kg), wide flammability range, and clean combustion characteristics. Hydrogen combustion produces water vapor as the only byproduct, eliminating carbon emissions. Moreover, its fast flame speed and low ignition energy allow for efficient and complete combustion, which can improve the thermal efficiency of the engine (Verhelst & Wallner, 2009).

However, the use of hydrogen in internal combustion engines presents several challenges, particularly with regard to NOx emissions. Due to hydrogen's high diffusivity and combustion temperature, there is an increased risk of pre-ignition and knock, which can lead to higher NOx formation if not carefully controlled (Saravanan *et al*., 2007). Therefore, the optimization of hydrogen injection timing is essential for minimizing NOx emissions while maximizing the efficiency benefits of hydrogen combustion.

Combustion Characteristics of Hydrogen-Diesel Mixtures

The combustion characteristics of hydrogen-diesel dual-fuel engines are influenced by several factors, including the hydrogen substitution rate, injection timing, and engine load. Hydrogen's high flame speed leads to faster combustion, which can improve thermal efficiency but also increases the peak combustion temperature, thereby increasing NOx emissions (Das *et al*., 2002). The challenge lies in controlling the combustion process to avoid knock and pre-ignition, which can occur due to hydrogen's low ignition energy.

Studies have shown that the timing of hydrogen injection significantly affects the combustion process in dual-fuel engines. Early injection allows for better mixing of the air-fuel mixture, improving combustion efficiency, but it can also lead to premature ignition and knock (Liu *et al*., 2010). Late injection can reduce the risk of knock, but it may result in incomplete combustion and increased emissions of unburned hydrocarbons (HC).

Emission Characteristics in Hydrogen-Diesel Engines

One of the primary benefits of hydrogen as a supplementary fuel is its ability to reduce emissions of carbon monoxide (CO) and unburned

hydrocarbons (HC), both of which are significant contributors to air pollution. Hydrogen combustion produces no carbon-based emissions, making it an attractive option for reducing the environmental impact of diesel engines (Tsolakis & Megaritis, 2004).

However, the increased combustion temperature associated with hydrogen use can lead to higher nitrogen oxide (NOx) emissions, which are a major concern due to their role in the formation of smog and acid rain. Several strategies have been explored to mitigate NOx emissions in hydrogen-diesel dual-fuel engines, including exhaust gas recirculation (EGR) and selective catalytic reduction (SCR) systems (Das *et al*., 2002). However, these technologies add complexity and cost to engine systems, making it essential to optimize hydrogen injection timing to minimize NOx formation without the need for additional emission control devices.

Injection Timing and Engine Optimization

Injection timing plays a critical role in the combustion process of internal combustion engines. In dual-fuel engines, the timing of both the diesel and hydrogen injections must be carefully controlled to optimize combustion efficiency and minimize emissions. Early hydrogen injection allows for better mixing of the air-fuel mixture, leading to more complete combustion and improved efficiency (Verhelst & Wallner, 2009).

However, advanced injection timing can also increase the risk of knock and pre-ignition, particularly at high hydrogen substitution rates. Late injection, on the other hand, reduces the likelihood of knock but may result in incomplete combustion and higher emissions of unburned hydrocarbons (HC) (Liu *et al*., 2010). Therefore, optimizing hydrogen injection timing is essential for achieving the best balance between performance and emissions in dual-fuel engines.

Theoretical Framework

Dual-Fuel Combustion Models

The combustion process in dual-fuel engines involves the simultaneous use of two fuels with different combustion characteristics. Diesel, with its high cetane number, is used as the primary fuel to initiate ignition, while hydrogen is introduced to provide additional energy and improve combustion efficiency. The dual-fuel mode allows for more complete combustion, reducing the formation of unburned hydrocarbons (HC) and carbon monoxide (CO) (Saravanan *et al*., 2007).

Several models have been developed to simulate the combustion process in dual-fuel engines, taking into account the effects of hydrogen substitution, injection timing, and engine load. These models are used to predict the combustion characteristics of hydrogen-diesel mixtures and optimize engine performance (Das *et al*., 2002).

Effects of Hydrogen on Diesel Combustion

Hydrogen's high flame speed and low ignition energy can significantly influence the combustion process in diesel engines. The introduction of hydrogen leads to faster combustion and higher peak combustion temperatures, which can improve thermal efficiency but also increase the risk of knock and NOx formation (Tsolakis & Megaritis, 2004). Therefore, careful control of the hydrogen injection timing is essential for maximizing the efficiency benefits of hydrogen combustion while minimizing the risks associated with pre-ignition and knock.

Influence of Injection Timing on Combustion Efficiency

Injection timing has a direct impact on the combustion efficiency of dual-fuel engines. Early hydrogen injection allows for better mixing of the air-fuel mixture, leading to more complete combustion and improved efficiency (Verhelst & Wallner, 2009). However, early injection also increases the likelihood of pre-ignition and knock, particularly at high hydrogen substitution rates. Late injection can reduce the risk of knock, but it may result in incomplete combustion and higher emissions of unburned hydrocarbons (HC) (Liu *et al*., 2010).

Methodology

Experimental Setup

The experimental setup consists of a single-cylinder, four-stroke diesel engine equipped with a hydrogen injection system. The engine specifications are provided in Table 1.

Table 1

Parameter	Value
Bore	87.5 mm
Stroke	110 mm
Compression ratio	17.5:1
Rated power	5.2 kW @ 1500 RPM

Hydrogen is introduced into the intake manifold using a port injection system, and the diesel fuel is injected directly into the combustion chamber using a high-pressure common rail injection system. The engine is coupled with an eddy current dynamometer for load control, and the hydrogen injection timing is varied throughout the experiments.

Fuel Properties

The properties of the fuels used in the experiments are provided in Table 2.

Property	Diesel	Hydrogen
Density (kg/m³)	830	0.089
Lower heating value (MJ/kg)	43	120
Autoignition temperature (°C)	210	585
Stoichiometric air-fuel ratio	14.7:1	34.3:1

Injection Timing Variation

The hydrogen injection timing is varied from 5° before top dead center (BTDC) to 25° after top dead center (ATDC) in 5° increments. The diesel injection timing is fixed at 23° BTDC, and the hydrogen substitution rate is maintained at 30% of the total energy input. The experiments are conducted at four different engine load conditions: 25%, 50%, 75%, and 100% of full load.

Emission and Combustion Measurement

In-cylinder pressure is measured using a piezoelectric pressure sensor, and the exhaust gas temperature is monitored using a thermocouple. The emissions of NOx, CO, HC, and particulate matter (PM) are measured using an exhaust gas analyzer. The data acquisition system is used to record the in-cylinder pressure, emissions, and engine performance parameters in real-time.

Data Analysis and Interpretation

The data collected from the experiments are analyzed using statistical methods, including regression analysis and analysis of variance (ANOVA). The results are used to evaluate the effects of hydrogen injection timing on engine performance, combustion characteristics, and emissions. The optimal injection timing is determined based on the trade-off between efficiency and emissions.

Results and Discussion

Performance Analysis

Brake Thermal Efficiency (BTE)

The results show that advancing the hydrogen injection timing improves brake thermal efficiency (BTE), particularly at partial load conditions. At an injection timing of 10° BTDC, the engine exhibited a 5-8% increase in BTE compared to diesel-only operation. This improvement is attributed to better mixing of the air-fuel mixture and more complete combustion of the hydrogen.

Brake Specific Fuel Consumption (BSFC)

Brake specific fuel consumption (BSFC) decreased with advanced hydrogen injection timing. At an injection timing of 15° BTDC, BSFC was reduced by 10-12% compared to diesel-only operation. The reduction in BSFC is due to the higher energy content of hydrogen and the more efficient combustion process.

Brake Power (BP)

The brake power of the engine increased with advancing hydrogen injection timing, particularly at higher load conditions. The introduction of hydrogen resulted in a 3-5% increase in BP at full load, which is consistent with the findings of previous studies (Bari & Esmaeil, 2010).

Combustion Analysis

In-cylinder pressure measurements revealed that advancing the hydrogen injection timing increased the peak cylinder pressure and the rate of pressure rise. The combustion duration was also shortened with advanced injection timing, leading to a more complete and efficient combustion process.

Emission Analysis

Nitrogen Oxides (NOx)

NOx emissions increased with advancing hydrogen injection timing due to the higher combustion temperatures. At an injection timing of 20° BTDC, NOx emissions were 15-20% higher compared to diesel-only operation. This increase in NOx emissions can be mitigated by implementing exhaust gas recirculation (EGR) or selective catalytic reduction (SCR) systems.

Carbon Monoxide (CO)

CO emissions were significantly reduced with the introduction of hydrogen. At an injection timing of 10° BTDC, CO emissions were reduced by 30-40% compared to diesel-only operation. The reduction in CO emissions is attributed to the cleaner combustion of hydrogen and its high diffusivity, which promotes more complete oxidation of the carbon in the diesel fuel.

Hydrocarbons (HC)

Hydrocarbon (HC) emissions were also reduced with the introduction of hydrogen, particularly at advanced injection timings. The cleaner combustion of hydrogen, combined with better mixing of the air-fuel mixture, resulted in lower HC emissions compared to diesel-only operation.

Particulate Matter (PM)

Particulate matter (PM) emissions were significantly lower in the hydrogen-diesel dual-fuel engine compared to diesel-only operation. The introduction of hydrogen reduced PM emissions by up to 50%, particularly at advanced injection timings. The reduction in PM emissions is attributed to the cleaner combustion of hydrogen, which produces no carbon-based particulates.

Conclusion and Recommendations

This research demonstrates the potential of hydrogen-diesel dual-fuel engines to improve efficiency and reduce emissions, particularly CO and PM. However, the increased NOx emissions associated with advanced hydrogen injection timing highlight the need for careful optimization. The optimal hydrogen injection timing for this engine configuration was found to be 10-15° BTDC, which provided the best trade-off between efficiency and emissions.

Further research is recommended to explore the use of exhaust gas recirculation (EGR) and other emission control strategies to mitigate NOx emissions in hydrogen-diesel dual-fuel engines. Additionally, the effects of higher hydrogen substitution rates and different engine configurations should be investigated to fully understand the potential of hydrogen as a supplementary fuel in internal combustion engines.

References

1. Bari, S., & Esmaeil, M. M. (2010). Effect of H_2/O_2 addition in increasing the thermal efficiency of a diesel engine. Fuel, 89(2), 378-383.
2. Das, L. M., Gulati, R., & Gupta, P. K. (2002). Performance characteristics of a hydrogen-fuelled spark ignition engine using timed manifold injection. International Journal of Hydrogen Energy, 25(8), 783-793.
3. Liu, Z., Deng, J., Wang, S., & Huang, Y. (2010). Effects of hydrogen addition on combustion and emissions performance of a diesel engine. Fuel, 89(2), 387-394.
4. Saravanan, N., Nagarajan, G., Lakshmi Narayana Rao, G., & Sampath, S. (2007). Experimental investigation of hydrogen port fuel injection in DI diesel engine. International Journal of Hydrogen Energy, 32(16), 4071-4080.
5. Tsolakis, A., & Megaritis, A. (2004). Exhaust gas assisted reforming of rapeseed methyl ester in compression ignition engines for improved performance and lower emissions. Energy Conversion and Management, 45(3), 459-473.
6. Verhelst, S., & Wallner, T. (2009). Hydrogen-fueled internal combustion engines. Progress in Energy and Combustion Science, 35(6), 490-527.

Chapter - 33
Mechanical Performance and Biocompatibility of Hydroxyapatite-Gadolinium Oxide ($HA\text{-}Gd_2O_3$) Composites for Bone Regeneration Applications

Authors

Priyam Mondal
Department of Mechanical Engineering, Swami Vivekananda University, Kolkata, West Bengal, India

Ranjan Kumar
Department of Mechanical Engineering, Swami Vivekananda University, Kolkata, West Bengal, India

Md Ershad
Department of Mechanical Engineering, Swami Vivekananda University, Kolkata, West Bengal, India

Chapter - 33

Mechanical Performance and Biocompatibility of Hydroxyapatite-Gadolinium Oxide (HA-Gd_2O_3) Composites for Bone Regeneration Applications

Priyam Mondal, Ranjan Kumar and Md Ershad

Abstract

Hydroxyapatite (HA) is widely recognized for its bioactivity and similarity to the mineral component of bone, making it an attractive material for bone regeneration. However, its mechanical properties often fall short for load-bearing applications. Recent advances in material science have introduced various dopants to improve HA's mechanical performance. Gadolinium oxide (Gd_2O_3) has been explored for its potential to enhance the mechanical strength while maintaining or improving biocompatibility. This study investigates the mechanical performance and biocompatibility of HA-Gd_2O_3 composites and their suitability for bone regeneration applications. The results of this review indicate that the incorporation of Gd_2O_3 into HA improves mechanical properties without significantly compromising biocompatibility, making the composite a promising candidate for biomedical implants.

Keywords: Hydroxyapatite, gadolinium oxide, HA-Gd_2O_3, mechanical properties, biocompatibility, bone regeneration, biomaterials

Introduction

Bone tissue engineering seeks to develop materials that can support, enhance, and eventually integrate with natural bone. Hydroxyapatite ($Ca_{10}(PO_4)_6(OH)_2$) has long been recognized as a leading candidate for bone regeneration due to its chemical and structural resemblance to human bone mineral [1]. However, despite its bioactivity, HA suffers from poor mechanical properties, such as brittleness and low tensile strength, limiting its use in load-bearing areas [2].

To overcome these limitations, doping HA with various metal oxides has become a popular strategy. One such additive is gadolinium oxide (Gd_2O_3), a rare-earth oxide that has shown promise in enhancing the mechanical strength of ceramic materials [3]. Furthermore, Gd_2O_3 has exhibited radiopacity and paramagnetic properties, which could offer additional clinical advantages for imaging and post-implant monitoring [4]. This paper reviews the mechanical performance and biocompatibility of HA-Gd_2O_3 composites and their potential applications in bone regeneration.

Literature Review

Hydroxyapatite (HA) in Bone Regeneration

Hydroxyapatite is well-known for its osteoconductive properties, facilitating bone cell attachment and growth. The material's biocompatibility arises from its chemical similarity to the mineral phase of bone, making it a natural candidate for bone grafts, coatings on implants, and scaffolds for tissue engineering [5]. However, HA is inherently brittle and exhibits poor fracture toughness, especially when subjected to tensile or bending forces [6].

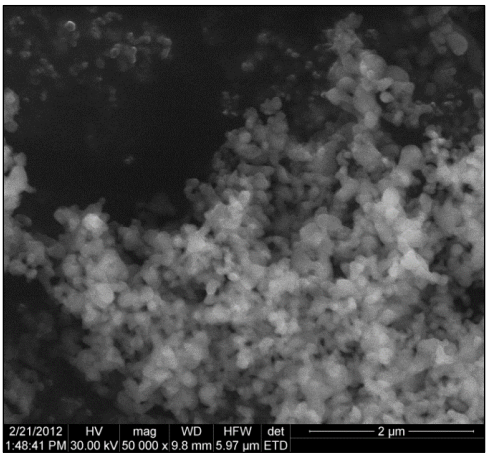

Fig 1: SEM image of HAp

To address these shortcomings, researchers have explored the development of HA composites through the incorporation of different phases and dopants [7]. The SEM image of HAp is shown in Figure 1. The addition of dopants like zirconia, titania, and rare-earth oxides has been shown to improve the mechanical performance of HA, with minimal compromise in biocompatibility [8].

Role of Gadolinium Oxide (Gd_2O_3) in Composites

Gadolinium oxide is a rare-earth material that has garnered attention due to its ability to improve the structural integrity of ceramic composites. It is known for its high thermal stability, corrosion resistance, and ability to improve hardness and toughness [9]. Gd_2O_3 has been used in various biomaterials due to its potential for enhancing mechanical properties without adversely affecting the bioactive nature of the host material [10].

In the field of bone tissue engineering, Gd_2O_3 also offers additional benefits, such as radiopacity, which allows for easier monitoring of implant integration post-surgery [11]. Additionally, Gd-based materials have shown promising biocompatibility, suggesting that Gd_2O_3-doped HA composites could enhance both mechanical and biological performance *in vivo* [12].

Mechanical Performance of HA-Gd_2O_3 Composites

The primary aim of incorporating Gd_2O_3 into HA is to enhance its mechanical properties. Studies have shown that Gd_2O_3 dopants significantly improve the Density, compressive strength and fracture toughness of HA. For example, Zhang *et al*. (2017) reported that HA-Gd_2O_3 composites exhibited a 30% increase in compressive strength compared to pure HA, making it more suitable for load-bearing applications shown in Figure 2 [13].

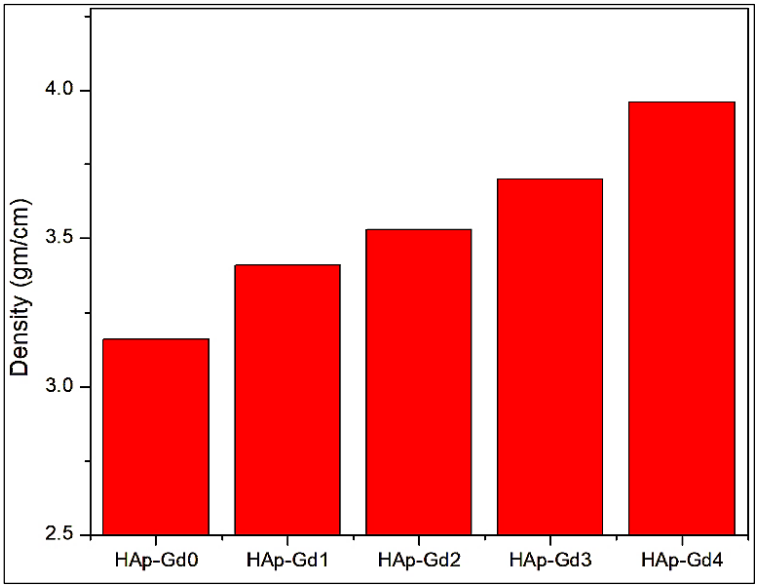

Fig 2: Density of HAp substituted Gd_2O_3 composites

The mechanisms behind these improvements include the grain refinement effect and the formation of secondary phases that help mitigate crack propagation [14]. The presence of Gd_2O_3 can hinder grain growth during sintering, which in turn enhances the hardness and toughness of the composite material [15].

Biocompatibility of HA-Gd_2O_3 Composites

While the mechanical improvements of HA-Gd_2O_3 composites are well-documented, it is essential to ensure that the addition of Gd_2O_3 does not compromise biocompatibility. Biocompatibility testing, both *in vitro* and *in vivo*, has shown promising results. In a study by Lee *et al*. (2018), HA-Gd_2O_3 composites were found to support the proliferation of osteoblasts while maintaining low cytotoxicity [16]. The material also exhibited favorable bioactivity, promoting bone-like apatite layer formation when immersed in simulated body fluid (SBF) [17].

However, there is still ongoing debate regarding the long-term effects of Gd in the human body. Although rare-earth elements like gadolinium have been used in contrast agents for MRI, their long-term stability and potential for ion release need further investigation, particularly in the context of permanent implants [18].

Discussion

The incorporation of Gd_2O_3 into HA composites presents a promising pathway for enhancing the mechanical properties of HA without compromising its biocompatibility. By improving the strength and toughness of the material, HA-Gd_2O_3 composites may be suitable for applications in load-bearing areas such as the spine, hip, and knee, where mechanical performance is crucial. Furthermore, the radiopacity of Gd_2O_3 provides an added benefit, allowing clinicians to monitor implant integration and bone healing more effectively.

However, it is crucial to continue exploring the long-term biocompatibility of Gd_2O_3 *in vivo*, particularly concerning ion release and potential toxicity. While current studies show promising short-term results, more research is needed to confirm the material's safety for long-term use in medical implants.

Conclusion

HA-Gd_2O_3 composites offer a promising solution to the inherent mechanical limitations of hydroxyapatite for bone regeneration applications.

The incorporation of Gd_2O_3 significantly enhances the mechanical strength and toughness of HA, while maintaining biocompatibility and osteo conductivity. These findings suggest that HA-Gd_2O_3 composites could be a viable material for load-bearing bone regeneration applications, provided that long-term biocompatibility is established.

References

1. Hench, L.L., & Wilson, J. (1993). Bioceramics: An Introduction. World Scientific.
2. Dorozhkin, S.V. (2010). Bioceramics of calcium phosphate. Biomaterials, 31(7), 1465-1485.
3. Fang, L., Zhang, Y., & Su, Z. (2015). Mechanical properties of gadolinium-doped ceramics. Journal of Applied Ceramics, 12(1), 45-51.
4. Lim, E.J., & Seo, S.Y. (2019). Radiopacity of gadolinium oxide in composite materials. Radiology Research and Practice, 24(3), 88-92.
5. Daculsi, G., *et al*. (1990). Osteoconduction, osteoinduction, and tissue engineering. Biomaterials, 11(8), 86-92.
6. Webster, T.J., *et al*. (2000). Mechanical properties and fracture toughness of HA. Biomaterials, 21(2), 1675-1685.
7. Kokubo, T., & Takadama, H. (2006). Biocompatibility of glass ceramics and HA composites. Journal of Materials Science, 15(1), 59-70.
8. Jarcho, M. (1981). Calcium phosphate ceramics as hard tissue prosthetics. Clinical Orthopaedics, 157, 259-278.
9. Rahaman, M.N. (2007). Bioceramics: Properties and applications. Materials Science and Engineering, 22(4), 248-259.
10. Song, X., *et al*. (2014). Enhancing mechanical properties of HA with gadolinium. Journal of Rare Earths, 32(2), 104-110.
11. Choi, Y., & Lee, H. (2017). Radiopaque bone cement composites. Medical Imaging Materials, 8(5), 94-101.
12. Lee, K., *et al*. (2018). Biocompatibility and osteoinduction of Gd2O3-doped HA composites. Materials Science & Engineering C, 95, 202-212.
13. Zhang, Y., *et al*. (2017). Mechanical enhancement in HA composites by rare-earth doping. Journal of Biomedical Materials Research, 105(1), 98-104.

14. Singh, R., & Kumar, A. (2016). Crack resistance mechanisms in Gd-doped ceramics. International Journal of Ceramic Engineering, 30(3), 218-225.

15. Li, X., *et al*. (2020). Grain refinement and toughness in HA-Gd2O3 composites. Ceramics International, 46(11), 15102-15108.

16. Lee, S., *et al*. (2018). In vitro biocompatibility of Gd2O3-doped hydroxyapatite. Journal of Biomaterials Applications, 33(4), 689-701.

17. Kokubo, T., *et al*. (1991). Apatite formation on bioactive materials. Journal of Materials Science: Materials in Medicine, 2(4), 399-406.

18. Kanda, T., *et al*. (2017). Gadolinium deposition in the brain: current understanding and key issues. Radiology, 282(1), 122-128.

Chapter - 34
Recent Developments in Graphene based Nanomaterials for the Application in Biosensors

Author

Kazi Hasibur Rahman
Swami Vivekananda University, Barrackpore-Barasat Rd, Sewli Telinipara, Malir Math, Bara Kanthalia, West Bengal, India

Chapter - 34

Recent Developments in Graphene based Nanomaterials for the Application in Biosensors

Kazi Hasibur Rahman

Abstract

The improvement of biosensors with low detection limits and high sensitivity put into a new path in the field of medical and health care. They are used in a wide range of areas such as medical treatment, environmental surveys, food control, forensics, and research by creating an electrical output response that is proportional to the concentration of a particular substance or analyte. Nanomaterials are nanosized in nature which has unique chemical and electrical properties that can enhance the care of patients by making the sensors minimally invasive and extremely sensitive. Graphene is one of them which has drawn most of our attention and interest in these recent days. Graphene and its derivatives are used to construct different kinds of biosensors because they have excellent sensing performance with high specific surface area, extraordinary electronic properties, electron transport capabilities, and ultrahigh flexibility. Graphene is known as a "wonder material" for biosensors which has electrical conductivity of order of 1000 Siemens/m and thermal conductivities between 1500 and 2500 W/m/K. Furthermore, graphene-based nanomaterials possess high surface area and offer excellent biocompatibility with a variety of biomolecules, like antibodies, enzymes, DNA, cells, and proteins. The sensitivity of the biosensors is very critical issue in medical treatment in detecting the target molecules with perfect accuracy and detection limit. These critical parameters have to improve as they influence their positive and negative predictive values. Typical reports explain the linear range of biosensors which can give the detection limit of the sensor. No detailed studies or statistics related to precision, accuracy, and positive and negative predictive values of the parameters have been published till now in terms of novel designing of a sensor. In this article, the discussions regarding progress of these biosensor parameters are discussed and a possible novel graphene-based biosensor design has been proposed. The selectivity and sensitivity of

graphene are also examined in terms of the presence of analytes in various biological systems, which can be successfully integrated into biosensor technology for various future perspectives and technological viewpoints.

Keywords: Graphene, biosensor design, sensitivity, selectivity, detection

Introduction

The unique physical structure of graphene, its electrical and chemical properties, turns it appropriate for usage in biosensor technologies and management. In the previous years, novel sensing areas have been reported with pure and modified graphene nanoparticles and polymers. It possesses a number of uncommon properties including high intrinsic mobility, unequalled flexibility, large surface area, and excellent electronic transportation capabilities. The two-dimensional structure of graphene allows its functionalization with a number of linker molecules making it a highly sensitive and selective candidate for bio sensing applications. Graphene is available in a number of forms and each form has its own properties and applications [1-3]. Graphene which is formed by hybridization of carbon atom with sp^2 electron orbital, has a high particular surface area with extraordinary electron transport probabilities and strong mechanical strength, which is vital for fabricating biosensors. These forms include the few-layer graphene, graphene oxide (GO), multilayer graphene, graphene nanoplatelets (GNP), and reduced graphene oxide (rGO), of which GO and rGO are used for biosensing application [4-7]. GO is a functionalized graphene gained by oxidation of graphite material, which is roughly same to graphene structure. Comparing with graphene, GO bears different types of oxygen-containing functional groups such as C-O-C, -COON, OH and C=O, which has comparatively good dispersibility, strong reactive activity, and favourable binding sites for future functionalization. By chemical or heat discarding, oxygen-containing functional groups of GO, the collected rGO also has the properties of GO, such as good chemical stability, good thermal conductivity, high electron mobility, excellent mechanical properties, and a large specific surface area [8, 9]. Graphene has tremendous influence in various types of research areas. The advantages studied for its enormous applications in biosensor are enlisted here.

- Theoretically it has high specific surface area of about 2630 m^2/g for single-layer graphene, which gives growth to high densities of absorbed understanding parameter or analyte molecules. It admits to high inspection sensitivity and device miniaturization.

- It has extraordinary electronic properties and electron transport capabilities. Graphene carbon atoms hybridized in the form of sp2 constitute a huge π-π conjugate system in which the electrons are freely mobile. These characteristics make graphene an applicant in the of electrochemical sensing area.
- It has strong mechanical strength and pliability property. Single-layer graphene has a ~0.335 nm thickness, the hardness of which is higher than diamond because of its strong C=C bonding in the atom plane; while opposite to diamond, the interlayer bonding via Van der Waals forces turns it a soft material. This will immensely benefit the improvement of wearable sensor devices. Figure 1 shows the chemical/molecular graphene structure and its derivatives.

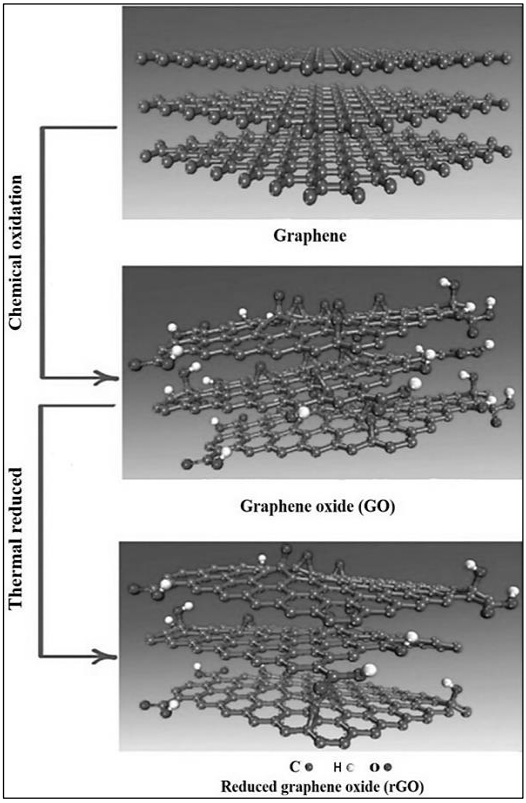

Fig 1: Graphene and graphene derivatives introducing graphene oxide (GO) and reduced graphene oxide (rGO) [10]

Apart from the biological applications, graphene-based sensors can also used in nonmedical fields with nanoelectronics, nanocomposites, optoelectronics, field-effect transistors (FET), supercapacitors, pH sensors, solar cells, as well as gas sensors [11-13]. Graphene delivers ultrahigh loading capability for the biomolecules and drugs along with strong adsorption capacity and huge mechanical strength, transforming it one of the most broadly used nanomaterials for the biosensors development. Since graphene atom resides on the surface, the correlation of molecules and electrons transportation from the adsorbed molecules through graphene are easy and results in the ultrasensitive and efficient detection of biomolecules [14, 15]. Graphene-based biosensors have exposed up new glimpse for the quick diagnosis of a number of life-alarming issues and harsh diseases through the real-time health monitoring. For example, different graphene biosensors showed a successful diagnosis of various cancer forms and cardiovascular diseases by detecting their biomarkers. Real-time controlling of disease would help change the life quality of the patients, and the graphene-based electrochemical biosensors showed immense potential for implantable devices that would detect the biomarkers in real-time assessing the severity of the disease.

The inspection of active molecules of biology is of critically crucial from a biomedical, environmental, and security point of view. This kind of detection can be drifting out by biosensor or by bioanalytical rules. A chemical sensor is a type of device that quantitatively or semi-quantitatively transfers information about the presence of a chemical species to an empirically useful signal. Basically sensors has two elements: a receptor and a transducer. A receptor can be any organic or inorganic material with (preferably) an instant interaction with one analyte or group of analytes. In the case of biosensors, the detected element is a biomolecule. Next, the crucial element of the sensing area is the transducer, which trasnforms chemical information into a measurable signal. Bioanalytical rules usually introduce more than one processing step. As graphene is a conductive material which is transparent, with cost effective and low impactness in environment, it is an effective and ideal substance for the fabrication of sensors and biosensor-based devices in different transduction modes, from electrical and electrochemical transduction to optical transduction. The schematic diagram of receptor and transducers attachment and their working mechanism is displayed in figure 2.

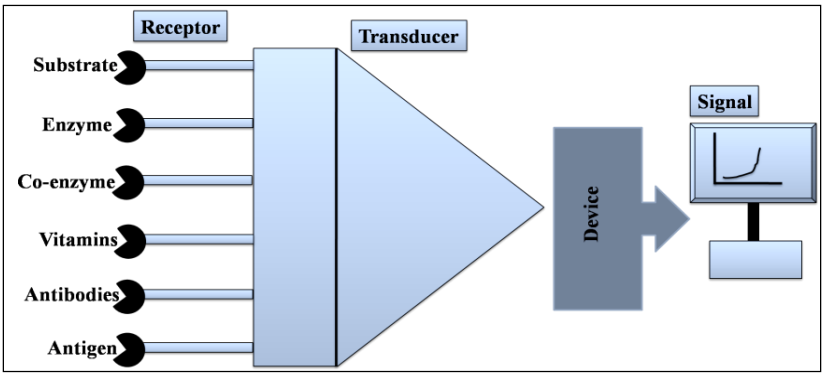

Fig 2: Role of receptor and transducer in a biosensor device

Background of Graphene

Graphene was discovered in 2004 by Andre Geim and Konstantin Novoselov, who received the Nobel Prize in Physics for this in 2010 "for innovative experiments related to the 2D material graphene". Geim and Novoselov cited graphene from graphite, by using the "scotch tape" techniques, to gain a piece of graphene (or carbon) of one atom thick. They performed simple mechanical exfoliation techniques for removing thin layers of graphite from a graphite crystal with scotch tape and then conveyed these layers to a silicon substrate. Moreover, they handled to arrangement samples which contains only a few layers of graphene into a Hall bar and connect electrodes to it. It is a material made of a single layer of carbon atoms arranged in a hexagonal lattice. Being a million times thinner than a human hair, it is the thinnest object ever created. Not only is graphene lightweight and flexible, it is also the world's strongest material, being 200 times stronger than steel. It also conducts electricity faster than most other materials and if stacked in layers it forms graphite, which is also found in pencils. During the panel for the future of science and technology (STOA) workshop chaired by Austrian EPP member Paul Rübig, MEPs discussed with experts the potential of using graphene in various sectors-ranging from energy and engineering to electronics and health-and its impact on the European economy and society. Polish EPP member Jerzy Buzek, chair of the industry and research committee, commented: “We need more graphene-like flagship initiatives in applied sciences and cooperation with the industry”. Greek S&D member Eva Kaili, the first vice-chair of STOA, added: “The stone, bronze and iron ages were defined by materials bearing new technologies. It might be that we are entering the graphene age”. Over

the next 10 years the EU will invest €1 billion in developing graphene-based technologies through the Graphene Flagship initiative, which was part of the Horizon 2020 programme. The motivation is to improve graphene and related layered materials into something that can be used for everyday products. Novoselov said: "The most vital results would be that Europe keeps playing a leading role in innovation and production. By the end of the 10 years [of the Flagship programme], we need to have the new graphene - the next wonder material". 2D matrix of carbon atoms of graphene spread out in a honeycomb graphene lattice, is the strongest, thinnest, lightest material, as well as the excellent heat and electricity conductor ever discovered. Graphene is the course of harsh research and is revolutionize towards entire industries, as researchers cerebrate many potential types of graphene-based materials and its applications. A long history is hidden behind the graphene and had already been in alterness since the nineteenth century. English chemist Benjamin Collins Brodie discovered the highly layered nature of thermally reduced graphite oxide in the year 1859 having reported the atomic weight of graphite in the Philosophical Transactions of the Royal Society of London that year. Many more graphene research works took place from the time, and in the year 1947 a work by P.R. Wallace is a good example-he depicted the electronic structure and reported the linear dispersion relation. Later on, in the year 1962, Boehm and colleagues had proposed their work details on graphite flakes. They isolated and inspected single graphene sheets by transmission electron microscopy (TEM) and X-ray diffraction in the year 1961. The term graphene was first used in the year 1987 to discuss the single sheets of graphite, and it was also worned in early descriptions of carbon nanotubes. In the early 70s chemists find out deposition techniques of carbon in graphene monolayers onto other materials.

Disregarding of its intricate history, graphene is an alluring material that holds great commitment, which is drastically turning a reality as companies and researchers are working tirelessly to fabricate techniques for generating, using and applying graphene in everyday products.

Synthesis and Characterization of Graphene

Synthesis:

The existence of an industrial revolution with respect to graphene and its usage into several products surrounding us including drugs and their delivery, medical devices, as well as many products and devices that

advance the quality of life. Generally, graphene is formed by using two main blueprint and each of them bears various fabrication methods. In a top-down approach, graphene derivatives can be gained from any carbon source such as graphite flakes or powder that is mechanically or electrochemically exfoliated and is leads to chemical oxidation-reduction reactions. For example, scotch tape methods, sonication in a Brodie methods, liquid phase, Hummers method, etc., are the top-down methods used in the fabrication of graphene derivatives. In contrast, the bottom-up strategy is dependable on the synthesis of graphene layers from the carbon atom bases and includes numerous fabrication techniques such as chemical vapour deposition, epitaxial growth, thermal pyrolysis, etc. All these fabrication methods have their own merits and demerits. The two synthesis methods such as top-down and bottom-up are estimated by layer numbers, the nature thickness, and average size of the graphene materials. In top-down method growth mechanism process, graphene sheets are generated by exfoliation/separation of graphite and its derivatives introducing graphite oxide (GO). Different synthesis technique of graphene and its derivatives are illustrated in a classification tree stepwise.

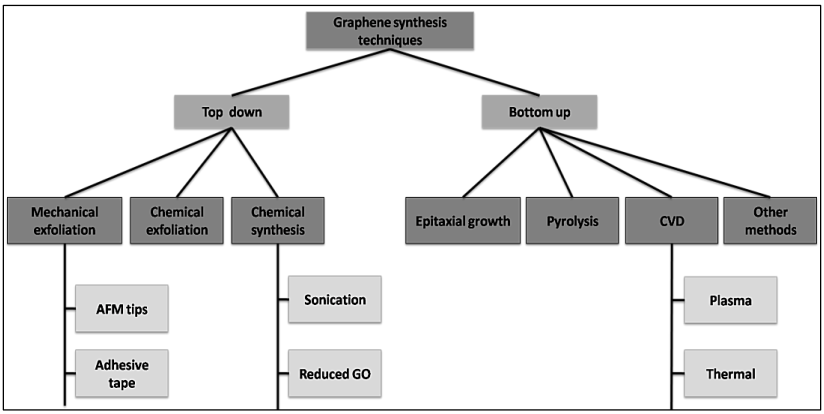

Fig 3: Classification of graphene synthesis methods

Some of the Techniques of Exfoliation are Discussed Below

Micromechanical exfoliation:

The general scotch type of peel off method is called mechanical exfoliation. It was the very first technique utilized by Novoselov and Geim for the generation of graphene by an adhesive tape to force the graphene layers apart [16, 17]. In this method, multiple layers of graphene stick on the

tape after peeling off, but with frequent peeling, it breakdown into few graphene flakes. For disengagement, the tape is stuck to an exact substrate (acetone) and a final scotching with a fresh tape which is carried out to get flakes in different in both size and thickness which can be searched under a light microscope on SiO_2/Si substrates [18]. This process is slow and not precise, hence the material formed is most frequently used to analysis the graphene properties rather than using it in a commercial way [19]. This method can also be accomplished by using various agents such as electric field [20], epoxy resin [21], and by transfer printing technique [22].

Electrochemical exfoliation:

Graphite exfoliation method by electrochemical has turns into a simple but yet high generating process in recent times for the generation of huge quantity of graphene [23]. This method involves the usage of various types of graphite structure such as plates, graphite foils, graphite, rods and powders as electrodes in an aqueous or non-aqueous electrolyte and electric current to extract out the expansion of electrodes. The electrodes are basically of two types based on the power applied, i.e., Cathodic (Negative) and Anodic (Positive) electrodes [24, 25]. Wang *et al*. in their reports used pristine Graphite as electrodes and PSS (Polysodium-4-styrenesulfonate) which is soluble in DI water to embodied the electrolyte [26]. They gathered the graphite rods in an electrochemical cell which was fulfilled with the electrolyte. A persistent current of 5 V was supplied. After a certain time of electrolysis techniques, there is aggregation of a black material at the anode surface. The exfoliation technique was performed for 4 h to separate the product from the cell. It was then centrifuged at 1000 rpm and then the product was drastically poured out. The dispersion gained fis extremely stable. Powder dry graphene was obtained by cleaning the dispersion with DI water and alcohol which was followed by vacuum drying. Then the production was indicated by weighing the dry powder and sediment [27].

Pyrolysis:

The pyrolysis word is from the Greek-derived product pyro and lysis. Pyro means fire and lysis means separating. The simple method for the fabrication of few layer graphene, carbon atom is synthesized on metal surface. Synthesis of carbon atom on a metal surface is a simple technique which is used to produce few-layer graphene. One of the common and unique process of synthesis of graphene is the thermal decomposition of silicon carbide (SiC). At high temperature, Si is desorbed while C atom

which forms few graphene layers is left behind. This method has acknowledged an excellent improvement through the continuous generation of graphene films in mm scale at a temperature of 750 ℃ on a thin film of nickel coated on SiC substrate [28]. The merits of using this technique is the random fabrication of graphene films over the total SiC coated surface. Although, this technique may not be used in graphene synthesis in large scale. A same path is practiced in the thermal decomposition of ethylene at 1000 k. The benefits of this synthesis process is the generation of mono-layer of high purity graphene [29].

Hummers' method:

This is a chemical technique which can be used to generate graphite oxide through the addition of potassium permanganate to a solution of graphite, sodium nitrate, and sulfuric acid. Hummers' method was employed to prepare GO and reduced GO (rGO) was obtained with the aid of NH_3H_2O aqueous and hydrazine hydrate. The mixture of flake graphite/$NaNO_3$ was prepared in a weight concentration of 2 : 1. Next, the mixture was mixed into a beaker with an instant amount of 98 wt.% H_2SO_4 at 15 °C and a suspension was seized. Then, $KMnO_4$ powder which has role as an oxidation agent was mixed gradually into the suspension with continuous magnetic stirring. $KMnO_4$ powder is 3 times more weight as much as the one of the mixture. There were 3 steps for the following process. First of all, it is the low temperature reaction. The mixture temperature was monitored below 20 °C for 2 hours; at the same time, the suspension should be stirred continuously. The second step is the mid temperature reaction. The temperature of the mixture was controlled at 35 °C for 30 minutes after $KMnO_4$ was totally dissolved. Finally, it is the high temperature reaction. A particular amount of DI water was mixed into the mixture in slow manner; therefore a large amount of heat was discharged when con. H_2SO_4 was diluted. After 15 minutes, particular amounts of hot water and 30% H_2O_2 aqueous were mixed into the mixture, respectively, with continuous stirring. A bright yellow suspension was filtered by the filter paper when it was still hot, and the solid mixture was cleaned with dilute HCl aqueous and distilled water and dried in vacuum oven at 70 °C for 24 h.

400 mg GO was dispersed in 400 mL water followed by 30 minutes of ultrasonic treatment. Thus, a homogeneous brown aqueous suspension of GO was gained. The pH of the suspension was maintained to 10 by adding NH_3H_2O. A arise of hydrazine hydrate was mixed into solution and heated at temperature 80 °C for 24 hours, and the weight ratio of hydrazine hydrate

and GO was maintained at 10 : 7. A type of black flocculent material was drastically precipitated out of the solution. The product was achieved by filtered with the filter paper. Lastly, the resulting black element was cleaned with water and methanol followed by drying at 80 °C for 24 h. The steps of the process are shown in the figure 4.

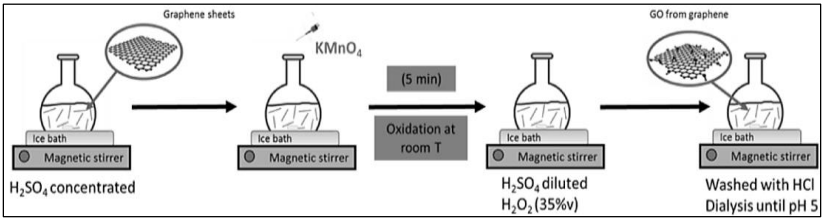

Fig 4: Synthesis of graphene oxide from graphene by Hummers method [30]

Chemical vapour deposition (CVD):

CVD is a bottom-up synthesis process, which is used for generation of highly pure graphene material on a broad-scale basis [31]. This process involves combination of gas molecule inside a reaction chamber with a surface substrate under conditionally pressure, applied temperature and gas flow rate [50]. A common CVD instrument is found to be have quartz reaction chamber, a pump, a mass flow controller, thermocouples for temperature measurement, a vacuum system, a gas delivery system, a computer for auto-control and an energy system [32]. Various kind of substrates are used in CVD for graphene film growth, such as Nickel (Ni), Copper (Cu), Iron (Fe), and Stainless steel [33-36]. Methane (CH_4) and acetylene (C_2H_2) are normally used as a carbon source. There are two CVD method by which the carbon source is activated; thermal CVD and plasma-enhanced CVD (PECVD). Transition metal atoms such as Cu and Ni have commonly been used for graphene growth in the CVD process. This thin films growth on the substrate follows two steps:

i) Formation of carbon by pyrolysis of the precursor of the gas.

ii) Formation of graphene carbon structure by using the segregated carbon on the surface of the metal catalyst.

For example, the generation of graphene by using polycrystalline Ni is gained by first annealing Ni in an H_2 atmosphere at the applicable temperature of 900-1000 ℃ with particle size. The substrate is disclosed to H_2/CH_4 gas mixture; here CH_4 is used as the carbon source. The deterioration of hydrocarbon turns the C atom to disperse in the Ni film where the solid

solution is formed. Ni is highly soluble at high temperature and the solid Ni solution is cooled down in argon gas to generate precipitate of Ni-C which engraves graphene. However Ni is a good substrate for the graphene generation, the Ni film quality can affect the size and percentage of the monolayer graphene. The figure 5 illustrate the techniques of CVD process for the fabrication of layered structure of graphene and its oxides.

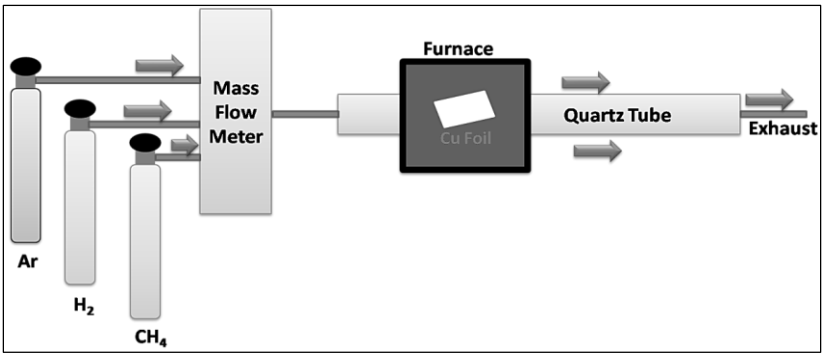

Fig 5: Schematic diagram of CVD process for the deposition of layers of graphene and its derivatives

Characterization of Graphene

Characterization of graphene is very important for study of graphene and derivatives and its research. It includes the investigation of graphene properties, structure, defects, and the number of layers based on microscopic and spectroscopic measurements.

Ultraviolet Visible Spectroscopy (UV-Vis):

It can be applied to analyze the types of graphene, such as pure graphene, graphene oxide, and a few layers of graphene. The UV-vis absorbance spectra results from electron transition at carbon π bonds (ππ* transitions). Single-layer, pristine graphene and graphene oxide exhibit absorption peaks around 250nm, 270 nm and 230 nm, respectively [37]. For analyzing a number of graphene layers, typical thicknesses of graphene can be estimated and calculated from UV transmittance data. Single-layer graphene has 97% transmittance at 550 nm wavelength and this value of transmittance decreases with increasing layers of graphene at the same wavelength.

Transmission Electron Microscopy (TEM):

Images are formed by the electron interaction with materials when an electron beam is transmitted through a material. When graphene material is dipped in dimethyl sulfoxide (DMSO) solution the layers can be clearly visible from the TEM image. Three, four, five, and six layers of graphene can be observed as three, four, five, and six dark fringes, respectively. Carbon atomic layers are parallel to the electron beam [38].

Scanning electron microscope (SEM):

This is used to investigate the morphology of graphene. SEM images detect impurities, graphene folds, and discontinuities during the synthesis process. However, it's restricted in the resolution of ultrathin layers of graphene. Due to the interaction of PET and graphene, the thickness of the graphene sheets increased from 1.57 nm to 50 nm. Large surface area of graphene nanosheets enhances the area between interface of PET and graphene. This provides many tunnelling sites for electron transport [39].

Raman spectroscopy:

Quality of Graphene structure and the number of graphene layers can be estimated by Raman spectroscopy. Usually three main peaks are there in graphene and other carbon nanostructures, namely D, G, and 2D peaks. The D peak, situated at 1350 cm^{-1}, explains defects in sp^2 bonded carbon atoms and as a results the backscattering phonon conserve momentum. The G peak displays at 1580 cm^{-1}, which corresponds to lattice vibrational modes (E_{2g} symmetry) [40]. The 2D peak situated at 2700 cm^{-1} which appears from second-order Raman scattering, which involves two phonons near the Dirac point. The ratio of peak intensities, I_D/I_G and I_{2D}/I_G, can be used to estimate defects in graphene and the number of graphene layers, respectively [41, 42]. The ratio I_D/I_G increases when disorder in graphene increases. The increasing ratio results from a higher defect density which creates more elastic scattering. However, an increase in the I_D/I_G ratio occurs until the carbon structure becomes more amorphous [43]. Then, the ratio begins to decrease. To investigate the number of graphene layers, the $I_{2D}/1_G$ ratio and the position and shape of the 2D peak have been mainly used [44]. If the number of graphene layers increases, G peak intensity increases, as well as the position and shape of the 2D peak change.

X-Ray Diffraction (XRD):

This is an important process for the identification of phase of materials which is based on information from unit cell dimensions. A high and sharp

diffraction peak of pure graphite appeared at 2θ=26.6°. After pure graphite is oxidized, the peak shifted to 13.9°, resulting from the presence of oxygen molecules which was functionalized between graphite layers. After complete graphite oxide exfoliation, there was no diffraction peak present, which indicates that the graphite oxide structure was removed and graphene nanosheets were formed.

Properties of Graphene

The property of graphene is unique because of its carbon structure and nanoscale geometrically stable. Various properties are enlisted and discussed in details.

Electronics properties:

This is the most important properties of graphene is that it is a zero-overlap semimetal which have electrons and holes as charge carriers and has very high electrical conductivity. Carbon atoms have a total of 6 electrons; 2 in the inner shell and 4 in the outer shell. In an individual carbon atom the 4 outer shell electrons forms chemical bonding, but in graphene, each atom is interconnected to 3 other carbon atoms on the 2D plane, whereas 1 electron is freely available in the 3D plane and it is responsible for electronic conduction. These highly-mobile electrons are called pi (π) electrons and are situated above and below the graphene sheet. The overlapping of pi orbitals help to increase the carbon to carbon interactions in graphene material. The fundamental of this property of graphene are discussed by the bonding and anti-bonding (the valance and conduction bands) of these pi orbitals. Due to the presence of delocalized pi-electron system across the entire surface in graphene, the electrons movement is very fluid. Because of the overlapping pi-electrons, the graphene system has no band gap allows for an easy movement of electrons without the need to input energy into the system. The mobility of electronic graphene is very high and the electrons behave like photons. From the experiments executed up to date the electron mobility more than 15,000 $cm^2V^{-1}s^{-1}$, with the potential of producing about 200,000 $cm^2V^{-1}s^{-1}$.

Thermal properties:

The repeating chain structure of graphene turns it an ideal material for conduction of heat in plane. Interplane conductivity is problematic and commonly other nanomaterials such as CNTs are composited to increase the interplane conductivity. The regular structure allows the movement of

phonons through the material without impediment at any point along the surface. Graphene has two types of thermal conductivity-in-plane and inter-plane. The in-plane conductivity of a single-layered sheet is 3000-5000 W m^{-1} K^{-1}, but the cross-plane conductivity can be as low as 6 W m^{-1} K^{-1}, because of its the weak inter-plane van der Waals forces. The specific heat capacity for graphene has never been calculted directly, but the specific heat of the electronic gas in graphene has been estimated to be ~2.6 $\mu Jg^{-1}K^{-1}$ at 5 K.

Mechanical Strength:

Graphene is one of the strongest materials ever discovered. It has a tensile strength of 1.3 x 10^{11} Pa. Although it has an excellent strength, it is also very lightweight (0.77 mgm^{-2}). In 2007, Atomic force microscopic (AFM) tests were done on graphene sheets that were suspended over SiO_2 cavities. These experiments showed that graphene sheets (with thicknesses of between 2 and 8 Nm) had spring constants from 1 to 5 N/m and a Young's modulus (different to that of three-dimensional graphite) of 0.5 TPa.

Flexibility/Elasticity:

The repeating chains of sp^2 hybridized are the backbone of graphene molecules which are very flexible, due to the presence of rotation around some of the bonds, whilst still supplying enough rigidity and stability that the molecule can combat changes in arrangement and support other ions. This is a very fascinating property as there are not many molecules that can be flexible and supportive at the same time. In terms of its elasticity, graphene has spring constant between 1-5 Nm^{-1}, with a Young's modulus of 0.5 TPa.

Optical:

Graphene can absorb a rather 2.3% of white light, which is one of the interesting characteristics, mainly considering the thickness is 1. Due to its aforementioned electronic properties; the electrons roled as massless charge carriers with very high mobility. A few years ago, it was reported that the amount of white light absorbed is based on the Fine Structure Constant. Compositing another layer of graphene enhances the intensity of white light which is absorbed by the same value (approx. 2.3%). Opacity of Graphene's of $\pi\alpha \approx 2.3\%$ equates to a universal dynamic conductivity value of $G=e2/4\hbar$ (±2-3%) over the visible frequency range.

Application and Advancement of Different Types of Graphene-based Biosensors

Graphene-based electrochemical biosensors:

Graphene-based materials have been used in large scale for the fabrication of highly sensitive and efficient electrochemical sensors as they have unique and extraordinary electric and physical properties. These biosensors calculate the transformed electrical signals which are caused by the generated electrons by the chemical reactions occurred between the target and biorecognition elements. The application of graphene-based materials for the electrochemical inspection of biomolecules is extremely vital to the development of biomedical instruments, clinical diagnosis, and disease treatment. Electrochemical sensors are dependent on the change of current, potential or impedance upon the circumstances of reaction on the electrode surface has a great affect on its performance. Electrochemical methods have obtained enormous attention as they are relatively low-cost, simple, low detection limits and easy to miniaturize [45]. The large specific surface area and extraordinary electrical conductivity of graphene and its derivatives allows the adsorption of protein and rapid transfer of electron between the redox centers and the surface of the electrode. This ensures the accuracy and selectivity to detect the target biomolecules.

Guo *et al*. studied a graphene-based electrochemical biosensor to determine ultrahigh sensitive DNA with a 9.4 zM detection limit [46]. Huan *et al*. proposed a label-free electrochemical biosensor to detect DNA which is based on gold nanoparticles (AuNPs)-toluidine blue-GO nanocomposites rapidly with a detection limit of 2.95 pM [47]. Label-free ultrasensitive findings of miRNA electrochemical sensor based on sandwiched silver nanoparticles (AgNPs) in polyaniline and N-doped graphene was also improved [48]. Such a graphene-based biosensor has high sensitive detection towards target miRNA with a wide range of detection range from 10 fM to10 μM and a low detection limit of 0.2 fM. A variety of graphene-based immune electrochemical biosensors are steadily being improved for sensitive identification of cancer-based proteins. Chih *et al*. suggested a reusable immunosensor which is based on a GO-modified Au electrode. The use of GO implement an effective carrier for the avastin antibody, and a transforming of amperometric signal permit significant detection of VEGF in human plasma with a limit of 31.25 pg/mL [49]. He *et al*. deposited a platform by electrophoretic deposition of rGO onto a gold electrode with post-functionalized folic acid which act as ligand for the sensitive detection of

folic acid protein with a value of 1 pM. Upon the target binding, an efficient decreasing of current can be estimated by using differential pulse voltammetry [50]. Astillo *et al*. discussed a peptide nanotube-folic acid-modified graphene electrochemical biosensor to detect the human cervical cancer cells. The identification of human cervical cancer cells was based on the specific binding of folic acid and the folate receptors described in cell surfac [51]. Erika *et al*. proposed a label-free graphene-based electrochemical immunosensor for inspection of cystatin C. The detection limit of this immune sensor was 0.03 ng/mL [52]. Lv *et al*. discussed an electrochemical sandwich immune sensor by using nitrogen/sulfur co-doped GO and Au@Ag nanocubes [53]. Such a sandwich immune sensor gained detection of cardiac troponin I (cTnI) with a linear range from 100 fg/mL to 250 ng/mL and a detection limit of 33 fg/mL. A sandwich-format electrochemical immune sensor for simultaneous determination of alpha-fetoprotein (AFP) and carcinoembryonic antigen (CEA) was prepared by using carboxyl graphene nanosheets acted as sensing probes, which were performed by immobile toluidine blue and antibody of CEA and AFP [54]. A graphene flowers-modified electrochemical sensor was improved for determination of three targets simultaneously. The graphene flowers-modified electrode has high electrocatalytic activities, which was crucial for the detection of ascorbic acid, dopamine and uric acid in urine simultaneously having advanced selectivity and sensitivity [55].

Graphene-based electrochemical sensors also involved for the development of environmental analysis to detect heavy metal ions (Pb^{2+} and Cd^{2+}) [56, 57]. Li *et al*. proposed that Nafion-graphene composite film which is based on electro-chemical sensors not only has advanced sensitivity for the metal ion (Pb^{2+} and Cd^{2+}) detections, but also encourages the interferences as there is synergistic effect of graphene nanosheets and Nafion. The stripping current signal is immensely improved on graphene electrodes. The linear range for the detection of Pb^{2+} and Cd^{2+} is wide (0.5 μgL^{-1}, 1-50 μgL^{-1}, 1and 1.5 μgL^{-1}, 1-30 μgL^{-1} for Pb^{2+} and Cd^{2+}, respectively). The detection limits (S/N=3) are 0.02 μgL^{-1}1 for both Pb^{2+} and Cd^{2+}, which are more sensitive than those of Nafion film modified bismuth electrode [58], and comparable to Nafion/CNT coated bismuth film electrode [59]. The improved performance is indicated to one of the unique characteristics of the graphene (nano-scale thickness of these sheets, nanosized graphene sheet, and high conductivity), which equipped with the ability to strongly adsorb target ions, increased the surface concentration, improved the sensitivity, and mitigate the fouling

effect of surfactants. The main merits of such biosensors are cheap, high sensitivity and quick detection, and the future pathways of graphene-based electrochemical biosensors devices are portable, high throughput, and miniaturized.

Graphene-based DNA and enzyme biosensors:

Deoxyribonucleic acid (DNA) has a wide range of chemical, physical, and biological characteristics transforming this biomolecules highly efficient for biosensor technologies. Among the important characteristics of DNA for a biosensor is its flexibility, ease of synthesis, facile chemistry to attach to simple regeneration, distinct platforms, and high specificity due to uncommon sequences of nucleotides [60, 61]. The response of DNA biosensor was confirmed by using several genomic soybean samples which contains different concentration of genomic GM DNA. For that purpose, standard certified genomic GM samples for soybean of 0% and 100% GM contents (Roundup Ready GM-soybean, Monsanto, USA) were used [62]. The electrochemical DNA biosensor was then applied under optimized conditions to determine the GM DNA content of soybean genomic DNA extracts. The electrochemical voltammetric response obtained was compared with the original certified GM DNA concentrations. The percentage of GM DNA recovery of the DNA biosensor was also calculated. Most recently, graphene nanospheres (GNS) were also synthesized using various methods [63, 64]. These spherical shaped graphene nanoparticles may have good potential for biosensor applications, especially for DNA biosensing. However, several merits and demerits of DNA biosensors have been investigated. Significant advantages of DNA biosensors exist high specificity, ability to be used for real time investigation, to be fabricated as a small measurement system, and to achieve multiplex evidence of various targets [65, 66]. Moreover, one of the important disadvantages of DNA biosensors is that DNA can be easily discarded, thus, compelling particular storage and analysis conditions, such as specific media or a buffer to keep the DNA stable and control its attachment to the transducer. Additionally, DNA-based sensors' effectiveness can be influenced by changes occur in pH or temperature [67]. For instance, the sensitivity of DNA biosensors depends on experimental temperatures because the hybridization event of the probe with the target molecules will occur at optimum temperatures to be determined prior to the deployment of the sensor. In the case of pH, the current response shows the highest signal at pH 7.0, while there is almost no signal at pH below 7.0. Hence, a buffer with potassium or sodium phosphate

is required to increase the effectiveness of the sensor [68, 69]. The electrochemical sensor is based on measurements of the change in voltage, current, or impedance that can result from changes in electrochemical factors, such as electron loss, conductivity or capacitance changes, which occurs by the hybridization of DNA or the oxidation of adenine (A), thymine (T), cytosine (C) and guanine (G) of the DNA. Depending on the sensing material and target, the sensor can have a wider detection range and sensitivity. Graphene-based DNA biosensors have been estimated with focus on lowering the detection limits, speeding time of measurements and facilitating the fabrication process and biomedical applications.

Lactate oxidase (LOx) and lactate dehydrogenase (LDH) are the most unique enzymes used as catalysts to crunch the reactant molecule and catalyze the enzymatic reaction resulting in the product molecule [70-73]. The lactate oxidase enzyme is important for the generation of pyruvate and hydrogen peroxide through the catalyzation of lactate and oxygen [74, 75]. However, the LOx is unstable since it loses its activity in a short time. Individually, the lactate dehydrogenase enzyme catalyzes lactic acid into pyruvic acid. In anaerobic metabolism, pyruvic acid is transformed to lactic acid when there is a lack of oxygen during the glycolysis process. Moreover, the lactate dehydrogenase enzyme can act over other substrate molecules in particular conditions, enhancing the final product. The quantification of lactate has been broadly marked in the literature; there are several devices proposed as a lactate sensor by using various measurement methods, materials, device structure, and biological fluids. Most of the literature are attracting on sweat and saliva samples to generate non-invasive device, but these biological fluids exist a bad signal response because of contamination, pH values, and low concentration of the target. The lactate was depicted by using the LDH enzyme to catalyze the chemical reaction in the biological fluid. The enzyme was immovable by using different substances to guarantee stability and selectivity over the active layer.

Graphene-based glucose biosensors:

Glucose biosensors happen to be crucial in the process of insulin delivery to effectively manage diabetes. The system provided quick and accurate results. Fast and efficient methods for the determination of glucose are becoming increasingly important in biology, chemistry, and the food industry; glucose determination is also important in the medical field for controlling diabetes. Diabetes is a worldwide public health problem and one of the leading causes of death and disability in the world [76-78]. The drastic

changes in the glucose level were assessed well, which could become crucial to develop therapeutic inventions concerning hypo-and hyperglycemia. Amperometric enzyme electrodes were utilized in most of the sensors being used for constantly monitoring the transitions in the glucose level. Closed-loop glycemic control required innovative approaches to address the issues of biofouling, calibration, selectivity, inflammatory response, stability, and miniaturization, which happened to be common for most of the other remote sensors. To measure the glucose levels successfully, the issues and challenges in the process were discussed thoroughly. The impact in the treatment and management of the diseases was deliberated through the concepts applied to manage diabetes. The crude estimated prevalence of diabetes in adults in the United States (US) has been reported to be 9.6% (20.4 million) in 2003-2006 [79]. Moreover, it is predicted that 48.3 million people in the US will have diabetes by 2050 [80]. Numerous studies have been performed to develop simple, sensitive, and accurate approaches for glucose detection, especially those using glucose oxidase (GOx), which has high selectivity and sensitivity [81-83]. Glucose act as an important role in human metabolism techniques and abnormal glucose levels in blood or body fluids are precisely related to some diseases, such as diabetes mellitus. Therefore, high-performance glucose sensors have auspicious applications in medical diagnosis and healthcare products. Different types of glucose sensors such as optical and electrochemical sensors have been researched, in which the electrochemical sensors can be more efficiently used in practical applications. Many electrochemical glucose sensors have been successfully improved by using various functional materials, including carbon-based nanomaterials (e.g. carbon nanotubes, graphene), metal nanoparticles and oxides [84-86]. In 2010, Huang *et al*. firstly proposed glucose sensors which is based on SGGTs by advancing the graphene layers with an enzyme glucose oxidase (GOx) [87]. The devices can detect the glucose levels down to 0.1 mM. They studied that the products from the oxidative reaction of glucose were pledged for the increase of channel current while the accurate mechanism was not estimated. In 2012, Kwak *et al*. proposed a similar SGGT glucose sensor with GOx immobilized on its graphene channel [88]. The response of the device was affected to be related to H_2O_2, produced in the oxidation of glucose catalyzed by GOx. Graphene quantum dots (GQDs) are a outstanding illustration of a graphene nanomaterial that is used to form novel electrochemical sensors (Razmi and Mohammad-Rezaei, 2013). GOx was immovable on GQD-modified carbon ceramic electrode (CCE), and well-defined quasi-reversible redox peaks were reported. The UV-Vis

photoluminescence spectroscopy, transition electron microscopy, field emission SEM, EIS and cyclic voltammetry techniques were used for characterizing the electrochemical biosensor. The table indicates various kinds of Graphene based glucose biosensors fabricated by researchers for last two decades:

Table 1: Proposed fabricated of Graphene based biosensors, its linear range and sensitivity level

Graphene Modified Electrode	Linear Range (LOD)	Sensitivity	Reference
Reduce graphene sheet/GOx	1-10 mM	100 µM	Zhang *et al.* (2014)
Graphene/PANI/GNPs/GOx	0.004-1.12 mM	0.6 µM	Xu *et al.* (2014)
Graphene platelet/GOx	2-22 mM	20 µM	Liu *et al*. (2011)
GQDs/GOx	5-1270 µM	1.73 µM	Razmi and Mohammad-Rezaei (2013)
MGF/GOx	1-12 mM	0.25 mM	Wang *et al.* (2014)
Graphene/TiO_2/GOx	0.1-8 mM	10 µM	Jang *et al*. (2012)
Graphene/chitosan/GOx	0.08-12 mM	0.02 mM	Kang *et al*. (2009)
Chitosan/Prussian blue/graphene/GOx	0.025-3.2 mM	0.01 mM	Zhong *et al*. (2012)
Reduce graphene/GOx/Nafion	10-500 µM	3.33 µM	Gu *et al.* (2012)
Reduced carboxyl graphene/GOx	2-18 mM	0.02 mM	Liang *et al.* (2015)
Graphene/SiO_2/Ag NPs/GOx	0.1-0.26 M	4 µM	W. Lu *et al.* (2011)
Graphene/GNPs/GOx	0.02-2.26 mM	4.1 µM	Cao *et al.* (2013)

Challenges in Recent Progress in Accuracy, Selectivity and Sensitivity

A biosensor is a unified receptor-transducer device, which can disciple a biological response into an electrical signal. The design and improvement of biosensors devices have taken a center stage for researchers in the recent time period owing to the broad range of biosensor applications, such as health care and disease diagnosis, water, environmental monitoring, and drug delivery and food quality monitoring. The crucial challenges included in the biosensor advancement are

i) The efficient capturing of biorecognition signals and the transformation of these signals into electrochemical, electrical, optical, gravimetric, or acoustic signals (transduction process).

ii) Increasing transducer performance i.e., shorter response time, increasing sensitivity, reproducibility, low detection limits even to detect individual molecules.

iii) Miniaturization of the biosensing devices using micro-and nano-fabrication technologies.

Those objections can be met through the integration of sensing technology with nanomaterials, which range from 0D to 3D, exhibiting a large surface-to-volume ratio, good conductivities, shock-bearing abilities, and color tunability. The conventional three-electrode electrochemical system compose of a reference electrode (RE), working electrode (WE) and a counter electrode (CE) (Kimmel *et al*., 2012). The corelation of the sensor with target analyte produces an electrical signal that is a measure of the analyte concentration. This techniques bring about by permitting charged molecules to change through a thin electrolyte layer. This classical method offers several benefits, including high sensitivity and selectivity, linearity of response in a broad range of analyte concentrations, minimal space and power needs, onsite detection capability, and affordable instrumentation (Wang, 2007). Nevertheless, it has its own challenges, such as reliance on an electrolyte, which introduces pH working range limitations, susceptibility to pH-related interferences that reduce stability, electrode degradation, and the need for frequent maintenance and calibration. Additionally, sensitivity can be hampered by non-specific reactions between electroactive impurities on the electrode surface and the sample (Sang *et al*., 2013). graphene and its derivatives has significantly advanced the application of electrochemical sensors for real-time detection and monitoring of pesticides. In the three electrode electrochemical sensors, graphene's large surface area and exceptional electrical conductivity make it an ideal candidate for the working electrode (WE) (Zafar *et al*., 2023a). Its high surface to volume ratio enhances the interaction between analytes and the electrode surface resulting into improved sensitivity and detection limits. Additionally, its excellent electron transfer properties facilitate rapid and efficient redox reactions, crucial for electrochemical sensing applications.

Various approaches have been improved to cripple enzymes onto graphene surfaces to produce enzyme-based biosensors. Some of the most unique process are mixing, ultrasound, cyclic voltammetry and sonication. These process permits the attachment of the enzymes via covalent bonding, adsorption, or physical entrapment. Another process which is used to disable enzymes on the nanomaterial is the EDC/NHS chemistry. An appreciable advance has been made in the synthesis; processing, characterization and applications of nanomaterials used to design electrochemical sensors and biosensors with considerably enhanced sensitivity. Most important, (bio)

sensors have to be specific, reusable and to have high sensitivity toward specific analyte. The graphene synthesis can be accomplished by two main approaches i.e. top-down (destruction) and bottom-up (construction) techniques. By the top-down techniques (mechanical and electrochemical exfoliation, liquid-phase exfoliation, oxidative exfoliation-reduction, arc discharge, and unzipping of carbon nanotubes) usually, the layers of larger precursors (graphite or other carbon-based materials) are exfoliate in to single, bi-and few-layer graphene. Among these, the graphene generated through the electrochemical exfoliation of graphite has lower oxidation degree, better crystallinity, and fewer layers making it a very appropriate material for electrodes. This method verified to be a very auspicious technique for graphene synthesis and processing. The bottom-up methods (epitaxial growth, chemical vapour deposition, total organic synthesis and template route) build up graphene from smaller molecules. However graphene created by these process are almost impurity free with a large surface area, the demerits are the high production costs low yield, and elaborated experimental set-ups. The revolution of biosensors devices has been categorized into three generations which is based on the attachment of the components, that is, in accordance with the process of integration of the bio-recognition element (bioreceptor) to the transducer. In the first generation, the biosensors measure the content of the analytes and products of the bioreceptor reactions, which diffuse to the surface of the transducer and generates an electric response. In the second generation, original components such as auxiliary enzymes and co-reactants (artificial or partially toxic mediators or nanomaterials), are unified into the biological component layer of the biosensor with the view of increasing analytical efficiency. These types of sensors are called mediator amperometric biosensors. In the third generation, the bioreceptor molecule becomes an integral part of the base sensing element, i.e., biosensors improved toward involving enzymes and mediators on the same electrode rather than freely diffusing mediators in the electrolyte. A direct synergy was entrenched between the enzymes and electrode through the transfer of electrons, without any concern of intermediate stages like in nanomaterials. Besides the interaction, cost effective design and feasibility of having duplicated measurements are the convenience of this biosensor generation.

The minimal concentration of analyte that can be correctly identified in a minimal number of steps and in low concentrations (ng/mL or fg/mL) to authenticated the presence of analyte residue in the sample. Linearity commit

to the certainty of the consistent results. A bioreceptor can find out a specific target analyte molecule in a sample which is a composition of spices and undesirable contaminants. Graphene has high conductivity, luminescence, and flexibility. Graphene sensors are applicable in early cancer recognition [89]. Graphene-based MoS_2 sensor detects formalin which is present in food and harmful to our body [90] Graphene perturbations added to waveguide structure increase the sensitivity [91]. Graphene-based plasmonic sensors and nano-ring resonators are linked with biomolecules that are used for the detection of hemoglobin through the finite element method (FEM) [92]. Graphene-based metasurface infrared sensor using C-shaped material as tungsten increases sensitivity and it is obtained through shift absorption peak by adding biomolecules. Graphene-based long-period fiber grating (LPFT) with glucose is useful in the pharmacy field where the sample is detected from a linear response of graph which shows better detection. These graphene biosensors are tuned in terms of various properties to increase and control the sensitivity of the device probe. Single-mode fiber-based sensors are sensible for detection and protection from most harmful gases by depositing graphene through various techniques such as UV spectroscopy, atomic force microscope (AFM), etc. The graphene-based polarization-independent sensors are applicable in environmental applications [93]. Graphene fabricated sensors using coated papers as the substrate has an immense effect on cost with increased flexibility. The mixture of electronics and substrate improves the fabrication process of porous material used in application devices such as monitoring, e-textiles, etc. The optical biosensors can be fabricated for the detection of DNA, glucose, hemoglobin, etc. with high sensitivity [94-96]. The demand for tunable and highly sensitive biosensors is increasing for medical applications. We proposed a tunable and highly sensitive biosensor based on graphene-GST material. The H-shape metamaterial is placed above the graphene GST layer to achieve high sensitivity. The tunability is achieved for two phases of GST material. A detailed discussion on various phases of GST, i.e., the crystalline and amorphous phases and the characteristics between these two phases based on the different basis can be found in [97]. The sensitivity analysis is presented using equation below where $\Delta\lambda$ is wavelength change and Δn is refractive index change [98]:

$$S = \frac{\Delta\lambda}{\Delta n}$$

Biosensors are utilized for sensing and encryption and many other purposes. Biosensors are exceptionally fast and accurate at diagnosing bacterial and viral diseases. Using grating sensors, these infections can also be identified with high sensitivity [99]. The sensitivity of biosensors can be increased by using laser-induced graphene (LIG). In 2014, it was found that polymers, such as polyimide, can be directly converted into porous three-dimensional graphene using an infrared CO_2 laser. The discovery of LIG has attracted a significant attention due to its wide range of applications. The advantages of the technology for obtaining LIG compared to conventional methods for the synthesis of graphene are the environmental friendliness of the process and the possibility of controlling the morphology of samples.

Selectivity is another crucial property to acknowledge when choosing a bioreceptor for a biosensor device. A bioreceptor can detect a specific target analyte molecule in a sample combined of admixture spices and undesirable contaminants. To increase the selectivity of the sensor to certain molecules, the surface of the receptor is chemically modified so that these molecules can be immobilized on it. Thus, a high level of selectivity of the biosensor is achieved. The main trends in the improvement of biomedical means of registration and measurement are a decrease in the size of sensor elements, as well as an increase in their selectivity. It is assumed that nanodevices that can be implanted in the human body for continuous monitoring of its parameters will find mass application. Biosensors as chemical sensors that include biological material were first reported by L. Clark and S. Lyons at the symposium of the New York Academy of Sciences in 1962 [100]. They suggested using electrodes modified with glucose oxidase embedded in membranes to create more advanced electrochemical sensors. These results in sensors that are specifically sensitive to certain substrates, since they detect the formation of an enzymatic reaction product or the consumption of one of the substances involved in this reaction. Clark and his coauthors, using the idea mentioned above, developed biosensors for determining glucose and lactate in the blood [101, 102]. The authors deposited monolayer graphene from a suspension onto a preliminarily structured Si substrate. To increase the selectivity, graphene was chemically modified. Selectivity was assessed by nanoscale mechanical deflection of the sheet plane, as the biomarker generates a force that deforms planar graphene into a dome shape, resulting in spectral shifts in optical interference between graphene and silicon substrate. Using the interference properties of light, the authors estimated the magnitude of the deformation from the change in color.

Graphene is an allotropic modification of carbon, formed by a layer of sp^2 carbon atoms and representing a 2D crystal one atom thick. Less than two decades have passed since the discovery of graphene. Graphene has a record-high mechanical strength. Despite this, it has elasticity and can be subjected to 20% deformation without the network structure breaking [103]. Monolayer graphene has a constant optical transparency in the visible range (97.7%) and a transmittance value that linearly decreases depending on the number of layers for *n*-layer graphene. The monatomic thickness of a graphene sheet provides the highest possible surface to volume ratio, a specific surface area of ~2630 m^2/g, and high sorption properties. In addition, it has biocompatibility, which is crucial for biomedical applications. The metasurface thickness of Graphene which is very important in achieving resonance and high absorption is checked between 0.1 µm and 0.5 µm. The higher increase than this in metasurface thickness changes the resonance and due to this, the metasurface thickness of 0.4 µm is selected. The angle of incidence is quite important in the absorption of the structure and the angle of incidence is varied from 0° to 80°. The angular range can be selected based on these angles with higher absorption. The substrate thickness which is quite important in achieving high absorption is checked between 0.2 µm and 1 µm. The best substrate thickness that is observed from the response is 0.6 µm.

Chemical modification of graphene nanomaterials in biomedicine is a necessary step in the development of biosensors. This can advance the dispersion of nanoparticles of these materials in water, ensuring their biocompatibility, and decreasing their toxicity and the ability to correlate with specific analytes. Inferior to the modification types, the synergistic energy between the adsorbed molecule and graphene, as well as the charge transfer in the system, can vary drastically. Besides, functional groups have vital role in certain reaction centers during the adsorption and covalent bonding of various molecules with graphene and its related derivatives [104, 105]. The authors of [106] describe a multiplex portable wireless electro-chemical device based on graphene electrodes with laser engraving for ultrafast detection of COVID-19: Rapid Plex SARS-CoV-2. In this sensor, graphene structures are connected to antibodies and immune system molecules that are sensitive to specific proteins, such as those found on the surface of the COVID virus. When connected to auxiliary electronics, the sensor can transmit data wirelessly to the user's mobile phone via Bluetooth. The applicability of the Rapid Plex SARS-CoV-2 platform with

positive and negative blood and saliva samples in COVID-19 has been successfully evaluated. Based on the results of the pilot study, the authors claim that the multiplex immunosensor platform developed by them, will allow self-testing at home for telemedicine diagnosis and monitoring of COVID-19 and get the result in less than 10 minutes. Such sensors can monitor conditions such as gout and stress levels by detecting extremely low levels of certain compounds in blood, saliva, or sweat. The sensitivity and selectivity of the biosensor based on molecularly imprinted LIGs were comparable to those of sensors fabricated using commercial graphene-based screen-printed electrodes.

Conclusions and Future Prospects

In this review, a brief historical background, various synthesis process and characterizations of graphene, properties of graphene and applications of graphene-based biosensors is discussed in details. Necessary challenges and recent progress on the graphene-based biosensors and their applications are also hypothesized in detail. We also have proposed recent studies discussing graphene and graphene-based biosensors with possible applications in biomedical applications and health related issues. Graphene is reported as one of the most interesting functional nanomaterials in daily life applications because it bears excellent unique properties such as high electrical conductivity, high tensile strength, high elasticity, high carrier mobility, optical transparency and high thermal conductivity of about 97%. From the discussion on synthesis process of graphene, it is noted that CVD is one of the best synthesis process by which a high quality graphene can be fabricated in a large scale basis. In the world of biosensing technology, usage of DNA is the cost-effective method for the gradual detection of viruses, microbes, bacteria or biological markers. A meta surface absorber refractive index biosensor based on graphene-GST is described for high sensitivity of biomolecules.

Commercialization improvement of graphene-based nanomaterials is very encouraging. There are a lot ongoing innovative researches in research institutes around the world for advancement of the current growth mechanisms of graphene to generate fine chemical products in a vast area. Although graphene is an extraordinary electrode material for bio sensing applications in the medical research, novel and original methods for tunable synthesis and processing of graphene shows great attention and should be explored in future studies. The current chemical blueprint for modification of the graphene surface with biomolecules is efficient in specific target

analytes. Nevertheless, the sensing-based platform may be further cultivated to restrict the adsorption of undesirable molecules on graphene surface and boost up the biomolecule's orientation on graphene podiums. Further investigation of physics and chemistry of graphene surface and their interaction of biomolecules for the role of graphene-based biosensors for health-related issues. Now a days miniaturize production of biosensor device has become a trending and most challenging research among various parts of the world for clinical and medical applications. This sensor technology needs to improve in terms of reliability, reproducibility and cost effectiveness with high sensitivity, selectivity and accuracy. However, considerable and remarkable research must go on to ensure, guarantee, and corroborate the biocompatibility and non-toxicity of graphene-based nanomaterials such that their long-term use does not pose any health risk. Futuristic research direction on the graphene-based application in the fabrication of ultra-thin flexible displays, smartphones with transparent touchscreens, biosensors in medical science, nanorobots, and super light cables in aircraft and satellites.

References

1. Geim, A. K., & Novoselov, K. S. (2010). The rise of graphene. Nanosci Nanotechnol: a collection of reviews from nature journals (pp. 11–19).
2. Park, S., & Ruoff, R. S. (2009). Chemical methods for the production of graphenes. Nature nanotechnology, 4(4), 217-224.
3. Park, S., & Ruoff, R. S. (2009). Chemical methods for the production of graphenes. Nature nanotechnology, 4(4), 217-224.
4. Stoller, M. D., Park, S., Zhu, Y., An, J., & Ruoff, R. S. (2008). Graphene-based ultracapacitors. Nano letters, 8(10), 3498-3502.
5. Park, H. J., Meyer, J., Roth, S., & Skákalová, V. (2010). Growth and properties of few-layer graphene prepared by chemical vapor deposition. Carbon, 48(4), 1088-1094.
6. Krajewska, A., Pasternak, I., Sobon, G., Sotor, J., Przewloka, A., Ciuk, T., ... & Strupinski, W. (2017). Fabrication and applications of multi-layer graphene stack on transparent polymer. Applied Physics Letters, 110(4).
7. Nieto, A., Lahiri, D., & Agarwal, A. (2012). Synthesis and properties of bulk graphene nanoplatelets consolidated by spark plasma sintering. Carbon, 50(11), 4068-4077.

8. Bielawski, C. W., Dreyer, D. R., Park, S., & Ruoff, R. S. (2010). The chemistry of grapheme oxide. Chem. Soc. Rev, 39(1), 228-240.

9. Georgakilas, V., Tiwari, J. N., Kemp, K. C., Perman, J. A., Bourlinos, A. B., Kim, K. S., & Zboril, R. (2016). Noncovalent functionalization of graphene and graphene oxide for energy materials, biosensing, catalytic, and biomedical applications. Chemical reviews, 116(9), 5464-5519.

10. Lawal, A. T. (2019). Graphene-based nano composites and their applications. A review. Biosensors and Bioelectronics, 141, 111384.

11. Craciun, M. F., Russo, S., Yamamoto, M., & Tarucha, S. (2011). Tuneable electronic properties in graphene. Nano Today, 6(1), 42-60.

12. Kang, X., Wang, J., Wu, H., Liu, J., Aksay, I. A., & Lin, Y. (2010). A graphene-based electrochemical sensor for sensitive detection of paracetamol. Talanta, 81(3), 754-759.

13. Du, M., Yang, T., Ma, S., Zhao, C., & Jiao, K. (2011). Ionic liquid-functionalized graphene as modifier for electrochemical and electrocatalytic improvement: comparison of different carbon electrodes. Analytica chimica acta, 690(2), 169-174.

14. Alhazmi, H. A., Ahsan, W., Mangla, B., Javed, S., Hassan, M. Z., Asmari, M., ... & Najmi, A. (2021). Graphene-based biosensors for disease theranostics: Development, applications and recent advancements. Nanotechnology Reviews, 11(1), 96-116.

15. Chen, L., Tang, Y., Wang, K., Liu, C., & Luo, S. (2011). Direct electrodeposition of reduced graphene oxide on glassy carbon electrode and its electrochemical application. Electrochemistry communications, 13(2), 133-137.

16. Novoselov, K. S., Jiang, D., Schedin, F., Booth, T. J., Khotkevich, V. V., Morozov, S. V., & Geim, A. K. (2005). Two-dimensional atomic crystals. Proceedings of the National Academy of Sciences, 102(30), 10451-10453.

17. Edwards, R. S., & Coleman, K. S. (2013). Graphene synthesis: relationship to applications. Nanoscale, 5(1), 38-51.

18. Casiraghi, C., Hartschuh, A., Lidorikis, E., Qian, H., Harutyunyan, H., Gokus, T., ... & Ferrari, A. C. (2007). Rayleigh imaging of graphene and graphene layers. Nano letters, 7(9), 2711-2717.

19. Van Noorden, R. (2012). Production: Beyond sticky tape. Nature, 483(7389), S32-S33.

20. Liang, X., Chang, A. S., Zhang, Y., Harteneck, B. D., Choo, H., Olynick, D. L., & Cabrini, S. (2009). Electrostatic force assisted exfoliation of prepatterned few-layer graphenes into device sites. Nano letters, 9(1), 467-472.

21. Prakash, H., Chandra, N., & Prakash, R. (2007). Effect of decoherence on fidelity in teleportation using entangled coherent states. Journal of Physics B: Atomic, Molecular and Optical Physics, 40(8), 1613.

22. Liang, X., Fu, Z., & Chou, S. Y. (2007). Graphene transistors fabricated via transfer-printing in device active-areas on large wafer. Nano letters, 7(12), 3840-3844.

23. C.-Y. Su, et al., High-quality thin graphene films from fast electrochemical exfoliation. 2011. 5(3): p. 2332-2339

24. Liu, F., Wang, C., Sui, X., Riaz, M. A., Xu, M., Wei, L., & Chen, Y. (2019). Synthesis of graphene materials by electrochemical exfoliation: Recent progress and future potential. Carbon Energy, 1(2), 173-199.

25. Yang, S., Lohe, M. R., Müllen, K., & Feng, X. (2016). New-generation graphene from electrochemical approaches: production and applications. Advanced Materials, 28(29), 6213-6221.

26. Luheng, W., Tianhuai, D., & Peng, W. (2009). Influence of carbon black concentration on piezoresistivity for carbon-black-filled silicone rubber composite. Carbon, 47(14), 3151-3157.

27. Shams, S. S., Zhang, R., & Zhu, J. (2015). Graphene synthesis: a Review. Mater. Sci. Pol, 33(3), 566-578.

28. Juang, Z. Y., Wu, C. Y., Lo, C. W., Chen, W. Y., Huang, C. F., Hwang, J. C., ... & Tsai, C. H. (2009). Synthesis of graphene on silicon carbide substrates at low temperature. Carbon, 47(8), 2026-2031.

29. Pan, Y., Zhang, H., Shi, D., Sun, J., Du, S., Liu, F., & Gao, H. J. (2009). Highly ordered, millimeter-scale, continuous, single-crystalline graphene monolayer formed on Ru (0001). Advanced Materials, 21(27), 2777-2780.

30. Costa, M. C., Marangoni, V. S., Ng, P. R., Nguyen, H. T., Carvalho, A., & Castro Neto, A. H. (2021). Accelerated synthesis of graphene oxide from graphene. Nanomaterials, 11(2), 551.

31. Brownson, D. A., & Banks, C. E. (2012). The electrochemistry of CVD graphene: progress and prospects. Physical Chemistry Chemical Physics, 14(23), 8264-8281.

32. Shi, Z., Ci, H., Yang, X., Liu, Z., & Sun, J. (2022). Direct-chemical vapor deposition-enabled graphene for emerging energy storage: versatility, essentiality, and possibility. ACS nano, 16(8), 11646-11675.

33. Yavari, F., Chen, Z., Thomas, A. V., Ren, W., Cheng, H. M., & Koratkar, N. (2011). High sensitivity gas detection using a macroscopic three-dimensional graphene foam network. Scientific reports, 1(1), 166.

34. Seekaew, Y., Phokharatkul, D., Wisitsoraat, A., & Wongchoosuk, C. (2017). Highly sensitive and selective room-temperature NO2 gas sensor based on bilayer transferred chemical vapor deposited graphene. Applied Surface Science, 404, 357-363.

35. An, H., Lee, W. J., & Jung, J. (2011). Graphene synthesis on Fe foil using thermal CVD. Current Applied Physics, 11(4), S81-S85.

36. Ghaemi, F., Abdullah, L. C., Tahir, P. M., & Yunus, R. (2016). Synthesis of different layers of graphene on stainless steel using the CVD method. Nanoscale research letters, 11, 1-6.

37. Liu, W. W., Chai, S. P., Mohamed, A. R., & Hashim, U. (2014). Synthesis and characterization of graphene and carbon nanotubes: A review on the past and recent developments. Journal of Industrial and Engineering Chemistry, 20(4), 1171-1185.

38. Li, X., Cai, W., Jung, I. H., An, J. H., Yang, D., Velamakanni, A., ... & Ruoff, R. S. (2009). Synthesis, characterization, and properties of large-area graphene films. ECS Transactions, 19(5), 41.

39. Steinert, B. W., & Dean, D. R. (2009). Magnetic field alignment and electrical properties of solution cast PET–carbon nanotube composite films. Polymer, 50(3), 898-904.

40. Yang, W., Chen, G., Shi, Z., Liu, C. C., Zhang, L., Xie, G., ... & Zhang, G. (2013). Epitaxial growth of single-domain graphene on hexagonal boron nitride. Nature materials, 12(9), 792-797.

41. Ferrari, A. C., Meyer, J. C., Scardaci, V., Casiraghi, C., Lazzeri, M., Mauri, F., ... & Geim, A. K. (2006). Raman spectrum of graphene and graphene layers. Physical review letters, 97(18), 187401.

42. Ni, Z., Wang, Y., Yu, T., & Shen, Z. (2008). Raman spectroscopy and imaging of graphene. Nano Research, 1, 273-291.

43. Allen, M. J., Tung, V. C., & Kaner, R. B. (2010). Honeycomb carbon: a review of graphene. Chemical reviews, 110(1), 132-145.

44. Ferrari, A. C., & Robertson, J. (2000). Interpretation of Raman spectra of disordered and amorphous carbon. Physical review B, 61(20), 14095.

45. Wongkaew, N., Simsek, M., Griesche, C., & Baeumner, A. J. (2018). Functional nanomaterials and nanostructures enhancing electrochemical biosensors and lab-on-a-chip performances: recent progress, applications, and future perspective. Chemical reviews, 119(1), 120-194.

46. Akhavan, O., Ghaderi, E., & Rahighi, R. (2012). Toward single-DNA electrochemical biosensing by graphene nanowalls. ACS nano, 6(4), 2904-2916.

47. Peng, H. P., Hu, Y., Liu, P., Deng, Y. N., Wang, P., Chen, W., ... & Lin, X. H. (2015). Label-free electrochemical DNA biosensor for rapid detection of mutidrug resistance gene based on Au nanoparticles/toluidine blue–graphene oxide nanocomposites. Sensors and Actuators B: Chemical, 207, 269-276.

48. Salahandish, R., Ghaffarinejad, A., Omidinia, E., Zargartalebi, H., Majidzadeh-A, K., Naghib, S. M., & Sanati-Nezhad, A. (2018). Label-free ultrasensitive detection of breast cancer miRNA-21 biomarker employing electrochemical nano-genosensor based on sandwiched AgNPs in PANI and N-doped graphene. Biosensors and Bioelectronics, 120, 129-136.

49. Lin, C. W., Wei, K. C., Liao, S. S., Huang, C. Y., Sun, C. L., Wu, P. J., ... & Ma, C. C. M. (2015). A reusable magnetic graphene oxide-modified biosensor for vascular endothelial growth factor detection in cancer diagnosis. Biosensors and Bioelectronics, 67, 431-437.

50. He, L., Wang, Q., Mandler, D., Li, M., Boukherroub, R., & Szunerits, S. (2016). Detection of folic acid protein in human serum using reduced graphene oxide electrodes modified by folic-acid. Biosensors and Bioelectronics, 75, 389-395.

51. Castillo, J. J., Svendsen, W. E., Rozlosnik, N., Escobar, P., Martínez, F., & Castillo-León, J. (2013). Detection of cancer cells using a peptide nanotube-folic acid modified graphene electrode. Analyst, 138(4), 1026-1031.

52. Trindade, E. K., Silva, B. V., & Dutra, R. F. (2019). A probeless and label-free electrochemical immunosensor for cystatin C detection based on ferrocene functionalized-graphene platform. Biosensors and Bioelectronics, 138, 111311.

53. Lv, H., Zhang, X., Li, Y., Ren, Y., Zhang, C., Wang, P., ... & Dong, Y. (2019). An electrochemical sandwich immunosensor for cardiac troponin I by using nitrogen/sulfur co-doped graphene oxide modified with Au@ Ag nanocubes as amplifiers. Microchimica Acta, 186, 1-10.

54. Chen, X., Jia, X., Han, J., Ma, J., & Ma, Z. (2013). Electrochemical immunosensor for simultaneous detection of multiplex cancer biomarkers based on graphene nanocomposites. Biosensors and Bioelectronics, 50, 356-361.

55. Du, J., Yue, R., Ren, F., Yao, Z., Jiang, F., Yang, P., & Du, Y. (2014). Novel graphene flowers modified carbon fibers for simultaneous determination of ascorbic acid, dopamine and uric acid. Biosensors and bioelectronics, 53, 220-224.

56. Shao, Y., Wang, J., Wu, H., Liu, J., Aksay, I. A., & Lin, Y. (2010). Graphene based electrochemical sensors and biosensors: a review. Electroanalysis: An International Journal Devoted to Fundamental and Practical Aspects of Electroanalysis, 22(10), 1027-1036.

57. Li, J., Guo, S., Zhai, Y., & Wang, E. (2009). Nafion–graphene nanocomposite film as enhanced sensing platform for ultrasensitive determination of cadmium. Electrochemistry Communications, 11(5), 1085-1088.

58. Kefala, G., Economou, A., & Voulgaropoulos, A. (2004). A study of Nafion-coated bismuth-film electrodes for the determination of trace metals by anodic stripping voltammetry. Analyst, 129(11), 1082-1090.

59. Shao, Y., Wang, J., Wu, H., Liu, J., Aksay, I. A., & Lin, Y. (2010). Graphene based electrochemical sensors and biosensors: a review. Electroanalysis: An International Journal Devoted to Fundamental and Practical Aspects of Electroanalysis, 22(10), 1027-1036.

60. Premkumar, T., & Geckeler, K. E. (2012). Graphene–DNA hybrid materials: Assembly, applications, and prospects. Progress in Polymer Science, 37(4), 515-529.

61. Pedersen, R., Marchi, A. N., Majikes, J., Nash, J. A., Estrich, N. A., Courson, D. S., ... & LaBean, T. H. (2014). Properties of DNA. Handbook of nanomaterials properties, 1125-1157.

62. Ulianas, A., Heng, L. Y., Ahmad, M., Lau, H. Y., Ishak, Z., & Ling, T. L. (2014). A regenerable screen-printed DNA biosensor based on acrylic microsphere-gold nanoparticle composite for genetically modified soybean determination. Sensors and Actuators B: Chemical, 190, 694-701.

63. Chen, Q., Zhang, C., Xue, F., Zhou, Y., Li, W., Wang, Y., ... & Xiao, M. (2013). Enhanced hot-carrier luminescence in multilayer reduced graphene oxide nanospheres. Scientific reports, 3(1), 2315.

64. Zangmeister, C. D., Ma, X., & Zachariah, M. R. (2012). Restructuring of graphene oxide sheets into monodisperse nanospheres. Chemistry of Materials, 24(13), 2554-2557.

65. Rajpoot, K. (2017). Recent advances and applications of biosensors in novel technology. Biosens. J, 6(2), 1-12.

66. Bora, U., Sett, A., & Singh, D. (2013). Nucleic acid based biosensors for clinical applications. Biosens. J, 2(1), 1-8.

67. Koyun, A., Ahlatcolu, E., Koca, Y., & Kara, S. (2012). Biosensors and their principles. A Roadmap of Biomedical Engineers and Milestones, 117-142.

68. Kavita, V. J. J. B. B. S. (2017). DNA biosensors-a review. J. Bioeng. Biomed. Sci, 7(2), 222.

69. Ray, M., Ray, A., Dash, S., Mishra, A., Achary, K. G., Nayak, S., & Singh, S. (2017). Fungal disease detection in plants: Traditional assays, novel diagnostic techniques and biosensors. Biosensors and Bioelectronics, 87, 708-723.

70. Stanfield, C. L., Germann, W. J., Niles, M. J., & Cannon, J. G. (2011). Principles of human physiology. London: Benjamin Cummings.

71. Rathee, K., Dhull, V., Dhull, R., & Singh, S. (2016). Biosensors based on electrochemical lactate detection: A comprehensive review. Biochemistry and biophysics reports, 5, 35-54.

72. Currano, L. J., Sage, F. C., Hagedon, M., Hamilton, L., Patrone, J., & Gerasopoulos, K. (2018). Wearable sensor system for detection of lactate in sweat. Scientific reports, 8(1), 15890.

73. Tur-García, E. L., Davis, F., Collyer, S. D., Holmes, J. L., Barr, H., & Higson, S. P. (2017). Novel flexible enzyme laminate-based sensor for analysis of lactate in sweat. Sensors and Actuators B: Chemical, 242, 502-510.

74. Labroo, P., & Cui, Y. (2013). Flexible graphene bio-nanosensor for lactate. Biosensors and Bioelectronics, 41, 852-856.

75. Gamero, M., Pariente, F., Lorenzo, E., & Alonso, C. (2010). Nanostructured rough gold electrodes for the development of lactate oxidase-based biosensors. Biosensors and Bioelectronics, 25(9), 2038-2044.

76. Ghindilis, A. L., Atanasov, P., & Wilkins, E. (1997). Enzyme-catalyzed direct electron transfer: Fundamentals and analytical applications. Electroanalysis, 9(9), 661-674.

77. Pandey, P., Singh, S. P., Arya, S. K., Gupta, V., Datta, M., Singh, S., & Malhotra, B. D. (2007). Application of thiolated gold nanoparticles for the enhancement of glucose oxidase activity. Langmuir, 23(6), 3333-3337.

78. Keay, R. W., & McNeil, C. (1998). Separation-free electrochemical immunosensor for rapid determination of atrazine. Biosensors and Bioelectronics, 13(9), 963-970.

79. Cowie, C. C., Rust, K. F., Byrd-Holt, D. D., Gregg, E. W., Ford, E. S., Geiss, L. S., ... & Fradkin, J. E. (2010). Prevalence of diabetes and high risk for diabetes using A1C criteria in the US population in 1988-2006. Diabetes care, 33(3), 562-568.

80. Narayan, K. V., Boyle, J. P., Geiss, L. S., Saaddine, J. B., & Thompson, T. J. (2006). Impact of recent increase in incidence on future diabetes burden: US, 2005-2050. Diabetes care, 29(9), 2114.

81. Oliver, N. S., Toumazou, C., Cass, A. E. G., & Johnston, D. G. (2009). Glucose sensors: a review of current and emerging technology. Diabetic medicine, 26(3), 197-210.

82. Chen, C., Xie, Q., Yang, D., Xiao, H., Fu, Y., Tan, Y., & Yao, S. (2013). Recent advances in electrochemical glucose biosensors: a review. Rsc Advances, 3(14), 4473-4491.

83. Guiseppi-Elie, A., Lei, C., & Baughman, R. H. (2002). Direct electron transfer of glucose oxidase on carbon nanotubes. Nanotechnology, 13(5), 559.

84. Lin, Y., Lu, F., Tu, Y., & Ren, Z. (2004). Glucose biosensors based on carbon nanotube nanoelectrode ensembles. Nano letters, 4(2), 191-195.

85. Song, Y., Qu, K., Zhao, C., Ren, J., & Qu, X. (2010). Graphene oxide: intrinsic peroxidase catalytic activity and its application to glucose detection. Advanced Materials, 22(19), 2206-2210.

86. Ikariyama, Y., Yamauchi, S., Yukiashi, T., & Ushioda, H. (1987). One step fabrication of microbiosensor prepared by the codeposition of enzyme and platinum particles. Analytical letters, 20(11), 1791-1801.

87. He, R. X., Lin, P., Liu, Z. K., Zhu, H. W., Zhao, X. Z., Chan, H. L., & Yan, F. (2012). Solution-gated graphene field effect transistors integrated in microfluidic systems and used for flow velocity detection. Nano letters, 12(3), 1404-1409.

88. Lu, X., Zhang, Q., Zhang, L., & Li, J. (2006). Direct electron transfer of horseradish peroxidase and its biosensor based on chitosan and room temperature ionic liquid. Electrochemistry Communications, 8(5), 874-878.

89. Kulakova, I. I., & Lisichkin, G. V. (2022). Potential Directions in the Use of Graphene Nanomaterials in Pharmacology and Biomedicine. Pharmaceutical Chemistry Journal, 56(1), 1-11.

90. Pumera, M. (2011). Graphene in biosensing. Materials today, 14(7-8), 308-315.

91. Patolsky, F., Zheng, G., & Lieber, C. M. (2006). Nanowire-based biosensors.

92. Clark Jr, L. C., & Sachs, G. (1968). Bioelectrodes for tissue metabolism. Annals of the New York Academy of Sciences, 148(1), 133-153.

93. Lee, C., Wei, X., Kysar, J. W., & Hone, J. (2008). Measurement of the elastic properties and intrinsic strength of monolayer graphene. science, 321(5887), 385-388.

94. Kumar, R., Mehta, B. R., Bhatnagar, M., Mahapatra, S., Salkalachen, S., & Jhawar, P. (2014). Graphene as a transparent conducting and surface field layer in planar Si solar cells. Nanoscale research letters, 9, 1-9.

95. Stoller, M. D., Park, S., Zhu, Y., An, J., & Ruoff, R. S. (2008). Graphene-based ultracapacitors. Nano letters, 8(10), 3498-3502.

96. Yang, Y., Ruan, G., Xiang, C., Wang, G., & Tour, J. M. (2014). Flexible three-dimensional nanoporous metal-based energy devices. Journal of the American Chemical Society, 136(17), 6187-6190.

97. Lin, J., Peng, Z., Liu, Y., Ruiz-Zepeda, F., Ye, R., Samuel, E. L., ... & Tour, J. M. (2014). Laser-induced porous graphene films from commercial polymers. Nature communications, 5(1), 5714.

98. Wang, T., Huang, D., Yang, Z., Xu, S., He, G., Li, X., ... & Zhang, L. (2016). A review on graphene-based gas/vapor sensors with unique properties and potential applications. Nano-Micro Letters, 8, 95-119.

99. Jiang, H. (2011). Chemical preparation of graphene-based nanomaterials and their applications in chemical and biological sensors. Small, 7(17), 2413-2427.

100. Patel, S. K., Parmar, J., Kosta, Y. P., Charola, S., Zakaria, R. B., Nguyen, T. K., & Dhasarathan, V. (2020). Graphene-based highly sensitive refractive index biosensors using C-shaped metasurface. IEEE Sensors Journal, 20(12), 6359-6366.

101. Xu, B., Huang, J., Ding, L., & Cai, J. (2020). Graphene oxide-functionalized long period fiber grating for ultrafast label-free glucose biosensor. Materials Science and Engineering: C, 107, 110329.

102. Nejad, H. E., Mir, A., & Farmani, A. (2019). Supersensitive and tunable nano-biosensor for cancer detection. IEEE Sensors Journal, 19(13), 4874-4881.

103. Vishnubhotla, R., Sriram, A., Dickens, O. O., Mandyam, S. V., Ping, J., Adu-Beng, E., & Johnson, A. C. (2020). Attomolar detection of ssDNA without amplification and capture of long target sequences with graphene biosensors. IEEE Sensors Journal, 20(11), 5720-5724.

104. Romano, S., Lamberti, A., Masullo, M., Penzo, E., Cabrini, S., Rendina, I., & Mocella, V. (2018). Optical biosensors based on photonic crystals supporting bound states in the continuum. Materials, 11(4), 526.

105. Patel, S. K., Parmar, J., Ladumor, M., Ahmed, K., Nguyen, T. K., & Dhasarathan, V. (2020). Numerical simulation of a highly directional optical leaky wave antenna using diamond-shaped graphene perturbations. Applied optics, 59(8), 2225-2230.

106. Torrente-Rodríguez, R. M., Lukas, H., Tu, J., Min, J., Yang, Y., Xu, C., ... & Gao, W. (2020). SARS-CoV-2 Rapid Plex: a graphene-based multiplexed telemedicine platform for rapid and low-cost COVID-19 diagnosis and monitoring. Matter, 3(6), 1981-1998.